TECHNISCHE UNIVERSITÄT MÜNCHEN
Department Chemie
Lehrstuhl I für Technische Chemie

Kinetic and Reactor Modeling for the Methanation of Carbon Dioxide

David Schlereth

Vollständiger Abdruck der von der Fakultät für Chemie der Technischen Universität München zur Erlangung des akademischen Grades eines

Doktor der Naturwissenschaften (Dr. rer. nat.)

genehmigten Dissertation.

Vorsitzender:	Univ.-Prof. Dr. T. Brück
Prüfer der Dissertation:	1. Univ.-Prof. Dr. K.-O. Hinrichsen
	2. Univ.-Prof. Dr. K. Köhler
	3. Univ.-Prof. Dr. K. Reuter

Die Dissertation wurde am 02.03.2015 bei der Technischen Universität München eingereicht und durch die Fakultät für Chemie am 28.04.2015 angenommen.

Acknowledgments

There have been so many people who contributed to this work, may it be in scientific or non-scientific ways. I would like to thank all, who have supported or helped in either way during the last years.

I would like to thank Prof. Dr.-Ing. Kai-Olaf Hinrichsen, first of all for the opportunity to work in his group on this interesting topic. I appreciate the given freedom and trust of letting me direct my work according to my interests, his supervision, and steady interest in my work as well as the given opportunities to present our results on conferences.

The last three years would have never been the same without my colleagues. Working atmosphere and cooperativeness could not have been better and might be unique at the Chair of Chemical Engineering. Thanks to all of you for this throughout the years! I would also not have missed our non-scientific leisure activities. I would like also to thank Tassilo von Aretin, Matthias Fichtl and Franz Koschany, who have always been open for discussion and brought up new ideas and solutions. Special thank goes to my peer Franz Koschany, who performed all the kinetic measurements forming the basis for the developed kinetic models. I highly appreciate his effort, stamina and patience in doing so.

Many students contributed with their theses or research practicals to this work, which I am grateful for. I would like to mention in particular Markus Hammerl, Katrin Mietaschk and Philipp Donaubauer.

Parts of this thesis have been worked out in context of the COOMeth project at TU München. I would like to thank our project partners from TUM Prof. Dr. Klaus Köhler and Oliver Thomys as well as our partners from industry Prof. Dr.-Ing. Rolf Bank, Prof. Dr. Richard Fischer, Dr. Andreas Geisbauer, Hans-Joaching Kuhs, Dr. Nicole Schödel, Florian Winkler, and Dr. Alexander Zipp.

Last but not least I would like to thank my family for the support and confidence not only during the doctorate, but also during the years of study before.

Abstract

Due to fluctuating and locally concentrated availability of renewable power, so-called Power-to-Gas (PtG) concepts are in discussion as technology to store energy in large scale, potentially for time scales from hours to months. The methanation of carbon dioxide constitutes the central process in methane-based PtG concepts, which are thought of as promising since they could be integrated in the existing and reliable infrastructures of the natural gas and power grids instead of installing a completely new, not yet field-tested technology. Though the methanation of carbon dioxide, for example as heterogeneously, by metallic nickel catalyzed reaction has been well known since beginning of the 20th century, essential questions towards technical realization have not yet been answered. This thesis focuses on aspects of both kinetics and reaction engineering for the methanation of carbon dioxide.

The high exothermicity makes temperature control in reactors a key issue in view of requirements to reactors and catalyst lifetime. For this reason, by means of reactor modeling externally cooled, single-pass fixed-bed reactors of technical dimension are studied in the first part of the thesis. Four differently detailed reactor models are adopted and compared for the methanation reaction. A simple 1D pseudo-homogeneous plug-flow reactor model neglecting all possible mass and heat transfer limitations constitutes the reference. By comparison to different 2D pseudo-homogeneous models it is found that 1D description is sufficient for assessment of conversion and maximum temperatures. Even at diluted feed gas compositions, pronounced radial temperature profile cannot be established without runaway of the reactor. With increasing cooling temperatures, fixed-bed reactors are operated almost isothermally up to a certain threshold before entering a parametric sensitive region, where a slight increase in cooling temperature provokes maximum temperatures to rise above 900°C. This runaway behavior is predicted similarly by 1D and 2D models. In contrast, transition to heterogeneous models, which take intraparticle and external heat and mass transfer into account, is necessary to evaluate the reactor performance. Hereby, the dusty gas model is chosen to describe mass transport on the pellet scale. Results show that in particular intraparticle mass transfer decreases reaction rates in the hot spot region of the reactor, thus slows down the heat release and limits hot spot temperatures.

Aside from exploiting mass transfer limitations on the pellet scale, two measures are presented to reduce maximum temperatures. By separately feeding CO_2 and H_2 to the reactor, which is exemplified by modeling of a fixed-bed membrane reactor, heat release can be distributed over a larger volume and maximum temperatures can be limited. As second concept, reactors equipped with metallic honeycombs are studied as example of structured reactors with facilitated radial heat transport. Hereby, a 2D heterogeneous model proposed in literature is first validated by comparison to a detailed 3D CFD

model. In the latter one, the honeycomb structure is implemented and heat, mass and momentum balances are solved. For the test case of an exothermic first-order reaction, the continuum model predicts conversions and temperature profiles in close agreement to the 3D model. Systematic deviations found at conditions that provoke sharp radial temperature gradients could be explained by usage of global heat and mass transfer coefficients and by the intrinsic disregard of radial dispersion of mass in the continuum model. After validation, the continuum model is adopted to the methanation reaction and compared to fixed-bed reactors. Modeling results confirm conclusions drawn from the assessment of effective overall heat transfer coefficients that honeycomb reactors are superior in terms of heat transfer properties in case of compact reactors. Thus, they can be operated isothermally up to higher temperatures. Yet, the approach to equilibrium suffers from a lower catalyst inventory in comparison to fixed-bed reactors.

Thirdly, methanation kinetics are studied. Ni/Al_2O_3 catalysts are prepared by co-precipitation at constant pH value and characterized by elementary analysis, XRD, N_2 physisorption, H_2 chemisorption and temperature programmed reduction (TPR). It is found that Takovite with its characteristic hydrotalcite layer structure is formed by precipitation thus allowing for high specific surfaces after calcination. All XRD reflexes of calcined samples can be assigned to a mixed oxide (disordered oxide spinel intermediate), whose nickel content is fully reduced under the reduction conditions employed to metallic nickel according to TPR results. Kinetic models are derived and discriminated after parameter estimation on basis of a supplied dataset reflecting intrinsic kinetics. It proved crucial to consider the inhibiting influence of product components on the kinetics, in particular in approach to equilibrium. Langmuir-Hinshelwood-Hougen-Watson-type rate equations allow a significantly better representation of the kinetics in comparison to power law and extended power law rate equations. The derived model is capable of reflecting the kinetics in a wide range of compositions and from differential to almost complete conversion in thermodynamic equilibrium.

In consequence of high temperatures probably inevitably present in technical operation, an understanding of catalyst deactivation phenomena is desirable. In contrast to methanation catalysts, $Cu/ZnO/Al_2O_3$ methanol synthesis offer unique possibilities to study in particular sintering of a coprecipitated catalyst system in differentiation to classical supported metals due to the available amount and quality of characterization results. In the last part of the thesis, the deactivation and in particular sintering behavior is studied with numerical methods on basis of supplied transmission electron microscopy characterization results for methanol synthesis catalysts. Copper particles agglomerate more randomly as predetermined by structure than predicted by classical agglomeration models based on radius dependent mobilities of metal particles. Evolving copper particle size distributions can be described by a proposed random collision model.

Contents

1 Introduction

1.1 Motivation

Against the background of climate change, expected depletion of easily exploitable fossil fuels and the projection of a worldwide doubled electricity demand by the middle of the century [1, 2], economies face the challenge to shift energy supply towards sustainable and renewable resources in economically feasible manner. The European Commission formulated a roadmap [3] for long-term climate and emission objectives: the European Union should cut its emissions to 80% below 1990 levels by 2050 with milestones of 40% reduction by 2030 and 60% by 2040 in view of the aim approved by the Framework Convention on Climate Change of the United Nations in Cancun in 2010 [4] to hold global warming below 2°C compared to the temperature in preindustrial times. Plans of the German Government are not less ambitious. In 2012, the electric power consumption of Germany amounted to 606.7 TWh with a portion of 23.6% renewable energy sources [5]. By 2025, 40 to 45% of electric energy should stem from renewable energy sources according to the "Erneuerbare-Energien-Gesetz 2014" [6]. In particular, an expansion of 2500 MW capacity each of solar energy and on-shore wind energy are aspired per year, in addition to 6500 (15000) MW off-shore wind energy capacity by 2020 (2030).

However, the transition from conventional power plants to renewable resources not only drives the progress in power generation technologies, but also demands changes in infrastructure and consumption. First of all, renewable solar and wind energy is not constantly available as power from nuclear, coal or gas sources is, but fluctuates on different time scales. As exemplary depicted in figure 1.1 for 2013, the monthly amount of available wind energy fluctuated from 37% in May in relation to the maximum amount offered in December. Solar energy in contrast was hardly available with amounts $< 10\%$ in winter months compared to July. Also fluctuation in scale of days and hours is enormous. Apart from the temporal aspect, also the local one needs to be considered. Today's power generation and power grid is - as historically evolved - concentrated relatively close to centers of consumption [7] in view of feasible transport costs for transport of conventional energy sources. In contrast, power generation by wind is expected to be predominantly located in areas of advantageous climate conditions: regarding Germany, the North German Plain as well as off-shore areas are most suitable.

The main centers of consumption, however, are located in the South (Southern Bavaria, Baden-Württemberg), South-West (Rhein-Main area) and West (Ruhr). Photovoltaics and power generation on basis of biomass will furthermore cause many local units that need to be managed and integrated in the power grid.

As consequences on temporal fluctuations and local shift of power generation, a mix of new and established technologies will have to be promoted to handle the transition to renewables. Beside the extension of the power grid and implementation of 'smart grids', new energy storage and transport technologies are expected to be employed. Concerning energy storage, a study of the "Verband der Elektrotechnik, Elektronik, Informationstechnik" prognosticates a demand of 14 GW (70 GWh) for short-term (5h) and 18 GW (7.5 TWh) for long-term (17 days) storage capacity for Germany on basis of a portion 80% renewable energy supply [9]. Electrical energy storage (EES) technologies for large-scale, stationary applications are categorized into four groups: mechanical, electrical, chemical, and electrochemical [10]. Today, almost exclusively mechanical storage systems are employed: pumped hydroelectric systems (PHS) account with 127000 MW for 99% of the worldwide storage capacity, followed with large gap by compressed air storage (CAES) (440 MW). Concerning electrochemical storage systems for large-scale grid application, today only sodium/sulfur battery technology is available with a power capacity of 315 MW installed worldwide (year 2011) [1]. However, facing the demands of site selection, initial investment and construction times in case of PHS, research and development on alternative storage systems has been intensified during the last years, beginning from electrical high-power supercapacitors over mechanical high-power flywheels to different electrochemical approaches comprising batteries, fuel cells, and redox flow cells [1, 2, 10, 11]. Furthermore, in view of various requirements in dependence of storage function in terms of discharging time, power-to-energy ratio, capacity and others, it seems unlikely that a single technology will fulfill the different demands and rather a so-called portfolio approach may be the most effective [1]. Electrochemical energy storage, which probably is the most traditional form of EES, might offer decent features like direct storage and release of electric energy, flexible power and energy characteristics, pollution-free operation, high safety at modest site requirements as well as modularity and scalability [1, 11]. However, high costs up to now do not meet the economic requirements and limit the propagation of electrochemical energy storage, in particular in large scale energy application [1, 2].

In this context, the so-called Power-to-Gas (PtG) concept represents a promising technology for large-scale long-term energy storage with the potential of storage capacities of TWh: energy is 'stored' in form of chemical bond energy of gas phase molecules like hydrogen, methane or ammonia. For this reason, the approach is also referred to as chemical energy storage. As a common to suggested power-to-gas concepts, energy to

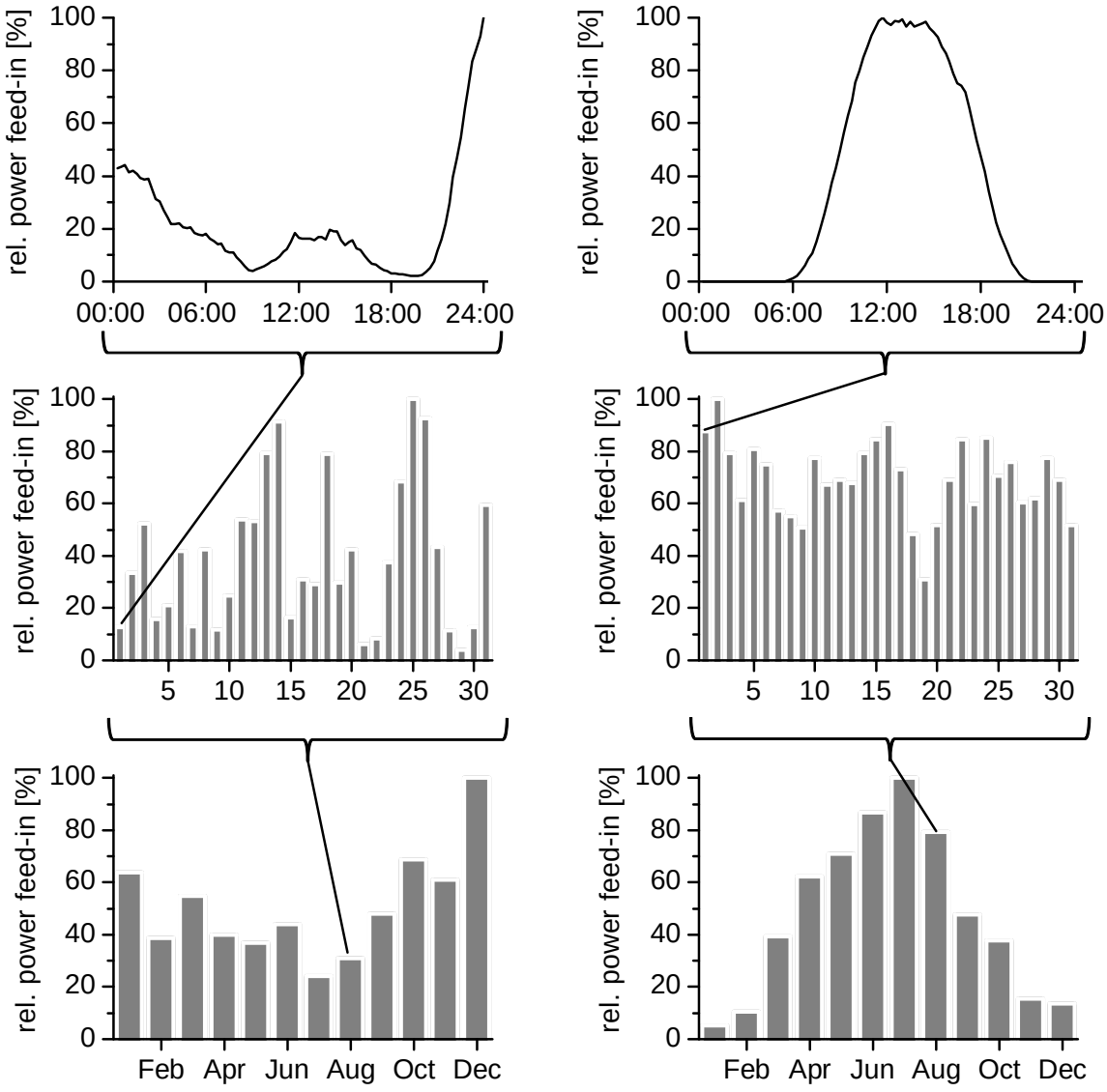

Figure 1.1: Fluctuation in renewable energy provided in 2013 in scale of hours, days and months for the control zone throughout the northern and eastern part of Germany[1] (based on data provided by 50Hertz [8])
left: wind energy, right: solar energy
bottom: year 2013, center: August 2013, top: 1st August 2013

[1] The control zone of 50Hertz covers approximately 30% of the German territory, about 40% of wind and 20% of photovoltaics power capacity installed in Germany [8].

be stored is used for electrolyzing water to oxygen and hydrogen in the first step. In principle, hydrogen itself can be referred to as chemical energy carrier that can be stored, transported, and reconverted to electric energy in fuel cells or gas turbines. However, one might argue that hydrogen as energy carrier suffers from a row of drawbacks: in case of gaseous hydrogen it requires large volumes because of a relatively low energy density, which is about one third of that of natural gas, and ensuring of of leak-tight vessels might be difficult. Liquefaction is an alternative, however suffers from relatively sophisticated engineering and handling. Research concerning storage as hydride is still needed to reduce weight and costs of the host material [11]. Despite those issues, there are recent developments that try to establish a hydrogen infrastructure (cf. [12]). As interim solution, hydrogen could also be fed to the natural gas grid to some extent. Currently, regulations allow to feed a maximum of 5vol.% hydrogen as additional gas [13]. Higher contents might imply the necessity of additional investment in compressor, measurement and control system of the gas grid and a careful investigation of end user processes. In particular, gas turbines might be sensitive towards considerable hydrogen contents in natural gas [14].

According to the concept of Renewable Power Methane (RPM) suggested by M. Sterner in 2009 [15], hydrogen is, however, not the chemical energy carrier, but an intermediate that is reacted with carbon dioxide to methane and water. With methane as chemical energy carrier, one can fall back on existing infrastructure and technology. There is no new storage or transport infrastructure to be established, but the natural gas grid as largest existing storage facility with available and reliable technology can be used. With the capacities of hundreds of TWh it enables in principle even a seasonable storage of renewable energy virtually without capacity and time limits [15, 16]. In Germany, the current storage capacity of the natural gas grid amounts to more than 200 TWh (in comparison to 0.04 TWh of pumped hydro storage)[16], which corresponds to 20% of the annual natural gas consumption [14]. Also the energy transfer capacities are an order of magnitude larger compared to electrical power lines. Transport via the gas grid might as well be interesting: the transmission losses add up to 0.5% per 1000 km, which outperforms the electricity grid with 3-10% per 1000 km [14].

There are different scenarios proposed, how RPM can be integrated into the energy system in dependence of the source of carbon dioxide [14, 15]:

- Concepts with bioenergy plants: CO_2 is either separated from the biogas upgrading process or the biogas consisting of CH_4 and CO_2 is directly fed into the methanation process. This way methane leakage is minimized and methane yields compared to conventional biogas plants with gas conditioning by CO_2 separation can be doubled [15, 16].

- Concepts with waste management: CO_2 emissions of sewage plants, landfill sites and CO_2-intensive industries are used as feedstock. In particular, waste gases from cement industries or iron and steel production might offer potential: in clinker production around 0.5 kg of CO_2 are emitted while burning 1 kg of limestone. In the latter one, coke is used as reducing agent and carbon dioxide is released as oxidized product. On the worldscale, 6 and 9% of carbon dioxide emission stem from the steel and cement sector, respectively. Furthermore, the CO_2 concentration in flue gases of those processes is very high with up to 30 mol% [14].

- Stand-alone concepts: CO_2 is recovered directly from the air. This is the most costly scenario and unlikely as long as more concentrated sources are available, but probably the only way to separate past and spread emissions of small and mobile CO_2 sources which is discussed to be necessary in future to mitigate climate change [15].

- Concepts with fossil fuels: CO_2 is separated from flue gases of fossil power plants in case of post-combustion capture. Alternatively, the gas mixture is processed prior to the combustion process, if fuel is first reacted with water steam and air or oxygen and further shifted to hydrogen and carbon dioxide in the so-called pre-combustion or oxy-combustion configuration [14].

However, the ease in handling methane instead of hydrogen is paid for by a lower overall efficiency in comparison. The conversion efficiency concerning the electrolysis of water to hydrogen and oxygen ranges between 60-80% for alkaline water electrolysis [17]. In case of RPM, additionally an efficiency of approximately 75-80% has to be accounted for by methanation of the gas mixture of hydrogen and carbon dioxide. In contrast to the electrolysis, where there still is large optimization potential, the optimization of the methanation efficiency is limited due to the exothermicity of the reaction to a better heat use for instance [16]. Concerning the methanation reaction itself, the maximum value achievable is limited to 83% since 17% are converted to heat during the reaction according to thermodynamics [14]. Combining the electrolysis and methanation efficiency, the total RPM efficiency values range between 46-64% without accounting withdrawals of carbon dioxide separation for the feed and its compression according to the methanation process conditions. In addition to the loss in efficiency, also investment cost will rise due to additional unit operations necessarily associated with the methanation process. In contrast, the reconversion to electricity can rely fully on existing technology such as gas turbines and combined heat and power plants which allow efficiencies about 60% in combined cycle power plants [15, 18]. All efficiencies combined, the total power storage efficiency amounts to the range of about 30%-40%.

In total, power-to-gas seems currently as a possible technology for large scale storage in the long term, though not yet economically feasible with the current energy mix. Aside from reconversion to electricity as part of load and generation management described above, one can also think of employing RPM as renewable heat source or as transport fuel.

1.2 Objectives

Though the methanation reaction of carbon dioxide as heart of the RPM power-to-gas concept has been well known since the beginning of the 20th century - it was first described by Paul Sabatier in 1902 [19] -, essential questions concerning catalyst systems, kinetics and reaction engineering have not been answered. In this thesis, general reaction engineering aspects with emphasis on temperature control as well as heat and mass transport processes in fixed-bed and structured reactors are studied by reactor modeling. Furthermore, kinetic models are derived and parameters are estimated for a coprecipitated Ni/Al_2O_3 catalyst system. The work is rounded up by a modeling study of deactivation of another coprecipitated catalyst system technically employed, ternary $Cu/ZnO/Al_2O_3$ catalysts for methanol synthesis from synthesis gas. The latter catalysts have been investigated and characterized thoroughly in literature by various techniques and for this reason offer unique opportunities to study possible deactivation mechanisms of coprecipitated catalysts systems, in particular sintering of metal crystallites. As will be shown in the kinetic study of CO_2 methanation, understanding of deactivation phenomena also plays a crucial role in case of the Ni catalyzed methanation reaction. In detail, the thesis is subdivided into the following secluded chapters:

Chapter 1 gives a basic introduction in motivation and objectives of the work. In particular, the integration of the methanation process in power to gas concepts and their relevance have been highlighted against the background of a shifted energy mix towards renewable resources.

Chapter 2 lays down the theoretical setting of the thesis: first, selected catalyst systems that have been reported as catalytically active for the Sabatier reaction are introduced, followed by a survey on proposed mechanisms and kinetic models for Ni based catalysts. Second, an overview over CO_2 methanation and - in view of the similarity - conventional synthetic natural gas (SNG) processes based on synthesis gas is given.

Chapter 3 exposes the methodological background: basic concepts of reactor modeling on different levels of details are presented. Finally, modeling of mass transport is porous media is described in detail.

Chapter 4 evaluates single-pass fixed-bed reactors of technical dimension for the methanation of carbon dioxide by reactor modeling comprising 1D and 2D pseudo-homogeneous and heterogeneous reactor models. Thermal runaway behavior and its influencing parameters are discussed. The mitigating effect of intraparticle mass transport limitations to the temperature rise on the reactor level is assessed by implementation of a dusty gas modeling approach for convective and diffusive mass transport in porous catalyst pellets into a 1D reactor model. Finally, the potential of structured reactors is highlighted by simulation of a fixed-bed membrane reactor. This chapter has already been published in a peer-reviewed journal under the title *"A fixed-bed reactor modeling study on the methanation of CO_2"* [20].

Chapter 5 covers the modeling of metallic honeycombs as catalyst support structures for highly exo- or endothermic reactions. First, a continuum model adapted from literature is compared to a more detailed 3D CFD model for validation and evaluation of the model feasibility to honeycombs of structures designed for handling of thermally demanding reactions. In the second part, the methanation of carbon dioxide is implemented in the continuum model. Advantages and drawbacks in comparison to fixed-bed reactors are discussed based on modeling results. Section 5.1 of this chapter has also been published in a peer-reviewed journal under the title *"Comparison of a pseudo-continuous, heterogeneous 2D conductive monolith reactor model to a 3D CFD model"* [21], section 5.2 has been submitted for publication under the title *"Metallic honeycombs as catalyst supports for the methanation of carbon dioxide"* [22].

Chapter 6 presents a kinetic study on Ni/Al_2O_3. A series of catalyst with varying Ni:Al ratio is prepared by coprecipitation at constant pH and characterized by elementary analysis, powder X-ray diffraction (XRD), temperature programmed reduction (TPR) as well as N_2 physisorption and H_2 chemisorption. Different approaches for the derivation of kinetic models are evaluated and parameters of the models are estimated based on a dataset supplied for a chosen catalyst sample. This chapter has been submitted for publication in a peer-reviewed journal entitled as *"On the kinetics of the methanation of carbon dioxide on coprecipitated Ni/Al_2O_3"* under joint first authorship by Franz Koschany and David Schlereth [23].

Chapter 7 contains a study on the deactivation kinetics of ternary $Cu/ZnO/Al_2O_3$ catalysts for methanol synthesis. It includes a modeling approach for describing the sintering behavior of coprecipitated catalyst systems that might also be transferable as a toolbox to coprecipitated methanation catalysts. However, in contrast to the methanol catalyst system, which has been studied extensively in the past

because of its technical relevance, a deeper insight in deactivation phenomena and kinetics by detailed in- and ex-situ characterization also of aged catalyst samples is required first in case of the methanation catalyst system. This chapter has been submitted for publication in a peer-reviewed journal entitled as *"Kinetics of Deactivation on $Cu/ZnO/Al_2O_3$ Methanol Synthesis Catalysts"* under joint first authorship by Matthias Fichtl and David Schlereth [24].

Chapter 8 summarizes the results of this thesis and gives an outlook on possible future research directions.

2 Theoretical and technological background

2.1 Catalyst systems

The methanation of carbon dioxide is an exothermic as well as exergonic reaction with volume contraction:

$$\mathrm{CO_2} + 4\,\mathrm{H_2} \rightleftharpoons \mathrm{CH_4} + 2\,\mathrm{H_2O} \quad \Delta H_\mathrm{R}^0 = -165\ \mathrm{kJ/mol} \quad \Delta G_\mathrm{R}^0 = -114\ \mathrm{kJ/mol}$$

According to Le Chatelier's principle, low temperatures and high pressures shift the equilibrium to the product side (see section 4.4.1 for quantitative evaluation). Nevertheless, though thermodynamically favored, the reduction of carbon dioxide to methane comprising the transfer of eight electrons is kinetically hindered, so that reaction rates are not measurable under common conditions in absence of catalysts. In contrast, heterogeneous catalysts facilitate fast reaction rates and selectivities close to 100% for the Sabatier reaction. Many metals of group VIII, i.a. Ni, Pd, Pt, Co, Rh, Fe, and Ru, have been reported as catalytic active, with marked differences in turnover frequencies and selectivities. Concerning the selectivity, next to the direct conversion of CO_2 to CH_4, also the reverse water-gas-shift (RWGS) reaction, possibly followed by CO methanation, chain-growth reactions on basis of CO_2 or CO as well as carbon deposition might be catalyzed (table 2.1).

Commonly, Ni and Ru are rated as most promising for the Sabatier reaction (cf. the review in [25]). In contrast, Pt preferably catalyzes the RWGS [26], while chain-growth reactions catalyzed by Co and Fe are exploited in Fischer-Tropsch synthesis [27]. Apart from the metal, also various oxides have been employed as carrier. Ni has, amongst others, been supported on Al_2O_3, SiO_2, MgO, $MgAl_2O_4$, TiO_2, ZrO_2 and CeO_2 as well as on mixtures of those and mixed oxides as catalyst for CO_2 methanation. Most catalyst studies address the preparation of classical supported metal catalyst systems by different impregnation techniques, characterized by a relative low metal content, which, however, allow high metal dispersion. For instance, Vance and Bartholomew [28] studied adsorption properties and methanation activity of Ni supported on SiO_2, Al_2O_3 and

Table 2.1: Overview reaction paths

	ΔH_R^0 [kJ/mol]	ΔG_R^0 [kJ/mol]
Reverse water-gas-shift reaction (RWGS)		
$CO_2 + H_2 \rightleftharpoons CO + H_2O$	41	29
CO methanation		
$CO + 3\,H_2 \rightleftharpoons CH_4 + H_2O$	-204	-142
chain growth (CO_2)		
$CO_2 + 3\,H_2 \rightleftharpoons -CH_2- + 2\,H_2O$	~ -110	-
chain growth (CO)		
$CO + 2\,H_2 \rightleftharpoons -CH_2- + H_2O$	~ -150	-
Carbon deposition/Boudouard reaction		
$2\,CO \rightleftharpoons C + CO_2$	-172	-120

TiO_2 and found increasing activity and selectivity in this order, which was attributed to increasing metal support interaction. Similarly, Chang and coworkers [29, 30] supported Ni on silica gel, silica derived from rice husk ash and alumina modified samples thereof for CO_2 methanation. Due to the formation of mixed oxides of nickel oxide and alumina as well as strong interaction between metal and oxide concerning the alumina samples, high dispersion could be obtained in particular with these systems.

Apart from classical supported systems, also the preparation of high-loaded metal catalysts, which might rather be characterized as full-catalysts, has been addressed in the literature: Abelló et al. [31] prepared a nickel-alumina catalyst by coprecipitation out of nitrate solutions of Ni and Al in molar ratio of five at constant pH value, which resulted in catalysts with a Ni loading of about 70wt%, still preserving small Ni crystallites in the range of 6 nm crystallite size. Upon characterization by XRD, TEM, TPR and N_2-physisorption, the catalyst was tested for CO_2 methanation under varying conditions in terms of temperature, pressure, H_2/CO_2 molar ratio and space velocity. It was appraised as active, stable and selective: a comparison by the authors to other Ni systems in literature revealed its superior activity, which, however, seems difficult to assess because of differing reaction conditions. The catalyst moderately deactivated from an initial conversion of 92.4% close to equilibrium to 83.5% within 500 h of operation at 400°C. The selectivity to methane was above 99% with carbon monoxide and traces of ethane as byproducts. Since high Ni loadings proved advantageous, as it did in case of CO methanation catalysts, fully metallic catalysts have also been proposed for the Sabatier reaction: Raney® nickel known as common hydrogenation catalyst was studied and appeared to show a high reactivity [32]. Pure metallic nickel, prepared by decomposition of nickel oxalate, was employed for mechanistic studies. However, this system revealed low specific surface areas of about 2 m^2/g and poor stability due to sintering [33].

Different conditions in terms of temperatures, pressures, feed composition and residence times impede a qualified comparison of systems investigated in different studies. Nevertheless, there seems consensus on Ru showing the highest selectivity and in particular activity at low temperatures [25, 34, 35]. However, in view of economic feasibility concerning a large scale technical application and the fact that Ni catalysts allow fast reaction rates between 200 and 300°C such that heat removal and temperature control are the most critical issues in operation of fixed-bed reactors, this work focuses on Ni systems and their kinetics. But since reaction engineering aspects investigated in this work arise from the interaction of fast reaction rates, thermochemistry and transport phenomena, it is expected that findings might qualitatively be transferred to other catalyst systems, though they may be operated in a different temperature range.

2.2 Mechanism and Kinetics

2.2.1 Mechanistic proposals

Though the methanation of CO_2 in principle seems to be a simple reaction, the prevalent mechanism catalyzed for example by metallic Ni is still far from being understood and many proposals comprising various surface intermediates have been published, either based on experimental investigation or theoretical calculation. The mechanisms might be grouped into two classes: (1) mechanisms comprising adsorbed CO and subsequent reaction identical to the CO methanation as well as (2) "direct" methanation without CO intermediate to methane. The hypothesis of a CO intermediate was supported in the 1980s via a surface science approach: Peebles and coworkers [36] investigated the reaction of CO_2 and H_2 on Ni(100). They found that the activation energy of methane formation is in close agreement to the one of carbon monoxide methanation. Temperature programmed desorption (TPD) and temperature programmed surface reaction (TPSR) studies also supported the hypothesis: carbon dioxide was adsorbed on Ni surfaces under elevated temperature. The system was then cooled, and subsequently overflowed by hydrogen while heating with a defined heating ramp. First water desorbed. This was interpreted as reaction product of hydrogenation of oxygen on the Ni surface, stemming from the dissociative adsorption of CO_2 to CO and O. The TPSR spectrum after the desorption step of water closely resembled that obtained after adsorbing molecular carbon monoxide [37]. Fujita et al. [38] observed marked differences concerning the transient kinetics of the methanation of CO and CO_2. Yet, a CO intermediate was postulated: upon switching the flow to pure hydrogen after steady state has been reached for methane formation out of CO_x and hydrogen, in case of CO an instant increase in methane formation to a factor of about 20 in relation to steady state reaction rates

occurred. This was interpreted as consequence of reversibly adsorbed CO in steady-state, which strongly inhibits methane formation. In contrast, in case of CO_2, water formation decreased instantly to one half of the steady state value, followed by a monotonic decrease of methane and water formation in ratio 1:1. This was attributed to water being formed in two distinct steps of considerably different rates. After the first step, strongly adsorbed carbon monoxide species were postulated in appreciable extent that subsequently react to surface carbon and oxygen, in analogy to CO methanation.

Schild et al. [39] prefer a direct route: via DRIFT spectroscopy surface formate is identified as abundant surface species, which is assumed as immediate precursor to methane. This conclusion, however, seems ambiguous since also doubly and singly bound CO species are detected, which might be precursors to methane. The role of formate is also investigated by Vesselli and coworkers [40, 41], who combined DFT calculations and experimental UHV techniques to gain mechanistic insights. First, on basis of DFT calculations for a Ni(110) surface, it was concluded that formate is formed via reaction of chemisorbed carbon dioxide and hydrogen at temperatures as low as 150 K. However, formate proves very stable, does not yield CO as intermediate and acts just as a dead-end spectator. To compensate for the well-known pressure gap in UHV studies, experiments with atomic hydrogen beams were conducted. XPS spectra after exposure to carbon dioxide and atomic hydrogen led to the conclusion that hydrogen-assisted C-O bond cleavage of CO_2 proceeds readily at 90 K to adsorbed carbon monoxide. This was also supported by TPD and HREEL spectroscopy. It was concluded that formate, which is always detected at standard conditions as well, is a spectator molecule formed via a Langmuir-Hinshelwood reaction, while the reaction proceeds through competing parallel Eley-Rideal processes, yielding formate or adsorbed CO at very low temperatures by hydrogen assisted C-O bond cleavage via a hydrocarboxyl intermediate. A direct mechanism was derived on the contrary by Bothra et al. on basis of DFT calculations [42]. Starting from adsorbed carbon dioxide on Ni(110), the pathway requiring the lowest activation barrier was found to proceed over hydroxyl carbonyl COOH, whose formation is the rate determining step:

$$^*CO_2 \xrightarrow{+H_2} {}^*COOH + {}^*H \longrightarrow {}^*C(OH)_2 \xrightarrow[-H_2O]{+H_2} {}^*CHOH \xrightarrow{+H_2} {}^*CH_2OH + {}^*H$$

$$\xrightarrow[-H_2O]{+H_2} {}^*CH_3 + {}^*H \longrightarrow CH_4(g)$$

Adsorbed carbon monoxide can also be formed by dissociation of the dihydroxy intermediate $C(OH)_2$, but its subsequent reaction to methane is clearly disfavored due to larger activation barriers. Starting from a formate intermediate, however, the reaction proceeds over a methoxy intermediate that is subsequently dissociated to methane and adsorbed oxygen [42]:

$$^*OCHO + {}^*H \xrightarrow{+H_2} {}^*OCH_2OH + {}^*H \xrightarrow[-H_2O]{} OCH_2 \xrightarrow{+H_2} {}^*OCH_3 + {}^*H$$

$\xrightarrow[-CH_4]{} {}^{*}O \xrightarrow{+H_2} H_2O(g)$

Both studies by Vesselli et al. [41] and Bothra et al. [42] are highly interesting in view of results of chemical transient kinetics which indicate that there may be two mechanisms operating in parallel [33]: one fast route dominating instantly after switching to reactive gases where the Ni surface is less covered and a slow route becoming dominant because a covered surface hinders the fast pathway. Candidates for the fast mechanism might be mechanisms comprising hydroxycarboxyl species while the mechanism prevalent at high coverages might involve "formate-derived" [33] species that have accumulated on the surface due to their low hydrogenation.

Independent on the question about a CO or direct mechanism, also the mechanism of CO methanation is still an open discussion in literature and a coherent microkinetic model describing the prevalent elementary reaction is still to be presented, though in contrast to the CO_2 methanation proposals have been formulated. A mechanism comprising adsorbed carbon is often assumed:

$$
\begin{aligned}
1: &\quad CO + {}^{*} \rightleftharpoons {}^{*}CO \\
2: &\quad H_2 + 2\,{}^{*} \rightleftharpoons 2\,{}^{*}H \\
3: &\quad {}^{*}CO + {}^{*} \rightleftharpoons {}^{*}C + {}^{*}O \\
4: &\quad {}^{*}C + {}^{*}H \rightleftharpoons {}^{*}CH + {}^{*} \\
5: &\quad {}^{*}CH + {}^{*}H \rightleftharpoons {}^{*}CH_2 + {}^{*} \\
6: &\quad {}^{*}CH_2 + {}^{*}H \rightleftharpoons {}^{*}CH_3 + {}^{*} \\
7: &\quad {}^{*}CH_3 + {}^{*}H \rightleftharpoons CH_4 + 2\,{}^{*} \\
8: &\quad {}^{*}O + {}^{*}H \rightleftharpoons {}^{*}OH + {}^{*} \\
9: &\quad {}^{*}OH + {}^{*}H \rightleftharpoons {}^{*}H_2O + {}^{*} \\
10: &\quad {}^{*}H_2O \rightleftharpoons H_2O + {}^{*}
\end{aligned}
$$

After adsorption of CO and C-O bond cleavage carbon and oxygen are hydrogenated via carbenes and hydroxyl to methane and water, respectively [43–45]. The mechanism was for instance promoted by Araki and Ponec based on experiments with labeled ^{13}CO [43]. If adopted to CO_2 methanation, carbon dioxide is either assumed to adsorb dissociatively to CO and O [46], to adsorb molecularly and to be readily dissociated in the next step [47] or to involve hydrogenated species like hydrocarboxyl species, as has been presented above [41]. However, some authors doubt direct C-O cleavage in adsorbed carbon monoxide according to the proposed mechanism. Instead, a so-called hydrogen assisted C-O bond-cleavage is postulated: adsorbed carbon monoxide first reacts with adsorbed hydrogen to a formyl HCO, carbon-hydroxyl COH or some COH_x

species before bond cleavage to CH, C or CH_x and O or OH [48–52]. A hydrogen assisted pathway is also supported by DFT calculations: activation barriers for CO dissociation on clean Ni(111) surfaces range about 300 kJ/mol [53, 54] and accordingly well above the adsorption enthalpy of -121 kJ/mol. In fact, CO bond cleavage turns to be structure sensitive and the activation energy is drastically reduced at steps or kinks [54, 55], but hydrogen assisted cleavage at steps or kinks over HCO or COH is even faster with carbon-hydroxyl being the most likely reaction intermediate [51]. A hydrogen assisted pathway was also suggested by Lapidus et al. for the methanation of CO_2 based on transient kinetic experiments [56]. A consecutive scheme through CO involving a formyl complex and hydrogen in the rate determining step was deduced for methane formation.

In total, many proposals about intermediates and mechanism for the methanation of CO_2 have been formulated, but a conclusive picture has not emerged, yet. A combination of theoretical methods and in-situ spectroscopy under working conditions might be necessary to further elaborate mechanistic models and derive a comprehensive elementary step kinetic model, which is capable of describing both steady-state and transient kinetics.

2.2.2 Kinetic rate equations

In this section, published kinetic rate equations for the Ni catalyzed Sabatier reaction will be reviewed. Apart from the rate equations summarized in table 2.2, also relevant experimental conditions will be presented in order to assess the possible transferability to technical conditions and check for limitations.

The first extensive study of methanation kinetics was performed at the University of Michigan in the 1950s [57, 58]. In their first paper, Binder and White [57] investigated the kinetics under ambient pressure on a Nickel-Kieselguhr catalyst containing 60 wt% Ni. Reaction rates for methane formation were correlated by various rate equations. Also small amounts of carbon monoxide were measured, however they never exceeded 3.5%. Dew et al. extended the study to high pressures up to 30 bar [58]. In a differential reactor system, kinetics were measured on the catalyst in form of cylindrical pellets of about 3x3 mm size in an externally cooled fixed-bed reactor in the temperature and pressure range of 280-400°C and 2-30 atm, respectively, without dilution of the catalyst bed and H_2/CO_2 ratios between 0.1 and 20. Unfortunately, one might expect the measured kinetics to be biased by mass and heat transfer limitations as well as non-uniform temperature levels inside the catalyst bed. Methane and carbon monoxide in the product gas were analyzed by infrared spectroscopy, while carbon dioxide was quantified after absorption in potassium hydroxide solution. The authors also struggled with catalyst deactivation. To maintain a stable activity level during parameter variation, first an

extensive stabilizing treatment was performed, which involved reduction (50 hours), methane synthesis (300 hours), reduction again (1600 hours) and maintaining in an atmosphere of CO_2 (400 hours). Second, during parameter variation over several weeks, the catalyst was reactivated each day by partial oxidation in 0.5% air in CO_2. The observed loss in activity without these measures was attributed to thermal deactivation and carbon deposition. The experimental data of this study were limited to initial reaction rates. Runs in which methane was added to the reactants did not show any influence of the products. It was found that there is a maximum rate of methane formation as function of the H_2/CO_2 ratio, which increased with temperature from about 0.5 to 1.5. Initial reaction rates were fitted by a so-called generalized rate equation of the form

$$r = \frac{k p_{\mathrm{CO_2}}^{(x-1)} p_{\mathrm{H_2}}^{(y-4)} \left(p_{\mathrm{CO_2}} p_{\mathrm{H_2}}^4 - \frac{p_{\mathrm{CH_4}} p_{\mathrm{H_2O}}^2}{K} \right)}{\left(1 + K_1 p_{\mathrm{H_2}} + K_2 p_{\mathrm{CO_2}} + K_3 p_{\mathrm{H_2O}} + K_4 p_{\mathrm{CH_4}} \right)^n} \tag{2.1}$$

For the measured rates, this type of equation was simplified and best results were obtained for the expression given in table 2.2. Also a kinetic rate equation for the reverse water-gas-shift reaction was parametrized. It was found that the selectivity shifts during thermal deactivation to carbon monoxide [58].

In contrast to Dew's study, which addresses the kinetics of the methanation under undiluted feed gas conditions aiming at the production of SNG, Šolc [59] as well as van Herwijnen and coworkers [60] investigated kinetics relevant for the removal of CO_x out of hydrogen rich gases by methanation in a fixed-bed reactor. Concerning the latter, the kinetics accordingly cover reaction conditions with excess hydrogen and H_2/CO_2 ratios between 41 and 450. A rather narrow temperature interval between 200 and 230°C was studied at ambient pressure. The kinetics could be described by a Langmuir-type rate equation. Extensions of this model like a temperature dependence of the adsorption constant did not significantly improve the sum of squares of residuals, which, however, might arise from the narrow temperature interval. The reaction order of carbon dioxide changed from first order below partial pressures of 0.004 to zero order above 0.015 atm. Concerning the co-methanation, CO above 200 ppm poisons the methanation of CO_2 such that a decrease in CO_2 is not measurable. Water and methane were found to have no effect on the reaction rates for the small product concentrations occurring in this study.

The most detailed study on the methanation kinetics by now was presented by Weatherbee and Bartholomew in 1982 [46]. Intrinsic kinetics were measured for temperatures between 500 and 600 K at 1.4 bar total pressure on 3 wt% Ni/SiO_2 prepared by incipient wetness impregnation, however at diluted feed gases containing less than 10% and 2%

Table 2.2: Rate equations presented in literature

Catalyst (Ni wt%)	T [°C]	p_{max} [bar]	rate equation	reference
Ni/SiO_2 (60)	260-400	1	$r_{CH_4} = \frac{k\left(p_{CO_2}p_{H_2}^2 - p_{CH_4}p_{H_2O}^2/K_{eq}p_{H_2}^2\right)}{\left(1+K_{H_2}p_{H_2}^{0.5}+K_{CO_2}p_{CO_2}\right)^5}$ $r_{CH_4} = \frac{k\left(p_{CO_2}p_{H_2}^4 - p_{CH_4}p_{H_2O}^2/K_{eq}\right)}{\left(1+K_{H_2}p_{H_2}^{0.5}+K_{CO_2}p_{CO_2}\right)^9}$	[57]
Ni/SiO_2 (60)	280-400	30	$r_{CH_4} = \frac{kp_{CO_2}p_{H_2}^4}{\left(1+K_{H_2}p_{H_2}+K_{CO_2}p_{CO_2}\right)^5}$	[58]
Ni/Cr_2O_3 (62)	160-180	1	$r_{CH_4} = kp_{CO_2}^{0.5}$	[59]
Ni/Al_2O_3 (28)	200-230	1	$r_{CH_4} = \frac{kp_{CO_2}}{1+A_{CO_2}p_{CO_2}}$	[60]
Ni/SiO_2 (3)	227-327	0.16	$r_{CH_4} = \frac{kp_{CO_2}^{0.5}p_{H_2}^{0.5}}{\left(1+K_1p_{CO_2}^{0.5}p_{H_2}^{0.5}+K_2p_{CO_2}^{0.5}/p_{H_2}^{0.5}+K_3p_{CO}\right)^2}$	[46]
Ni/SiO_2 (58)	275-320	17	$r_{CH_4} = kp_{CO_2}^{0.66}p_{H_2}^{0.21}$ $r_{CH_4} = \frac{kp_{CO_2}p_{H_2}}{\left(1+K_{CO_2}p_{CO_2}+K_{H_2}p_{H_2}\right)}$	[61]
Ni	250-350	n.a.	$r_{CH_4} = \frac{kp_{CO_2}^{1/3}p_{H_2}}{1+K_{CO_2}p_{CO_2}+K_{H_2}p_{H_2}+K_{H_2O}p_{H_2O}}$	[62]
$Ni/La_2O_3/Al_2O_3$ (17)	240-320	1	$r_{CH_4} = \frac{kp_{CO_2}^{1/3}p_{H_2}^{1/2}}{\left(1+K_{CO_2}p_{CO_2}^{1/2}+K_{H_2}p_{H_2}^{1/2}+K_{H_2O}p_{H_2O}\right)^2}$	[63]
$Ni/MgAl_2O_4$ (15)	300-400	10	$r_1 = \frac{k_1}{p_{H_2}^{2.5}}\frac{p_{CH_4}p_{H_2O} - \frac{p_{H_2}^3p_{CO}}{K_1}}{DEN^2}$ $r_2 = \frac{k_2}{p_{H_2}}\frac{p_{CO}p_{H_2O} - \frac{p_{H_2}p_{CO_2}}{K_2}}{DEN^2}$ $r_3 = \frac{k_3}{p_{H_2}^{3.5}}\frac{p_{CH_4}p_{H_2O}^2 - \frac{p_{H_2}^4p_{CO_2}}{K_3}}{DEN^2}$ $DEN = \left(1 + K_{CO}p_{CO} + K_{H_2}p_{H_2} + K_{H_2O}p_{H_2O}/p_{H_2} + K_{CH_4}p_{CH_4}\right)$	[64]

hydrogen and carbon dioxide, respectively, in a one-pass differential fixed-bed reactor. Imposing gas hourly space velocities between 30 000 and 90 000 h^{-1}, the conversion was kept below 10% for all data points. Similar to findings by Herwijnen et al. [60], the methanation rate shows a moderate dependence on the partial pressure of carbon dioxide at low values approaching zero-order for higher partial pressures. Qualitatively, the same behavior holds for hydrogen. Concerning CO formed, a so-called "equilibrium" concentration was observed at each temperature independent of the CO_2 conversion or space velocity. If CO was fed in excess of this value, CO_2 methanation was inhibited and CO preferably reacted so that its concentration decreased towards the "equilibrium" level. In a first step, reaction rates for each temperature were fitted to a simple power law of the form

$$r = k_0 p_{CO_2}^{x} p_{H_2}^{y}$$

The Arrhenius plot according to this equations did not yield a constant activation energy, but it shifted from 89 kJ/mol to 39 kJ/mol with increasing temperature. Also reaction orders were observed to be temperature dependent: the CO_2 order dropped steadily with increasing temperature while the H_2 order increased. For these reasons it was concluded, that the simple power law was inadequate to reflect the kinetics. Langmuir-Hinshelwood kinetics were derived based on the following mechanism comprising dissociative CO_2 adsorption and subsequent reaction according to the widely assumed C-mechanism in analogy to CO methanation:

$$\begin{aligned}
1: &\quad CO_2 + 2\,{}^* \rightleftharpoons {}^*CO + {}^*O \\
2: &\quad H_2 + 2\,{}^* \rightleftharpoons 2\,{}^*H \\
3: &\quad {}^*CO + {}^* \rightleftharpoons {}^*C + {}^*O \\
4: &\quad {}^*C + {}^*H \rightleftharpoons {}^*CH + {}^* \\
5: &\quad {}^*CH + {}^*H \rightleftharpoons {}^*CH_2 + {}^* \\
6: &\quad {}^*CH_2 + {}^*H \rightleftharpoons {}^*CH_3 + {}^* \\
7: &\quad {}^*CH_3 + {}^*H \rightleftharpoons {}^*CH_4 + {}^* \\
8: &\quad {}^*CH_4 \rightleftharpoons CH_4 + {}^* \\
9: &\quad {}^*O + {}^*H \rightleftharpoons {}^*OH + {}^* \\
10: &\quad {}^*OH + {}^*H \rightleftharpoons {}^*H_2O + {}^* \\
11: &\quad {}^*H_2O \rightleftharpoons H_2O + {}^*
\end{aligned}$$

For derivation of rate equations, the adsorption of CO_2, the adsorption of H_2, C-O bond cleavage of adsorbed CO and hydrogenation of C and of CH, respectively,

have been assumed as rate determining. Along with different surface species being most abundant surface intermediates and the hydrogenation of oxygen being in quasi-equilibrium or irreversible so that the surface coverage of O was found from the steady state assumption, over 30 Langmuir-Hinshelwood type rate equations were formulated. The rate equations based on adsorption as the rate determining step were not capable of predicting the experimentally observed positive reaction orders of both reactants. Best results were obtained by assuming C-O bond cleavage as rate determining and the hydrogenation of oxygen as irreversible. As most abundant surface intermediates, oxygen and carbon monoxide were considered. Unfortunately, the transferability of the model to other conditions is limited because the values of the sorption constants are only listed for the five temperatures studied by the authors. Graphical evaluation shows that in particular K_1 does not follow van't Hoff's law. Furthermore, equilibrium contents of carbon monoxide cannot be derived from the model, but must be known a-priori for evaluation of the rate equation's denominator.

Chiang and Hopper [61] studied intrinsic methanation kinetics at higher pressures ranging between 11 and 17 bar on a 58 wt% Ni/SiO_2 catalyst. Conversions up to 45% were measured and used for parameter estimation of simple power law comprising reaction orders of hydrogen and carbon dioxide. The model was capable of reflecting the experiments with a mean residual of 6.9 %. This value could be reduced to 4.6% using a Langmuir-Hinshelwood model, but the power law was preferred by the authors because of its simplicity. In many experiments, the carbon monoxide content in the product gas was below the quantification limit of the GC analysis. It was only measurable at a H_2/CO_2 ratio of 2 and always amounted to less than 2.0%.

In contrast to the previous studies, Inoue and Funakoshi [62] investigated the methanation kinetics in a catalytic wall reactor. For preparation, nickel was electrodeposited on the inner wall of aluminum tubes. As main products, methane and water were detected. At high partial pressures of carbon dioxide, carbon monoxide was measured and interpreted as reaction intermediate of a consecutive reaction leading to methane. Since the presence of water was observed to appreciably decrease the methanation rates, an adsorption term for water was introduced in a Langmuir-Hinshelwood kinetic model for the first time. The mechanism for derivation comprises molecular adsorption of carbon dioxide, cleavage to carbon monoxide and oxygen and hydrogenation upon dissociation of carbon monoxide to carbon and oxygen, in accordance with the mechanism assumed by Weatherbee and Bartholomew [46]. Inoue and Funakoshi [62] emphasize that their model was also capable to adequately describe results concerning the co-methanation of CO and CO_2.

Further progress was accomplished by Kai et al. [63], who used both a differential and an integral reactor for kinetic studies on an alumina supported Ni catalyst promoted by

La_2O_3. By doing so and operating the integral reactor up to conversions of 90%, the influence of the products water and methane on the kinetics was accessible in more detail than in previous studies and the kinetic regime close to thermodynamic equilibrium could be investigated for the first time. Kinetics were described by a Langmuir-Hinshelwood rate equation based on the mechanism proposed by Weatherbee and Bartholomew[46], but assuming the hydrogenation of carbon instead of CO dissociation as rate determining step. First, the parameters of the rate equation were estimated while considering only the data measured in the differential reactor with conversions less than 3% comprising various H_2/CO_2 ratios between 0.6 and 30. Predictions of the model were then compared to results of the integral reactor. It was found that measured conversions at integral operation were smaller than predicted. This was attributed to the adsorption of products on the catalyst surface. As a consequence, the adsorption of water was accounted for in the Langmuir-Hinshelwood rate equation and an excellent fit of the data was obtained this way. Apart from methane and water, CO was the only byproduct measured, however in fractions below 1% of produced methane. Thus it was concluded to be sufficient to take only the Sabatier reaction into account and neglect the reverse water-gas-shift reaction for describing the kinetics.

The kinetic study by Xu and Froment presented in 1989 [64] is in this sense different to the previous studies that a typical $Ni/MgAl_2O_4$ steam reforming catalyst was employed because the authors were primarily interested in the kinetics of steam reforming. Since it was not possible to reject most of the formulated rate equations in a model discrimination procedure for steam reforming, experiments relating to the CO_2 methanation and reverse water-gas-shift reaction were performed as well, also in order to gain further mechanistic insight, as its combination can be seen as reverse reaction to steam reforming. In contrast to the previous works, that considered only the Sabatier reaction (and in case of Dew et al. [58] the reverse water-gas-shift reaction), this model comprises three reactions (figure 2.1): the methanation of carbon dioxide, the methanation of carbon monoxide as well as the reverse water-gas-shift reaction.

Thus, the model is experimentally validated for steam reforming and the methanation of carbon dioxide, in contrast to the methanation of carbon monoxide that was not studied in experiments. Concerning the methanation of CO_2, total pressures up to 10 bar and temperatures between 300 and 400°C are in a technically relevant range. Excellent fits were obtained with the model covering also high hydrogen conversions at the investigated feed compositions with $H_2/CO_2 = 1.0$ and 0.5. All parameters are estimated significantly showing a small confidence interval and obey Arrhenius equation or van't Hoff's law, respectively. Both prefactors and enthalphies are rated as thermodynamically consistent by the authors, though the adsorption enthalpy of water is estimated as positive.

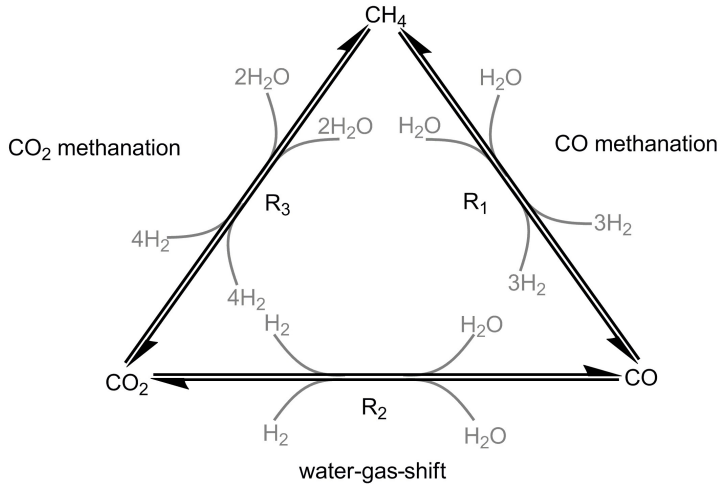

Figure 2.1: Reaction scheme according to Xu and Froment [64]

2.3 SNG-processes

As has been presented in chapter 1, power-to-gas concepts comprising a methanation step are seen as a promising technology for large scale storage of electrical energy, but have not been implemented in technical dimension, yet. By now, several demonstration plants up to a capacity of 6 MW have been realized [65]. In this section, processes with emphasis on reactor types for the methanation of carbon dioxide will first be introduced. Afterward, in view of the similarity to SNG production from synthesis gas, selected SNG processes for coal- or biomass-based synthesis gas will be presented.

2.3.1 CO_2/H_2 methanation technology

In 2009, Solar Fuel patented a process for the catalytic methanation of feed gases containing carbon dioxide and hydrogen with a CO content smaller than 0.1% [66]. The reactor system consists of at least two reactor stages in series (see flow scheme in figure 2.2). Before fed to the first reactor, hydrogen and carbon dioxide are mixed in a mixing section and preheated to avoid inactive reactor volume because of low temperatures. After entering the reactor, the temperature of the gas mixture rises to values between 300 and 600°C because of the exothermicity of the methanation reaction. Due to external counter stream cooling, the temperature decreases towards the reactor end so that the equilibrium is shifted to more favorable compositions. After the first reactor stage, cooling and a water condenser are installed to partially remove water and adjust the dew point of the gas. This way, the patented process combines two favorable effects: as a result of a reduced water content, (1) equilibrium is shifted to the product

site according to Le Chatelier's principle. However, since not all water is removed, but the dew point can be adjusted by controlling the temperature of the cooler, (2) deactivation due to carbon deposition is limited and catalyst lifetime prolonged this way. The resulting gas stream is again preheated before entering the second, also externally counter stream cooled reactor stage with temperatures between 250 and 300°C. After removal of water, the product gas fulfills the criteria to be fed into the gas grid without further purification or separation steps. Preferable total pressures range between 2 and 8 bar, while gas hourly space velocities (GHSV) are preferably between 2000-4000 h^{-1} for the first stage and 1500-4000 h^{-1} for the second stage, respectively. According to the embodiments, methane contents of 99% in the dried product gas are obtained at conditions consistent with the values listed above.

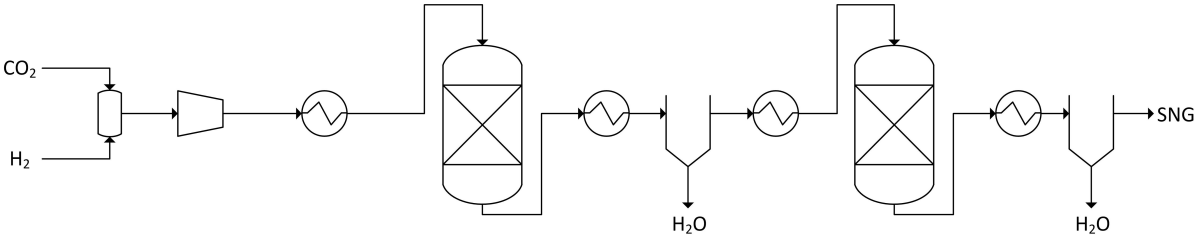

Figure 2.2: Simplified flow scheme of Solar Fuel's patented process [66]

In contrast, MAN Diesel & Turbo SE patented in 2011 a sophisticated, single reactor concept, also for pure CO_2/H_2 methanation [67]. The reactor is designed as shell-and-tube reactor with at least two separate reactor zones. Tubes filled with catalyst pellets are externally cooled by cooling medium, preferably molten salt. Each reactor zone has an separate cooling zone and cooling cycle so that the temperatures of the zones can be adjusted individually. The first zone is operated at higher temperatures to facilitate fast reaction rates for gases with large fractions of H_2 and CO_2, while the temperature in the last zone, where the gas composition is closer to equilibrium, is reduced so that the equilibrium is shifted to higher methane fractions. Preferably, the reactor tubes feature distinct hydraulic diameters in different zones. In the first zone, a smaller hydraulic diameter is advantageous, because a larger exchange area is provided per catalyst volume, transport distances for radial removal of heat are shorter and heat transfer is consequently enhanced. This way, heat can be removed efficiently such that hot spot temperatures are limited and still the controlled temperature rise is exploited for accelerating reaction rates. In the last zone, however, only a small fraction of the reaction heat is released and for this reason larger hydraulic diameters and accordingly higher catalyst-to-reactor-volume ratios facilitate the approach to equilibrium. Whilst maintaining the same tube diameter over the whole length of the reactor, the hydraulic diameter in the first zone can be reduced by centrally placing a tube of smaller diameter

not filled with catalyst pellets. Apart from the relative ease of design, the central tube can be used beneficially to dispense the feeding of reactant gas over an extended reactor volume, if the central tube is designed with gas outlets at distinct positions and feed gas is also dosed directly in the central tube. Thus, the heat release, which initially is very rapid, is spread over a larger volume and can be removed faster due to larger exchange area available. Hence, the catalyst is less stressed locally and the maximum temperature rise can be limited, which in view of the catalyst lifetime proves advantageous. Preferable hydraulic tube diameters are listed in the range between 10-22 mm. According to the embodiment, a methane gas content in the dried product gas of 92.3% can be obtained for a mixture of H_2 and CO_2 at a total pressure of 20 bar and a GHSV of 5000 h^{-1} using this reactor type.

2.3.2 Synthesis gas methanation technology

The methanation technology for SNG production on basis of synthesis gas has recently been reviewed by Rönsch and Ortwein [68] as well as by Kopyscinski et al. [69]. Here, a selection of processes and reactor types will be presented since in view of the similarity of the thermochemistry of CO and CO_2 methanation processes and reactor types similar to conventional SNG technology might also be adopted for the Sabatier process.

SNG methanation processes are categorized into two classes: fixed-bed and fluidized-bed methanation. Apart from those, also other concepts have been proposed, for instance methanation in slurry reactors [70] or in structured reactors [71, 72]. Concerning the latter ones, see section 5.2 for an overview.

2.3.2.1 Fixed-bed methanation processes

In order to control the local temperature rise due to the strong exothermicity of the methanation reactions, processes are mainly based on several reactors, often operated adiabatically and advantageously at different temperature levels, with limited conversion and heat release each. Reactors are arranged in series, in parallel or in form of more complex networks of reactors, respectively. To limit maximum temperatures, gas is cooled by intermediate cooling via heat exchangers or cooled and recycled so that feed gas of a reactor is mixed with already reacted product gas or inert gas in order to limit the adiabatic temperature rise [68].

The first commercially available SNG process was the Lurgi process [73], which comprises two adiabatic fixed-bed reactors with internal gas recycle concerning the first reactor and inter stage cooling (figure 2.3 (a)). The technology was employed in Schwechat (Austria) for methanation of refinery gases and in Sasolburg (South Africa) for methanation of a side stream of synthesis gas for the Fischer-Tropsch process

implemented there. Moreover, it has been adopted since 1984 in North-Dakota (USA) to commercially produce SNG from a coal plant. With the Lurgi process, an availability of 98.7% has been reached in over 20 years and up to 4.8 Mio m^3/day SNG have been produced [74].

Similarly, the TREMP process by Haldor Topsøe (Topsøe's Recycle Energy efficient Methanation Process) [75] employed for example in the ADAM/EVA project at the Kernforschungszentrum Jülich relies on three adiabatic reactors with inter stage cooling [77]. The first reactor comprises an internal gas recycle while the second and third reactor are put in series. Removed heat in inter stage cooling is used to produce high pressure superheated steam. Further processes based on adiabatic fixed-bed reactors were designed: for instance, the RMP process comprising four to six adiabatic reactors in series with intermediate gas cooling and reactant gas fed to the first three reactors in variable ratio [78], the ICI process with three adiabatic reactors in series or the HICOM process with several adiabatic reactors with intermediate cooling and recycling [68, 69, 79]. In contrast, the Linde process involves one cooled and one adiabatic reactor, which are put in series or both are fed with synthesis gas [76]. A portion of the effluent of the cooled reactor could also be fed to the adiabatic reactor to increase the performance. The cooled reactor is designed as tube bundle heat exchanger placed in the fixed bed of catalyst pellets.

2.3.2.2 Fluidized-bed methanation

In contrast to fixed-bed reactors, fluidized-bed reactors for methanation can be operated almost isothermal due to movement of catalyst particles, advantageous heat transfer and homogeneous reaction conditions throughout the reactor. Reaction heat is removed from the reactor via a heat exchanger in the fluidized-bed [68]. However, this reactor type suffers for example from catalyst abrasion and more difficult scale-up.

In 1952, the US Bureau of Mines began the development of fluidized-bed technology for the methanation of syngas in lab scale. To ensure isothermicity, multiple feed inlets had to be installed. Similarly, Bituminous Coal Research Inc. developed a fluidized-bed process for SNG production (Bi-Gas process). For better temperature control, two in-tube heat exchanger were placed above to separate feed inlets. The lab scale reactor had a diameter of 150 mm and height of 2.5 m [68, 69]. A further process was developed by Thyssengas GmbH (Comflux process) [80]. At the site of Ruhrchemie in Oberhausen (Germany), a plant of technical scale with 3 m inner diameter and catalyst load up to 3000 kg was erected. Further development of the technology was stopped in the 1980s, when the price of oil dropped [69].

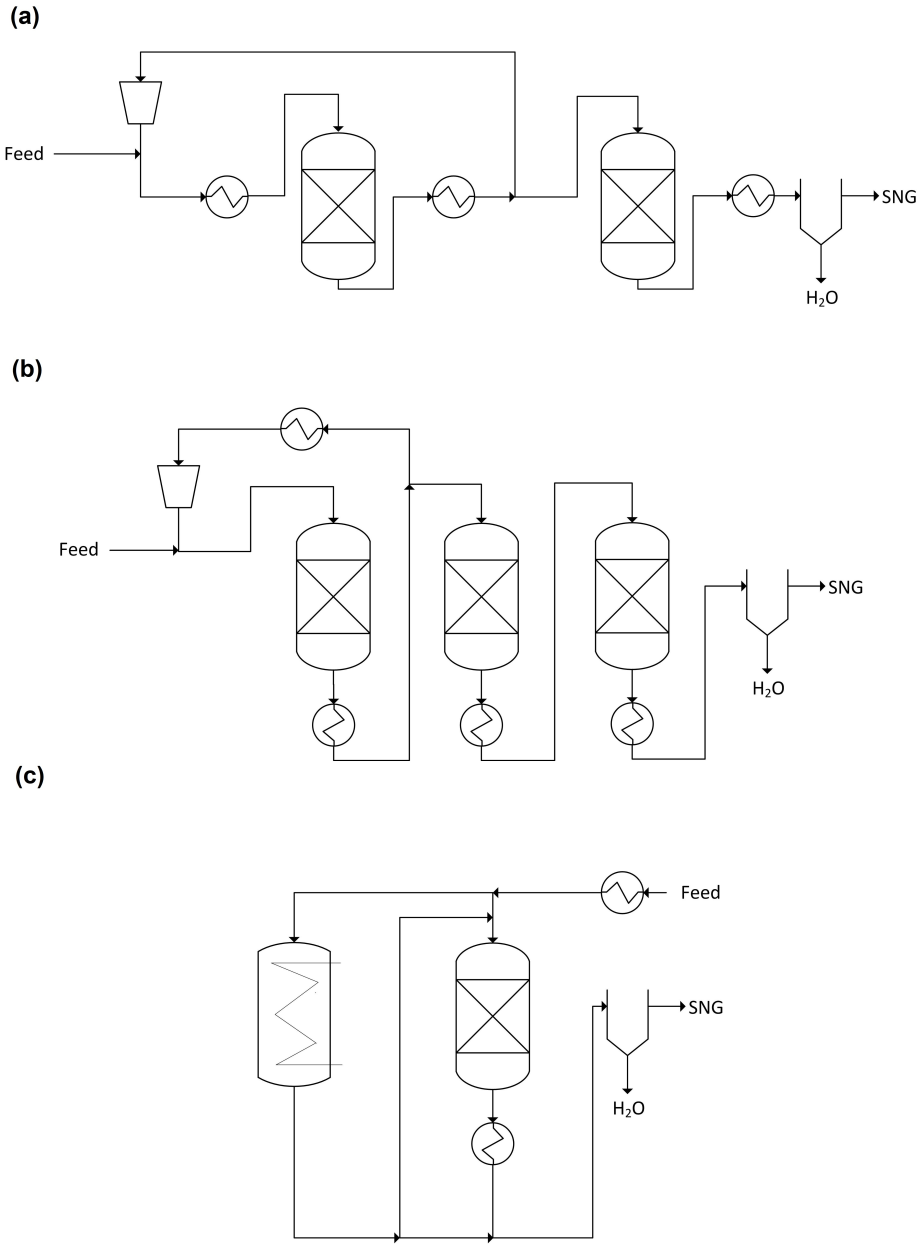

Figure 2.3: Simplified flow schemes of (a) Lurgi SNG process [73], (b) TREMP [75] and (c) Linde's SNG process [76]

3 Methodology

3.1 Modeling of fixed-bed reactors

3.1.1 Fundamental transport processes in fixed-bed reactors

Before fixed-bed reactor models of different level of detail will be introduced and systematically categorized, first fundamental aspects concerning the transport processes are discussed. Though fixed-bed reactors are the most widely adopted reactor in chemical industries, in particular for heterogeneously catalyzed gas phase reactions because of their relative ease in design and operation, flexibility and reliability, the underlying processes are complex mainly for two reasons: the stochastic nature of packed beds and the interplay of fluid flow to a variety of coupled heat and mass transfer processes and mechanisms running in parallel.

This thesis focuses on externally cooled fixed-bed reactors, as they are schematically depicted in figure 3.1. Catalysts in form of pellets are packed in tubes which are flowed through by the reacting gas. To remove heat in case of exothermic reactions, the reactor tubes are cooled by a cooling medium that may flow in ideal case according to three borderline cases: co-current (a), counter current (b) or cross flow (c). For sake of temperature control, tube diameters cannot be enlarged arbitrarily in view of heat exchange area and transport distances inside the packed bed. For this reason, fixed-bed reactors for highly exo- or endothermic reactions of large-scale technical dimension are often designed as tube bundle reactor comprising tubes of diameters above 1 in. Design and modeling of tube-bundle heat exchangers are complex for themselves. In this thesis, as it is mostly done in modeling of fixed-bed reactors, a detailed description of flow and temperature devolution of the cooling medium is omitted. Instead it is assumed that cooling ensures that the temperature of the cooling medium fairly is constant over the whole tube circumference and length.

Despite this simplification, still processes involving multiple length scales need to be understood: concerning the heat transfer, heat, which is released due to chemical reaction on an active site on a catalyst grain in a porous pellet, is transported through the packed bed, to the metallic tube, conducted inside the metallic wall to the lateral surface and transferred to the cooling medium. Processes underlying the heat transport

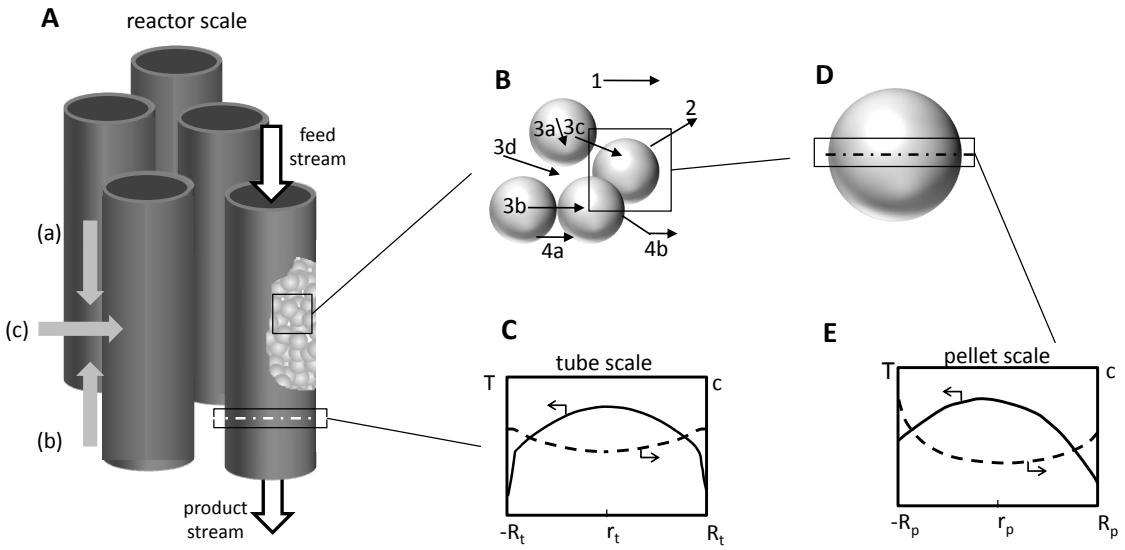

Figure 3.1: Multiple scales in fixed-bed reactors

in packed beds are schematically summarized in figure 3.1 B. Following Lemcoff et al. [81], at least eight processes involving three mechanisms of heat transfer can be distinguished and categorized:

- convection by fluid (1)
- solid-fluid transfer (2)
- conduction through solid (3a)
  contact conduction (3b)
  conduction through stagnant film (3c)
  conduction through fluid (3d)
- radiation between adjacent solid (4a)
- radiation between solid surfaces separated by more than a void space (4b)

The situation adjacent to the inner tube wall is different to the core zone, where typically a parabolic temperature will evolve in radial direction (figure 3.1 C). Experimentally, sharper temperature gradients are found in contrast in the wall zone. Heat is transported via the fluid and solid phase to the tube wall, again as interplay of the mechanisms of convection, conduction and radiation. Also temperature profiles inside individual pellets will evolve (figure 3.1 E). Though fluid flow inside the catalyst pellets due to the surrounding, interstitial flow can be neglected, next to conduction also convection might need to be considered as a consequence of evolving pressure difference, which can be caused by non-volume-conserving reactions.

By now, detailed modeling, which dissolves the different processes concerning fluid dynamics as well as heat and mass transfer, is limited up to few pellets. These studies, however, do not aim at simulating fixed-bed reactors in total, but at understanding the fundamental processes and their influencing parameters. In today's state of the art reactor models for the full tube scale, these processes are lumped and treated via effective properties. They have in common that the different underlying mechanistic processes are described analogously to Fourier's or Fick's law concerning heat or mass transfer, respectively:

$$j_H = -\lambda \frac{\partial T}{\partial x} \qquad \text{and} \qquad j_M = -D \frac{\partial c}{\partial x}$$

Here, j_H and j_M denote heat and mass fluxes, T and c temperature and concentration and x the corresponding spatial variable in the chosen one-dimensional form. λ and D do not necessarily correspond to an intrinsic heat conductivity or binary diffusion coefficient, but rather reflect effective properties. For instance, the radial transport of heat in tubes filled with pellets is described by means of an effective property λ_r^e that lumps contributions by the mechanisms of (turbulent) convection, conduction in the solid, in the gas phase and between them as well as of radiative transport. To emphasize that these effective properties lump different contributions, they are often denoted as heat and mass dispersion coefficients in contrast to thermal conductivity of diffusion coefficient. Since they are not only dependent on intrinsic physical material properties, but also on operating conditions and the geometry of tube and pellets etc., correlation equations need to be evaluated (see section 3.1.2).

In case of transfer of heat or mass from a solid to a gas phase or vice versa, Fourier's and Fick's law are further simplified. The boundary layers are not dissolved locally, but heat and mass flux are assumed to be proportional to the difference between solid surface and gas phase bulk value:

$$j_H = k_h \left(T_g - T_s\right) \qquad \text{and} \qquad j_M = k_m \left(c_g - c_s\right)$$

k_h and k_m are heat and mass transfer coefficients which are again calculated by means of correlation equations (see section 4.3.2.3). If these equations are for instance used for calculation of the heat flux to a catalyst pellet, the transfer coefficients can be interpreted as an averaged value, since also the surface temperature of the pellet will locally vary as consequence of the surrounding flow as shown in the schematic temperature profile in figure 3.1 E.

3.1.2 Fixed-bed reactor models

Fixed-bed reactor models used in this thesis can be classified as continuum models. As exposed in the previous section, the detailed structure of fixed-beds is not accounted for, but balances are formulated either for one single phase, which is assumed as continuous throughout the reaction volume of the reactor. Its effective properties are a function of both gas and solid phase. For this reason these models are termed as 'pseudo-homogeneous reactor models'. Or in the other case, if it is abstracted to two phases, a solid phase and a gas phase, which are also assumed as continuous, the models are referred to as 'heterogeneous fixed-bed reactor models'. In order to stress that gas and solid phase in the model are assumed as continuous phases and not identical though related to the interstitial gas phase and the solid pellets, respectively, the phases are often also called 'pseudo-phases' and the models 'pseudo-heterogeneous' models. A possible categorization of fixed-bed reactors following the definition by Froment and Bischoff [82] is given in table 3.1. The models will be introduced subsequently in order of increasing level of detail.

Table 3.1: Categorization of fixed-bed reactor models [82]

	Pseudo-homogeneous models	Heterogeneous models
One dimensional	PH1: ideal PFR model PH2: + axial dispersion	HET1: + interfacial gradients HET2: + intraparticle gradients
Two dimensional	PH3: + radial dispersion	HET3: + radial dispersion

3.1.2.1 Pseudo-homogeneous reactor models

The simplest model PH1, the 1D pseudo-homogeneous plug flow reactor (PFR) model, neglects any differences in the cross section and instead assumes uniform profiles of temperature, concentrations and pressure. With this assumption, balances can be derived based on a differential cylindrical volume element comprising the whole cross section. In stationary state, they read as follows:

mass balance:

$$\frac{\partial(uc_i)}{\partial z} = \rho_{bed} \sum_{j=1}^{N_{\mathrm{Rx}}} \nu_{i,j} r_j \tag{3.1}$$

heat balance:

$$(uc_{tot})\bar{c}_p\frac{\partial T}{\partial z} = \rho_{bed}\sum_{j=1}^{N_{\mathrm{Rx}}} r_j(-\Delta H_j) - \frac{4}{d_{tube}}U_A(T - T_c) \tag{3.2}$$

momentum balance:

$$\frac{dp}{dz} = \frac{f\rho u^2}{d_p} \tag{3.3}$$

Concerning the mass balance, only the convective term in axial direction is considered next to chemical reactions. Any non-idealities due to axial dispersion are neglected. Consequently, fluid flow is characterized as ideal plug flow. In the heat balance, the removal of heat released due to chemical reactions is described by the convective contribution and by a transfer term in relation to the characteristic temperature difference between cooling temperature and temperature in the pseudo-homogeneous phase at the corresponding axial position. The pressure drop is proportional to the square of the superficial velocity u. The proportionality constant is characterized by a friction factor f, which for fixed-beds is often evaluated according to Ergun's equation:

$$f = \frac{1-\epsilon}{\epsilon^3}\left(1.75 + 150\frac{1-\epsilon}{Re_p}\right) \tag{3.4}$$
$$\text{with} \qquad Re_p = \frac{\rho u d_p}{\eta}$$

The assumption of uniform levels of temperature, concentration and pressure implies two major drawbacks of common basic 1D models. First, the effective overall heat transfer coefficient U_A has to consider not only the heat transfer resistance adjacent to the tube wall, which is accounted for by so-called wall heat transfer coefficients, but also the resistance to heat conduction caused by heat transport through the fixed-bed (radial dispersion). This issue is mostly addressed by assuming these two resistances in series. For derivation of the resistance due to dispersion, the temperature in the pseudo-homogeneous models is rather assumed as a radially averaged value than as constant throughout the cross section. Since radially parabolic temperature profiles will evolve according to two dimensional models, the characteristic transport length for calculation of the resistance can be derived. The second drawback is closely related. In 1D models, reaction rates are evaluated at the radially averaged temperature. However, the reaction rate at this average temperature deviates from the radially averaged reaction

rate because of the exponential dependence of the reaction rate on the temperature. To circumvent this, more sophisticated 1D models have been proposed in literature [83, 84].

Apart from radial non-uniformity of temperature, concentrations and pressure, one might criticize the PFR model to neglect mixing effects due to the packing and radial variations of the flow velocity in particular in the wall zone. To account for this, PH2 comprises axial heat and mass dispersion terms formulated in analogy to Fourier's and Fick's law. In principle, axial mixing will smooth axial gradients of temperature and concentration. The implementation of axial dispersion terms, however, gives rise to a two-point boundary value problem, while PH1 is a simple initial value problem with $c_i(z=0) = c_{i,0}$ and $T(z=0) = T_0$. The inlet boundary conditions of models accounting for axial dispersion have long been subject to discussion, as they should ensure continuity of concentration and temperature, which, however, requires consideration of the concentration and temperatures in front of and in the inlet of the reactor. Most often, the following boundary conditions are imposed:

$$
\begin{aligned}
z = 0: \qquad & u_0 c_{i,0} - u c_i = -D_e^{ax} \frac{dc_i}{dz} \qquad && \rho_0 u_0 c_{p,0} T_0 - \rho u c_p T = -\lambda_e^{ax} \frac{dT}{dz} \\
z = L: \qquad & \frac{dc_i}{dz} = 0 && \frac{dT}{dz} = 0
\end{aligned}
$$

There seems to be consensus that axial mixing has a negligible effect at flow velocities used in industrial practice in case of long beds (bed depth > 50 particle diameters) [82]. Since solving of the boundary value problem raises in addition computational times and decreases the stability, axial dispersion terms are not considered in this thesis in fixed-bed reactors models. For modeling of honeycomb reactors, where balances are formulated in analogy to fixed-reactors (see section 5), axial dispersion of heat needs to be taken into account. That axial dispersion models have attracted much interest in academic chemical engineering, has risen rather from the controversy about boundary conditions as well as from mathematical features like multiplicity of steady-states [85, 86] than from use in technical application.

Two dimensional models clearly mark a step forward for continuum models. They consider the tube's radial coordinate next to the axial one and generally assume axial symmetry, that is variations of packed-beds in angular directions are excluded from consideration. Radial transport is again described by the effective transport concept according to Fick's and Fourier's laws and superposed on the axial convective transport. Balances derived from a differential volume element in the reaction volume are nonlinear second order partial differential equations and read as follows:

mass balance:

$$\frac{\partial(uc_i)}{\partial z} = \rho_{bed} \sum_{j=1}^{N_{\mathrm{Rx}}} \nu_{i,j} r_j + D_e^r \left(\frac{\partial^2 c_i}{\partial r^2} + \frac{1}{r} \frac{\partial c_i}{\partial r} \right) \tag{3.5}$$

heat balance:

$$(uc_{tot})\bar{c}_p \frac{\partial T}{\partial z} = \rho_{bed} \sum_{j=1}^{N_{\mathrm{Rx}}} r_j(-\Delta H_j) + \lambda_e^r \left(\frac{\partial^2 T}{\partial r^2} + \frac{1}{r} \frac{\partial T}{\partial r} \right) \tag{3.6}$$

with the boundary conditions:
$r = 0$:

$$\frac{\partial T}{\partial r} = 0 \qquad\qquad \frac{\partial c_i}{\partial r} = 0$$

$r = d_{tube}/2$

$$\lambda_e^r \frac{\partial T}{\partial r} = \alpha_W (T - T_c) \qquad\qquad \frac{\partial c_i}{\partial r} = 0$$

Key parameters that determine removal of heat next to convection are the effective radial dispersion coefficient λ_e^r and the wall heat transfer coefficient α_W. Both rely on the properties of the gas and solid phase. Furthermore, they are based on a static and a dynamic contribution each. The static contribution, which also is valid in absence of flow, lumps the transport processes 3(a-c) and 4(a-b) of figure 3.1 B in case of the effective radial dispersion coefficient. For derivation of the static contribution, each of these contributions is translated to a thermal resistance. By arranging the resistances in analogy to electrical networks, different expressions can be derived depending on the chosen assembly of resistances [82]. In contrast, the dynamic contribution of the effective radial dispersion coefficient and the wall heat transfer arises from transport in flowing fluid and is a function of the operating variables and physical fluid properties, in particular, of the Reynolds and the Prandtl number. As recommended for example in the VDI-Wärmeatlas, correlations by Zehner, Bauer and Schlünder for the conductivity of packed beds with stagnant fluid and by Martin and Nilles for their adoption in packed-beds with fluid flow are used in this thesis and listed in section 4.6 [87, 88]. In the presented 2D model, sharp temperature gradients are accounted for via the wall heat transfer coefficient. An alternative description is based on a radial effective dispersion coefficient which is a function of the radial position. This way, the local void fraction,

which is considerably higher in the wall zone due to contact of (spherical) particles and the wall, can directly be taken into account (see chapter 4 for a detailed description).

3.1.2.2 Heterogeneous reactor models

Whereas it is intrinsically assumed in pseudo-homogeneous models that neither concentration nor temperature differences exist between the gas phase and the solid catalyst pellets, since only one pseudo-phase is balanced, mass and heat balances for both a gas and a solid phase are formulated in heterogeneous models. By doing so, temperature and concentration differences between the phases can be dissolved (HET1). Moreover, also gradients inside the catalyst pellets can be considered (HET2). The balances for a two dimensional heterogeneous reactor model (HET3) can be formulated as follows:

gas phase:

mass balance:

$$\frac{\partial(uc_i)}{\partial z} = D_e^r \left(\frac{\partial^2 c_i}{\partial r^2} + \frac{1}{r}\frac{\partial c_i}{\partial r} \right) + k_m a \left(c_{s,i}^{\text{surf}} - c_i \right) \tag{3.7}$$

heat balance:

$$(uc_{tot})\bar{c}_p \frac{\partial T}{\partial z} = \lambda_e^r \left(\frac{\partial^2 T}{\partial r^2} + \frac{1}{r}\frac{\partial T}{\partial r} \right) + k_h a \left(T_s^{\text{surf}} - T \right) \tag{3.8}$$

solid phase:

mass balance:

$$k_m a \left(c_{s,i}^{\text{surf}} - c_i \right) + \rho_{bed} \sum_j^{N_{\text{Rx}}} \nu_{i,j} \eta_j r_j^{\text{surf}} = 0 \tag{3.9}$$

heat balance:

$$k_h a \left(T_s^{\text{surf}} - T_i \right) + \rho_{bed} \sum_j^{N_{\text{Rx}}} \eta_j r_j^{\text{surf}} (-\Delta H_j) = 0 \tag{3.10}$$

In this formulation, the solid phase balances are algebraic equations, where k_m and k_h relate to mass and heat transfer coefficients and a to the specific external surface area of pellet per unit reactor volume. Noteworthy, the dispersion is treated via the gas phase

balance equations. The dispersion coefficients are identical to the pseudo-homogeneous models and still lump also the transport processes related to the solid phase. Differing models have been formulated in literature, which separate heat transport in the solid and in the gas phase, that is also the solid phase balance considers a radial dispersion term. However, these models require additional parameters, while most published dispersion coefficients combine these contributions. Moreover, separation of conduction in the solid phase and conduction through the contact areas of particles from other contributions does not obviously improve the model adequacy.

Reaction rates in equations (3.9 and 3.10) are expressed as $\eta_j r_j^{\mathrm{surf}}$, where r_j^{surf} represents the reaction rate of reaction j at surface conditions, that is the reaction rate at $c = c^{\mathrm{surf}}$ and $T = T^{\mathrm{surf}}$ throughout the pellet, and η_j the effectiveness factor of reaction j. The latter one arises from intraparticle gradients of temperature and concentrations and in this case is defined as

$$\eta = \frac{\text{reaction rate with intraparticle transport limitations}}{\text{reaction rate at surface conditions}}$$

Incorporation of this effectiveness factor adds another dimension to the reactor model. In the simplest case, characterized as Thiele modulus approach, effectiveness factors can directly be evaluated from the analytical solution of a simplified pellet balance. However, analytical solutions can only be derived for simple kinetics and isothermal conditions, likewise. Though approximations have been formulated in literature also for Langmuir-Hinshelwood rate equations relying on so-called generalized Thiele moduli, multicomponent systems, multiple reactions, for instance according to the kinetic scheme by Xu and Froment in figure 2.1, and consideration of heat transport also on the pellet scale require numerical solution of heat and mass balances for the catalyst pellets. Section 3.2.3 summarizes a detailed model for description of mass transfer in porous media, that has been implemented in a particle model and coupled to a heterogeneous reactor model in this thesis.

To summarize this section, continuum models today are still the most common approach to simulate fixed-bed reactors in view of their convenience and proven validity. Since they rely on effective transport properties, the trustworthiness of underlying (semi-)empirical correlation equations is crucial. Continuum models are formulated in various level of detail. Apart from the categorization by Froment and Bischoff [82] in six models, many modifications and combinations are possible. Dispersion terms are often neglected in mass balances, while they are considered in heat balances. Interfacial gradients are often taken into account in heat but not in mass balances, and vice versa concerning intraparticle transport. Which model to choose, depends on the required model accuracy, available degree of detail and trustworthiness of kinetics and

effective transport parameters as well as on relevance of various transport processes for the particular reaction and reaction conditions. In order to preliminarily assess their relevance and influence, different criteria have been developed for various transport limitations (see section 6.7.1). In chapter 4 a different approach is chosen. Transport limitations are discussed by comparing models of differing degree of detail. Apart from classical continuum models including Fickian and Fourier-type dispersion terms, also cell, wave and CFD models have proposed for fixed-bed reactors. Cell models abstract from a fixed-bed reactor to a network of connected ideal continuously stirred tank reactors (CSTRs). As they can be traced back to finite-difference approximations of continuum models, one might also classify them as continuum models in a less strict definition. However, the algebraic equations of cell models often allow different and easier solution procedures than common finite-difference schemes [89]. Wave models rely on the concept of heat and mass transport by waves instead of Fickian-type dispersion. They avoid the drawbacks of infinite speed of signal propagation and the necessity of formulating of outlet boundary conditions [90]. Nevertheless, reports of their adoption are rare. In contrast, CFD modeling of packed beds or at least sections of packed beds is an emerging field of research, possible due to now available computational resources, see e.g. the review by Dixon et al. [91].

3.2 Mass transport in porous media

3.2.1 Mechanisms of mass transfer in porous media

In order to be able to describe mass transfer in porous media and to subsequently couple pellet balances to a heterogeneous reactor model, a mechanistic understanding of transport processes is required. The following diffusion mechanisms are distinguished:

Free molecular diffusion: Momentum is only transferred by collisions between gas phase molecules. Collisions with pore walls can be neglected because the mean free path of the molecules is well below pore diameters. Mathematically, free molecular diffusion can be described according to Fick's law or the Stefan-Maxwell equation (section 3.2.2). Binary molecular diffusion coefficients can be approximated according to Fuller's method [92]:

$$\frac{D^{mol}}{cm^2/s} = \frac{0.00143 \ \left(\frac{T}{K}\right)^{1,75} \ \left[\left(\frac{M_1}{g/mol}\right)^{-1} + \left(\frac{M_2}{g/mol}\right)^{-1}\right]^{1/2}}{\frac{p}{bar} \ \sqrt{2} \ \left[\left(\sum \Delta v_1\right)^{1/3} + \left(\sum \Delta v_2\right)^{1/3}\right]^2} \tag{3.11}$$

M_i and $(\sum \Delta v_1)$ are the components' molar mass and specific diffusion volumina, respectively. Specific diffusion volumina can approximately be evaluated by summation of group contributions.

Knudsen diffusion: If the mean free path of the species is considerably larger than pore diameters d_p, collision with pore walls will dominate. The Knudsen diffusion coefficient in

$$J_i^{\text{Knudsen}} = c_{\text{tot}} D_i^{\text{Knudsen}} \nabla x_i \tag{3.12}$$

is calculated according to

$$D_i^{\text{Knudsen}} = \frac{d_p}{3} \sqrt{\frac{8RT}{\pi \cdot M_i}} \tag{3.13}$$

Thus, it is proportional to the pore diameter and the mean velocity of the gas phase species following kinetic theory of gases [93].

Surface diffusion: Adsorbed species on inner surfaces of the porous medium exhibit lateral mobility so that a mass flux results in direction of the concentration gradient.

Configurational diffusion: If van-der-Waals diameters of gas phase species d_{mol} are close to pore diameters, mass transport is categorized as configurational diffusion. An oversimplified approach assumes diffusion coefficients as

$$D_{ij}^{\text{konf}} = D_{ij}^{\text{mol}} \cdot \left(1 - \frac{d_{mol}}{d_P}\right)^4 \tag{3.14}$$

Description of configurational diffusion is, however, complex due to effects like single-file diffusion, that is molecules of high diffusivity cannot pass slower ones in pores of porous media (see e.g. [94]).

The first three mentioned diffusion mechanism can also operate in parallel. Molecular diffusion and Knudsen diffusion are border cases. The Knudsen number, which correlates the mean free path to the pore diameter, can be evaluated to assess which regime is dominant:

$$\text{Kn} = \frac{\lambda}{d_P} = \frac{k_B T}{\sqrt{2}\pi d_{mol}^2 p_{\text{tot}} d_P}$$

For Kn $>>$ 1 Knudsen diffusion dominates, while at Kn $<<$ 1 molecular diffusion prevails. Next to diffusion, also convective transport as consequence of pressure gradients

might have to be considered. Pressure gradients can for instance result from non-volume conserving chemical reactions. Hagen-Poiseuille's law for convection in the laminar region for cylindrical channels reads

$$J_i^{\text{convection}} = x_i \cdot p_{\text{tot}} \frac{d_P^2}{32\eta} \frac{dp_{\text{tot}}}{dz} \tag{3.15}$$

3.2.2 Mathematical description of free molecular diffusion

3.2.2.1 Fick's law

Fick's law captures diffusive mass transport in binary, gaseous mixtures. The diffusive flux of one component is proportional to the gradient of its mole fraction. The proportionality constant is defined as molecular binary diffusion coefficient D_{12}.

$$J_1 = -c_{\text{tot}}\ D_{12}\ \nabla x_1 \tag{3.16}$$

Formally, following the formulation of Taylor and Krishna [95], Fick's law can also be extended to multicomponent mixtures based on the assumption that each of the $(N-1)$ linear independent driving forces might affect the molar flow of every single component. For the component $(N-1)$, the molar flux is expressed as

$$J_{N-1} = -c_{\text{tot}}\ D^F_{N-1\ 1}\ \nabla x_1\ -\ c_{\text{tot}}\ D^F_{N-1\ 2}\ \nabla x_2\ -\ ...\ -\ c_{\text{tot}}\ D^F_{N-1\ N-1}\ \nabla x_{N-1}$$

Noteworthy, the proportionality constants $D^F_{N-1\ j}$ are not synonymous with binary diffusion coefficients, but are - as experimentally found - a function of the gas composition [96]. For infinitely diluted solutions, that is

$$x_i \to 0 \text{ for } i = 1\ ...\ N-1$$
$$x_i \to 1 \text{ for } i = N$$

one finds:

$$D^F_{ij} = 0 \text{ for } i \neq j$$
$$D^F_{ii} = D^{mol}_{i\ N}$$

The molar flow of a component in infinitely diluted solutions solely is a function of its mole fraction gradient. Further possible driving forces, the mole fraction gradients of other species, do not influence its transport. Descriptively, species of the infinitely

diluted components collide and transfer momentum only with component N. The Fickian diffusion coefficients D_{ii}^{F} are in this case equal to the molecular diffusion coefficients $D_{i\,N}^{mol}$.

Fick's law captures diffusive transport in binary mixtures as well as in infinitely diluted multicomponent solutions. The generalized form does not provide information on the Fickian diffusion coefficients D_{ij}^{F} without this restriction. In contrast to the experimentally founded Fick's law, the Stefan-Maxwell equation presented in the next section has a theoretical basis, i.e. the kinetic theory of gases. By comparing the Stefan-Maxwell equation to the generalized Fick's law, relations can be derived for the Fickian diffusion coefficients D_{ij}^{F}. Fick's law for infinitely diluted solutions are also predicted by the Stefan-Maxwell equation.

3.2.2.2 The Stefan-Maxwell equation

Basis for the derivation of the Stefan-Maxwell equation is Newton's second law, which is applied to a differential control volume of a gaseous mixture [95]. The volume element may move with the mean velocity of the mixture so that for every molecule leaving the control volume another molecule enters into the control volume on the same facet. This ensures that no change in momentum in relation to the control volume will occur. Inside the differential volume element, however, momentum is transferred between gas phase molecules of different species by collisions. Following the kinetic theory of gases, the mean momentum transfer at a collision of species 1 with mass m_1 and mean velocity u_1 to species 2 with mass m_2 and mean velocity u_2 equals

$$\Delta P = m_1(u_1 - u_1') = \frac{m_1 m_2 (u_1 - u_2)}{m_1 + m_2}$$

Here, u_1' denotes the mean velocity after collision. Referring again to the control volume, the total momentum transfer ΔP from one species to another is proportional to the number of collisions per time and momentum transfer per collision. The number of collisions per time itself is proportional to the concentration of both components $c_1 = c_{\mathrm{tot}} x_1$ and $c_2 = c_{\mathrm{tot}} x_2$. It thus follows:

$$\frac{\Delta P}{\Delta t} \propto (x_1 x_2, (u_1 - u_2))$$

According to Newton's second law a force is equal to the rate of change of momentum:

$$F = \dot{P}$$

The balance of forces concerning species 1 with regard to two opposite facets reads:

$$\lim_{\Delta z \to 0} Ap_1|_z - Ap_1|_{z+\Delta z} = -A\frac{dp_1}{dz}$$

Thus, the gradient of the partial pressure of species 1 is proportional to product of mole fractions and the difference of mean velocities:

$$\nabla p_1 \propto (x_1 x_2, (u_1 - u_2))$$

After dividing by the total pressure and defining the constant of proportionality as binary molecular diffusion coefficients, the gradient of the mole fraction of species 1 is expressed in a binary mixture as

$$\nabla x_1 = \frac{-x_1 x_2 (u_1 - u_2)}{D_{12}}$$

and analogously in a arbitrary multicomponent mixture of N components as

$$\nabla x_i = -\sum_{j=1}^{N} \frac{x_i x_j (u_i - u_j)}{D_{ij}}$$

For the usual formulation of the Stefan-Maxwell equations, the products of mole fractions and linear velocities are substituted by the diffusive molar fluxes $J_i = c_{\text{tot}} x_i u_i$ [95]:

$$\nabla x_i = -\sum_{j=1}^{N} \frac{x_i J_j - x_j J_i}{c_{\text{tot}} D_{ij}} \tag{3.17}$$

According to the Stefan-Maxwell equations, the gradient of the mole fraction of each component is dependent on the molar fluxes of all other species and the gas composition. Hence, diffusive mass transport in arbitrary gas mixtures can be described on basis of binary molecular diffusion coefficients.

3.2.3 The dusty-gas model for mass transfer in porous media

For adequate modeling of mass transfer in porous media, relevant transport mechanisms presented in section 3.2.1 next to molecular diffusion need also to be considered. The easiest way to cover also the transition region between the border cases of Knudsen diffusion and molecular diffusion offers the resistance law according to Bosanquet in conjunction with Fick's law. If one interprets the reciprocal of Knudsen and molecular

diffusion coefficient as resistances to diffusive flux, the diffusion coefficient D_{ij} for the transition region can be derived from a series arrangement:

$$D_{ij} = \left(\frac{1}{D_{ij}^{\text{mol}}} + \frac{1}{D_i^{\text{Knudsen}}} \right)^{-1} \tag{3.18}$$

Also on basis of the Stefan-Maxwell equations, free molecular and Knudsen diffusion can be combined using the so-called dusty-gas model [97]. As underlying principle, so-called dust particles are added as $N{+}1^{\text{st}}$ species to the N gas phase components. By collision of gas phase molecules with dust particles collisions with pore walls of porous media are treated. Following assumptions are made for the dust particles:

- The dust concentration is spatially uniform.
- Dust particles do not move, that is $J_{N+1} = 0$.
- The molar mass of dust particles goes towards infinite.

In order to fulfill the last condition, an external force has to act on the dust particles, because they would have been moved as a consequence of the gradients of the mole fractions of the gaseous components. This external force needs to be accounted for in derivation of the dusty-gas model based on a control volume in analogy to the Stefan-Maxwell equations. After transition from the system comprising the dust particles to the pure gas phase system, the molar flux of component i reads [97]

$$\nabla x_i = -\sum_{j=1}^{N} \frac{x_i J_j - x_j J_i}{c_{\text{tot}} D_{ij}} + \frac{J_i}{D_i} \tag{3.19}$$

with

$$D_i = \frac{d_P}{3} \cdot \sqrt{\frac{8RT}{\pi \cdot M_i}} \tag{3.20}$$

D_i is exactly the Knudsen diffusion coefficient from equation 3.13. The other terms are identical to the formalism of the Stefan-Maxwell equations. To account for effective properties of the porous medium, all diffusion coefficients are multiplied by the factor ϵ/τ, which is best determined experimentally. Based on this derivation, the mass transport in porous media according to the dusty-gas model is coupled to convective flux and integrated in the balance of a catalyst pellet in section 4.3.2.3, which then is solved as part of a heterogeneous reactor model.

4 A fixed-bed reactor modeling study on the methanation of CO_2

4.1 Abstract

The methanation of carbon dioxide has gained renewed interest during the last years as a possible technology to synthesize a feasible chemical energy carrier. This modeling study aims at a basic understanding of the aspects relevant for designing an externally cooled fixed-bed reactor for the methanation of a pure, stoichiometric feed gas. It is shown that the reaction rates and the exothermicity $\Delta H_0 = -165\,kJ/mol$ prevent a fixed-bed reactor of technical dimensions to be operated at high conversions without runaway of the reactor. The model predictions of differently detailed pseudo-homogeneous reactor models and a heterogeneous reactor model where the intraparticle transport of mass is described according to a dusty-gas approach are compared to assess the needed level of detail in terms of modeling the heat transfer, fluid flow characteristics and transport resistances on the pellet scale. Under specific conditions, intraparticle mass transfer and external heat transfer need to be considered for describing the temperature and concentration profiles adequately. The study is completed by modeling a fixed-bed membrane reactor as an example of a structured reactor that offers improved temperature control by separated and controlled feeding of hydrogen and carbon dioxide.

Keywords: methanation, Sabatier reaction, carbon dioxide, reactor modeling

4.2 Introduction

The transition of the energy supply from conventional towards renewable resources implies the need for adequate energy storage technology and capacity as a consequence of the unsteady onset of wind and solar energy. The electrolysis of water and the reaction of hydrogen with carbon dioxide to methane offer a possible next generation storage technology [15]:

$$CO_2 + 4\,H_2 \rightleftharpoons CH_4 + 2\,H_2O$$

Biomass, flue gases from power plants or emissions of the cement industry at lime burning are thought of as possible sources for carbon dioxide. Being a feasible chemical energy carrier, methane can easily be stored, transported and converted back into electric energy whilst solely employing existing infrastructure and technology. Though the methanation of carbon dioxide has been well known since the beginning of the 20th century, no commercial process has been established and essential questions concerning catalytic systems, kinetics and reaction engineering have not been answered yet. The renewed interest in the Sabatier reaction during the last years has provoked efforts primarily in developing new and improved catalytic systems and studying the mechanism on different catalytic systems both experimentally by spectroscopy and theoretically by DFT calculations.

For example, Park and McFarland [98] investigated a Pd-Mg/SiO_2 catalyst in detail and compared it to other multicomponent systems where Mg was replaced by various metals. A bifunctional mechanism was proposed where carbon dioxide is first adsorbed on a magnesium containing oxide species while highly dispersed Pd(0)-particles provide atomic hydrogen via spillover for reducing carbon dioxide selectively to methane. They confirmed this mechanism by DFT calculations and a carbon dioxide temperature-programmed desorption study later on [99]. Extensive work was carried out by Vesselli et al. in studying the mechanism on metallic Ni experimentally and theoretically [33, 40, 41]. Via UHV techniques certain surface intermediates of a mechanism proposed for a (110) surface by DFT calculations were detected spectroscopically. Besides, in transient kinetic experiments under ambient pressure the methane formation on highly dispersed Ni(0) was studied in detail. It was found that the adsorption of carbon dioxide is strongly affected by the presence of hydrogen. The results of the transient kinetic runs could be explained by two reactions operating in parallel [33]. Except for Ni and Pd, also Ru and Rh have been shown to be catalytically active for the CO_2 methanation (see e.g. [100, 101]).

Less attention has been paid to reaction engineering aspects for the Sabatier process so far though the high exothermicity calls for consideration of the heat management and the

coupling of heat and mass transfer. Moreover, due to the high reaction rates transport limitations might affect the catalyst performance under technical conditions. In order to assure a precise temperature control, Brooks et al. [100] developed a microchannel reactor for the Sabatier process intended for producing 16 g/h of methane for usage in space-related applications, i.e. propellant production on Mars. A Ru-based catalyst system was chosen, for which a kinetic rate equation was fitted to experimental data. The performance of the microchannel reactor could successfully be simulated by solving mass, momentum and energy balances. Sudiro et al. [102] simulated a structured catalytic reactor consisting of an externally cooled reactor tube loaded with metallic honeycomb catalysts for the methanation of a mixture of CO and CO_2 using a 1D heterogeneous single-tube model. At the Paul Scherrer Institut, the fluidized-bed technology has been studied in detail for the methanation of biomass-derived feed gases [103, 104]. Generally, the methanation of synthesis gas from coal or biomass which is characterized by high carbon monoxide content has by now attracted more attention both by industry and academia, see for example the review by Kopyscinski et al. [69] on SNG processes.

This reactor modeling study aims at gaining insight in reaction engineering aspects relevant for fixed-bed reactors in the methanation of a pure, stoichiometric gas mixture of CO_2 and H_2. Though also networks of adiabatic reactors with bypassing and recycle streams well known from SNG processes could be adopted to the CO_2 methanation the focus is laid on externally cooled, single-pass fixed-bed reactors of dimensions typically found in tube-bundle reactors, since in the power-to-gas concept the reactor needs to be started and shut down fast and easily as well as to be capable of handling load changes.

At first, different pseudo-homogeneous reactor models will be compared in order to evaluate the level of detail needed in modeling of the heat transfer and fluid flow characteristics. Secondly, results for a heterogeneous reactor model and the influence of transport phenomena on the reactor performance will be discussed. Based on these results, the potential of structured reactors will be highlighted by simulating a fixed-bed membrane reactor.

4.3 Model development

4.3.1 Kinetics

The focus is laid on Ni-systems since from an economic point of view any different choice must offer considerable improvements in activity and selectivity. Nevertheless, this study will also help to clarify the requirements for other catalytic systems because -as will be shown- heat management on the reactor scale and transport phenomena are of particular importance. Concerning Ni-systems, Weatherbee and Bartholomew [46] published Langmuir-Hinshelwood rate equations for Ni/SiO_2 describing the intrinsic kinetics at a total pressure of 1.4 bar, temperatures between 500 and 600 K and space velocities between 30.000 and 90.000 h^{-1}. Since the mole fractions of hydrogen (carbon dioxide) were varied between 2% and 10% (0.2% and 2.0%), the partial pressures are considerably lower than in a technical process operating at the stoichiometric feed gas composition at elevated pressure. For this study, the rate equations proposed by Xu and Froment [64] for the intrinsic kinetics of the steam reforming, CO_2 methanation and the reverse water-gas shift reactions on $Ni/MgAl_2O_4$ are used (see figure 4.1). The conditions for the methanation and reverse water-gas shift experiments were temperatures between 300 and 400°C and pressures between 3 and 10 bar at undiluted feed gas compositions. An excellent fit of the data was obtained by Xu and Froment with Langmuir-Hinshelwood-Hougen-Watson rate equations [64].

Aparicio [105] used the data by Xu and Froment and supplemented them by transient experiments, i.a. concerning transient CO methanation runs, to develop a comprehensive elementary step kinetic model. In order to justify the usage of the methanation kinetics developed for a typical steam reforming catalyst, we also compared the kinetics to data recently published for the methanation of a stoichiometric feed gas composition on Ni/ZrO_2 by Schoder et al. [35]. After merely adjusting the number of active sites (to 46% of the fresh $Ni/MgAl_2O_4$ catalyst by Xu and Froment) the kinetics describes the temperature and pressure dependence at the stoichiometric feed gas composition adequately though the model slightly overestimates the apparent activation energy (see figure 4.11 in the supplementary information). In view of the different metal loading (15.2% and 5%) and oxide carrier of the catalyst systems, the ratio concerning the number of active sites seems in a plausible range. In total, the excellent fit of the steady-state data by Xu and Froment, the previous usage of the data for developing a comprehensive microkinetic model and the adequate description of steady state data on Ni/ZrO_2 validate this kinetics for a reactor modeling study.

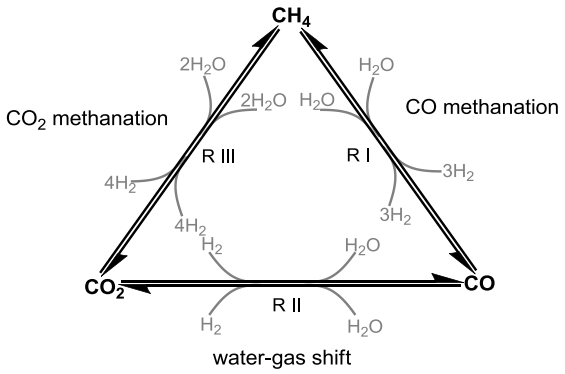

$$r_1 = \frac{k_1}{p_{H2}^{2.5}}\left(p_{CH4}p_{H2O} - \frac{p_{H2}^3 p_{CO}}{K_1}\right)/DEN^2$$
$$r_2 = \frac{k_2}{p_{H2}}\left(p_{CO}p_{H2O} - \frac{p_{H2}p_{CO2}}{K_2}\right)/DEN^2$$
$$r_3 = \frac{k_3}{p_{H2}^{3.5}}\left(p_{CH4}p_{H2O}^2 - \frac{p_{H2}^4 p_{CO2}}{K_3}\right)/DEN^2$$

$$DEN = 1 + K_{CO}p_{CO} + K_{H2}p_{H2} + K_{CH4}p_{CH4} + K_{H2O}\,p_{H2O}/p_{H2}$$

Figure 4.1: The kinetic model by Xu and Froment

4.3.2 Modeling of fixed-bed reactors

4.3.2.1 One-dimensional pseudo-homogeneous PFR model

The simplest model used is a one-dimensional pseudo-homogeneous plug-flow reactor (PFR) model. Mass and heat balances are formulated as follows:

mass balance:

$$\frac{\partial(uc_i)}{\partial z} = \rho_{\text{bed}} \sum_{j=1}^{3} \nu_{i,j} r_j \tag{4.1}$$

heat balance:

$$(uc_{\text{tot}})\bar{c}_p \frac{\partial T}{\partial z} = \rho_{\text{bed}} \sum_{j=1}^{3} r_j(-\Delta H_j) - \frac{4}{d_{\text{tube}}} U'_A(T - T_c) \tag{4.2}$$

The pressure drop along the axial reactor coordinate is neglected and the partial pressures p_i of the components are calculated assuming ideal gas behavior. The specific heat capacity $c_{p,i}$ of component i is calculated with the Shomate equation using data

from the NIST database. It was furthermore verified that for the chosen conditions the cooling temperature can well be approximated as constant in case of a molten salt reactor for example. U'_A describes an effective, overall heat transfer coefficient that results from a series of resistances caused by the effective heat transfer coefficient for the tube insight, the conductivity of the metallic tube wall and the heat transfer coefficient for the tube outside. The resistance of the tube wall is neglected and the heat transfer coefficient for the tube outside is set constant to $2000\,\mathrm{W/(m^2K)}$.

$$\frac{1}{U'_A} = \frac{1}{\alpha_{\mathrm{eff}}} + \frac{1}{\alpha_{\mathrm{out}}} \tag{4.3}$$

According to de Wasch and Froment [106], in a 1D model the effective heat transfer coefficient for the tube insight can be approximated by

$$\frac{1}{\alpha_{\mathrm{eff}}} = \frac{1}{\alpha_W} + \frac{d_{\mathrm{tube}}}{8\Lambda_r^{\mathrm{eff}}} \tag{4.4}$$

assuming again a series of resistances concerning the wall heat transfer coefficient and the radial dispersion of heat. α_W characterizes the heat transfer adjacent to the wall while Λ_r^{eff} describes the transport in the fixed-bed. According to the VDI-Wärmeatlas the radial dispersion and the effective wall heat transfer coefficient are split into a stagnant and a dynamic contribution each [87, 88], see equations 4.19 to 4.25 in the appendix for details about the correlation equations. The thermal conductivity of the gas mixture is calculated by the mixing rule of Wassiljeva, where the temperature dependent thermal conductivity and viscosity are approximated by polynomials using data from the VDI-Wärmeatlas [107].

4.3.2.2 Two-dimensional, pseudo-homogeneous reactor models

In order to take the radial profiles of temperature and gas composition into account, also two-dimensional models were implemented. The α_W model assumes constant values of the properties describing the pseudo-homogeneous continuum, i.e. porosity and dispersion coefficients are independent of the radial position. Heat and mass transfer balances are formulated as follows:

mass balance:

$$\frac{\partial(uc_i)}{\partial z} = \rho_{\mathrm{bed}} \sum_{j=1}^{3} \nu_{i,j} r_j + D_r^{\mathrm{eff}} \left(\frac{\partial^2 c_i}{\partial r^2} + \frac{1}{r} \frac{\partial c_i}{\partial r} \right) \tag{4.5}$$

heat balance:

$$(uc_{\mathrm{tot}})\bar{c}_p\frac{\partial T}{\partial z} = \rho_{\mathrm{bed}}\sum_{j=1}^{3} r_j(-\Delta H_j) + \Lambda_r^{\mathrm{eff}}\left(\frac{\partial^2 T}{\partial r^2} + \frac{1}{r}\frac{\partial T}{\partial r}\right) \tag{4.6}$$

In the α_W model a third type boundary condition is introduced to consider the resistance for the heat transfer close to the wall. The wall heat transfer coefficient α_W and effective heat dispersion coefficient Λ_r^{eff} are identical to the contributions of the effective heat transfer coefficient in eq. 4.4 for the 1D model in section 4.3.2.1. The mass dispersion coefficient is calculated analogously to eq. 4.19 where the molecular Péclet number is used and the diffusion coefficient is substituted for the thermal conductivity (see [88] for details). The boundary conditions for the α_W model are:

$$\begin{aligned} r = 0: \quad & \frac{\partial T}{\partial r} = 0 && \frac{\partial c_i}{\partial r} = 0 \\ r = d_{\mathrm{tube}}/2: \quad & \Lambda_r^{\mathrm{eff}}\frac{\partial T}{\partial r} = U_A''(T - T_c) && \frac{\partial c_i}{\partial r} = 0 \end{aligned}$$

In contrast, the so-called $\Lambda(r)$-model is based on a radial distribution of porosity [108]. Numerous empirical equations have been published to describe the porosity profiles as a function of shape and dimension of pellet and tube. Here, an empirical equation by Giese [109] for spherical catalyst pellets in circular tubes is used. It considers a porosity close to 1 near the tube wall that decreases monotonically towards the center to the value of 0.4 for infinite beds (see figure 4.2):

$$\Psi(r) = 0.4\left(1 + 1.36exp\left(-5\frac{r_{\mathrm{tube}} - r}{d_p}\right)\right) \tag{4.7}$$

In the $\Lambda(r)$-model, the overall heat transfer coefficient is equivalent to the wall heat transfer coefficient at the tube outside:

$$\frac{1}{U_A''} = \frac{1}{\alpha_{\mathrm{out}}} \tag{4.8}$$

Consequently, it characterizes the heat transfer from the cooling medium to the tube inner wall (the resistance due to conduction in the metallic wall is neglected). The introduction of an artificial wall heat transfer coefficient for the tube inside can be avoided in this model as the heat dispersion coefficient is a function of the radial position and thus also captures the resistance adjacent to the tube wall (see eq. 4.26). This way, there is no artificial jump in temperature between the inner tube wall and the continuum phase but a continuous profile. In addition to the mass and energy balances also the

extended Brinkman equation is solved as momentum balance. After the implementation of an effective viscosity [109], that accounts for turbulent flow fluctuations in the packed bed, the superficial velocity field can be modeled.

$$\frac{\partial p}{\partial z} = -f_1 u(r) - f_2 u^2(r) + \frac{\mu_{eff}}{r}\frac{\partial}{\partial r}\left(r\frac{\partial u(r)}{\partial r}\right) \tag{4.9}$$

with

f_1, f_2 from Ergun equation

and

$$\frac{\mu_{\text{eff}}}{\mu_{\text{gas}}} = 2\exp\left(2\cdot 10^{-3} Re\right)$$

The example of a radial flow profile for the axial superficial velocity $u(r)$ in figure 4.2 illustrates a bypassing flow close to the wall which is in accordance with the high porosity in this region. The velocity at $r = r_{tube}$ is 0 as a consequence of the non-slip boundary condition.

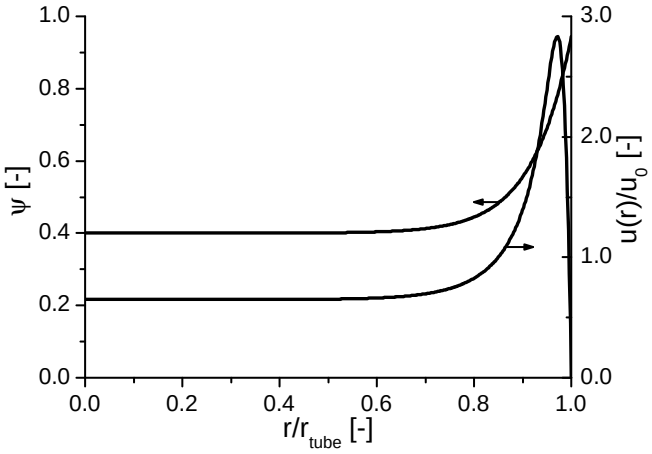

Figure 4.2: radial profiles of the normalized axial velocity in the $\Lambda(r)$-model and of porosity according to Giese's correlation

4.3.2.3 Particle model for the one-dimensional, heterogeneous PFR model

In order to quantify the effects of transport phenomena on the reactor performance, the 1D pseudo-homogeneous reactor model is extended to a heterogeneous reactor model, i.e. coupled balances for the reactor and the pellet level are solved now. On the reactor level, the reaction rates in the mass and the energy conservation are substituted for effective reaction rates.

$$r_i^{\text{eff}} = \eta_j r_j^{\text{intrinsic}} \tag{4.10}$$

As a particle model the dusty-gas approach is chosen for calculating the effective reaction rates because a network of three reactions in a five-component system has to be considered. It accounts for the transport mechanisms of molecular and Knudsen diffusion as well as for viscous flow. By this model no further assumptions and parameters except the pore radius, the tortuosity for the effective diffusion coefficients as well as the permeability B_0 for viscous flow are introduced. The latter one is approximated by the Hagen-Poiseuille law for laminar flow in a capillary. Pore radii r_{pore} can easily be obtained experimentally via BET or Hg-porosimetry. For setting up the dusty-gas model (DGM) the formalism developed by Skrzypek et al. [110] is adopted. In a system of N components and M reactions, M differential equations are solved for the auxiliary variables Ω_j correlated to the reaction j, (N-1) differential equations for mole fractions x_i of the components 1 - (N-1) and one differential equation for the total pressure p.

$$\frac{d\Omega_j}{dy} = y^2 r_j \qquad j = 1,2,3 \tag{4.11}$$

$$\frac{dx_i}{dy} = -\frac{1}{y^2}\left(\sum_{j=1}^{3}\Omega_j \sum_{k=1}^{5}\nu_{k,j}F_{ik}\right) \qquad j = 1,2,3,4 \tag{4.12}$$

$$\frac{dp}{dy} = -\frac{1}{y^2}\frac{RT}{w}\left(\sum_{i=1}^{5}\frac{1}{D_i^{eff}}\sum_{j=1}^{3}\nu_{j,i}\Omega_j\right) \tag{4.13}$$

with

$$F_{ii} = \frac{RT}{p}\left(\frac{1}{D_i^{eff}} + \sum_{k=1}^{5}\frac{x_k}{D_{ik}^{eff}} - \frac{x_i}{D_i^{eff}}\left(1 + \frac{B_0 p}{\eta D_i^{eff}}\right)\frac{1}{w}\right)$$

$$F_{ik} = -\frac{RT}{p}\left(\frac{x_i}{D_{ik}^{eff}} + \frac{x_i}{D_k^{eff}}\left(1 + \frac{B_0 p}{\eta D_i^{eff}}\right)\frac{1}{w}\right)$$

$$w = 1 + \frac{B_0 p}{\eta}\sum_{i=1}^{5}\frac{x_i}{D_i^{eff}}$$

$$B_0 = \frac{r_{pore}^2}{8}$$

The heat balance for the particle level is formulated as follows:

$$\frac{2}{y}\lambda_P \frac{dT}{dy} + \lambda_P \frac{d^2T}{dy^2} + \rho_{cat} \sum_{j=1}^{3} r_j(-\Delta_R H_j) = 0 \tag{4.14}$$

The effective diffusion coefficients D_i^{eff} and D_{ij}^{eff} are correlated by the factor ϵ/τ to the molecular and Knudsen diffusion coefficient which are approximated by Fuller's equation and by the kinetic theory of gases according to eq. 4.15, respectively.

$$D_i = \frac{2}{3} r_p \sqrt{\frac{8RT}{\pi M_i}} \tag{4.15}$$

The boundary conditions are summarized in table 4.1. Heat and mass transfer coefficients for the particle-to-fluid transfer are approximated by Wakao's correlation [111]:

$$Sh = 2 + 1.1 Sc^{(1/3)} Re^{0.6} \tag{4.16}$$

$$Nu = 2 + 1.1 Pr^{(1/3)} Re^{0.6} \tag{4.17}$$

Table 4.1: Boundary conditions for dusty-gas model

y=0	$\Omega_j = 0$	$j = 1, 2, 3$
	$\frac{dT}{dy} = 0$	
y=r_p	$\sum_{j=1}^{3} \nu_{i,j}\Omega_j = k_m \frac{p}{RT}(x_i - x_i^{\text{reactor}})$	$i = 1, 2, 3, 4$
	$p = p^{\text{reactor}}$	
	$\sum_{j=1}^{3} \Omega_j(-\Delta_R H_j) = k_h (T - T^{\text{reactor}})$	

4.3.2.4 One-dimensional pseudo-homogeneous reactor model for a fixed-bed membrane reactor

In the fixed-bed membrane reactor a component is fed via a membrane to the reactor (figure 4.3). The flux density Ω_{mem} through the membrane causes an additional source term in the mass and energy balance (see equations 4.30 to 4.36 in the appendix). It is assumed that the pressure drop of the membrane is large compared to the pressure drop in the fixed-bed and the central tube so that the flux density Ω_{mem} is constant over the whole reactor length. The heat transfer from the annulus to the central tube was also

taken into account. The hydraulic diameter was employed as characteristic length for correlation equations.

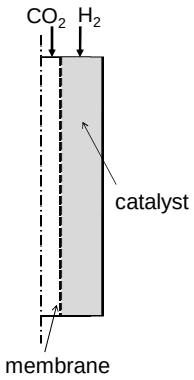

Figure 4.3: The principle of a fixed-bed membrane reactor

4.3.3 Computational Methods

The systems of ordinary and partial differential equations in the 1D pseudo-homogeneous PFR model, the α_W, the heterogeneous and the fixed-bed membrane reactor model were solved numerically in Matlab®. For ODEs the solver ode15s was used. In the 2D-model the PDEs were transformed to ODEs via orthogonal collocation. The boundary value problem on the particle level of the heterogeneous model was solved with the bvp4c-solver. For the $\Lambda(r)$-model Comsol Multiphysics® was employed.

4.4 Results and Discussion

4.4.1 Thermodynamics

Before discussing and comparing the results of the different reactor models, thermodynamic aspects of the CO_2 methanation are elucidated briefly. Figure 4.4 shows the yield of methane in thermodynamic equilibrium for the pure, stoichiometric feed gas composition of $H_2/CO_2 = 80/20$ considering the species CO_2, H_2, CH_4, H_2O and CO. Since the methanation is a highly exothermic reaction with volume contraction, the highest yields are obtained at low temperatures and high pressures. For e.g. a yield above 98% at a total pressure of 10 bar, the temperature needs to be below 300°C. If the pressure is reduced to 1 bar, this temperature is shifted to 235°C. In contrast to the yield the conversion rises again at temperatures of above 600-800°C depending on the pressure. The selectivity is shifted now towards carbon monoxide because of the endothermicity of the reverse water-gas shift reaction. In thermodynamic equilibrium, the CO content at 1 bar is in the low ppm-range (< 50 ppm) for temperatures below 300°C. Thus, thermodynamically it is possible to produce a synthetic natural gas that can be fed into the natural gas grid without further purification and separation steps except for the removal of water from the product gas.

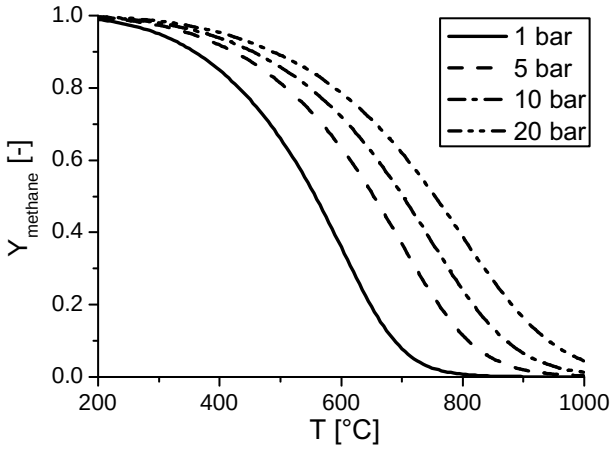

Figure 4.4: Yield of methane in thermodynamic equilibrium for the stoichiometric feed gas composition

4.4.2 Parametric sensitivity and runaway behavior

At first, the parametric sensitivity concerning the feed and cooling temperature is investigated using the 1D pseudo-homogeneous reactor model for the stoichiometric feed gas composition of $H_2/CO_2 = 80/20$ at a tube diameter of 2 cm and a total pressure of 10 bar. The reference conditions are summarized in table 4.2. If not specified otherwise, results relate to these data. Figure 4.5a shows that for a feed temperature of 279°C a moderate hot spot with a temperature rise of about 11°C is developed and a yield of 32% methane is obtained. A temperature rise of 3°C to 282°C provokes a pronounced hot spot and significantly raises the yield to 40.8%. A further increase in the feed temperature causes the runaway of the reactor: the heat release due to the chemical reaction exceeds the heat removal potential. The maximum temperature is above 690°C now and a yield of 91.9% is obtained. According to the phase diagrams in figure 4.5b the methanation reaction runs into equilibrium in the hot spot ($Y \approx 50\%$) for the feed temperature of 285°C. While cooling down, the equilibrium is shifted and the methanation proceeds. Nevertheless, falling below a certain temperature, the reaction rate is too low and the cooling is too fast respectively, so that the equilibrium composition cannot be maintained and at the reactor outlet temperature of 285°C the equilibrium yield 98.3% is not attained.

Table 4.2: Parameters in the reference case

space velocity	GHSV	5000 h^{-1}
catalyst mass	m_{cat}	3 kg
flow rate	Q	10.9 Nm^3h^{-1}
total pressure	p	10 bar
feed mole fraction H_2	$x_0(H_2)$	0.8
feed mole fraction CO_2	$x_0(CO_2)$	0.2
pellet diameter	d_p	3 mm
catalyst density	ρ_{cat}	2350 kgm^{-3}
bed density	ρ_{bed}	$(1-\Psi)\rho_{cat}$
bed porosity	Ψ	0.4
cooling temperature	T_c	T_{feed}
pore diameter	d_{pore}	20 nm
tortuosity	τ	4

A thorough parameter variation study concerning all process and design variables has been performed to screen whether moderate hot spots can be kept up in a parametric stable region to allow for high yields and stability likewise. Figure 4.6 for instance illustrates the influence of the tube diameter on the reactor performance. Lowering the tube diameter, the radial heat dispersion is facilitated because of shorter transport distances

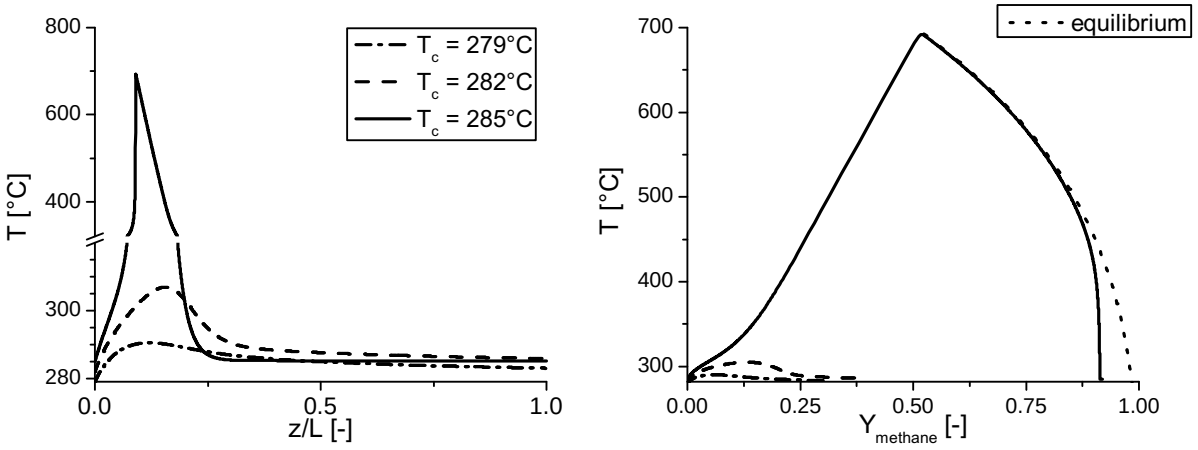

Figure 4.5: Parametric sensitivity of the cooling temperature ($d_{\mathrm{tube}} = 2\,\mathrm{cm}$); a: axial temperature profiles; b: phase diagrams

and higher Reynolds numbers. Consequently, the reactor is operated isothermally up to higher temperatures. Nevertheless, operation points with moderate hot spots are not found. The formation of a hot spot provokes a runaway even at a tube diameter of 1 cm. However, the heat removal is so efficient that the region of parametric sensitivity is shifted to temperatures $> 305°\mathrm{C}$ and yields $< 70\%$ are obtained. In addition to severe fluid flow maldistribution effects at the low $\mathrm{d_{tube}/d_p}$-ratio, that are not taken into consideration in the 1D model, an unfeasible reactor length $> 20\,\mathrm{m}$ results in this case. For $\mathrm{d} > 6\,\mathrm{cm}$, the worse heat transfer prevents appropriate cooling after the hot spot and accordingly the equilibrium is shifted less than for smaller diameters. Besides the tube diameter, the total pressure and dilution of the catalyst were found to be sensitive parameters. For the chosen space velocity the parameter variations point out that in the studied range it is not possible to operate the reactor in the parametric stable region and to attain yields close to the equilibrium composition for temperatures below 350°C.

4.4.3 Comparison of the pseudo-homogeneous reactor models

Next, it is studied how the different degree of detail in the three pseudo-homogeneous reactor models influences the model predictions. The porosity for the 1D and the α_W model is chosen as the mean of the radial distribution of the $\Lambda(r)$-model to ensure comparability. As the three models reveal almost the identical dependence of maximum temperature and yield on feed temperature for the reference case conditions (see figure 4.12 in the supplementary), the feed is diluted with 50% of pure product gas in order to be able to compare the models in detail. This way, intermediate yields and

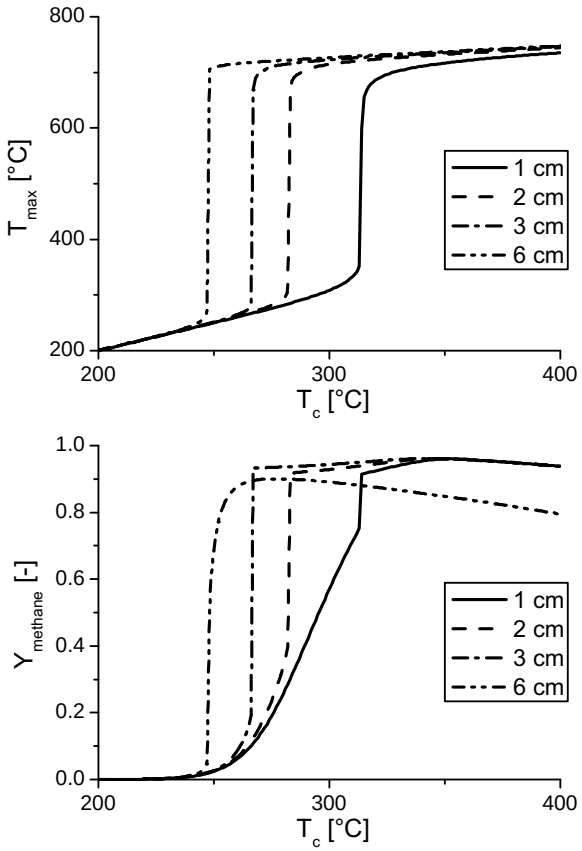

Figure 4.6: Maximum temperature and yield as a function of feed temperature in dependence on the tube diameter

conversions can be studied since on the one hand the reaction rates are lower due to the equilibrium and on the other hand the adiabatic temperature rise is less due to the lower concentration of reactants. Accordingly, maximum temperatures $< 550°C$ are found in the runaway region (figure 4.7). The maximum temperature in the 1D model is always lower than in the two-dimensional models because it reflects a radially averaged value. For calculating the effective heat transfer coefficient a series of resistances has been considered where the resistance due to radial dispersion is accounted for via

$$R_{\mathrm{Disp}} = \frac{d_{\mathrm{tube}}}{8\Lambda_r^{\mathrm{eff}}}. \tag{4.18}$$

As pointed out for example by Finlayson [112], this can be interpreted as a single-point collocation with the root of the polynomial being located at $r = 1/\sqrt{2}r_{\mathrm{tube}}$ where the value of a parabolic function symmetric to $r = 0$ is equivalent to the radial average. In addition, the radial dispersion of mass increases the hot spot temperature. Thus,

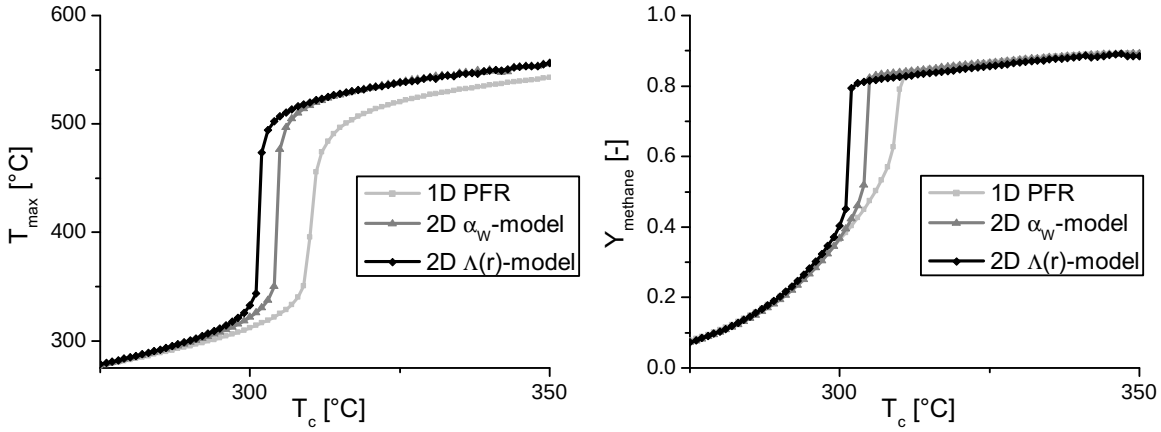

Figure 4.7: Maximum temperature and yield as a function of feed temperature in pseudo-homogeneous reactor models for the diluted feed gas $H_2/CO_2/CH_4/H_2O$=40/10/16.7/33.3 ($d_{\mathrm{tube}} = 3\,\mathrm{cm}$)

the runaway is found at higher feed temperatures for the 1D model since the radial dispersion of mass is not accounted for and the reaction rate at the average temperature $r(\overline{T})$ is lower than the radially averaged reaction rate $\overline{r(T)}$ because of the exponential dependence on temperature. To further improve the predictions of the 1D PFR model, the maximum temperature in the tube center could easily be approximated assuming a parabolic radial temperature profile. Also there are approaches to calculate a more appropriate radially averaged reaction rate, see for example the δ-model by Koning et al. [83].

The results concerning the runaway behavior for the 2D models are very similar among one another despite of deviations in the radial and also in the axial temperature profiles. The somewhat lower yields for the runaway region in the $\Lambda(r)$-model reflect the maldistribution of the fluid flow after the hot spot where the equilibrium is not attained anymore. The axial velocity is the highest in a region with a high porosity and accordingly a low volume-based reaction rate. Moreover, because of the vicinity to the tube wall, the temperature and accordingly also the mass-based reaction rate is lowered there. In total, the 1D PFR model reflects the main qualitative trends while the 2D models might be necessary for a quantitative evaluation and comparison to experimentally determined profiles. The differences at the methanation of the pure feed gas are less pronounced since distinct radial temperature gradients, which are the main reason for deviations, are not established without runaway of the reactor where the equilibrium composition is attained anyway. For a basic understanding of characteristics for a CO_2 methanation fixed-bed reactor the 1D model is evaluated as sufficient and used exclusively in the following.

4.4.4 The heterogeneous reactor model

The focus of this section is laid on how transport processes influence the reactor performance and how this can be used beneficially in improving the reactor design. Figure 4.8 shows the axial profiles for the temperature, the mole fractions and the overall effectiveness factor for methane formation at the reference conditions and a feed temperature of 320°C. The maximum temperature difference in the catalyst pellet is below 6°C which is interpreted in terms of the onset of an intraparticle diffusion limitation and the small Prater number (at the inlet conditions $\beta = 0.011$), i.e. the heat removal is fast compared to the potential of heat release regarding the pellet scale. The temperature difference decreases from the beginning of the reactor towards the hot spot. This reflects the decrease of the carbon dioxide on the reactor scale as well as the higher temperature level that shifts the equilibrium to larger carbon dioxide concentrations. In contrast, the maximum temperature difference between the catalyst surface and the reactor level representing the gas phase temperature is located at the point of maximum effective reaction rate and is significantly larger with a maximum value of 26°C. If the space velocity is reduced, the external heat transfer limitation is more severe and the temperature difference can exceed 100°C. This indicates that experimentally measured temperatures reflecting the gas phase temperature do not necessarily represent the maximum temperatures in the system which is in particular interesting concerning local catalyst deactivation phenomena. The profiles of the mole fractions reveal a mass transfer limitation in the beginning of the reactor where the concentration of carbon dioxide decreases close to zero in the pellet center. At the pore radius of 10 nm the transport is dominated by Knudsen diffusion. As a consequence of the lower mean velocity of carbon dioxide compared to hydrogen the transfer limitation is primarily caused by the diffusive flux of carbon dioxide. The gas composition in the bulk phase and on the pellet surface is almost identical and for reasons of clarity not shown in the graph. Accordingly, external mass transport limitations are negligible under the conditions chosen. The overall effectiveness factor for the formation of methane (figure 4.8c) points out that despite of the excess temperature of the catalyst pellets compared to the gas phase, mass transfer drastically slows down the reaction rates in the range of the hot spot where the effectiveness factor is below 5%.

The temperature profile in figure 4.8a itself indicates the influence of the intraparticle mass transfer limitation on the maximum temperature. As the limitation slows down the heat release due to chemical reaction, maximum temperatures below 600°C can be realized now. In comparison to the pseudo-homogeneous reactor model (see the phase diagrams in figure 4.8d), the temperature rise is not adiabatic anymore and the equilibrium is not attained in the hot spot. The range of the parametric sensitivity concerning the feed temperature is accordingly shifted to higher values (figure 4.9).

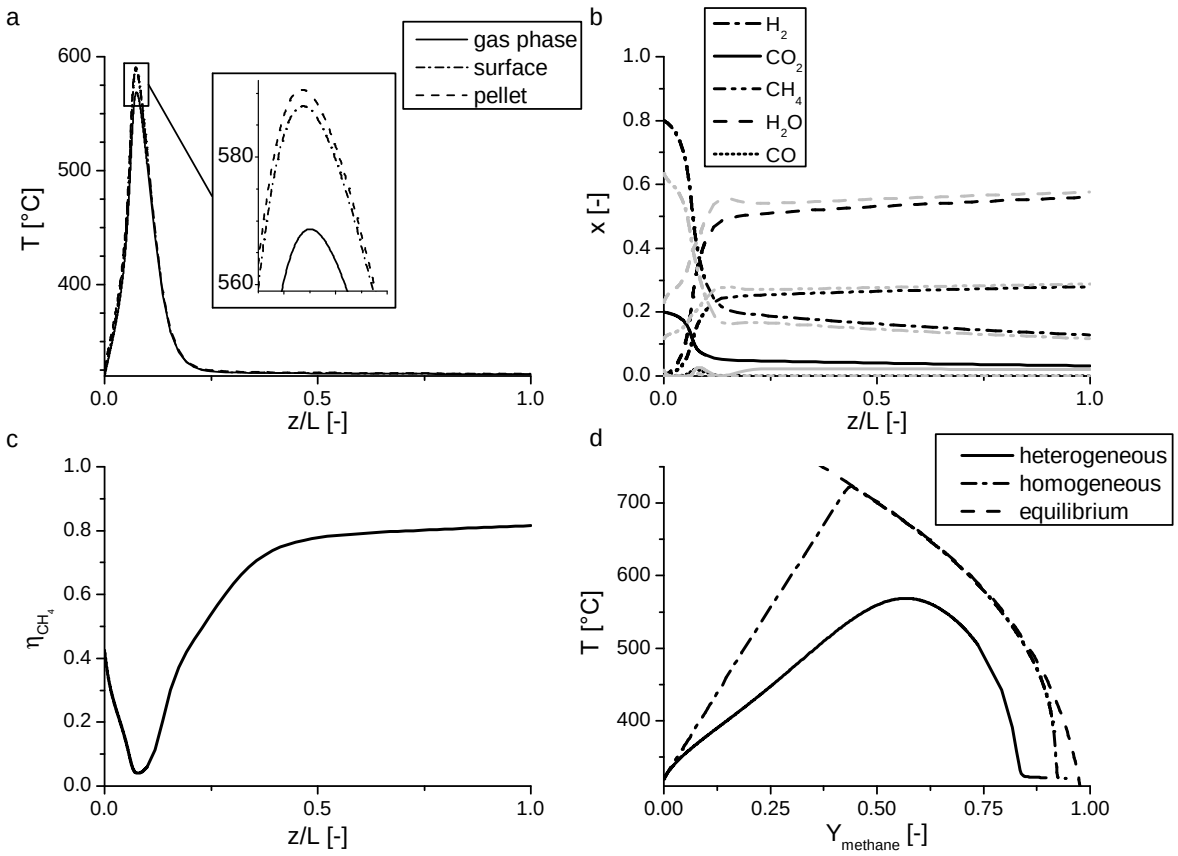

Figure 4.8: Axial profiles of temperature (a), mole fraction (black: gas phase; gray: pellet center) (b), effectiveness factor of CH_4 formation (c) and the phase diagram (d) for the heterogeneous reactor model ($T_{feed} = 320°C$, $d_{tube} = 2\,cm$, $d_p = 5\,mm$, $d_{pore} = 20\,nm$)

However, choosing for example $r_{pore} = 50\,nm$ and $d_p = 2\,mm$ gives results fairly similar to the pseudo-homogeneous model. The intraparticle mass transfer hardly affects the reactor performance now and the maximum temperatures in the models differ by less than 40°C. This emphasizes that in the CO_2 methanation process there is potential for optimization concerning the interplay of mass transport, reaction rates and heat transport on the pellet level also in terms of heat management and temperature control on the reactor scale. In comparison to a dilution of the catalyst with inert material, it is beneficial that the reaction rates are slowed down exactly at the position where the heat release needs to be limited while the reaction rates are less affected in the cooling and low temperature region.

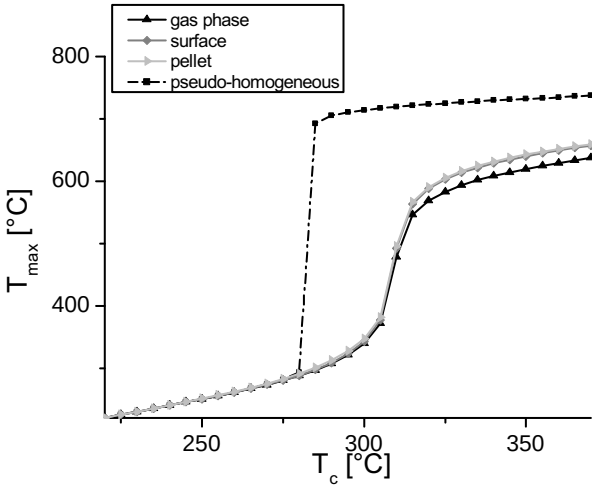

Figure 4.9: Comparison of the 1D pseudo-homogeneous and heterogeneous reactor model ($d_{\text{tube}} = 2\,\text{cm}$, $d_p = 5\,\text{mm}$, $d_{\text{pore}} = 20\,\text{nm}$)

4.4.5 Temperature control in a fixed-bed membrane reactor

This section addresses another option with respect to temperature control besides optimizing transport properties of the catalyst. Similarly, by controlling the gas composition on the reactor level in every point of the reactor, the local adiabatic temperature rise can be adjusted. One possibility is to feed the components hydrogen and carbon dioxide separately into the reactor and distribute one component appropriately. For this purpose a fixed-bed membrane reactor might be suited ideally (see figure 4.3) where a component is fed via a central tube that in a simple case is made of a porous steel membrane. The individual feeding is possible in principle since in the power-to-gas concept hydrogen and carbon dioxide originate from different sources and do not need to be separated first. As figure 4.10 illustrates, the temperature can be kept at values below 510°C, if the conditions are chosen adequately. In this example, a yield of 91.7% is obtained for a reactor length of 80 cm and catalyst mass of 700 g at the same flow rate as in the reference case which means that the equilibrium at the outlet temperature of 460°C is virtually attained ($Y_{\text{eq}} = 92.0\%$). However, decreasing the cooling temperature is not expedient since an accumulation of carbon dioxide in the beginning of the reactor has to be prevented for controlling the adiabatic temperature rise. For upgrading the product gas of the membrane reactor, a conventional fixed-bed reactor of large diameter could be put in series where the heat management now is simple since the gas composition allows for almost isothermal operation.

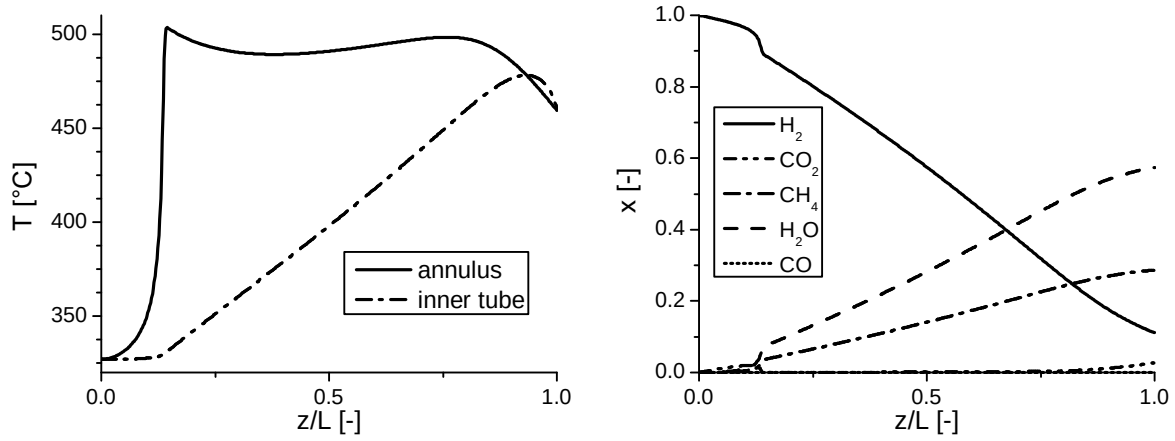

Figure 4.10: Axial profiles of temperature and mole fraction for the fixed-bed membrane reactor ($m_{\mathrm{cat}} = 0.7\,\mathrm{kg}$, $Q = 10.9\,\mathrm{Nm^3/h}$, $d_o = 3.5\,\mathrm{cm}$, $d_i = 2\,\mathrm{cm}$, $p = 20\,\mathrm{bar}$)

4.5 Conclusion

- Different pseudo-homogeneous reactor models were compared in order to assess the needed degree of detail for modeling externally cooled fixed-bed reactors. Even the comparison at modest conversions showed that a simple 1D PFR model is capable of describing the qualitative trends and can be used for screening possible process conditions. For quantitative evaluation and comparison to experimental results, however, in particular the 2D $\Lambda(r)$-model allows for a more detailed perspective.

- The comparison to results for a 1D heterogeneous reactor model using the dusty-gas approach as particle model showed that under specific conditions, i.e. large catalyst pellets, small pore radii and small Reynolds numbers, severe intraparticle mass transfer and external heat transfer limitations need to be considered. The results for the heterogeneous model also emphasized the potential for optimization on the pellet scale in terms of temperature control.

- This modeling study highlighted the two key challenges for the CO_2 methanation process: the reaction rates and exothermicity in the first part of the reactor call for an efficient heat removal if pure stoichiometric feed gas is converted without a product recycle or dilution by water or methane. Tubular reactors of common diameters suffer from a poor stability due to runaway under these conditions. The second challenge concerns the catalyst activity in the low temperature region. For a high quality SNG the equilibrium needs to be attained at temperatures well below 300°C where according to the kinetic model used here the activity is very

low for yields $>90\%$. This prevents to increase the GHSV which would be less problematic in terms of the high temperature region of the reactor.

- Finally, a fixed-bed membrane reactor has been modeled as an example for the capability of structured reactors. The separate feeding of the components enables for an excellent temperature control and allows for attaining near-equilibrium gas compositions at elevated temperatures.

4.6 Appendix

4.6.1 Calculation of the radial dispersion and effective wall heat transfer coefficient for the 1D PFR and the 2D α-model

The radial dispersion is split into a stagnant and a dynamic contribution [88].

$$\frac{\Lambda_r^{\text{eff}}}{\lambda_g} = \frac{\lambda_{\text{bed}}}{\lambda_g} + \frac{Pe}{8} \tag{4.19}$$

$$Pe = \frac{u_0 \rho_g c_{p,m} d_p}{\lambda_g} \tag{4.20}$$

The stagnant contribution λ_{bed} is a function of the conductivity of the solid phase and of the gas phase as well as of the porosity [87]:

$$\frac{\lambda_{\text{bed}}}{\lambda_g} = 1 - \sqrt{1-\Psi} + \sqrt{1-\Psi} k_c \tag{4.21}$$

$$k_c = \frac{2}{N}\left(\frac{B}{N^2}\frac{k_p - 1}{k_p} ln\frac{k_p}{B} - \frac{B+1}{2} - \frac{B-1}{N}\right) \tag{4.22}$$

$$N = 1 - (B/k_p), \quad k_p = \lambda_p/\lambda_g, \quad B = 1.25\left(\frac{1-\Psi}{\Psi}\right)^{10/9} \tag{4.23}$$

For estimating the effective wall heat transfer coefficient for a fixed bed, the correlation by Martin and Nilles is used which similarly is based on a stagnant and a dynamic contribution [88]:

$$Nu = \left(1.3 + \frac{5}{d_{\text{tube}}/d_p}\right)\frac{\lambda_{\text{bed}}}{\lambda_g} + 0.19 Re^{0.75} Pr^{0.33} \tag{4.24}$$

$$Nu = \frac{\alpha_W d_p}{\lambda_g} \tag{4.25}$$

4.6.2 Calculation of the radial dispersion coefficient for the $\mathbf{\Lambda(r)}$-model

The dispersion coefficient is split into a stagnant and dynamic contribution as well, but is a function of the radial position and the local porosity now:

$$\Lambda_r(r) = \lambda_{\text{bed}}(r) + \frac{1}{8} Pe \frac{u_{0,c}}{u0} f(r_{\text{tube}} - r)\lambda_g \tag{4.26}$$

with

$$0 < r_{\text{tube}} - r \leq K d_p : \qquad f(r_{\text{tube}} - r) = \left(\frac{r_{\text{tube}} - r}{K d_p} \right)^2 \tag{4.27}$$

$$K d_p < r_{\text{tube}} - r \leq R : \qquad f(r_{\text{tube}} - r) = 1 \tag{4.28}$$

$$K = 0.44 + 4 \exp\left(\frac{-Re}{70} \right) \tag{4.29}$$

4.6.3 Mass and heat balances for the fixed-bed membrane reactor model

Additionally to the balances for the 1D pseudo-homogeneous reactor model the flux through the membrane and heat transfer between central and annulus tube have to be considered:

annulus:

$$\text{mass balance:} \qquad \frac{d(uc_i)}{dz} = \rho_{\text{bed}} \sum_{j=1}^{3} \nu_{i,j} r_j + j_{i,mem} \frac{4 d_i}{d_o^2 - d_i^2} \tag{4.30}$$

$$\text{heat balance:} \qquad (uc_{\text{tot}}) \overline{c}_p \frac{dT}{dz} = h_{\text{reaction}} + h_{\text{exchange}} + h_{\text{membrane}} \tag{4.31}$$

$$h_{\text{reaction}} = \rho_{bed} \sum_{j=1}^{3} r_j \left(\Delta_R H_j \right) \tag{4.32}$$

$$h_{\text{exchange}} = U_{A,W} \frac{4 d_o}{d_o^2 - d_i^2} (T_c - T) + U_{A,BP} \frac{4 d_i}{d_o^2 - d_i^2} (T_{BP} - T) \tag{4.33}$$

$$h_{\text{membrane}} = j_{CO_2,mem} \frac{4 d_i}{d_o^2 - d_i^2} \int_{T_{BP}}^{T} c_{p,CO_2} dT \tag{4.34}$$

inner tube:

$$\text{mass balance:} \qquad \frac{d(uc_{CO_2})}{dz} = -j_{CO_2,mem} \frac{4}{d_i} \tag{4.35}$$

$$\text{heat balance:} \qquad (uc_{\text{tot}}) \overline{c}_p \frac{dT}{dz} = U_{A,BP} \frac{4}{d_i} (T - T_{BP}) \tag{4.36}$$

4.7 Supplementary information

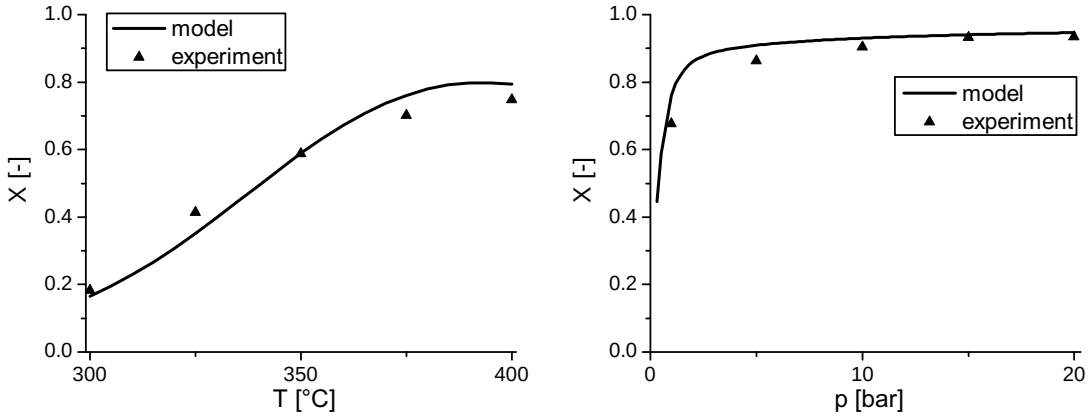

Figure 4.11: Comparison of experimental data by Schoder et al. [35] and the kinetics by Xu and Froment [64] (number of active sites fitted); a: variation of temperature, p = 1 bar; b: variation of pressure, T = 375°C

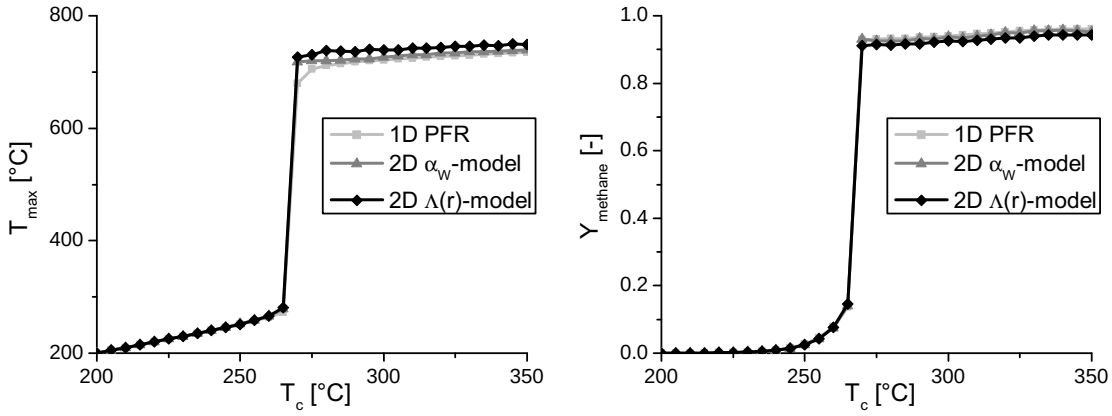

Figure 4.12: Maximum temperature and yield as a function of feed temperature in pseudo-homogeneous reactor models for pure feed gas (d_{tube} = 3 cm)

5 Metallic honeycombs as catalyst supports

Apart from the concepts for temperature control presented in the previous chapter, that is controlling the gas composition by more sophisticated reactor concepts like fixed-bed membrane reactors as well as exploiting mass transport limitations to slow down reaction rates and heat release, structuring in terms of improving heat transfer properties might be a versatile tool as well. As has been discussed above, both effective radial heat dispersion and wall heat transfer coefficients in fixed-beds are impacted by a dynamic contribution and a stagnant contribution. The latter one stems from conductive and radiative heat transport, while the first one is defined by fluid flow and its properties. In general, structuring can be intended at both contributions: the overall heat transfer can be improved by directing the fluid flow in pipes advantageously for instance towards the tube walls or by circulating the flow also radially to diminish the dimension of the hydrodynamic boundary layer. Probably the easiest way to facilitate heat transfer by conduction on the other hand might be the adoption of catalyst carriers of higher thermal conductivity. However, this approach is limited by point contacts of the catalyst pellets, which dominate the resistance concerning the heat conduction in this case. In contrast, continuous, highly conductive solid material matrices throughout the tube cross section have proven advantageously. Foam or honeycomb structures consisting of highly conductive metals like copper or aluminum or covalent structures like silicon carbide are reported for instance.

In this chapter, metallic honeycombs are studied as an example of structured reactors for the methanation reaction. Concerning the modeling, the two different approaches of continuum models and spatially resolved 3D CFD models are compared for the case of an irreversible 1st order reaction in the first part of the chapter. Having validated the continuum model this way, it is adopted for the Sabatier reaction under typical process conditions in the second part of the chapter. Here, the feasibility and also disadvantages of honeycombs for this specific reaction are emphasized and discussed in comparison to conventional single-pass fixed-bed reactors.

5.1 Comparison of a pseudo-continuous, heterogeneous 2D conductive monolith reactor model to a 3D CFD model

5.1.1 Abstract

Conductive catalytic honeycombs of low void fraction have gained renewed interest also for the production of bulk chemicals because of favorable heat transfer properties and a low pressure drop compared to fixed-bed reactors. In this work, a pseudo-continuous, heterogeneous 2D conductive honeycomb reactor model is compared to a detailed 3D CFD model for the case of an irreversible, exothermic first order reaction with emphasis on the description of heat transfer. Excellent agreement in terms of maximum temperature and conversion is found for moderate conditions preferable for technical purposes when using the symmetric model for calculation of the effective radial heat conductivity. Deviations of maximum temperatures at harsher conditions are attributed to the use of global heat and mass transfer coefficients in the 1D channel model and the inherent assumption of a radially fully segregated flow in the continuum approach.

Keywords: conductive catalytic honeycombs, structured reactors, reactor modeling

5.1.2 Introduction

Monolith catalysts are nowadays widely employed in catalytic combustion [113] and exhaust gas cleaning, both for mobile [114] and stationary [115] application. During the last years they have aroused interest also for the production of bulk chemicals since in addition to the low pressure drop in comparison to conventional pellet filled fixed-bed reactors the continuous solid matrix of honeycombs might offer beneficial heat transport properties. The heat transport in fixed-bed reactors for heterogeneously catalyzed gas phase reactions is often limited by the radial heat dispersion, which is dominated by convective heat transport at high particle Reynolds numbers. However, for exploiting beneficial heat transfer properties of honeycomb catalysts, different structures and materials are needed in comparison to honeycombs for exhaust gas applications [116]. In these cases mainly ceramic honeycombs of intrinsic low thermal conductivity are used in adiabatic operation. Therefore, for example metallic Al [117] and Cu [118] honeycombs have been developed to improve the heat transfer properties by shifting the main transport mechanism from convection to conduction in a continuous solid phase. A proof of principle was accomplished by Groppi et al. [119]. They studied the partial oxidation of *o*-xylene to phthalic anhydride up to the pilot scale using a tube reactor

filled with catalyst coated Al honeycombs. In comparison to a reactor filled with pellets a higher temperature level proved advantageous, which, however, could be achieved with lower axial temperature differences, thus ensuring safe operation and allowing equal or even better production rates than the fixed-bed reactor. Besides partial oxidations, conductive honeycombs have also been proposed for other exothermic processes including Fischer-Tropsch [120] and SNG [102] synthesis.

Concerning the modeling of conductive honeycomb catalysts for polytropic operation, mainly continuum models of different complexity are employed. A pioneering continuum model was proposed by Groppi and Tronconi [121] in 1996 in close analogy to fixed-bed reactor models. The model was then validated by a state-of-the art discrete model. In this discrete model, 1D gas phase mass balances and solid phase energy balances are formulated for individual channels after reconfiguration to concentric rings. A differential-algebraic system is finally set up by coupling the balances of channels representative for the different rings via a finite difference scheme that is directly related to the reconfigured monolith structure.

The key parameter in continuum models is the effective radial heat dispersion coefficient which is calculated according to semi-empirical thermal resistance models. The series model proposed by Groppi and Tronconi [121] has also been extended by taking the catalyst layer explicitly into account and it has been compared to a so called parallel model as well as the numerical finite element method (FEM) solution of an isolated channel in stagnant fluid exposed to a constant heat flux [122]. It was found that the exact solution is in between the prediction of the series and parallel model for a large variety of void fractions. Similar thermal resistance models have also been applied successfully for diesel particulate filters [123]. Recently, an improved model for the calculation of the effective thermal dispersion has been published [124]. Also based on an FEM simulation of an imposed heat flux perpendicular to a single channel, this symmetric thermal resistance model proved best compared to the other resistance models and results were very close to the exact solution.

In this research note we present a comparison of a pseudo-continuous, heterogeneous 2D conductive monolith reactor model using the symmetric thermal resistance model to a 3D CFD model where fluid flow as well as heat and mass transport are coupled in presence of an exothermic chemical reaction. It has previously been shown that the effective thermal conductivity models are also capable of describing heat transfer properties of a circular arrangement of channels for a coaxial heat source under non-reactive conditions and stagnant fluid [122]. Also 1D, 2D and 3D single channel models have been compared for adiabatic operation, see e.g. the review of Chen et al. [125]. Generally, it was reported that 1D models do not suffice for an adequate description under all operation conditions.

To the best of our knowledge, a comparison to a 3D CFD model under reactive conditions at polytropic operation comprising channel and tube scale has not been presented yet. This might, however, be preferable for validation since it takes the local heat release at the metallic wall into account, which differs from the boundary conditions imposed for the derivation of the effective thermal conductivity models. Also it enables to critically discuss the continuum approach for low channel number monoliths applied in practice for highly exo- or endothermic reactions, where the scale of a channel diameter differs only little to the macroscale, i.e. the monolith diameter.

5.1.3 Model development

5.1.3.1 Reference case

For the comparison of the models, an exothermic, irreversible first-order reaction is studied. The geometry of the honeycombs is similar to those employed by Groppi et al. for *o*-xylene oxidation [119]. The parameters of the reference case are summarized in table 5.1. If not stated otherwise, all results relate to these conditions. We chose a rather low value of the thermal conductivity of the solid material ($\lambda_s = 30\,\mathrm{W\,m^{-1}\,K^{-1}}$) in order to be able to compare the models also at sharp temperature profiles which is more demanding in contrast to flat profiles resulting at optimized honeycomb structures made of Al or Cu. The assumptions for the comparison are as follows:
(1) Diffusion limitations inside the washcoat are not considered, since the focus is laid on the heat transfer. The incorporation of a Thiele modulus approach for calculation of effectiveness factors is straightforward, but would increase the complexity of the comparison.
(2) The temperature of the lateral surface is set constant and equal to the inlet temperature. The issue of the resistance between honeycomb and tube wall, the so called gap resistance, is not addressed here. Nevertheless, the gap resistance could be implemented in both models via a heat transfer coefficient for the lateral surface and would not cause further differences between the models.
(3) The flow is distributed equally over all channels though the pressure drop might slightly differ due to different hydraulic diameters of the channels (see figure 5.1).
(4) For the heat transfer, the resistance caused by the washcoat is not taken into account. The conductivity of the solid phase is assumed as uniform.
(5) Material and gas phase properties are assumed independent on pressure and temperature.
(6) The first 5 cm of the honeycomb are assumed to be catalytically inactive. Under harsh conditions, maximum reaction rates and solid phase temperatures are observed in the inlet of the reactor otherwise and the results might be influenced by inlet effects.

(7) The washcoat is distributed uniformly over the metallic walls, i.e. the washcoat thickness is constant concerning the 3D model and the washcoat fraction is no function of space concerning the continuum model, respectively.
(8) Heat transfer via radiation is neglected.

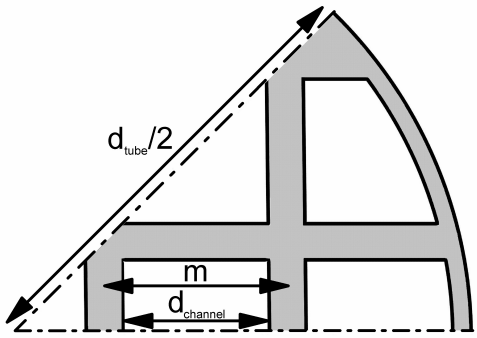

Figure 5.1: Honeycomb geometry

5.1.3.2 Continuum model

The pseudo-continuous, heterogeneous 2D monolith reactor model is adapted from Groppi and Tronconi [116]. It is based on a 1D description concerning the single channel level, which means that global heat and mass transfer coefficients are employed for describing heat and mass transfer to the washcoat layer. Since emphasis is laid on heat transfer properties the model is simplified by assuming constant pressure. The effective radial heat dispersion coefficient is calculated according to the symmetric model proposed in reference [124]. As with the model by Groppi and Tronconi [116], axial dispersion of mass is neglected. The compartment in individual channels prohibits a radial dispersion of mass. Stationary mass and energy balances for the solid and the gas phase are formulated as follows:

Gas phase

Mass balance:
$$W\frac{\partial w_{A,g}}{\partial z} + \frac{4d}{m^2}K_m\left(w_{A,g} - w_{A,s}\right) = 0 \tag{5.1}$$

Energy balance:
$$Wc_p\frac{\partial T_g}{\partial z} + \frac{4d}{m^2}K_h\left(T_g - T_s\right) = 0 \tag{5.2}$$

Solid Phase

Mass balance:
$$\frac{4d}{m^2}\frac{K_m}{\rho_g}\left(w_{A,g} - w_{A,s}\right) - \xi\frac{T_g}{T_s}kw_{A,s} = 0 \tag{5.3}$$

Table 5.1: Parameters and conditions for the reference case (DaI = 2.0)

$d_{channel}$	4 mm
d_{tube}	2.5 cm
m	5 mm
L	25 cm
δ	100 µm
W	0.376 g/s
D_A	$2 \cdot 10^{-5}$ m^2/s
c_p	1 kJ/(kg K)
λ_g	0.05 W/(m·K)
λ_s	30 W/(m·K)
M	100 g/mol
E_A	80 kJ/mol
ΔH_R	-1100 kJ/mol
μ	$2.5 \cdot 10^{-5}$ Pa·s
$w_{A,feed}$	0.05
T_{feed}	520 K
p_{tot}	3.18 bar

Energy balance:

$$\lambda_{e,ax}\frac{\partial^2 T_s}{\partial z^2} + \lambda_{e,r}\left(\frac{\partial^2 T_s}{\partial r^2} + \frac{1}{r}\frac{\partial T_s}{\partial r}\right) + \\ + \frac{4d}{m^2}K_h\left(T_g - T_s\right) + \xi(-\Delta H_r)\rho_g\frac{T_g}{T_s}k\frac{w_{A,s}}{M_A} = 0 \qquad (5.4)$$

Boundary conditions

$z = 0:$ $\quad \frac{\partial T_s}{\partial z} = 0 \qquad T_g = T_w \qquad w_{A,g} = w_{A,feed}$

$z = L:$ $\quad \frac{\partial T_s}{\partial z} = 0$

$r = 0:$ $\quad \frac{\partial T_s}{\partial z} = 0$

$r = R:$ $\quad T_s = T_w$

5.1.3.3 3D CFD model

Due to the symmetry of the honeycomb, only one eighth is incorporated in the model (see figure 5.1). Symmetric boundary conditions are set to the cut faces. The fluid flow inside the channels is modeled as laminar, accordingly no slip boundary conditions are imposed. Mass transfer is simplified according to Fickian diffusion.

Gas phase

Mass balance: $$\rho\left(\mathbf{u}\cdot\nabla\right)w_A = \nabla\cdot\left(\rho D_A \nabla w_A\right) \tag{5.5}$$

Energy balance: $$\rho c_p\left(\mathbf{u}\cdot\nabla T\right) = \nabla\cdot\left(\lambda\nabla T\right) \tag{5.6}$$

Momentum balance: $$\rho\left(\mathbf{u}\cdot\nabla\right)\mathbf{u} = \nabla\cdot\left(p\mathbf{I} + \mu\left(\nabla\mathbf{u} + \left(\nabla\mathbf{u}\right)^T\right) - \frac{2}{3}\mu\left(\nabla\cdot\mathbf{u}\right)\mathbf{I}\right) \tag{5.7}$$

Continuity: $$\nabla\cdot\left(\rho\mathbf{u}\right) = 0 \tag{5.8}$$

Solid phase

Energy balance: $$0 = \nabla\cdot\left(\lambda\nabla T\right) \tag{5.9}$$

Boundary conditions

Reacting boundary:

Mass flux: $$j_A = k_0\cdot exp^{\left(-\frac{E_A}{RT}\right)} c_A M_A \delta$$

Heat flux: $$h = k_0\cdot exp^{\left(-\frac{E_A}{RT}\right)} c_A \delta(-\Delta H_R)$$

No slip: $\mathbf{u} = 0$ (volume conserving reaction)

Lateral surface:

$$T = T_W$$

Inlet:

gas phase: $w_A = w_{A,feed}$ $T = T_W$ $u = u_{feed}$

solid phase: $\mathbf{n}\cdot\nabla T = 0$

Outlet:

$\mathbf{n}\cdot\nabla w_A = 0$ $\mathbf{n}\cdot\nabla T = 0$ $p = p_{tot}$

Both models are solved in Comsol Multiphysics® V4.3. Mass fractions and temperatures are discretized with a second order discretization scheme in the continuum model. The fully coupled linear system is solved with the MUMPS direct solver. In the 3D model, the pressure and velocity fields are discretized with a first-order, temperature and mass fractions with a second-order scheme. The iterative solver GMRES is used for solving the linear system.

5.1.4 Results and Discussion

5.1.4.1 Isothermal conditions

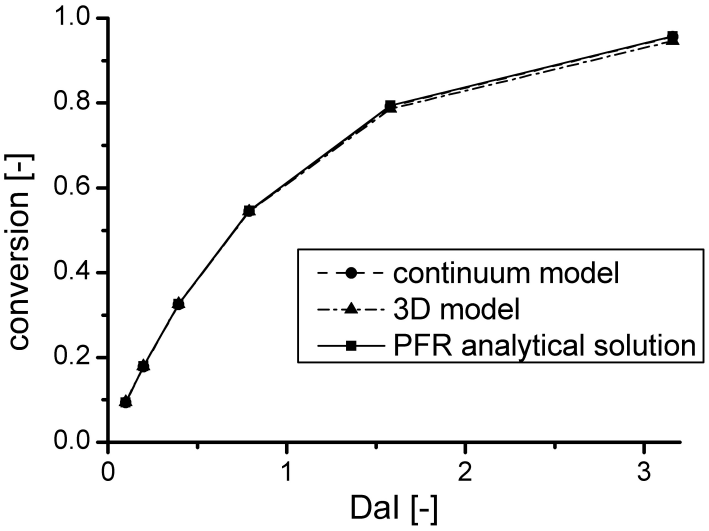

Figure 5.2: Validation at isothermal operation

In order to verify the implementation of both models, results for an isothermal, first-order reaction have been compared to the analytical solution of an ideal plug flow reactor (PFR). The diffusion coefficient had to be increased compared to the reference conditions to ensure a fully kinetic regime not affected by mass transfer to the wall surface. As illustrated in figure 5.2, the conversion in the continuum model is identical to the analytical solution while the 3D model slightly underestimates the results at high Damköhler numbers. It has been checked that this is not caused by a mass transfer limitation. A further reason for the discrepancy might be the non-ideality of the residence time distribution compared to plug flow. As the cumulative residence time distribution in figure 5.3 shows, the flow behavior in the continuum model resembles plug flow since no axial dispersion term is considered in the gas phase mass balance. In contrast, the distribution in the 3D model is broadened. Nevertheless, compared to a fully segregated laminar flow, where the breakthrough is expected at half of the mean residence time, molecular diffusion in lateral direction contracts the distribution. Under reference conditions, the product $Re \cdot Sc = 30$ is in the region where the residence time distribution is narrowest ($Re \cdot Sc = 13.9$) according to the Aris-Taylor model [126] for laminar flow in circular tubes. To estimate the influence of the broadened residence time distribution compared to plug flow, a simple axial dispersion model has been employed. It has been found that the residence time distribution is smaller than predicted by

the dispersion model at a Bodenstein number of $Bo = 100$ and hence the broadened residence time distribution has hardly any effect on the reactor performance. In fact, the discrepancy concerning the conversion at high Damköhler numbers is caused by a distinct washcoat to void ratio of the one deformed channel compared to the others (cf. figure 5.1). Accordingly, averaging of the washcoat fraction employed for the analytical solution and the continuum model lowers the prediction of conversion compared to the 3D model. Under the chosen conditions however, the differences caused by the residence time distribution and washcoat ratio only slightly influence the model predictions and hence enable for the comparison concerning the heat transfer properties.

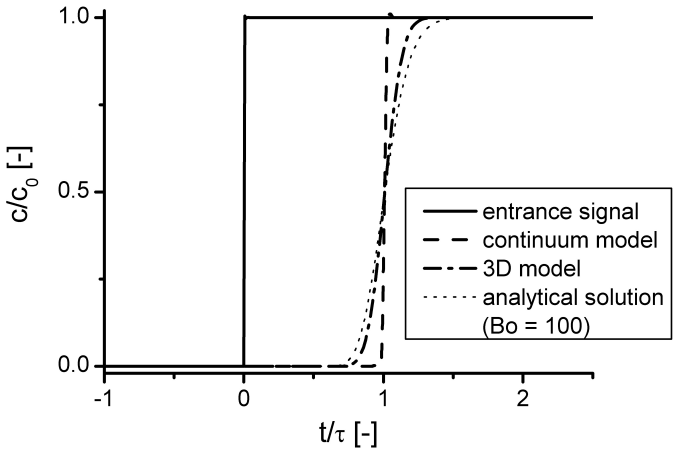

Figure 5.3: Cumulative residence time distribution

5.1.4.2 Thermal resistance models under non-reactive and stagnant fluid conditions

Before comparing the models under reactive conditions, it is studied whether the models for the effective radial dispersion coefficient are able to predict the properties of the low cell number monoliths adequately, since their derivation and validation were based on an imposed heat flux perpendicular to an elementary cell comprising a single channel. The boundary conditions are set similarly to the approach of Hayes et al. [122] for high channel number monolith structures. A constant heat flux is imposed at a coaxial tube completely located in the solid matrix while the temperature of the lateral surface is held constant (figure 5.4a). Figure 5.4b compares the radial temperature profiles of the different models concerning the effective radial dispersion coefficient to the predictions of the 3D model. If plotted as a function of distance to the center, the temperatures of

the mesh elements scatter due to the lack of axial symmetry in the 3D model. Good agreement is found for the symmetric model, though the direction of heat flux diagonal to an elementary cell significantly contributes to the heat flux (see heat flux lines in figure 5.4a). This is different to the boundary conditions set for an elementary cell at the validation of the symmetric model by Visconti et al. [124]. The series and parallel model under- and overestimate the maximum temperature, respectively, which is in line with the findings of Hayes et al. [122] for various void fractions concerning an array of channels. It is noteworthy that for calculation of the radial effective properties not the integral values of the void fraction over the whole cross-section (0.60) but over a single, non-deformed channel (0.64) need to be employed at this low channel number monolith.

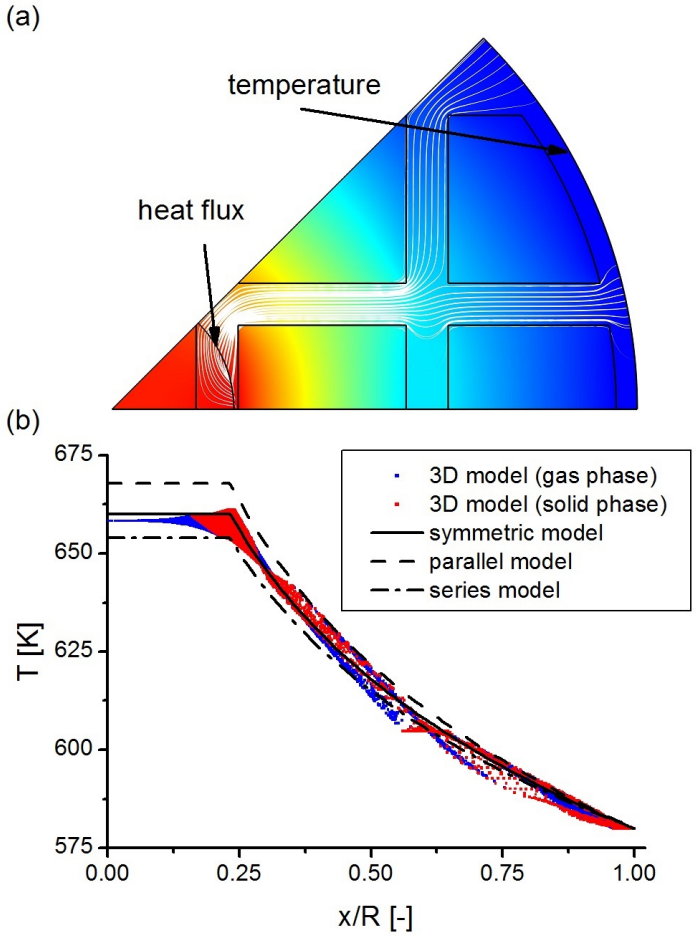

Figure 5.4: Temperature profiles under non-reactive conditions

5.1.4.3 Comparison at polytropic operation

At polytropic operation, sharp temperature gradients between wall and gas phase call for a finer mesh than at the conditions before. Figure 5.5 proves that results for the model comparison are independent of the mesh size. Slight differences are observed mainly for the temperature profile in the middle of the central channel (figure 5.5c) concerning the two coarsest meshes. The differences of maximum temperature are less than 1 K concerning all meshes. Due to low lateral concentration gradients under the reference conditions the concentration profiles vary only slightly even for the coarsest meshes.

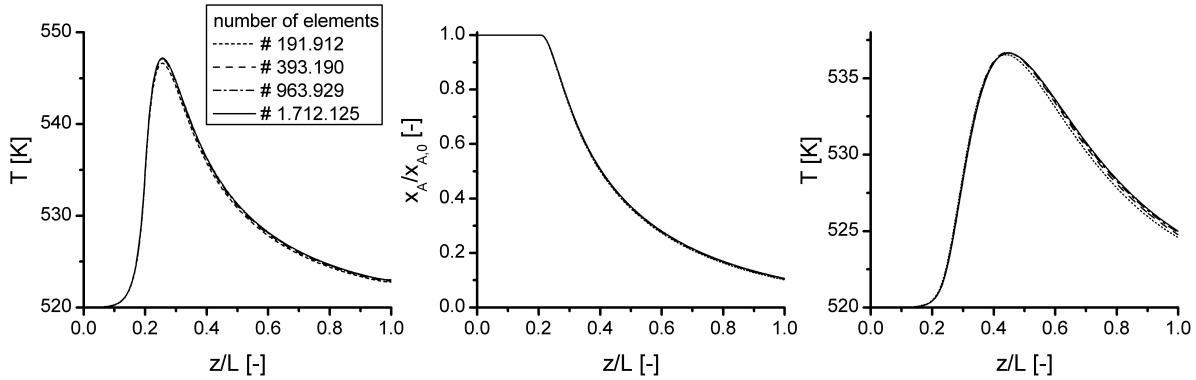

Figure 5.5: (a) axial profile of solid phase temperature (r = 2 mm), (b) axial profile of normed mole fraction (r = 0), (c) axial profile of gas phase temperature (r = 0)

Figure 5.6 compares the two models in terms of maximum temperature and conversion. An excellent agreement is found for the reference conditions: maximum temperatures differ by less than 0.5 K. In addition, figure 5.7 illustrates that the continuum model also predicts axial profiles of the solid phase temperature at various radial positions very well. This still holds when varying the conditions by either changing the activation energy or the feed concentration for moderate Damköhler numbers (figure 5.6). At higher reaction rates, however, the models deviate: maximum temperatures and conversions in the 3D model are systematically higher. There are numerous studies in the literature addressing the comparison of 1D, 2D axisymmetric and 3D single channel models for square ducts under adiabatic conditions [125]. In general, they come to the conclusion that 1D models do not guarantee an adequate description under all operation conditions. For example Groppi et al. [127] compared 1D and 3D single channel models at adiabatic operation for a catalytic combustion and revealed that the 1D model failed in describing the wall temperature profile. This was attributed to the lack in predicting local heat and mass transfer coefficients in the light-off region. Similarly Heck et al. [128] found a sharp increase in Nusselt numbers determined from radial gradient using a 2D model

in the region of the light-off. However, the performance could be described almost quantitatively using asymptotic Nusselt numbers in a 1D model. Canu and Vecchi [129] observed that even 2D and 3D models predict a different light-off behavior because of a faster heating of corners in a square channel which cannot be described using an axisymmetric 2D model. The continuum model employed in this study also suffers from the 1D channel assumption and the usage of global transfer coefficients. The correlations for calculation of the Nusselt and Sherwood number are based on the analogy with the Graetz problem with constant wall temperature [116].

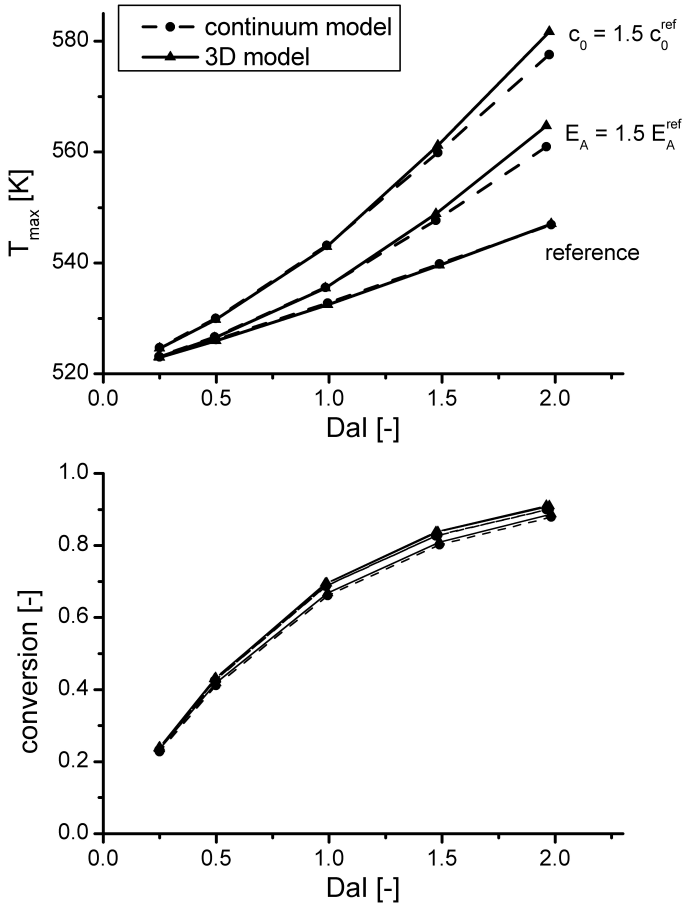

Figure 5.6: Model comparison at polytropic operation in terms of maximum temperature and conversion

However, possible inadequacies of heat and mass transfer coefficients are not the only reason for the deviations observed in figure 5.6 at high reaction rates. In fact, heat transfer from the solid to the gas phase is only a minor contribution to the total heat removal. If the heat transfer to the gas phase is neglected, the maximum temperature

will rise only about 3 K for the fastest reaction rate employed in figure 5.6 under reference conditions. We found that the deviations at fast reaction rates are highly sensitive on the diffusion coefficient. The difference is even more pronounced for high diffusion coefficients, where there are hardly any concentration gradients between wall and channel center in the 3D model and the solid and gas phase in the continuum model, correspondingly. If the concentration in the solid phase is set equal to the gas phase, the temperature rise in the continuum model will indeed be elevated, but won't reach the maximum temperature in the 3D model under harsh conditions and high diffusion coefficients. This indicates that not only the description of mass transfer via the mass transfer coefficient but the continuum approach itself is the reason for this deviation: in the chosen monolith structure there are only three channels in radial direction. A hot spot will form at the metallic wall of the inner channel and will locally cause faster reaction rates. Lateral diffusion in the central and the surrounding channels to the hot spot amplifies this effect. In the continuum model, however, it is intrinsically assumed that the channel size is small compared to the tube size. Consequently, the flow is radially completely segregated and hence diffusion to the position of higher reaction rates is not possible. Nevertheless, just as discrepancies between 1D and more detailed single channel models are observed mainly under harsh conditions near the light-off of highly exothermic reactions, the continuum model predicts results very close to the 3D CFD model at moderate conditions that are more relevant for industrial scale production of chemicals via a wide range of reactions like partial oxidations or hydrogenations.

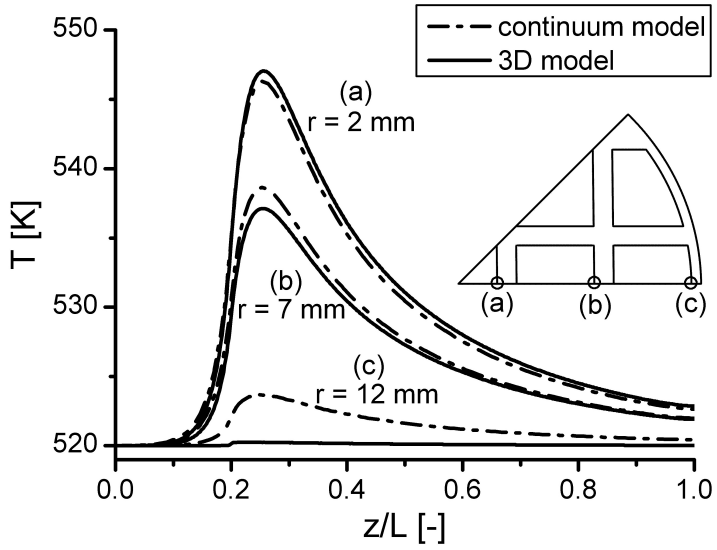

Figure 5.7: Axial profiles of solid phase temperature at different radial positions at reference conditions (DaI = 2.0)

5.1.5 Conclusions

In this work we presented a comparison of a pseudo-continuous, heterogeneous 2D conductive honeycomb model to a detailed 3D CFD model. First, we compared the models under isothermal conditions to the analytical solution of an ideal PFR to ensure correct implementation. As it has been reported in the literature that at adiabatic operation 1D channel models do not suffice for an adequate description under all conditions, we discussed and quantified the influence of the residence time distribution, mass transfer to the washcoat and the washcoat to void ratio of the individual channels on deviations between the models. The comparison under polytropic conditions revealed that the continuum model allows for an excellent description of the reactor performance. The deviations observed at high reaction rates could be attributed to the usage of global heat and mass transfer coefficients derived from the Graetz problem at constant wall temperature and the lack of the continuum model to include mass transfer via lateral diffusion to the hot spot. However, these effects influence the reactor performance only at harsh conditions of large radial temperature gradients that -following the conclusions of Groppi and Tronconi [116] concerning the optimum design of metallic honeycombs- are to be avoided by designing the honeycombs optimally in terms of structure, void fraction and material. In general, the continuum approach allows for an adequate description under polytropic conditions at low computational efforts and high flexibility in terms of different structures.

5.2 Metallic honeycombs for the methanation of carbon dioxide

5.2.1 Abstract

By means of reactor modeling, externally cooled tubular reactors equipped with metallic honeycombs as catalyst supports are investigated. A 2D pseudo-continuous reactor model is adopted to study in particular heat transfer properties and to identify the influencing parameters as well as transport processes on the reactor performance. It is found that honeycomb reactors can indeed be operated isothermally up to higher cooling temperatures in comparison to fixed-bed reactors. The reduced catalyst inventory, however, prevents attaining thermodynamic equilibrium at low temperatures. Exceeding cooling temperatures adequate for isothermal operation, moderate hot spots can be maintained in a narrow range of cooling temperatures before transition to maximum temperatures in excess of 500°C.

Keywords: Metallic honeycombs, methanation, carbon dioxide, reactor modeling

5.2.2 Introduction

Highly exo- or endothermic reactions are often operated in externally cooled or heated fixed-bed reactors, in technical dimension preferably designed as tube-bundle reactors comprising thousands of tubes with diameters in the scale above 1 in. Nevertheless, despite short radial transport distances in the fixed-bed and beneficial surface-to-volume ratios, some processes still call for a better temperature control to reduce maximum temperatures in case of exothermic reactions, in particular, in view of process safety or catalyst lifetime. But also put in a broader context, improved heat transfer characteristics would allow larger tube diameters, hence reduce the number of tubes, the reactor size and investment cost. So far, metallic honeycombs have successfully been adopted to the oxidation of *o*-xylene at the pilot-reactor scale [119] and based on reactor modeling or experimental investigation also proposed for processes of methanol synthesis [130, 131], methanol oxidation to formaldehyde, epoxidation of ethylene [132] and Fischer-Tropsch synthesis [133].

In context of heat removal and improved temperature control, the methanation of carbon dioxide is of particular interest. With a reaction enthalpy of -165 kJ/mol it is a highly exothermic reaction, which beyond that is to be operated with undiluted, pure hydrogen and carbon dioxide feed streams to avoid extensive gas purification of produced SNG. As has been presented in ref. [20], externally cooled single-pass fixed-bed reactors suffer either from low conversions due to low reaction rates at low temperatures,

which without separation of reactants results in a product gas that does not meet requirements for substitute natural gas, or from poor temperature control with maximum temperatures above 500°C, which, in turn, stresses catalysts and reduces their lifetimes. Aside from the approach of adopting networks of several reactors as in large scale CO methanation [69], which might not be ideally suited for a methanation process as part of a power-to-gas concept with repeated start-ups and load changes, structuring seems as a promising concept to improve heat transport characteristics and has been demonstrated in literature also in relation to methanation processes. With the measure of structuring, one might aim either at allowing preferable temperature profiles with marked hotspots but still in safe operation, or even at isothermicity.

In 2007, Brooks et al. [100] presented a microchannel reactor for the Sabatier reaction, which featured good conversion, selectivity and longevity with an excellent temperature control in a compact device and was intended for application in aeronautics such as propellant production on Mars. According to simulations, hot spots in the first region of the bed amounted to an increase in temperature of about 20 K. Linearly decreasing wall temperatures proved particularly advantageous since they facilitated fast reaction rates in the first part of the reactor, while the slow decrease in wall temperature shifted the equilibrium still allowing faster reaction rates compared to a rapid decline in wall temperature. To the best of our knowledge, metallic honeycombs have first been proposed by the Engler-Bunte-Institut (Karlsruhe, Germany) as catalyst support for the methanation of a synthesis gas produced from biomass [71, 72]. A simple comparison of effective radial heat conductivities of fixed-bed and honeycombs made Henrich et al. [71] and Bajohr and Henrich [72] to emphasize the potential of honeycombs for the methanation. Honeycombs consisting of Al or Cu would allow up to 4.4 fold radii compared to fixed-reactors while maintaining the same maximum radial temperature difference. However, the authors did not compare the reactor performances by reactor modeling, which takes process conditions, kinetics, catalyst load, wall heat transfer coefficients etc. into account. Sudiro et al. [102] presented reactor modeling results for the methanation of a synthesis gas using a 1D heterogeneous reactor model. For chosen conditions, maximum temperatures were limited to about 775 K in comparison to an outlet temperature of about 1000 K in adiabatic operation. It was concluded that the common issue of temperature control in synthesis gas methanation can be overcome by honeycomb reactors.

In this contribution we present a detailed modeling study on metallic honeycombs (HC) for the methanation of carbon dioxide and compare results to model predictions for fixed-bed reactors. First, the feasibility is preliminarily assessed by comparing the effective overall heat transfer coefficient of fixed-beds and honeycombs as function of operating conditions. Second, modeling predictions of a 2D heterogeneous conductive

reactor model are presented and discussed in terms of limiting transport processes, before they are finally compared to those of fixed-bed (FB) reactors.

All results relate to parameters as specified in table 5.2 as reference if not stated otherwise. As tube diameter, a typical value as found in common technical tube bundle reactors has been adopted. The honeycomb structure and parameters are oriented to 27 cpsi prototypes of Al honeycombs as adopted by Groppi et al. in ref. [119]. Assuming a constant washcoat thickness of 200 µm, a catalyst volume fraction of 0.13 results on basis of the supposed cross section as depicted in figure 5.1. Catalyst volume fraction, thermal conductivity and channel diameter are subject to variation in the following, so that their influence on the reactor performance can be evaluated.

5.2.3 Methodology

5.2.3.1 Reactor models

For modeling of fixed-bed reactors, a 1D pseudo-homogeneous or (where indicated) a 1D heterogeneous reactor model is employed according to ref. [20]. There, it has been shown that in case of fixed-bed reactors even at diluted feed gases 1D models prove sufficient, since marked temperature differences in radial direction are not established without runaway of the reactor. The runaway behavior in turn is predicted very similarly by 1D and 2D models. By comparison to a fixed-bed reactor model comprising axial dispersion of heat and mass, it has been checked that effects of axial dispersion have only minor influence under the conditions and constraints chosen and are for this reason neglected. As kinetics, the model by Xu and Froment [64] is adopted. Gas phase properties and thermodynamic values are calculated as presented in [20]. Diffusion coefficients in the gas mixture are approximated by Wilke's formula [134]:

$$D_j = (1 - x_j) \left(\sum_{\substack{i \\ i \neq j}} \frac{x_i}{D_{ij}} \right)^{-1} \tag{5.10}$$

For the HC reactor, a 2D heterogeneous reactor model is chosen as proposed by Groppi and Tronconi [116]. Balance equations, boundary conditions and geometry of the honeycomb are identical to ref. [21]. However, the resistance of heat transfer caused by the gap between the honeycomb and the tube needs to be considered when assessing the reactor performance of a tube reactor equipped with honeycombs in relation to a fixed-bed reactor. For this reason, the boundary condition at the tube radius reads as

$$\alpha \left(T_s - T_{\mathrm{cool}} \right) = -\lambda_{e,r} \frac{\partial T_s}{\partial r} \tag{5.11}$$

where α refers to the heat transfer coefficient caused by the so-called gap resistance arising from the clearance comprising few micrometers between outer honeycomb and inner tube wall [135]. It has been reported that the gap resistance is strongly dependent on gap size and on the thermal conductivity of the gas phase [136]. According to Tronconi and coworkers [130, 137], the heat transfer coefficient can be correlated for the case of a fixed gap size, which might practically be feasible by controlling the tube-monolith tolerances, by

$$\alpha = 2410.1 \cdot \lambda_g + 271.64 \tag{5.12}$$

5.2.3.2 Computational methods

The 1D fixed-bed reactor model constitutes an initial value problem which is solved in Matlab® with the ordinary differential equations solver for stiff systems *ode15s*. In contrast, the partial differential equations of the 2D honeycomb model represent a boundary value problem. It is discretized in radial direction with orthogonal collocation (OC) based on Jacobi polynomials in order to exploit axial symmetry. For the axial direction, where steep temperature gradients will evolve, orthogonal collocation on finite elements (OCFE) is employed (cf. [138]). This method is suited for many problems in reaction engineering since it combines advantages to easily increment the number of elements and by meanwhile relying on polynomials of chosen order to give accurate results. The resulting system is solved in Matlab® with the solver for non-linear systems *fsolve*. To handle the large number of coupled equations resulting from both gas and solid phase mass balances of the five components (CO_2, H_2, CH_4, H_2O, CO) as well as gas and solid phase heat balances, the sparsity of the Jacobian is exploited. *fsolve* approximates the derivatives by finite difference techniques. If the pattern of the Jacobian is supplied, that is positions of all non-zero elements, the number of function calls, computational times and memory resources are diminished. The pattern of the Jacobian results from the structure of the non-linear equation system of the form

$$\mathbf{M}\boldsymbol{\zeta} = F(\boldsymbol{\zeta}) \tag{5.13}$$

where $\boldsymbol{\zeta}$ represents the dependent variable vector (temperature or mass fraction in solid or gas phase) and F captures contributions to the partial differential equations which are not discretized in axial direction, for instance reaction and heat source terms. Contributions arising from OCFE are expressed by multiplication of the block diagonal matrix $\mathbf{M}$ with $\boldsymbol{\zeta}$. For clarity, the structure of $\mathbf{M}$ for a one component system is schematically depicted in figure 5.13. Blocks on the diagonal represent the individual finite elements. Equations correlated to the first and last collocation point of each

element (hatched areas) ensure the continuity of the dependent variable and its derivative from one element to the other, while derivatives of dependent variables in the balance equations are represented on the positions of the inner collocation points. The very first and last line (cross hatched areas) arise from the inlet and outlet boundary condition, respectively. For the sake of verification of the implementation of the OCFE-OC code, figure 5.14 compares the honeycomb model to the fixed-bed reactor model, which is solved by an ode solver, for the isothermal case under reference conditions and shows that both models predict identical results.

5.2.4 Results and Discussion

5.2.4.1 Assessment of heat transport parameters

Concerning fixed-bed reactors, heat transfer characteristics strongly differ in the core of the bed in comparison to regions adjacent to the tube wall. For this reason, the simplest 2D state-of-the-art fixed-bed reactor continuum models are based on two contributions: the radial dispersion coefficient, which lumps all processes originating from convective, conductive and radiative mechanisms concerning the core of the fixed-bed, and the wall heat transfer coefficient, which captures the resistances near the tube wall. Common correlations read as [87]:

$$\frac{\lambda_{e,r}}{\lambda_g} = \frac{\lambda_{\text{bed}}}{\lambda_g} + \frac{Pe}{8} \tag{5.14}$$

$$\frac{\alpha_W d_p}{\lambda_g} = \left(1.3 + \frac{5}{d_{\text{tube}}/d_p}\right) \frac{\lambda_{\text{bed}}}{\lambda_g} + 0.19 Re^{0.75} Pr^{0.33} \tag{5.15}$$

Both in turn rely on the sum of a stagnant part, which gives the contribution to heat transport in absence of fluid flow, and a dynamic part, which is based on the dimensionless particle Péclet or Reynolds number, respectively, to take the contribution of convective transport into account.

Figure 5.8 a illustrates the influence of fluid velocity on both coefficients in terms of gas hourly space velocity ($GHSV$) for the chosen reference conditions as given in table 5.2. Hereby, gas phase properties are calculated based on the gas phase inlet composition and temperature. Both the dispersion coefficient and wall heat transfer coefficient are strongly affected by flow velocity and high velocities are advantageous for heat transfer properties. At reasonable space velocities, one can conclude that heat transfer in fixed-beds is dominated by convection and also that for instance improving thermal properties of catalyst supports has little effect on the overall heat transfer performance since seen from a mechanistic point of view point contacts between individual catalyst pellets prevent fast heat conduction in the solid phase. In contrast, favorable heat transfer

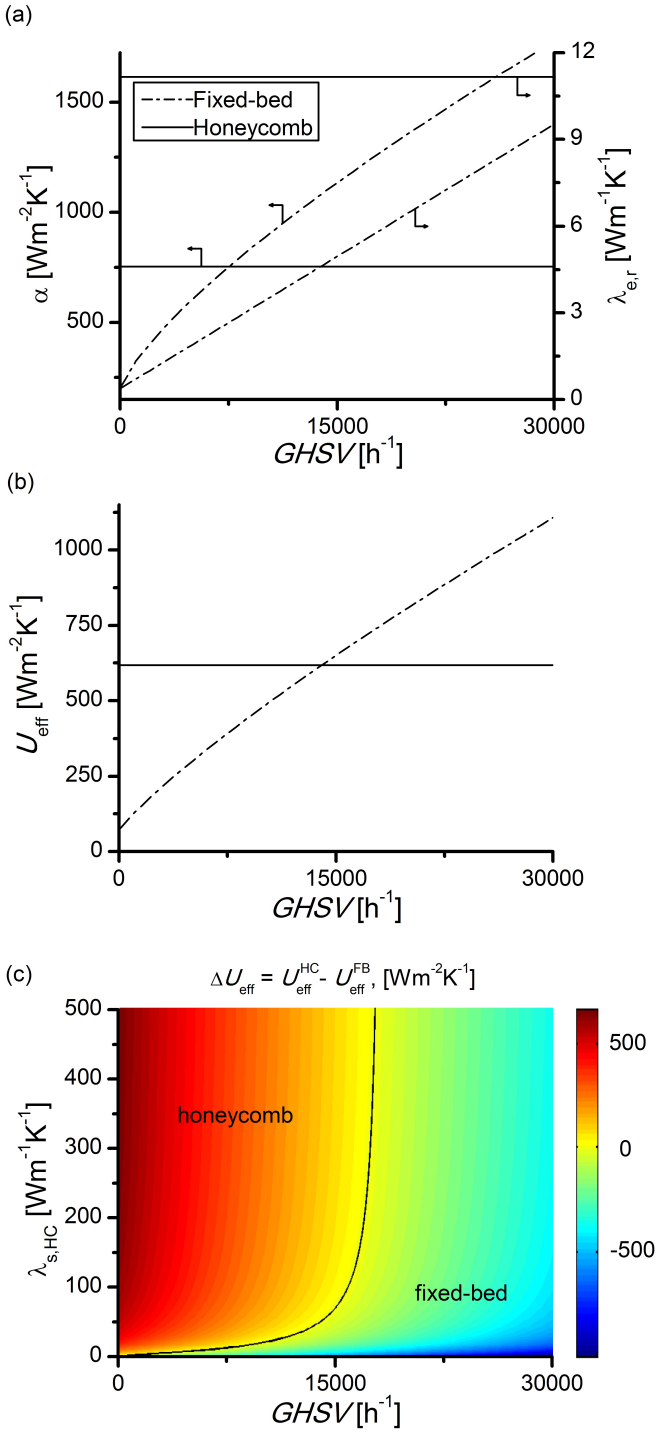

Figure 5.8: (a) Heat transfer coefficients and effective radial conductivities ($\lambda_{s,\mathrm{HC}} = 50\,\mathrm{Wm^{-1}K^{-1}}$, $\lambda_{s,\mathrm{FB}} = 0.5\,\mathrm{Wm^{-1}K^{-1}}$), (b) Effective overall heat transfer coefficients, (c) Difference in effective overall radial heat transfer coefficients in dependence of $\lambda_{s,\mathrm{HC}}$

characteristics of metallic honeycombs rely on conduction in a continuous solid matrix of high thermal conductivity, on which the catalyst is coated. Thus, the mechanistic principle can be seen as a shift of the prevalent heat transfer mechanism from (turbulent), non-directed convection in fixed-bed reactors to conduction in a continuous, highly conductive solid material. Similarly as in case of fixed-bed reactors two contributions concerning radial removal of heat need to be considered. First, transport through the monolith in radial direction is described by an effective radial heat conductivity according to so-called thermal resistance models that were derived in literature [121, 122, 124]. Here, the most recent, the so-called symmetric model is chosen which proved best compared to the previous ones [21, 124]. As second contribution, the gap resistance needs to be considered. According to correlations, both effective radial heat conductivity and gap resistance can be assumed as independent of the flow velocity (figure 5.8 a). Since any of those two respective contributions can be the limiting factor of both fixed-bed or monolith reactors, a preliminary comparison of overall heat transfer properties based on either radial effective heat conductivity/dispersion or transfer coefficients seems insufficient. However, lumping both contributions to a so-called effective overall heat transfer coefficient U_{eff}, which, in turn, would reflect the characteristic transfer coefficient for 1D models, allows such a preliminary comparison. In case of fixed-bed reactors for the methanation of CO_2, it has been shown that the following equation captures heat transfer adequately for a 1D model [20] so that this equation is adopted here for both reactor types.

$$U_{\text{eff}} = \left(\frac{1}{\alpha} + \frac{d_{\text{tube}}}{8\lambda_{e,r}} \right)^{-1} \tag{5.16}$$

A similar correlation, only slightly differing by a factor for weighting of the radial conduction term, has also been applied by Tronconi et al. for methanol synthesis in fixed-bed and monolith reactors in order to compare heat transfer characteristics [130, 131]. According to figure 5.8 b one would expect a certain threshold concerning flow velocity to which a reactor equipped with honeycombs outperforms heat transfer of fixed-bed reactors because of fast heat transport due to conduction, while at higher space velocity convective heat transfer in fixed-beds becomes so efficient that fixed-beds are expected to be superior in relation to honeycombs. As has been pointed out by Montebelli et al. [130], the position of this threshold is a function of reactor dimensions in terms of tube length and diameter etc.. According to patent literature space velocities for a methanation process based on carbon dioxide are expected to be below $5000\,\text{h}^{-1}$ (cf. [66]). Hence, for single-pass reactors one might conclude reactors equipped with honeycombs should feature a better heat transfer performance for the reactor dimensions chosen. However,

by for instance tripling the reactor length, similar heat transfer properties will arise for both reactors at a space velocity of $5000\,\mathrm{h}^{-1}$.

Assessing the contributions of effective radial heat conductivity and gap resistance in more detail in case of the honeycomb reactor, one finds gap resistance as clearly limiting factor. For the conditions chosen the gap resistance amounts to about $750\,\mathrm{Wm}^{-2}\mathrm{K}^{-1}$ at an effective overall heat transfer coefficient U_{eff} of about $600\,\mathrm{Wm}^{-2}\mathrm{K}^{-1}$. This is also the reason why the conductivity of the solid phase has little influence on the overall performance as long as conductivities above around $100\,\mathrm{Wm}^{-1}\mathrm{K}^{-1}$ are maintained. The impact of the solid phase conductivity of the honeycomb in addition to space velocity is illustrated in figure 5.8 c by means of the difference in U_{eff} between monolith and fixed bed. Keeping the conductivity above $100\,\mathrm{Wm}^{-1}\mathrm{K}^{-1}$, the threshold $\Delta U_{\mathrm{eff}} = 0$ as indicated by the solid line is almost constant at $17\,000\,\mathrm{h}^{-1}$, since increasing conductivity does not improve U_{eff} of the honeycomb significantly. Hence, we chose for reference conditions Al ($\lambda_S = 200\,\mathrm{Wm}^{-1}\mathrm{K}^{-1}$) as solid material, which has also been proven as feasible for fabrication of metallic honeycombs [119].

Table 5.2: Reference (ref) conditions and dimensions

$GHSV$	5000	h^{-1}
L	2	m
d_{tube}	2.54	cm
d_{channel}	4	mm
ϵ	0.64	
ξ	0.13	
$x_{\mathrm{feed}}(\mathrm{H_2})$	0.8	
$x_{\mathrm{feed}}(\mathrm{CO_2})$	0.2	
p	3	bar
λ_s	200	$\mathrm{Wm}^{-1}\mathrm{K}^{-1}$

5.2.4.2 Performance of reactors equipped with honeycomb reactors

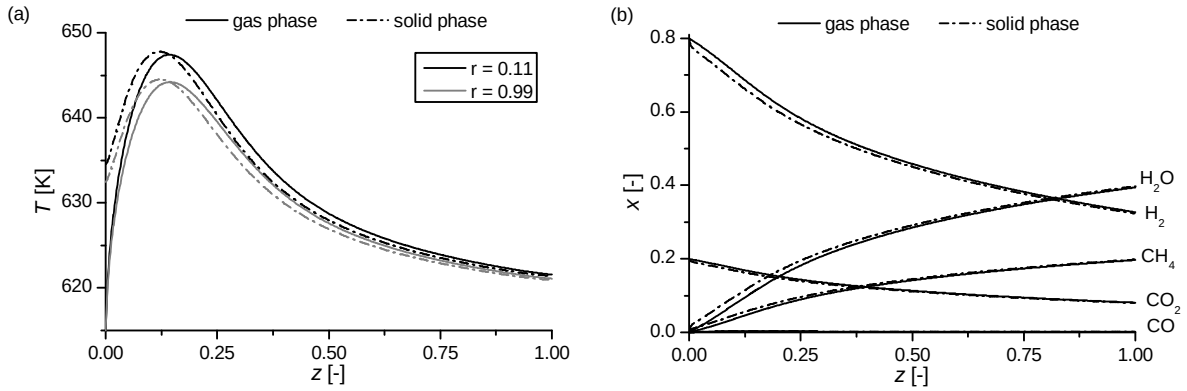

Figure 5.9: (a) Axial profiles of temperature, (b) Axial profiles of mole fractions ($T_{cool} = 615\,K$)

Figure 5.9 a depicts typical axial profiles of temperature in honeycomb reactors at two different radial positions. Hot spots concerning gas phase and solid phase temperatures are evolved near the inlet of the reactor, which amount to about 35 K. Most severe temperature differences between solid and gas phase are found in the inlet region. Due to heat release because of high reaction rates at the pure, undiluted feed gas stream, solid phase temperatures are found up to 15 K in excess of the gas phase temperature. As a consequence of the boundary conditions, heat cannot be removed in axial direction toward the inlet since the inlet is assumed as adiabatic. Hence, heat can only be transported in radial direction and potentially downstream in axial direction. However, the solid phase temperature is even increasing downstream. Due to the heated gas phase, heat transfer from the solid to the gas phase is worsened. In interplay with faster reaction rates as well as heat removal in axial and radial direction, this results in increasing solid phase temperatures and formation of a hot spot.

A maximum temperature difference in radial direction below 10 K as indicated in figure 5.9 a confirms the conclusion drawn from the assessment of heat transfer: largest temperature differences will be established at the honeycomb wall due to the gap resistance, while flat profiles are evolved in the cross section due to high effective radial conductivities which allow efficient removal of heat. As a consequence of radially relatively flat temperature profiles hardly any radial concentration profiles are evolved. The maximum relative difference in conversion in the cross section amounts to less than 7%. For this reason, only axial profiles at a single radial position are reported in figure 5.9 b. Minor differences in mole fractions are found between solid and gas phase for relatively large channel diameters of 4 mm. Hence, external mass transport does

slightly influence the performance. In disregard of external mass transfer limitation, conversion is increased from 70.0% to 73.2%. Evaluation of the Weisz-Prater criterion for the conditions applied indicates that diffusion limitations in the porous washcoat do not affect reaction rates.

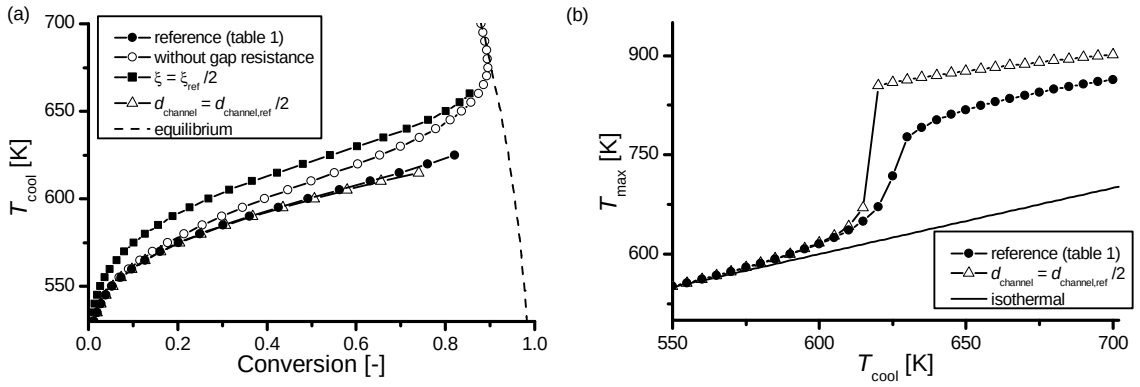

Figure 5.10: Influencing parameters on the performance of a honeycomb reactor

In the following, chosen influencing parameters on the reactor performance are discussed on basis of plots of cooling temperature over conversion obeying the constraint that the maximum temperature is kept below 750 K. If this temperature is exceeded, lines stop in the diagrams. According to figure 5.10, HC reactors can be operated under reference conditions up to cooling temperatures of about 625 K such that a conversion of about 80% is obtained at a maximum temperature of 720 K. Remarkably, maximum axial temperature differences amount to less than 20 K up to cooling temperatures of 600 K. As illustrated in figure 5.10 b, exceeding this cooling temperature, axial temperature differences up to 50 K can be maintained before the reactor response becomes more sensible towards changes in cooling temperatures. An increase of 10 K in this region results in a temperature rise of more than 100 K for reference conditions to temperatures in excess of 750 K. This is also the reason why this temperature was chosen as upper limit in order to separate high and low temperature region. Apart from deactivation of methanation catalysts [139], maximum temperatures need also to be carefully controlled in view of possible requirements of adopted reactors and honeycomb material. Note that the transition from low to high temperature region is relatively smooth under reference conditions because of the onset of severe mass transport limitations concerning external mass transfer. In disregard of mass transfer limitations, maximum temperatures instantly jump to values in excess of 900 K. In particular in this regime, mass transfer limits reaction rates and slows down the heat release such that maximum temperatures are reduced compared to the fully kinetic regime. Mitigating mass transfer limitations

by for instance reducing the channel size thus increases the sensitivity and maximum temperatures in the hot spot region (figure 5.10 b).

Comparison to the case which neglects the influence of the gap resistance (figure 5.10 a) again shows its dominating influence. Hereby, a reactor could be operated stably to temperatures above 700 K. Heat removal proves so fast that maximum axial temperature difference are below 20 K even at fast reaction rates in this high temperature region, while the equilibrium is attained at the reactor outlet at a cooling temperature of about 673 K. As attractive it might seem to construct a tube reactor not filled with honeycomb segments but directly consisting of tubular honeycombs, this might technically be hardly feasible for externally cooled tube bundle reactors, first in terms of construction and second also in terms of regenerating if the catalyst lifetime is reached. However, the tremendous influence of this resistance also towards technical feasibility of honeycomb reactors has provoked some effort to both understanding influencing parameters on this resistance [135–137] and also on measures to mitigate the resistance in patent literature, for instance by choosing materials of eligible coefficients of thermal expansion such that narrow gap clearances are maintained during operation [140].

A further parameter which can relatively easily be controlled and influences reactor performance and thermal stability is the catalyst load. So far, it has been assumed that the catalyst volume fraction amounts constant to 0.13. If decreased to one half corresponding to a washcoat thickness of 100 µm, a higher temperature level is consequently needed to maintain the same performance (figure 5.10). The maximum conversion under the constraint of maximum temperatures below 750 K is increased, since the potential of heat release is mitigated due to a lower available catalyst mass. Though one might argue a higher temperature level of the cooling medium is advantageous in terms of heat use, the thermodynamic equilibrium is shifted to the educt side such that the aim of potentially almost full conversion is even more afar and apart from kinetics and temperature control thermodynamically unreachable. Noteworthy, an improved methanation catalyst performance in relation to the steam reforming catalyst employed by Xu and Froment [64] for derivation of the kinetic model has the same effect as increasing the catalyst fraction: lower temperature levels are required, however maximum conversions with restricted maximum temperatures become less since even moderate hot spots cannot be maintained anymore without runaway of the reactor.

5.2.4.3 Comparison to fixed-bed reactors

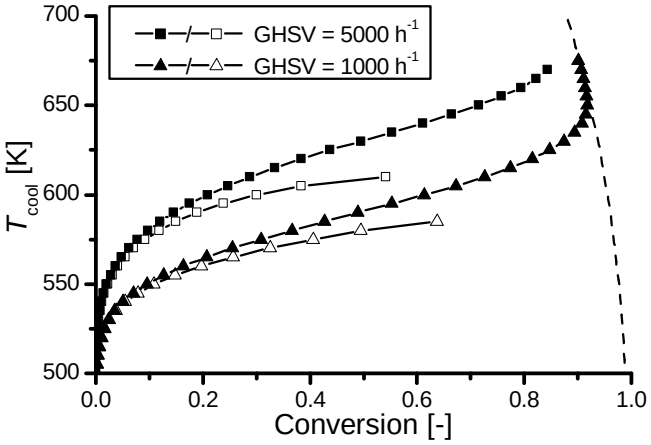

Figure 5.11: Comparison of honeycomb (closed symbols) and fixed-bed reactors (open symbols) at different space velocities ($\xi = 0.05$)

Figure 5.11 compares the reactor performances of a reactor equipped with honeycombs and a fixed-bed reactor for two space velocities. In case of the FB reactor, the catalyst inventory assumed is the same as for HC. As a result of figure 5.10, we chose a rather low catalyst volume fraction of 0.05. Higher values or even the assumption of the catalyst volume fraction of about 0.6 corresponding to an undiluted packed-bed would make temperature control for fixed-reactors even worse and favor HC reactors. Reported values in figure 5.11 relate to model predictions of the 1D pseudo-homogeneous reactor model, that is mass and heat transport limitations are not taken into account. Both assumptions concerning the volume fraction and in particular disregard of intraparticle mass transfer limitations enable for a comparison in relation to heat transfer parameters. As expected from the assessment of the effective overall heat transfer coefficient, HC reactors are superior to FB reactors at the low space velocities relevant. For instance, at $GHSV = 5000\,\mathrm{h}^{-1}$, HC reactors outperform FB reactors by more than 30% in conversion under the constraint of $T_{\max} < 750$ K. Whereas at $\mathrm{GHSV} = 1000\,\mathrm{h}^{-1}$ heat removal is fast enough so that the equilibrium can easily be attained with HC reactors, model predictions of the fixed-bed reactor show that not even there the equilibrium is approached. Note that decreasing the space velocity lessens power to be removed so that heat transfer in case of HC is capable to maintain almost isothermal operation to equilibrium. In contrast, this effect is foiled in case of FB because heat transfer is worsened with decreasing velocities.

However, while HC clearly outperform FB reactors in terms of heat transfer properties, a comparison cannot be adequate without taking into account the mitigating effect of intraparticle mass transfer limitations on the maximum temperatures in case of fixed-bed reactors [20]. Figure 5.12 depicts that in case of small catalyst pellets and/or large pore diameters, predictions of the heterogeneous model are close to the pseudo-homogeneous one and maximum conversions about 60% are reachable. By increasing pellet diameters and decreasing pore diameters so that mass transfer limitations become more severe, in particular in the region of the hot spot where reaction rates are fastest, maximum temperatures are considerably limited and improved reactor performances with conversions in excess of 60% can be obtained. However, exploiting mass transfer limitations for slowing down the heat release on the other hand compromises the approach to equilibrium such that even at maximum temperatures above 773 K equilibrium compositions are hardly attained.

In case of HC reactors, mass transport limitations concerning the external mass transfer to the washcoat surface less affect the reactor performance for $T < 750\,K$. For instance, halving the channel diameter slightly increases the conversion at constant cooling temperature (figure 3 b). However, at maximum temperatures in excess of 750 K, they do have a marked influence by limiting reaction rates and slowing down the heat release such that maximum temperatures are easily reduced by more than 100 K compared to the fully kinetic regime in absence of external mass transfer limitations.

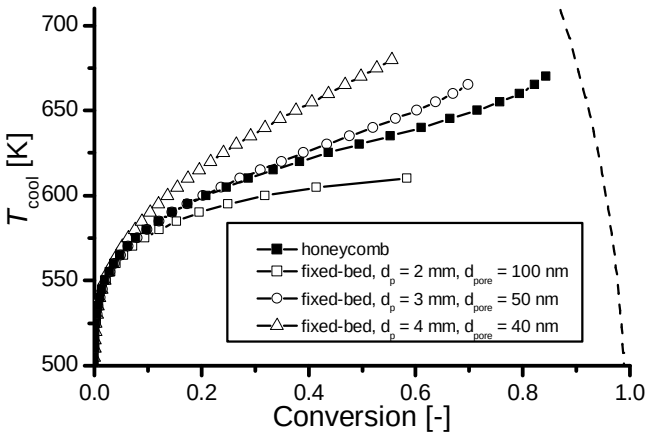

Figure 5.12: Comparison to model predictions of a 1D heterogeneous fixed-bed reactor model ($\xi = 0.05$)

5.2.5 Conclusion

The assessment of the effective overall heat transfer coefficient has revealed a superior performance of compact HC in comparison to FB reactors in terms of heat transfer characteristics for conditions that are expected to be relevant for a technical process realization of the Sabatier reaction integrated in a power-to-gas concept. This conclusion, however, is not to be generalized for any process or any given set of conditions, but has to be checked in dependence of process and design parameters. Since heat transfer in FB is dominated by convection, the overall effective heat transfer coefficient in FB reactors is a strong function of the particle Reynolds number, while this value in case of HC reactors depends on gap resistance, void fraction and thermal conductivity of the solid material. For the conditions chosen, the gap resistance could clearly be identified as limiting factor for the heat transfer in HC reactors. Consequently, flat temperature profiles evolve in the cross section, resulting in negligible radial concentration differences. Marked temperature differences between solid and gas phase are found in the inlet region of the reactor. Following main conclusions can be drawn from modeling results:

1. HC reactors are capable of maintaining isothermicity due to superior heat removal up to higher temperatures and conversions than fixed-bed reactors. If isothermicity is aspired and process conditions are chosen in a way that enable attaining the equilibrium under these conditions, honeycombs are ideally suited. The design of fixed-bed reactors adequate for isothermal operation and high conversion likewise would request very small tube diameters and consequently an unfeasible length or large number of tubes [20].

2. Despite worse heat transfer properties of FB reactors moderate hot spots can also be established without runaway because intraparticle mass transport limitations slow down heat release in the hot spot compared to the kinetic regime. Because of larger catalyst pellet dimensions in comparison to washcoat thicknesses below 100 µm, FB reactors are more prone to this effect. Temperature profiles with moderate hot spots in the first part of the reactor prove advantageous, since hot spot temperatures boost the reaction rates while equilibrium is shifted toward the reactor outlet to the product side, which cannot be attained at isothermal operation and constant cooling temperature.

3. If process design relies on adaption of a single reactor, the different catalyst inventory employable in HC and FB needs to be considered. While a low catalyst fraction might mitigate maximum temperatures in the hot spot and might be compensated by a higher cooling temperature level, it is of course counterproductive for approaching the equilibrium composition preferably at low temperatures for

exothermic reactions. This is even more severe in case of the Sabatier reaction, since the presence of product gases considerably slows down the approach to equilibrium. To attain the equilibrium at potentially low temperatures, catalysts of highest possible activity and highest possible catalyst load are preferable, in contrast of the first part of the reactor facing undiluted feed gases.

4. If, however, a setup of two reactors can be employed, heat transfer properties of honeycombs can be exploited in a first reactor, which is operated up to intermediate conversions with well controlled temperatures. For upgrading of the product gas of the first reactor, FB reactors are suited better, since they offer a higher catalyst load and heat removal is less critical as gas is already diluted by product gases which in addition will slow down reaction rates due to the kinetics inevitably.

Apart from reactor or process aspects, one can conclude concerning the methodology that comparison of effective thermal conductivities or preferably effective overall transfer coefficients has given first insights. However, more detailed reactor modeling is crucial in terms of understanding in particular the interplay with kinetics, mass transfer processes and process conditions so that questions about temperature control, reactor performance, optimal design of honeycombs etc. can be addressed.

5.2.6 Supporting information

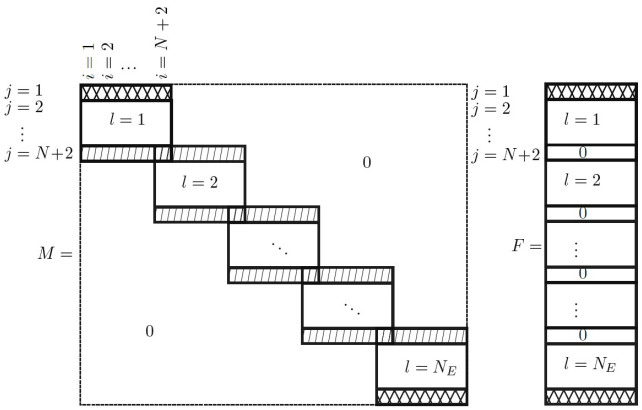

Figure 5.13: Structure of matrix **M** for OCFE adopted from ref. [138]

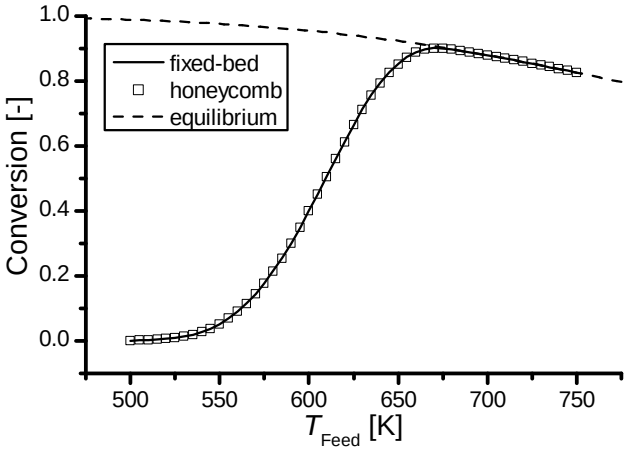

Figure 5.14: Validation under isothermal conditions

6 On the kinetics of the methanation of carbon dioxide on coprecipitated Ni/Al_2O_3

6.1 Abstract

A series of Ni/Al_2O_3 catalysts with varying Ni/Al ratio has been prepared by coprecipitation of the metal nitrate solutions with NaOH/Na_2CO_3 at constant pH. The samples have been analyzed by XRD, N_2 physisorption, temperature programmed reduction and H_2 chemisorption. For kinetic characterization, apparent activation energies and reaction orders are determined. The correlation of the catalytic acitivity and metallic surface area indicates a linear relationship. A dataset comprising over 200 data points with varying gas composition, temperature and pressure has been recorded as a basis to develop a kinetic model that captures the intrinsic kinetics of the methanation of carbon dioxide under process relevant conditions. As rate equations power laws, power laws with inhibition, for instance by water, and Langmuir-Hinshelwood-Hougan-Watson (LHHW) approaches are evaluated. Modeling results emphasize that the kinetics at differential conversions and pure H_2/CO_2 feed differ markedly from the regime closer to equilibrium. Power laws with inhibition and adequate LHHW approaches are capable of reflecting the kinetics over a wide range of conditions from differential conversion to thermodynamic equilibrium.

Keywords: methanation, Sabatier reaction, nickel-alumina catalysts, carbon dioxide, intrinsic kinetics

6.2 Introduction

The expected depletion and rising demand of conventional, easily exploitable fossil fuels as well as the intention to reduce carbon dioxide emissions, which is seen as a major driver of the green house effect and climate change, are widely expected to dramatically change the future energy and fuel supply. In particular, wind and photovoltaic energy as well as biomass will increasingly supplement the energy mix. The European Union, for instance, set the aim to cut its green house gas emissions to 80% below 1990 levels by the year of 2050 [3]. The transition to renewables will inter alia comprise two challenges: in contrast to conventional power plants, renewable energy will not be constantly available but will depend on weather, day and night, or season etc.. Furthermore, the generation of renewable energy might locally be preferred in remote areas. Consequently, there is a need to store energy when available, to provide it fast on demand and to transport it cheaply and efficiently. Also, one might think of converting renewable energy to transportable fuels for mobile applications that can make use of well established combustion engines. The chemical storage by means of so-called chemical energy carriers and in particular of synthetic natural gas (SNG) offers one possibility that might meet the mentioned requirements [14–16, 18]. When available, renewable energy can be used to electrolyze water to hydrogen and oxygen. Hydrogen can then be converted with carbon dioxide separated for instance from off gas of fossil power plants, cement industry, biomass conversion or even from atmosphere to methane. Methane can easily be stored in the gas grid or gas reservoirs, transported via the gas-grid and reconverted, using solely already existing infrastructure. The concept has also been transferred to the application as transport fuel [65].

The heart of the power-to-gas concept is the methanation process. The reaction of carbon dioxide with hydrogen to methane and water is a highly exothermic as well as under standard conditions exergonic reaction with volume contraction:

$$\mathrm{CO_2} + 4\,\mathrm{H_2} \rightleftharpoons \mathrm{CH_4} + 2\,\mathrm{H_2O} \qquad \Delta H_\mathrm{R}^0 = -165\ \mathrm{kJ/mol} \qquad \Delta G_\mathrm{R}^0 = -114\ \mathrm{kJ/mol}$$

According to Le Chatelier's principle, low temperatures and high pressures shift the equilibrium to the product side. Quantitatively, a yield of methane of 95% with a selectivity close to 100% is obtained at 300°C in thermodynamic equilibrium assuming a total pressure of 1 bar and stoichiometric feed gas composition of 80% hydrogen and 20% carbon dioxide. This corresponds to a methane content of 80% in the product gas after removal of water. The conversion of carbon dioxide passes a minimum at 585°C of 65%. Higher temperatures favor carbon monoxide over methane, which is formed via the endothermic reverse water-gas shift. The CO content at 1 bar is in the low ppm-range

(< 50 ppm) for temperatures below 300°C. A detailed analysis of thermodynamic aspects of carbon dioxide methanation has been presented in ref. [141].

Though the heterogeneously catalyzed reaction of carbon dioxide with hydrogen to methane and water has been well known since beginning of the 20th century - it was discovered by Nobel laureate Paul Sabatier in the 1900s [19] -, kinetic models applicable for technical conditions are scarce. Nevertheless, they are strongly needed for reactor design and optimization and also for a qualified comparison of different catalyst systems. In view of economic feasibility we focused on Ni though Rh [101, 142, 143], Ru [100, 144–146] and Pd [98, 99] have also been reported as catalytically active. Table 2.2 gives an overview of published models. First kinetic investigations have been presented in the 1950s. For instance, Dew et al. studied kinetics on a pelletized Ni kieselguhr catalyst [58]. As kinetics were measured on pelletized catalysts of about 3x3 mm size in an undiluted fixed-bed, one can, however, not exclude that they were biased by heat and mass transfer processes. Measurements were restricted to initial reaction rates, which were fitted by simple so-called "generalized rate equations". To the best of our knowledge, the first detailed mechanistic kinetic model for intrinsic kinetics on a Ni-based catalyst has been presented by Weatherbee and Barthomolomew [46] for 3 wt.% Ni/SiO_2, however at highly diluted gas composition. Accordingly partial pressures of carbon dioxide (2.76 to 27.6 mbar) and hydrogen (27.6 to 138 mbar) are far away from a possible technical realization of a SNG process where almost complete conversion to methane contents in the dried product gas of above 95% are desired so that the product gas can directly be fed into the gas grid without further purification or separation steps. In this respect, elevated pressures will be necessary to shift the equilibrium accordingly. Relevant process patents mention pressures between 2 and 15 bar and reactor outlet temperatures as low as 250°C [66]. Further progress concerning kinetics was accomplished by Kai et al. [63], who used both a differential and an integral reactor for kinetic studies at ambient pressure on an alumina supported Ni catalyst promoted by La_2O_3. By operating the integral reactor up to conversions of 90%, the influence of the products water and methane on the kinetics was accessible in greater detail than in previous studies. Kinetics were described by a Langmuir-Hinshelwood rate equation based on the mechanism proposed by Weatherbee and Bartholomew [46], but assuming the hydrogenation of carbon instead of CO dissociation as rate determining step. It was found that measured conversions at integral operation were smaller than predicted by rate equations based on experiments run in differential mode. This was attributed to the adsorption of products on the catalyst surface. As a consequence, the adsorption of water was accounted for in the Langmuir-Hinshelwood rate equation and an excellent fit of the data was obtained this way. As part of the comprehensive kinetics of steam reforming, also experiments on the methanation of CO_2 were performed on a typical steam reforming 15 wt.% $Ni/MgAl_2O_4$

catalyst and used for parameter estimation for steam reforming and methanation kinetics by Xu and Froment [64]. Experimental conditions were temperatures between 300 and 400°C and pressures between 3 and 8 bar, which are close to a technical implementation of CO_2 methanation.

Against the background of previously published kinetics, we present a kinetic model for a state-of-the-art catalyst system, which has recently been published and proven superior activity in comparison to other Ni based catalyst systems [31]. So far, investigations of intrinsic kinetics for the methanation of carbon dioxide were based on relatively low loaded systems as in case of Weatherbee and Bartholomew (3 wt%) [46] or Kai et al. (17 wt%) [63] or even on steam reforming catalysts as in case of Xu and Froment [64]. Furthermore, chosen conditions for kinetic experiments are relevant for technical operation intended to the production of SNG, i.e. elevated pressures and high hydrogen and carbon dioxide contents in the feed gas, in contrast to the studies by Weatherbee and Bartholomew [46] or Kai et al. [63]. Thereby, we measured not only both in differential and integral mode, but for the first time dosed methane and water already in the feed in order to capture their influence on the kinetics and apparent reaction orders in detail. In comparison to previous kinetic studies, we supply a characterization of the employed catalysts and relate to a series of catalysts with varying Ni content and specific Ni surfaces.

To summarize, the main objective of our paper is to derive a kinetic model, which is capable of reflecting intrinsic methanation kinetics for a state-of-the-art catalyst under industrially relevant conditions. In detail, we will first present and discuss characterization results comprising elementary analysis, powder X-ray diffraction (XRD), N_2 physisorption, temperature programmed reduction (TPR), and hydrogen chemisorption for a series of varying (1/5 - 5/1) Ni/Al molar ratio. We chose this relatively wide range in order to potentially study catalysts of varying precursor structure or varying physical properties like specific Ni surfaces or crystallite sizes. The catalytic activity of the systems will be compared and related to characterization results. For a selected catalyst different kinetic models comprising power laws, power laws with inhibition and Langmuir-Hinshelwood-Hougen-Watson (LHHW) approaches will be evaluated in order to assess the level of detail needed for reflection of kinetics from differential to almost complete conversion.

6.3 Experimental

6.3.1 Catalyst synthesis

The nickel-alumina precursors were prepared by coprecipitation at constant pH following the synthesis route described in ref. [31]. The purity of all used reagents was p.a., water was purified by a Millipore® water clearing rig, gas was purchased from Westfalen AG with a purity of 6.0 for H_2 and 5.0 for all other gases. For precipitation a double-walled glass vessel with a volume of 3 l was used, preloaded with 1 l H_2O, heated to 30°C and stirred by a KPG stirrer with 250 1/min. Additionally, two flow breakers were inserted in the vessel to improve mixing. 120 ml of the mixture of the aqueous solutions of the metal nitrates (1 M $Ni(NO_3)_2 \cdot 6\,H_2O$, Merck® and 1 M $Al(NO_3)_3 \cdot 9\,H_2O$, Sigma-Adlrich®) were added simultaneously by an medorex peristaltic pump with $8\,ml\,min^{-1}$. As precipitating agent a mixture of 0.5 M NaOH (Merck®) and 0.5 M Na_2CO_3 (Sigma-Aldrich®) was used. The Titrino Autotitrator 716DMS by Methrom® dosed the solution into the vessel to hold the pH constant at 9±0.1 during the precipitation. The molar ratio of Ni/Al was varied between 5/1 and 1/5, denoted for instance as NiAl51 and NiAl15, respectively. For reason of comparison, two samples containing only Ni or only Al were precipitated in the same way. The product slurry was stirred and aged in the mother liquor for 18 h. After washing until pH was constant and drying at 80°C overnight, the precursors were calcined at 450°C for 6 h under synthetic air flow (heating rate $5\,K\,min^{-1}$). For reduction the catalyst was heated up to 485°C by $2\,K\,min^{-1}$ in a 5 vol.% H_2 in Ar flow and kept there for 11 h.

6.3.2 Catalyst characterization

For powder X-ray diffraction analysis a Philips X'pert with Cu Kα radiation and a monochromator was used. The diffractogram resulted from a scanning in the range between $2\Theta = 5 - 70°$ stepwise with 0.017°/step and recording rate of 95.6 steps/min. The surface area of the calcined precursor was calculated, using BET analysis in the p/p_0 range between 0.05 and 0.30 of the N_2 adsorption isotherms at 77 K. It was measured by a NOVA 4000e from Quantachrome. Prior to measurement the samples were heated under vacuum up to 120°C for 3 h. H_2 chemisorption was performed with an Autosorb-1 (Quantachrome) at 35°C after activation as mentioned above (5% H_2 in N_2, heating ramp $2\,K\,min^{-1}$ to 485°C). The specific nickel surface area was calculated following the extrapolation theory, details are given in the appendix. Catalyst composition was determined by elementary analysis using an AA280FS atom absorption spectrometer from VARIAN. For thermogravimetric analysis a Netsch STA409 cell equipped with an

Omnistar QMS (Pfeiffer GSD 301 O2) was used. TPR was conducted with 5% H_2 in Ar with and total flow of 60 sccm (heating ramp 4 K min^{-1} to 500°C, holding for 390 min).

6.3.3 Experimental setup

For the kinetic measurements a two line setup was employed. The main parts consist of gas mixing and dosing, the reactor section and the analysis section. All gases were provided by Westfalen AG, for the measurements H_2 (6.0), CO_2 (5.0), Ar (5.0) and CH_4 (5.0) were used. The gases were dosed by mass flow controllers (MFC), before entering the reaction zone. Water can be added by a vaporizer. To prevent condensing, all tubing is heated. The reaction zone consists of two reactor lines, which can independently be heated up to 600°C and pressurized up to 20 bar. The catalyst bed is fixed with silica wool plugs in the isothermal zone of a glass lined steel tubing with an inner diameter of 4 mm. The reactor temperature is measured at the end of the catalytic bed. Leaving the reactors, the product gas is diluted with Argon, to prevent water condensation in the analytics. The latter includes a Pfeiffer Vacuum Thermostar mass spectrometer (MS), an Emerson MTL-4 online IR process gas analyzer (PGA) and a Perkin Elmer gas chromatograph (GC) which is equipped with two FID detectors for byproduct analysis. The PGA detects the concentration of CO, CO_2, CH_4, H_2, and H_2O in the gas stream and the results are used for the quantitative analysis. To ensure steady conditions and reproducibility, the catalyst is hold under the particular conditions for 45 min and the data point is averaged over the last three minutes.

6.3.4 Kinetic measurements

The kinetic data pool was recorded with 25 mg catalyst in the temperature range from 250 to 340°C and 75 mg between 180 and 250°C. The catalyst was diluted with purified SiC in the catalyst-to-SiC ratio of 1/9 using the same particle sizes of 0.15 - 0.20 mm. It has been checked that the purified SiC is not catalytically active. For reduction, the catalyst was heated with 2 K min^{-1} to 485°C in a flow of H_2/Ar = 5/95, the temperature kept for 11 hours and the hydrogen consumption monitored in the MS. This was followed by an aging period at 380°C and 7 bar for 300 h. The flow rate was 120 Nl h^{-1} g_{cat}^{-1} and the feed contains $H_2/CO_2/CH_4/H_2O$/Ar in the ratio of 4/1/1.25/2.5/1.25. A feed mixture containing water and methane during the aging period has proven advantageous to prevent deactivation during the parameter study concerning an activity loss, when the catalyst has first contact with water. In the subsequent measurements on the aged catalyst, a variation of the process parameters corresponding to table 6.1 was conducted. During parameter variation possible deactivation of the catalyst was monitored by reference point measurements at least every 24 h. It has been checked that all data

points of the parameter variation fulfill the Mears, Anderson and Weisz-Prater criteria so that intraparticle and external heat and mass transfer limitations are not expected to affect the kinetic measurements (see Appendix 6.7.1 for details).

Table 6.1: Variation of process parameters during the kinetic measurements

Temperature	Feed		Flow	Pressure	Mass
[°C]	H_2/CO_2	CH_4/H_2O	[Nl/h/g_{cat}]	[bar]	[mg]
180 - 240	0.25 - 4	-	36, 48	1 - 15	75
250 - 340	0.25 - 8	- and 0.5	120, 150, 180	1 - 9	25

6.4 Methodology

6.4.1 Kinetic rate equations

6.4.1.1 Power law rate equations

Different kinetic models will be evaluated and compared. The simplest model studied is a power law solely considering the reaction orders of hydrogen and carbon dioxide (PL):

$$r = k \cdot p_{\mathrm{H_2}}^{n_{\mathrm{H_2}}} p_{\mathrm{CO_2}}^{n_{\mathrm{CO_2}}} \left(1 - \frac{p_{\mathrm{CH_4}} p_{\mathrm{H_2O}}^2}{p_{\mathrm{H_2}}^4 p_{\mathrm{CO_2}} K_{\mathrm{eq}}}\right) \tag{6.1}$$

The equilibrium constant K_{eq} is calculated based on the species' enthalpies and entropies according to the Shomate equation and data provided by NIST Chemistry WebBook. Alternatively, the equilibrium constant could also be approximated by the empirical formula

$$K_{\mathrm{eq}} = 137 \cdot T^{-3.998} \exp\left(\tfrac{158.7\mathrm{kJ/mol}}{RT}\right) \qquad [105]. \tag{6.2}$$

The model PL will also be used to evaluate the reaction orders of carbon dioxide and hydrogen in dependence of feed composition. If an inhibiting influence of water is considered via a power term, the model is extended to five parameters (PL-H2O):

$$r = k \cdot \frac{p_{\mathrm{H_2}}^{n_{\mathrm{H_2}}} p_{\mathrm{CO_2}}^{n_{\mathrm{CO_2}}}}{p_{\mathrm{H_2O}}^{n_{\mathrm{H_2O}}}} \left(1 - \frac{p_{\mathrm{CH_4}} p_{\mathrm{H_2O}}^2}{p_{\mathrm{H_2}}^4 p_{\mathrm{CO_2}} K_{\mathrm{eq}}}\right) \tag{6.3}$$

Inhibition by adsorbed water (PL-WI) or adsorbed hydroxyl (PL-HI) can empirically be treated via the following equations comprising six parameters.

$$r = k \cdot \frac{p_{\mathrm{H_2}}^{n_{\mathrm{H_2}}} p_{\mathrm{CO_2}}^{n_{\mathrm{CO_2}}}}{1 + K_{\mathrm{H_2O}} p_{\mathrm{H_2O}}} \left(1 - \frac{p_{\mathrm{CH_4}} p_{\mathrm{H_2O}}^2}{p_{\mathrm{H_2}}^4 p_{\mathrm{CO_2}} K_{\mathrm{eq}}}\right) \tag{6.4}$$

and

$$r = k \cdot \frac{p_{\mathrm{H_2}}^{n_{\mathrm{H_2}}} p_{\mathrm{CO_2}}^{n_{\mathrm{CO_2}}}}{1 + K_{\mathrm{OH}} \frac{p_{\mathrm{H_2O}}}{p_{\mathrm{H_2}}^{1/2}}} \left(1 - \frac{p_{\mathrm{CH_4}} p_{\mathrm{H_2O}}^2}{p_{\mathrm{H_2}}^4 p_{\mathrm{CO_2}} K_{\mathrm{eq}}}\right) \tag{6.5}$$

All rate and adsorption constants are treated as Arrhenius-type, all adsorption constants as van't Hoff-type:

$$k = k_0 \exp\left(-\frac{E_A}{RT}\right) \quad \text{and} \quad K_{\mathrm{x}} = K_{\mathrm{x},0} \exp\left(-\frac{\Delta H_{\mathrm{x}}}{RT}\right)$$

They are parameterized in order to minimize the correlation between preexponential factor and activation energy or adsorption enthalpy, respectively, during parameter estimation:

$$k = k_{0,\mathrm{ref}} \exp\left(\frac{E_A}{R}\left(\frac{1}{T_{\mathrm{ref}}} - \frac{1}{T}\right)\right) \quad \text{and} \quad K_{\mathrm{x}} = K_{\mathrm{x},0,\mathrm{ref}} \exp\left(\frac{\Delta H_{\mathrm{x}}}{R}\left(\frac{1}{T_{\mathrm{ref}}} - \frac{1}{T}\right)\right)$$

6.4.1.2 LHHW rate equations

LHHW-type rate equations are derived analogously to the methodology of Weatherbee and Bartholomew [46] that recently was also adopted for the methanation of carbon monoxide by Kopyscinski et al. [103, 147]. The first mechanism assumed (table 6.2 left) considers the cleavage of carbon-oxygen bonds first and subsequent hydrogenation of carbon and carbenes to methane as well as hydrogenation of adsorbed oxygen to water. Hydrogen, carbon dioxide and methane are assumed to adsorb dissociatively. This mechanism is the same as assumed by Weatherbee and Bartholomew. It has been formulated in analogy to CO methanation based both on the observation that CO_2 adsorbs dissociatively and a TPSR study by Falconer and Zagli [37]. Therein, carbon dioxide was preadsorbed at elevated temperatures, subsequently cooled and hydrogen was fed. At room temperature, water was detected and the following signal was the same as found for CO methanation. For sake of comparison, a second mechanism is formulated in analogy to a so-called hydrogen assisted pathway in CO methanation where first hydrogen reacts with CO to carbon-hydroxyl COH or formyl HCO, respectively, before carbon oxygen bond cleavage [51, 103, 105, 148]. In table 6.2, a mechanism is exemplarily

formulated with adsorbed carbon monoxide, which results from the first carbon-oxygen bond cleavage of carbon dioxide, being first hydrogenated to a formyl species before the second C-O bond cleavage to a CH-species. Such a mechanism has for example also been formulated inter alia by Blaylock et al. in a DFT study about possible mechanisms for steam reforming [53]. The mechanism in table 6.2 comprising a formyl species is by no means unique. A formyl species has for example also been proposed by Aparicio in a microkinetic model for reforming and methanation [105]. There, formyl is assumed to be formed by cleavage of formate HCOO, resulting from the reaction of adsorbed carbon dioxide and hydrogen. Of course, further mechanisms could have been formulated comprising COH or HCOO, respectively (cf. [39, 40, 42, 149]). However, the variability introduced by this two mechanisms proved sufficient (see also the discussion in section 4.3 about inferring the mechanism). Based on the two formulated mechanisms, over 20 rate equations are derived by varying the rate determining step and assuming further irreversible steps. The rate equation assuming step 3 of mechanism b as rate determining step and step 8 in addition as irreversible is derived for clarity in the appendix. As most abundant surface intermediate hydrogen, the species present in the RDS and water or hydroxyl are considered.

Table 6.2: Mechanisms a (left) and b (right) for derivation of LHHW rate equations

1:	CO_2	+ 2*	⇌	CO*	+ O*		1:	CO_2	+ 2*	⇌	CO*	+ O*		
2:	H_2	+ 2*	⇌	2 H*			2:	H_2	+ 2*	⇌	2 H*			
3:	CO*	+ *	⇌	C*	+ O*		3:	CO*	+ H*	⇌	CHO*	+ *		
4:	C*	+ H*	⇌	CH*	+ *		4:	CHO*	+ *	⇌	CH*	+ O*		
5:	O*	+ H*	⇌	OH*	+ *		5:	CH*	+ 3H*	⇌	CH_4*	+ 3*		
6:	OH*	+ H*	⇌	H_2O*	+ *		6:	CH_4*		⇌	CH_4	+ *		
7:	H_2O*		⇌	H_2O	+ *		7:	O*	+ H*	⇌	OH*	+ *		
8:	CH*	+ 3H*	⇌	CH_4*	+ 3*		8:	OH*	+ H*	⇌	H_2O*	+ *		
9:	CH_4*		⇌	CH_4	+ *		9:	H_2O*		⇌	H_2O	+ *		

The LHHW models are discriminated using Bartlett's χ^2 test where the variances between experiments and all models are tested upon equality. If this hypothesis is rejected, the model with largest variance between experiment and prediction is discarded and the test is repeated with the retained models until no further model is rejected. The critical χ_c^2-value is calculated according to ref. [150, 151] and compared to the tabulated χ_t^2-value with corresponding degrees of freedom and a probability level of 0.95.

6.4.2 Computational Methods

The kinetics is integrated into an ideal plug flow reactor model. The ordinary differential equation is formulated as

$$\frac{d\dot{n}_i}{dm} = \nu_i \cdot r \tag{6.6}$$

where $\dot{n}_i$ is the molar flow of component i, m the catalyst mass, ν_i the stoichiometric coefficient of component i and r the reaction rate. By integration over the catalyst mass, directly the weighed catalyst sample is taken as integration limit and the exact bed volume is not needed. Athena Visual Studio® is employed for solving of the differential equations and parameter estimation. Its solver for ordinary differential equations is based on a Newton algorithm with a backward difference scheme for approximation of derivatives. Bayesian parameter estimation was chosen as provided by the built-in gregplus parameter estimation routine. For the parameter estimation the sum of squares of residuals of the integral methane production rate is minimized.

6.5 Results and discussion

6.5.1 Catalyst characterization

Figure 6.1 (top) shows the XRD patterns for the dried precursors with varying Ni/Al ratio. Concerning samples NiAl51 and NiAl31 all reflections can be assigned to Takovite (JCPDS 15-0087), a member of the hydrotalcite structure. Decreasing the Ni/Al ratio to 1, the main reflection at $2\theta = 11.7°$ representing the (003) plane disappears completely while the reflex assigned to (006) plane at 23.5° is still present, however in very low intensity. The reflexes at 37.4° and 61.1° in NiAl5 are gradually shifted to lower plane distances with increasing Al^{3+} content. Samples NiAl13 and NiAl15 show a new reflex at 20.4°. The comparison to Al^{3+} precipitated under the same conditions in absence of Ni^{2+} (not shown) reveals that the crystalline phase present in NiAl13 and NiAl15 requires Ni^{2+} since the reflexes in the reference diffractogram can all be assigned to Boehmite (γ-AlO(OH)) (JCPDS 21-1307) which is not detected in the binary NiAl samples. Generally, if precipitated fast in alkaline solutions Al^{3+} is expected to crystallize as metastable hexagonal α-aluminium hydroxide (Bayerite) which transforms to more stable γ-aluminium hydroxide (Gibbsite) [152]. Both phases are not detected in the precursor samples, either.

After calcination (figure 6.1 center), all reflexes in sample NiAl5 can be assigned to a NiO (Bunsenite) phase (JCPDS 78-0429). No separate crystalline alumina phases are detected. With increasing Al content, the intensity decreases and the reflexes at

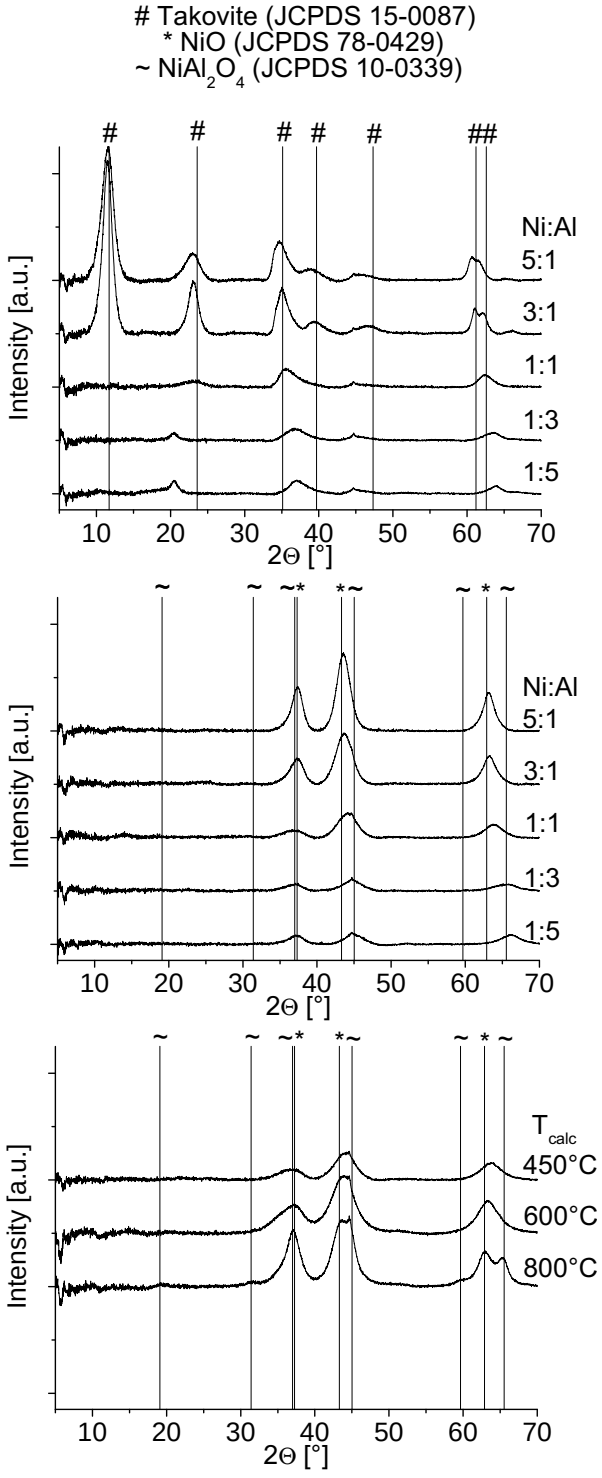

Figure 6.1: XRD patterns: precursors after drying at 80°C overnight (top), after calcination at 450°C (center), variation of calcination temperature for sample NiAl11 (bottom)

43.6° and 63.3° in NiAl51 are gradually shifted to lower plane distances. Interestingly, already the reflexes in NiAl51 are slightly shifted compared to the expected values of pure NiO. The results for variation of the calcination temperature for NiAl11 in figure 6.1 (bottom) shed light on this effect: with increasing calcination temperature a $NiAl_2O_4$ spinel phase (JCPDS 10-0339) is identified next to Bunsenite. Bunsenite crystallizes in NaCl structure, accordingly O^{2-} is located in fcc positions while Ni^{2+} occupies the octahedral vacancies. $NiAl_2O_4$ is reported as a (disordered) spinel structure with preference to the inversed configuration [153]. Hence, O^{2-} is also positioned in fcc where 1/8 of tetrahedral vacancies is preferably occupied by Al^{3+} while Ni^{2+} and the remaining Al^{3+} are located in 1/2 of octahedral vacancies. The cubic lattice parameter of Bunsenite and $NiAl_2O_4$ are 4.2 and 8.0 Å,where in the latter one elementary cell, however, comprises eight times the number of O^{2-}. Hence, the proximity of the main reflex positions of both phases results directly from the similarity of the structures and the little smaller lattice parameters in case of the spinel. One might speculate whether already after calcination at 450°C a spinel phase of low crystallinity and grain size is present besides other oxidic Al_2O_3 and NiO phases or a mixed oxide is formed which shifts the reflexes with increasing Al content. For instance, de Korte et al. also studied the calcination of similarly prepared precursors and named the mixed oxide phases with plane distances between NiO and $NiAl_2O_4$ as DOSI ('disordered oxide-spinel intermediate') and those with plane distances between $NiAl_2O_4$ and Al_2O_3 as NCA ('nickel oxide containing alumina') [154]. Noteworthy, γ-Al_2O_3 (formed after calcination of the pure Al sample (not shown)) crystallizes in a defect spinel structure with a lattice parameter of 7.9 Å. This might be the reason why the reflex at 66.2° in NiAl15 is slightly shifted to higher angles compared to the (440) reflex of $NiAl_2O_4$, e.g. measured on the sample calcined at 800°C at 65.5° and expected at 65.5°.

Concerning the BET surface areas of the calcined samples (table 6.3), NiAl11, NiAl13, NiAl15 show similar surface area compared to the pure alumina sample. Further increasing the nickel content, surface areas still remain rather large with values well above $100\,m^2/g$, but are significantly lower in comparison to the alumina sample. The pure NiO sample with a surface area $< 30\,m^2\,g^{-1}$ emphasizes the importance of the precursor phase for the morphology after calcination.

The specific nickel surface area determined by H_2 chemisorption monotonically increases with the nickel content. A maximum value of $36.1\,m^2/g$ is obtained for sample NiAl51. Correlating the specific surface area with the Ni content, the Ni dispersion increases with the Ni content up to sample NiAl11 before reaching a plateau around 6% which corresponds to an average Ni crystallite size between 16 and 17 nm. Interestingly, a precursor structure of lower Ni content does not lead to a better dispersion of reduced

Ni after calcination and reduction though one might expect a lower Ni fraction in the mixed oxide formed after calcination to result in smaller crystallites.

The reduction of the calcined samples has also been studied by TPR (figure 6.2). While heating in a hydrogen argon flow, first carbon dioxide and water are desorbed at temperatures $< 350°C$. In view of the calcination at 450°C before reduction, this suggests that carbon dioxide might have been adsorbed on basic oxides or hydroxides during exposure of the calcined catalyst in air. The water formation above 350°C follows from reduction to metallic Ni. To test for complete reduction, a TG-MS was measured with the catalyst overflowed by pure argon instead of hydrogen in argon. The first stage of decomposition accompanied by the release of carbon dioxide and water is identical. However, no further water is released above 350°C. The difference of the samples' masses after treatment at 500°C amounts to 9.1%. Based on the Ni/Al ratio determined in elementary analysis of the corresponding precursor, a mass loss of 8.8% is expected, assuming the calcined sample as pure NiO/Al_2O_3. We conclude that NiO is completely reduced within the error tolerance of the TG-MS measurements. Noteworthy this is not the case if the catalyst is calcined at higher temperatures and a spinel phase is formed. Before kinetic measurements, it is also checked that reduction is complete by monitoring that no more water is released.

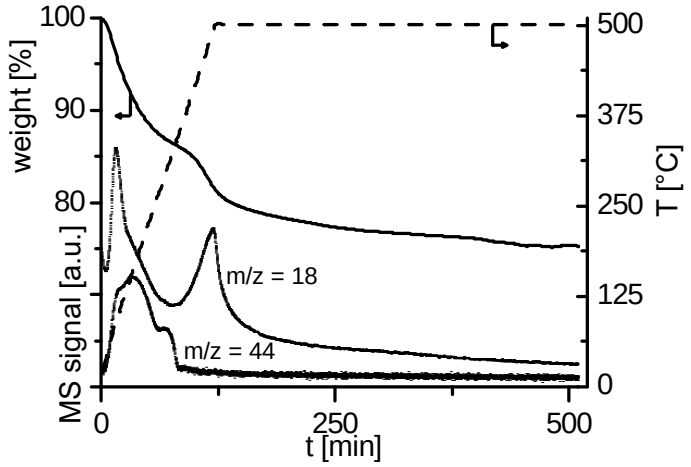

Figure 6.2: Temperature programmed reduction of NiAl11

Table 6.3: Characterization results

	Ni	NiAl51	NiAl31	NiAl11	NiAl13	NiAl15	Al
elementary analysis n_{Ni}/n_{Al} [-]	-	5.5	3.4	1.2	0.37	0.23	-
stoichiometric formula[1]	-	$NiAl_{0.18}(CO_3)_{0.2}(OH)_{2.1}$	$NiAl_{0.29}(CO_3)_{0.19}(OH)_{2.5}$	$NiAl_{0.86}(CO_3)_{0.29}(OH)_4$	$NiAl_{2.7}(CO_3)_{0.45}(OH)_{9.2}$	$NiAl_{4.4}(CO_3)_{0.55}(OH)_{14.1}$	-
BET surface area[2] $[m^2\,g_{cat}^{-1}]$	26.1	128	149	235	229	229	223
spec. Ni surface area[3] $[m^2\,g_{cat}^{-1}]$	1.2	36.1	31.6	21.3	9.2	4.4	0
Ni dispersion[3] [%]	0.17	6.3	5.9	6.1	4.6	3.2	-
average crystallite size[3] [nm]	583	16.1	17.1	16.6	22.0	32.1	-
WTY[4] $[\mu mol\,s^{-1}\,g_{cat}^{-1}]$ TOS=0 h	2.4	108	92.6	81.0	29.9	20.3	-

[1] based on elementary analysis of C, Ni, Al, [2] calcined samples, [3] following extrapolation theory, [4] T = 260°C, p = 7 bar, $H_2/CO_2/Ar$ = 1/4/5, 150 $Nl\,h^{-1}\,g_{cat}^{-1}$

6.5.2 Kinetic measurements

6.5.2.1 Comparison of the catalysts

First, the weight time yield of methane production (WTY) is determined after reduction for the series of catalysts at a temperature of 260°C at 7 bar total pressure and a 1/4/5 gas mixture of $CO_2/H_2/Ar$ with a total flow of $150\,\mathrm{Nl\,h^{-1}\,g_{cat}^{-1}}$ immediately after reduction so that deactivation does not bias measurements and results can be correlated to H_2 chemisorption measurements of fresh catalysts. In these experiments as in all catalytic test runs, CO_2 was selectively reduced to methane. The CO content in the product gas is below 1000 ppm. Higher hydrocarbons, in particular ethane and propane, were detected by gas chromatography, however, in traces < 50 ppm, close to the detection limit. For this reason, only the rate of methane formation is considered in the following and the reverse water-gas shift and chain-growth reactions are neglected.

Plotting the WTY measured immediately after reduction as a function of the specific nickel surface area determined by H_2 chemisorption (figure 6.3), a linear trend is found suggesting that the nickel surface acts as active site in the as-prepared catalysts. Furthermore, we do not observe any correlation between BET surface area and WTY. The linearity of specific Ni surface area and WTY also holds for samples of largely differing BET surface areas (128 - $235\,\mathrm{m^2\,g_{cat}^{-1}}$). This, however, does not necessarily mean the support does not influence the catalytic active phase, only the quantity of exposed surface area does not. Comparison of reaction rates per Ni surface for different supports could clarify, if the nature of the support influences the specific activity or just the dispersion of Ni. In this regard, the degree of hydroxylation of the support is reported to affect the reactivity and selectivity in CO_2 hydrogenation [155]. Also adsorption of carbon dioxide on oxidic supports is in discussion in literature as possible role of the support in the methanation reaction. Aksoylu et al. [156], for instance, observed for a series of coprecipitated Ni/Al_2O_3 catalysts with a Ni content less than 25 wt% that the methane production per Ni surface area rises with decreasing Ni content. This was attributed to carbon dioxide being also adsorbed on alumina, which via reverse spillover increases methane production per unit Ni surface especially for catalysts of low Ni loading. One might speculate if the high loadings of our samples prevents this effect to be observable throughout our series. The deviations to the linear trend as depicted in figure 6.3 do also not give rise to the conclusion that specific activity correlates with average crystallite size. Positive deviations are found both for the sample of largest crystallite size (NiAl15) and of NiAl11 with rather small Ni crystallites. The small number of samples and crystallite sizes above 15 nm, however, prohibit to draw any conclusions in regard of structure sensitivity and activity of flat surfaces versus steps and kinks. Concerning supported Ru catalysts it is reported that the turnover frequency

of methane production increases by over an order of magnitude with increasing crystallite sizes from 2 to 4 nm, the effect, however, leveling off at higher sizes [157].

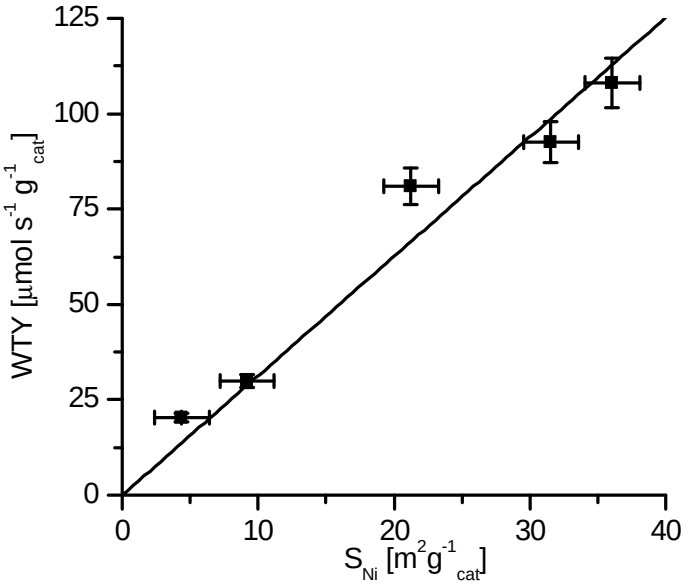

Figure 6.3: Correlation between WTY ($p = 7\,bar$, $260°C$, $H_2/CO_2/Ar = 4/1/5$, $150\,Nl\,h^{-1}\,g_{cat}^{-1}$) and specific Ni surface area

In the previous section, it has been shown that Ni dispersion of samples NiAl51, NiAl31 and NiAl11 is almost constant and higher than in samples of lower Ni content. If activity correlates linearly to Ni surface in the samples, highest yield per mass of Ni will be obtained for these samples. Since NiAl11 gives slightly higher WTY than predicted by the linear trend, this sample shows highest yield per mass of Ni concerning our samples ($140\,\mu mol\,s^{-1}\,g_{Ni}^{-1}$). Hence we conclude, optimum Ni/Al ratio is above 1/1 under chosen preparation conditions to synthesize a catalysts with optimum performance in relation to Ni content. Lower Ni/Al ratios result in Ni particles of higher crystallite size (lower dispersion) so that activity related to Ni content is worse. Highest activity per catalyst mass is found for the sample with highest Ni content.

Correlation of the catalyst activity to specific surfaces is indispensable in our view, but has hardly be performed in literature for CO_2 methanation.To gain understanding on structure-activity relationships further catalysts will have to be prepared according to other techniques comprising also different oxidic carriers. Nevertheless, for the series of our coprecipitated catalysts the linearity between specific Ni surface area and WTY holds and hence encourages to develop a kinetic model for this kind of system. To set up a kinetic model, the catalyst NiAl11 was chosen.

6.5.2.2 Catalyst deactivation

For temperatures below 250°C, the catalyst hardly showed any deactivation during parameter variation. However, in the measurements above 250°C the catalyst activity rapidly dropped after the first data points with water already dosed in the feed. To decouple the kinetic measurements from deactivation phenomena, the catalyst was for this reason stressed before parameter variation: for a period of 320 h the reactor was fed with a mixture of $H_2/CO_2/H_2O/CH_4/Ar$ at 380°C and 7 bar. It proved advantageous to feed product gases already in the feed during the formation period, since this way (i) a stable activity level could be reached faster than by feeding only carbon dioxide and hydrogen and (ii) kinetic measurements containing product gases in the feed did not cause further deactivation during parameter variation. During aging a reference point was measured periodically to track the decrease in activity since under aging conditions equilibrium was maintained and deactivation hence was not observable. After 320 h, parameter variation was started. The reference point was periodically measured between kinetic data points in order to ensure a stable activity level. As the reference measurements confirm (figure 6.4), the activity was stable after the aging period at around 40% of the initial activity during parameter variation so that measurements of kinetics used for parameter estimation are not biased by deactivation effects. It is a common feature of many published kinetics, that they do not relate to the initial activity, but to a stable level. Steam reforming kinetics by Xu and Froment [64], for instance, have to be multiplied by a factor of 2.2 to reflect initial activity. Concerning CO_2 methanation kinetics, most studies do not address deactivation, probably due to the fact that they were mostly measured under differential conditions and deactivation phenomena are less severe in this case according to our findings. Only Dew et al. [58] report on an extensive pretreatment (lasting over 2000 h) to maintain a stable activity in the following parameter variation. Abello et al. [31], who prepared a coprecipitated Ni/Al_2O_3 with molar ratio of 5.4, report on a lifetime test at 400°C. Conversion of carbon dioxide decreases from 92.4% to 83.5% during 490 h. Unfortunately, the initial conversion corresponds to equilibrium so that the decay does not reflect the decay in intrinsic activity. According to the kinetic model we present in section 6.5.3.2 the decrease in conversion from 92.4% to 83.5% corresponds to a loss in intrinsic activity of more than 45%. This makes us conclude that the deactivation we observe is in the range of what has to be expected for the catalysts employed.

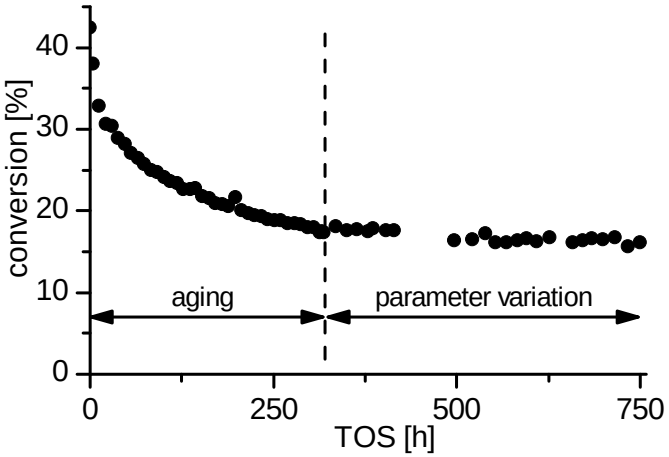

Figure 6.4: Deactivation during aging and parameter variation

In order to check for reproducibility, the same aging procedure was performed on a second fresh catalyst fill. After 320 h hours the catalyst reached almost the same activity level according to measurements of the reference point. Subsequently a reduced dataset was recorded on the deactivated catalyst. In figure 6.5 the two datasets are compared and a good agreement is observable. The overall deviation is calculated to 6.3%. As most data points are slightly above the angle bisector, the catalyst has obviously not been deactivated to exactly the same level. However, the experimental error within one dataset might for this reason be even smaller than by comparing two datasets.

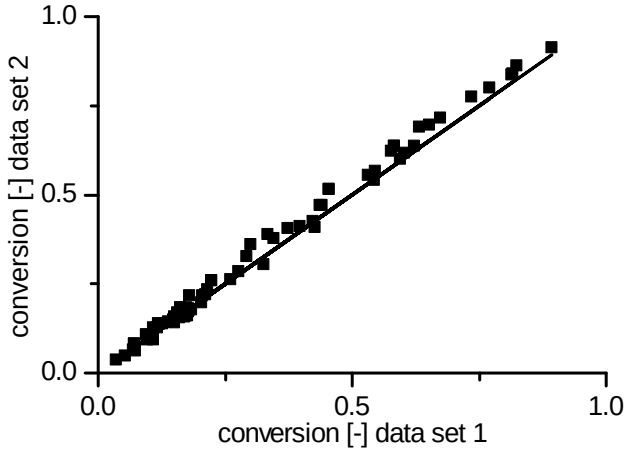

Figure 6.5: Comparison between first and second kinetic dataset

6.5.2.3 Apparent activation energy and reaction orders

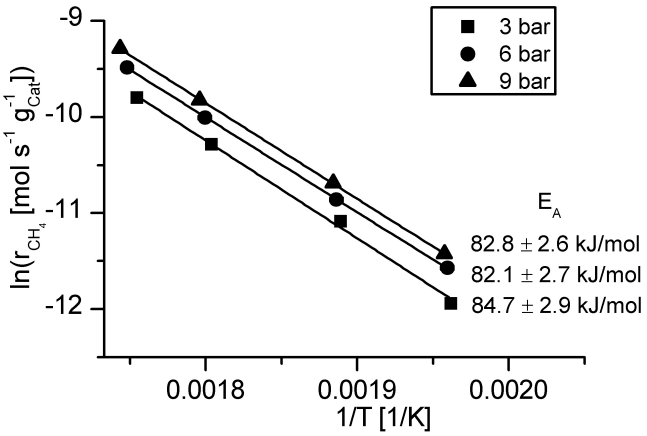

Figure 6.6: Arrhenius plots at varying total pressures ($Q = 2400\,Nl/h/g_{cat}$, $H_2/CO_2/Ar = 1.6/0.4/8$, $m_{cat} = 25\,mg$)

The apparent activation energy for the CO_2 methanation reaction is within error tolerance independent of the total pressure and determined to 83 kJ/mol (figure 6.6). This value is in line with literature where for instance values of 82 and 89 kJ/mol are reported for Ni/SiO_2 [46, 158], 80-106 kJ/mol for Ni/Al_2O_3 [60, 159] and 89 kJ/mol for Ni(100) in a surface science approach [36].

According to figure 6.7, the apparent reaction orders of hydrogen and carbon dioxide are almost constant in the investigated temperature range and close to 0.3 and 0, respectively, for pure $H_2/CO_2/Ar$ feed streams (closed symbols). The reaction order of hydrogen seems to slightly rise at higher temperatures, which however might be caused by increased conversion and accordingly higher product gas contents at these temperatures. The comparison to measurements with product gases already dosed in the feed stream reveals a marked increase in apparent reaction orders of both hydrogen and carbon dioxide (open symbols). Apparently, the presence of product gases will slow down the reaction rates more severely at depleting hydrogen and carbon dioxide contents. The trends of reaction orders for pure feed gas in absence of product gases are in accordance with the study of Weatherbee and Bartholomew: they report increasing (decreasing) reaction orders of hydrogen (carbon dioxide) with temperature in the range of 0.35 to 0.55 (0.24 to 0.07) at low partial pressures while both hydrogen and carbon dioxide dependence approach zero-order at higher partial pressures [46]. Similarly, van Herwijnen et al. report zero-order dependence of carbon dioxide at partial pressures above 0.015 atm [60].

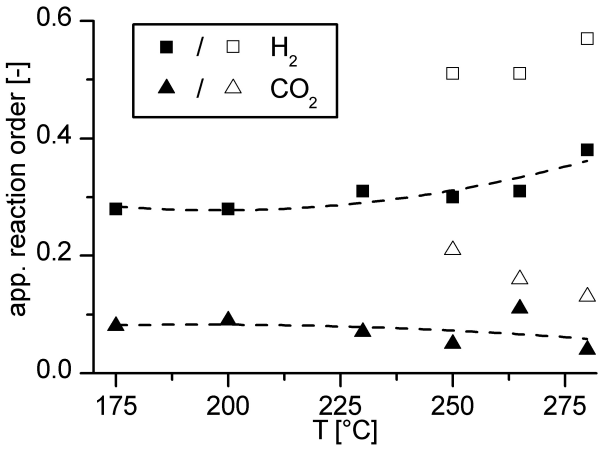

Figure 6.7: Apparent reaction orders of H_2 and CO_2, closed symbols: : H_2/CO_2/Ar feed, open symbols: $H_2/CO_2/H_2O/CH_4$/Ar feed

6.5.3 Kinetic rate equations

6.5.3.1 Power law rate equations

Based on the extensive dataset as described in the experimental section and recorded at TOS $>$ 320 h (cf. figure 6.4), parameters of the different rate equations were estimated. Figure 6.8 compares the parity plots of the integral methane production rate for PL, PL-H2O and PL-HI. PL-WI gives results similar to PL-HI with slightly higher residual so that it is not further considered. The parity plot of PL shows a wide spread compared to the experimental values and a mean absolute residual of over 20%. Consequently, it is inadequate to reflect the kinetics over the whole range of conditions employed. Nevertheless, this model allows an excellent description of data points with differential conversion in absence of product gases present over the whole temperature and pressure range. However, as soon as product gases are present in larger amounts, it systematically overestimates reaction rates and fails in describing the slow approach to equilibrium experimentally observed. On the one hand this emphasizes the need for more complex models that should be suitable for reactor modeling in technical scale, where the description of the approach to equilibrium is crucial for reactor design [20], and on the other hand the demand of kinetic measurements that have to cover conditions closer to equilibrium. For this reason, the dataset contains measurements where water and methane have been fed already in the gas supply and the reactor is operated in an integral mode. An inhibiting influence of product gases has been observed before by Kai et al. [63] by comparing methanation rates in a differential and integral reactor. Concerning Ru systems it has also been reported that addition of water shifts conversion

temperature curves to higher temperatures, which means reaction rates are decreased in presence of water [157].

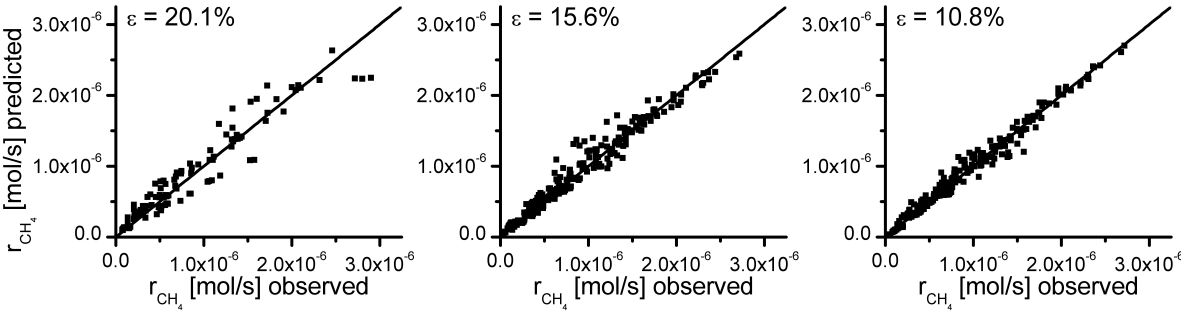

Figure 6.8: Parity plots for PL, PL-H2O and PL-HI (from left to right)

To the best of our knowledge, empirical power law equations for the methanation of carbon dioxide, which consider a retarding influence of water, have not been described in literature, probably because most studies address differential conversion with very low product gas contents. Similar empirical power law models as adopted here have, however, been successfully employed for methanol synthesis, for instance [160]. Parameter estimation for PL-H2O yields a negative reaction order, which reflects the inhibiting influence mentioned above. The residual is consequently considerably decreased. Nevertheless, the comparison to PL-WI emphasizes that the assumption of a constant reaction order of water over the whole temperature and pressure range proves restrictive. In contrast, PL-WI and in particular PL-HI are found superior since the reaction rate is even more drastically slowed down near equilibrium. The low mean absolute residual suggests PL-HI to be an adequate and meanwhile very simple model for reflection of kinetics from differential conversion to almost complete conversion in thermodynamic equilibrium. The parameters for PL-HI are summarized in table 6.4. The confidence intervals are rather small and show all parameters to be estimated significantly different from 0.

Table 6.4: Parameter estimation for PL-HI ($T_{ref} = 555\,K$)

$k_{0,555K}$	6.41e-05 ± 3.0e-6	$mol\,bar^{-0.54}\,s^{-1}\,g_{cat}^{-1}$
E_A	93.6 ± 2.5	$kJ\,mol^{-1}$
n_{H_2}	0.31 ± 0.02	-
n_{CO_2}	0.16 ± 0.02	-
$A_{OH,555K}$	0.62 ± 0.09	$bar^{-0.5}$
ΔH_{OH}	64.3 ± 6.3	$kJ\,mol^{-1}$

6.5.3.2 LHHW rate equations

The following rate equation, which has been derived by assuming formyl formation as rate determining step in mechanism b, proved best in a statistically significant way according to Bartlett's test. All other models (including all power law rate equations) could be rejected on basis of the dataset comprising 258 experiments.

$$r = \frac{k \cdot p_{\mathrm{H_2}}^{0.5} p_{\mathrm{CO_2}}^{0.5} \left(1 - \frac{p_{\mathrm{CH_4}} p_{\mathrm{H_2O}}^2}{p_{\mathrm{H_2}}^4 p_{\mathrm{CO_2}} K_{\mathrm{eq}}}\right)}{\left(1 + K_{\mathrm{OH}} \frac{p_{\mathrm{H_2O}}}{p_{\mathrm{H_2}}^{0.5}} + K_{\mathrm{H_2}} p_{\mathrm{H_2}}^{0.5} + K_{\mathrm{mix}} p_{\mathrm{CO_2}}^{0.5}\right)^2} \tag{6.7}$$

Nevertheless, based on stationary measurements in a lab scale fixed-bed reactor, any inference to the mechanism prevalent seems very doubtful without identification of surface species, a comparison to specific rate constants measured under UHV conditions or quantum mechanical calculations etc.. Apart from that, several identical rate equations could be derived for mechanisms a and b. This emphasizes the ambiguity about inferring the mechanism with the strict assumptions required for derivation of simple LHHW-type rate equations. Furthermore, the rate equation derived from mechanism b with formyl HCO formation as rate determining step is identically derived by assuming the formation of carbon-hydroxyl COH as rate determining and subsequent cleavage to adsorbed carbon and OH in analogy to the mechanism of CO cleavage according to ref. [51]. Those types of simple LHHW rate equations, however, have been adopted for describing and also extrapolating the kinetics of various reactions though the exact mechanism is not known except for few examples.

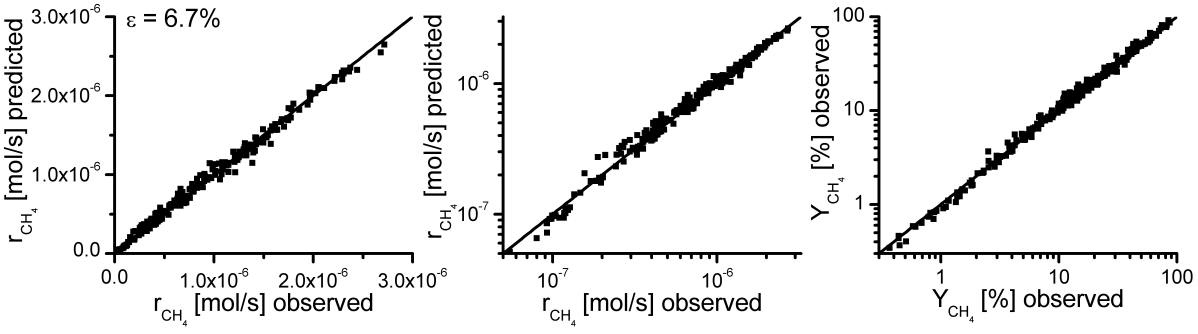

Figure 6.9: Parity plots for LHHW rate equation. Left: integral methane production rate, center: logarithmic methane production rate, right: yield of methane

Figure 6.9 shows the parity plot for the selected LHHW rate equation. The data are predicted very well by the model with a mean absolute residual of 6.7%. As illustrated

in the log-scale plot, the smallest methane formation rates are slightly systematically underestimated, which, however, is hardly accounted for in the parameter estimation because of the small absolute values. The mole fractions of methane of those values are below 1%. Apart from that, no systematic deviations are observable in the parity plots. For comparison, also the parity plots of yield related to carbon dioxide are given in order to show that the experiments cover the whole range from differential to almost complete conversion.

Figure 6.10 (a) and (b) report conversion in dependence of feed temperature and highlight the model's capability of reflecting H_2/CO_2 ratios over more than one order of magnitude very accurately. In agreement to determined reaction orders in section 6.5.2.3, the dependence of total pressure on reaction rates is rather low as depicted in figure 6.10 (c). Maintaining the same partial pressures of both reactants and experimental conditions, but feeding water and methane in addition slows down reaction rates considerably (figure 6.10 (c) and (d)). For instance, at a total pressure of 9 bar and temperature of 285°C, conversion of carbon dioxide is reduced from 53% to 37%, which is also captured by the model. If a model is adopted to technical SNG production, where water contents towards the reactor end will range in excess of 50 mol%, it will be crucial that the inhibiting effect of products is adequately represented by the model. Hence, all models parameterized on basis of initial reaction rates in absence of product gases will fail in this respect.

Table 6.5: Parameter estimation for LHHW rate equation ($T_{ref} = 555\,K$)

$k_{0,555K}$	3.46e-04 ± 4.1e-5	$mol\,bar^{-1}\,s^{-1}\,g_{cat}^{-1}$
E_A	77.5 ± 6.9	$kJ\,mol^{-1}$
$A_{OH,555K}$	0.50 ± 0.05	$bar^{-0.5}$
ΔH_{OH}	22.4 ± 6.4	$kJ\,mol^{-1}$
$A_{H_2,555K}$	0.44 ± 0.08	$bar^{-0.5}$
ΔH_{H_2}	-6.2 ± 10.0	$kJ\,mol^{-1}$
$A_{mix,555K}$	0.88 ± 0.10	$bar^{-0.5}$
ΔH_{mix}	-10.0 ± 5.7	$kJ\,mol^{-1}$

The estimated parameters for the selected LHHW rate equations are given in table 6.5. The 95% confidence intervals are rather large, in general. In particular, the adsorption enthalpy of H_2, ΔH_{H_2}, is not significantly different from 0. Hence, one might argue that the model contains an excessive number of parameters to describe the experiments in the dataset. However, in contrast to the power law rate equations, the model predictions are significantly better. Using Bartlett's test, all power law equations are rejected in comparison to the selected LHHW models despite the smaller number of parameters.

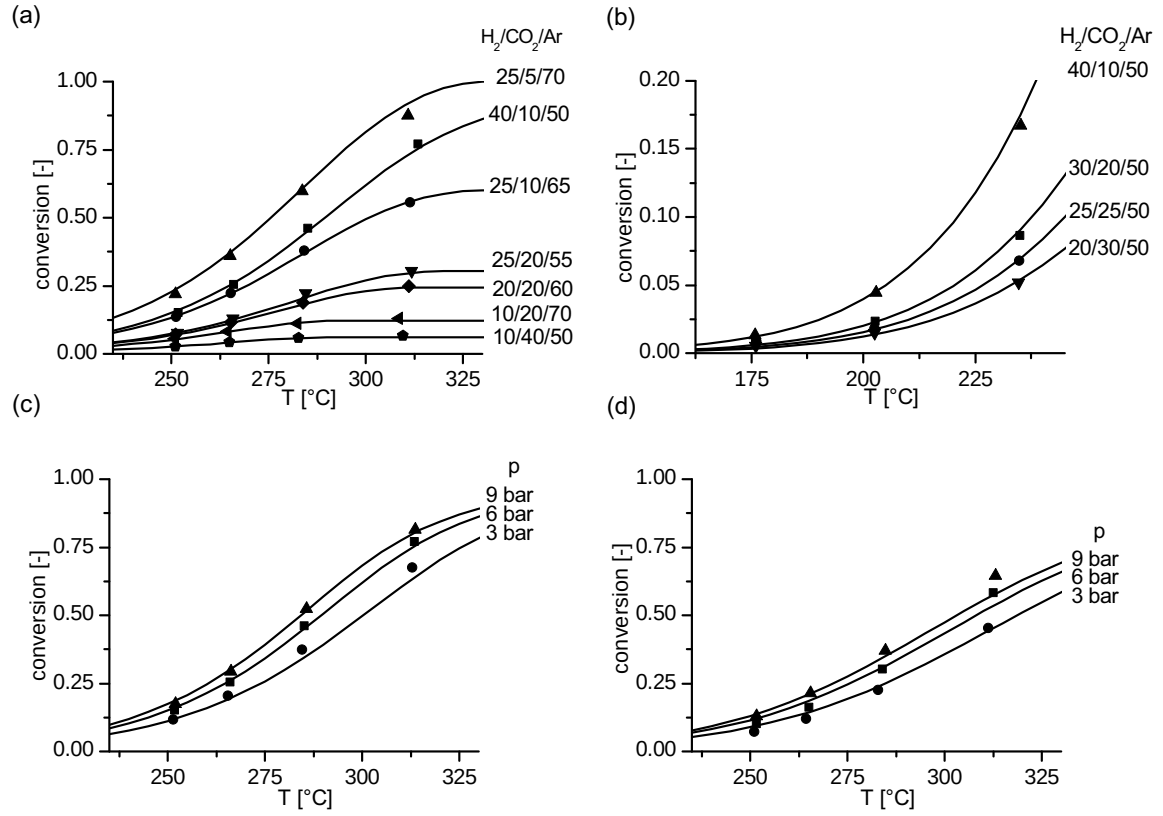

Figure 6.10: Comparison of experimental results (points) and model predictions (lines)
(a) H_2/CO_2 ratio ($Q = 120\,Nl\,h^{-1}\,g_{cat}^{-1}$, $m_{cat} = 25\,mg$, $p = 6\,bar$),
(b) H_2/CO_2 ratio ($Q = 48\,Nl\,h^{-1}\,g_{cat}^{-1}$, $m_{cat} = 75\,mg$, $p = 4\,bar$),
(c) pressure ($Q = 120\,Nl\,h^{-1}\,g_{cat}^{-1}$, $m_{cat} = 25\,mg$, $H_2/CO_2/Ar = 40/10/50$),
(d) pressure ($Q = 120\,Nl\,h^{-1}\,g_{cat}^{-1}$, $m_{cat} = 25\,mg$,
$H_2/CO_2/CH_4/H_2O/Ar = 40/10/12.5/25/12.5$).

The local sensitivities of the parameters calculated for all data points (figure 6.11) emphasize all parameters affect the reaction rates (see Appendix for calculation of sensitivities). Descriptively, a sensitivity of 1 for a parameter means that an increase of this parameter by 1% increases the overall reaction rate by 1%. Correspondingly, parameters with local sensitivity 0 do not affect the reaction rate under chosen reaction conditions, while negative sensitivities correspond to parameters which, if increased, slow down reaction rates. That the rate constant k_0 shows a sensitivity close to zero for few data points is due to the approach to equilibrium. K_{OH} affects the reaction rates at high water contents whereas it has hardly any influence at differential conversions. As discussed above, the apparent reaction order of carbon dioxide can be approximated

close to zero increasing with approach to equilibrium. In the LHHW rate equation this is reflected by ΔK_{mix}. With decreasing partial pressure of carbon dioxide the apparent reaction order in the model approaches 0.5 according to the exponent of carbon dioxide in the numerator.

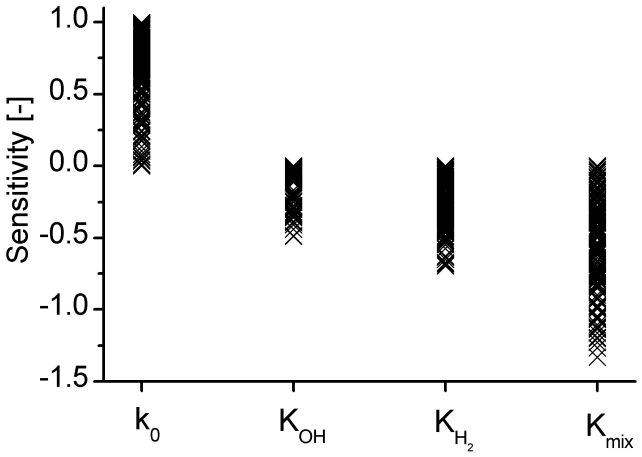

Figure 6.11: Local sensitivity analysis for LHHW rate equation for all measurements of the dataset.

For validation, the model predictions are compared to conversion temperature plots for the feed gas composition $H_2/CO_2/Ar = 4/1/5$ for pressures of 8 bar (figure 6.12). The conversion is reflected adequately over the whole temperature range. In particular, the model captures the slowed approach to thermodynamic equilibrium in contrast to simple power law model comprising only exponents for hydrogen and carbon dioxide (PL).

Figure 6.13 compares our kinetic model to predictions by several models from literature. The most obvious feature is that kinetics measured on our coprecipitated system are considerable faster than predicted by literature models. Consequently, we can confirm the conclusion by Abello et al. [31], who proposed coprecipitated high-loaded Ni/Al_2O_3 for CO_2 methanation. They also found their catalyst (molar ratio $Ni/Al = 5.4$) superior to literature systems. In relation to the model by Kai et al. [63], the high activity, however, seems plausible: with a 17 wt% $Ni/La_2O_3/Al_2O_3$ they employed a considerably less loaded system than the coprecipitated 58 wt% Ni/Al_2O_3 of this work. Also slopes of the conversion temperature plots are alike, which indicates that apparent activation energies are similar. The power law kinetics by Chiang and Hopper [61] deviate in this respect. The 15 wt% Ni steam reforming catalyst adopted by Xu and Froment [64] for methanation experiments is considerably less active. Conversion temperature plots are shifted by about 50°C to higher temperatures. We showed in a previous study that predictions by Xu and Froment's model are close to experimental

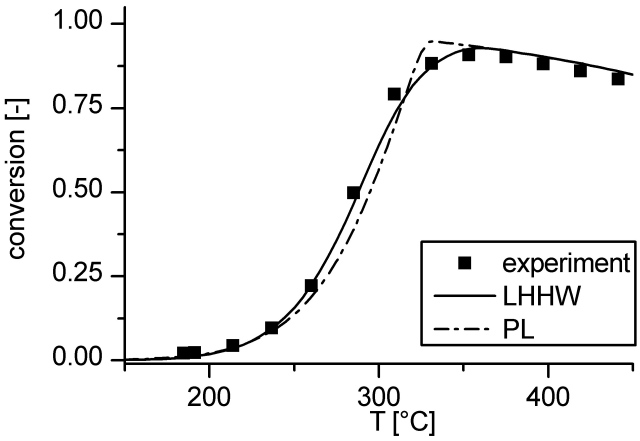

Figure 6.12: Conversion - temperature plot for $H_2/CO_2/Ar = 4/1/5$, $p = 8\,bar$, $Q = 150\,Nl/h/g_{cat}$, $m_{cat} = 25\,mg$

results for an impregnated 5 wt% Ni/ZrO_2 catalyst [20]. Figure 6.13 also emphasizes that it is indispensable to consider the thermodynamic equilibrium if the models are to be adopted for simulation of reactors intended for production of pure SNG. Not only is our model capable of capturing the equilibrium, but the approach to equilibrium is also described adequately due to the extensive dataset for parameter estimation. In comparison to previous kinetic models from literature as listed in table 2.2 our model for the first time combines the reflection of intrinsic (i) kinetics on a state-of-the-art catalyst system (ii) under industrially relevant conditions (iii) in terms of pressure, temperature and feed composition.

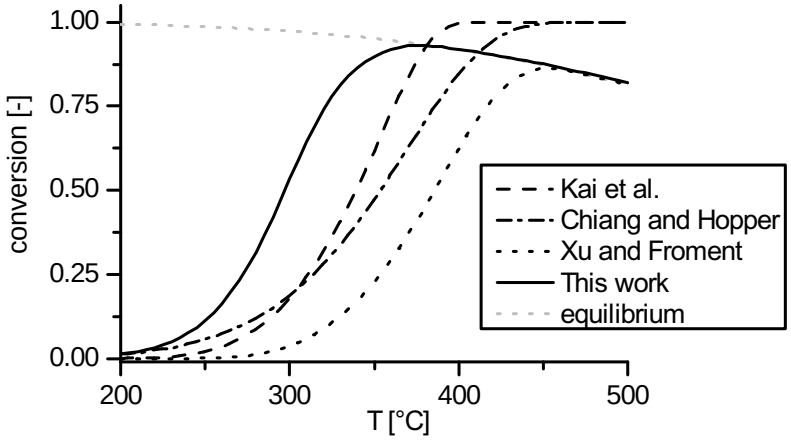

Figure 6.13: Comparison to predictions by kinetics from literature

6.6 Conclusion

A series of catalysts with varying Ni:Al ratio has been prepared by coprecipitation. After calcination of the hydrotalcite-like precursors, a mixed oxide phase ('disordered oxide spinel intermediate') was formed during calcination at 450°C. After reduction, specific nickel surface areas were measured by H_2 chemisorption. Nickel surface areas increased with Ni content, while average Ni particle sizes according to chemisorption and elementary analysis decreased with higher Ni content up to about 50 wt.% Ni before reaching a constant value around 17 nm.

The main conclusions of the kinetic characterization and modeling are:

1. A simple power law allows for an excellent description at differential conversions and pure H_2/CO_2 feed streams. Reaction orders of 1/3 and close to zero are found for hydrogen and carbon dioxide, respectively, for a wide range of conditions. However, the power law systematically overestimates reaction rates while approaching the thermodynamic equilibrium.

2. By introducing an empirical inhibition term concerning adsorbed water or preferable hydroxyl - both are similarly derived in the LHHW approaches - the kinetics can be reflected from differential to almost complete conversion for all reaction conditions applied in this study.

3. LHHW-type rate equations are best suited to describe the kinetics. Compared to the power law approaches comprising inhibition, the residuum is significantly lowered, however at the expense of a larger number and wider confidence intervals of the parameters. Though best results were obtained for rate equations derived on the assumption of a hydrogen assisted carbon oxygen bond cleavage, conclusions on the mechanism are not drawn solely based on our dataset comprising stationary experiments.

In view that coprecipated Ni/Al_2O_3 is regarded as promising catalyst system for the methanation of carbon dioxide, our work encourages also to further investigate aspects that aroused during our kinetic study, that is i.a. the influence of the calcination temperature and spinel formation on structure, reducibility and stability during reaction, deactivation phenomena like sintering, coking or structural changes and in particular the influence of water thereon. Finally, further mechanistic insight needs to be gained to support the development of a comprehensive elementary step kinetic model. This relates in particular to the open question of a direct CO_2 methanation route or a consecutive pathway with CO intermediate and to the influence of hydrogen on C-O bond cleavage. Since proposed elementary reactions in literature are very similar to the ones of methane

reforming reactions, it might be a promising approach to adopt these elementary step kinetic models derived and parameterized for reforming [161, 162] to the methanation reaction for mechanistic insights

6.7 Appendix

6.7.1 Assessment of transport limitations

For all criteria, gas phase properties were calculated on basis of the feed gas composition. The thermal conductivity of the gas phase was approximated by the rule of Wassiljeva based on data provided in VDI-Wärmeatlas [107]. As diffusion coefficient, the binary diffusion coefficient of carbon dioxide in hydrogen was assumed. Concerning the effective diffusion coefficient for the Weisz-Prater criterion also Knudsen diffusion of CO_2 was considered next to molecular diffusion according to the Bosanquet formula. The catalyst density and effective thermal conductivity were approximated with $2300\,\mathrm{kg\,m^{-3}}$ and $0.15\,\mathrm{W\,m^{-1}\,K^{-1}}$, respectively. Heat and mass transfer coefficients were estimated by correlation equations [111]. Measured integral methane formation rates are inserted as effective reaction rates r^{eff}. Following criteria have been checked for all data points in the parameter variation:
Intraparticle mass transport - Weisz-Prater criterion [163]

$$\frac{r^{\mathrm{eff}}\rho_{\mathrm{cat}}d_{\mathrm{cat}}^2}{4c_{\mathrm{CO_2}}D_{\mathrm{CO_2}}^{\mathrm{eff}}} < 1 \tag{6.8}$$

Intraparticle heat transport - Anderson criterion [164]

$$\frac{r^{\mathrm{eff}}\rho_{\mathrm{cat}}d_{\mathrm{cat}}^2|\Delta H|}{4\lambda^{\mathrm{eff}}T} < \frac{0.75RT}{E_A} \tag{6.9}$$

External mass transport - Mears criterion [165]

$$\frac{r^{\mathrm{eff}}\rho_{\mathrm{cat}}d_{\mathrm{cat}}}{h_m c_{\mathrm{CO_2}}} < 0.3 \tag{6.10}$$

External heat transport - Mears criterion [165]

$$\frac{r^{\mathrm{eff}}\rho_{\mathrm{cat}}d_{\mathrm{cat}}|\Delta H|}{h_t T} < \frac{0.3RT}{E_A} \tag{6.11}$$

6.7.2 Derivation of LHHW kinetic rate equations

The kinetic rate equations are derived analogously to the methodology of reference [46] which has also been adopted by Kopyscinsky et al. [103, 147] for the case of CO methanation. Exemplarily, the derivation will be presented for mechanism b assuming step 3 as rate determining and treating step 8 as irreversible.

The overall reaction rate is equal to the rate of elementary step 3, the formation of the formyl species, which is considered as rate determining step:

$$r = k_3 \Theta_{CO} \Theta_H \tag{6.12}$$

Θ_H and Θ_{CO} are the coverages of hydrogen and carbon monoxide, respectively, k_3 is the forward rate constant of elementary step 3. The coverage of hydrogen is easily accessible by assuming dissociative Langmuir adsorption that is in quasi-equilibrium:

$$\begin{aligned} k_2 p_{H_2} \Theta_*^2 &= k_{-2} \Theta_H^2 \\ \Theta_H &= \sqrt{K_{H_2} p_{H_2}} \Theta_* \end{aligned} \tag{6.13}$$

K_{H_2} represents the equilibrium constant of reaction 2 and Θ_* the fraction of free surface sites. Adsorbed carbon monoxide stems from dissociative adsorption of carbon dioxide which is also assumed as Langmuir adsorption in quasi-equilibrium:

$$\begin{aligned} k_1 p_{CO_2} \Theta_*^2 &= k_{-1} \Theta_{CO} \Theta_O \\ \Theta_{CO} &= K_{CO_2} p_{CO_2} \frac{\Theta_*^2}{\Theta_O} \end{aligned} \tag{6.14}$$

At steady state, the rate of oxygen hydrogenation must be twice the rate of the rate determining step. Furthermore, it is assumed that the equilibrium of reaction 7 is shifted far to the right, so this reaction can also be treated as irreversible.

$$\begin{aligned} &\frac{d\Theta_O}{dt} = 0 \Rightarrow r_7 = 2 r_3 \\ &r_7 \approx k_7 \Theta_O \Theta_H \\ &k_7 \Theta_O \Theta_H = 2 k_3 \Theta_{CO} \Theta_H \\ &\Theta_O = \frac{2 k_3}{k_7} \Theta_{CO} \end{aligned} \tag{6.15}$$

Inserting in the equation above finally results in the coverage of CO:

$$\Theta_{CO} = \sqrt{\frac{k_7}{2 k_3} K_{CO_2} p_{CO_2}} \Theta_* \tag{6.16}$$

The reaction rate can now be expressed as

$$r = k_3 \sqrt{\frac{k_7}{2k_3} K_{\mathrm{CO_2}} p_{\mathrm{CO_2}} K_{\mathrm{H_2}} p_{\mathrm{H_2}}} \Theta_*^2 \tag{6.17}$$

Assuming hydrogen, carbon monoxide and hydroxyl as most abundant surface intermediates (MASI) the balance over the adsorption sites can be formulated as follows:

$$1 = \Theta_{\mathrm{H}} + \Theta_{\mathrm{CO}} + \Theta_{\mathrm{OH}} \Theta_* \tag{6.18}$$

Assuming steps 8 and 9 in equilibrium the coverage of hydroxyl can be expressed as

$$\begin{aligned} \frac{K_8}{K_{\mathrm{H_2O}}} &= \frac{p_{\mathrm{H_2O}} \Theta_*^2}{\Theta_{\mathrm{H}} \Theta_{\mathrm{OH}}} \\ \Theta_{\mathrm{OH}} &= \frac{K_{\mathrm{H_2O}} p_{\mathrm{H_2O}}}{K_8 \sqrt{K_{\mathrm{H_2}} p_{\mathrm{H_2}}}} \Theta_* \end{aligned} \tag{6.19}$$

Finally, the fraction of free surface sites can be formulated as function of known variables:

$$\Theta_* = \frac{1}{1 + \sqrt{K_{\mathrm{H_2}} p_{\mathrm{H_2}}} + \sqrt{\frac{k_7}{2k_3} K_{\mathrm{CO_2}} p_{\mathrm{CO_2}}} + \frac{K_{\mathrm{H_2O}} p_{\mathrm{H_2O}}}{K_8 \sqrt{K_{\mathrm{H_2}} p_{\mathrm{H_2}}}}} \tag{6.20}$$

Considering the thermodynamic equilibrium, the reaction rate results in

$$r = \frac{k_3 \sqrt{\frac{k_7}{2k_3} K_{\mathrm{CO_2}} p_{\mathrm{CO_2}} K_{\mathrm{H_2}} p_{\mathrm{H_2}}} \left(1 - \frac{p_{\mathrm{CH_4}} p_{\mathrm{H_2O}}^2}{p_{\mathrm{CO_2}} p_{\mathrm{H_2}}^4 K_{\mathrm{eq}}}\right)}{\left(1 + \sqrt{K_{\mathrm{H_2}} p_{\mathrm{H_2}}} + \sqrt{\frac{k_7}{2k_3} K_{\mathrm{CO_2}} p_{\mathrm{CO_2}}} + \frac{K_{\mathrm{H_2O}} p_{\mathrm{H_2O}}}{K_8 \sqrt{K_{\mathrm{H_2}} p_{\mathrm{H_2}}}}\right)^2} \tag{6.21}$$

Grouping the constants for convenience, the reaction rate is written as

$$r = \frac{k p_{\mathrm{CO_2}}^{0.5} p_{\mathrm{H_2}}^{0.5} \left(1 - \frac{p_{\mathrm{CH_4}} p_{\mathrm{H_2O}}^2}{p_{\mathrm{CO_2}} p_{\mathrm{H_2}}^4 K_{\mathrm{eq}}}\right)}{\left(1 + \sqrt{K_{\mathrm{H_2}} p_{\mathrm{H_2}}} + K_{\mathrm{mix}} p_{\mathrm{CO_2}}^{0.5} + K_{\mathrm{OH}} \frac{p_{\mathrm{H_2O}}}{p_{\mathrm{H_2}}^{0.5}}\right)^2} \tag{6.22}$$

If instead of hydroxyl water is assumed as MASI, the last term in the denominator is replaced accordingly:

$$r = \frac{k p_{CO_2}^{0.5} p_{H_2}^{0.5} \left(1 - \frac{p_{CH_4} p_{H_2O}^2}{p_{CO_2} p_{H_2}^4 K_{eq}}\right)}{\left(1 + \sqrt{K_{H_2} p_{H_2}} + K_{mix} p_{CO_2}^{0.5} + K_{H_2O} p_{H_2O}\right)^2} \tag{6.23}$$

The following table pools all rate equations that have been derived assuming water as MASI. Where appropriate, also OH has been accounted for as MASI (not listed). Concerning mechanism a, steps 1, 3, 4, 5 and 7 have been set as RDS, respectively. All other steps have been assumed as equilibrated (case 1), or step 7, the hydrogenation of oxygen (case 2), or step 8, the hydrogenation of OH (case 3), have been assumed as irreversible. Concerning mechanism b, steps 4 and 5 have been assumed as RDS.

Table 6.6: Overview LHHW-type rate equations

	mechanism	RDS
$r = k p_{CO_2} \frac{\left(1 - \frac{p_{CH_4} p_{H_2O}^2}{p_{CO_2} p_{H_2}^4 K_{eq}}\right)}{\left(1 + \sqrt{K_{H_2} p_{H_2}} + K_{H_2O} p_{H_2O}\right)^2}$	a	1
$r = k \frac{p_{H_2} p_{CO_2}}{p_{H_2O}} \frac{\left(1 - \frac{p_{CH_4} p_{H_2O}^2}{p_{CO_2} p_{H_2}^4 K_{eq}}\right)}{\left(1 + \sqrt{K_{H_2} p_{H_2}} + K_{H_2O} p_{H_2O} + K_{mix} \frac{p_{H_2} p_{CO_2}}{p_{H_2O}}\right)^2}$	a	3
$r = k p_{H_2}^{0.25} p_{CO_2}^{0.5} \frac{\left(1 - \frac{p_{CH_4} p_{H_2O}^2}{p_{CO_2} p_{H_2}^4 K_{eq}}\right)}{\left(1 + \sqrt{K_{H_2} p_{H_2}} + K_{H_2O} p_{H_2O} + K_{mix} p_{H_2}^{0.25} p_{CO_2}^{0.5}\right)^2}$	a	3
$r = k p_{H_2}^{0.5} p_{CO_2}^{0.5} \frac{\left(1 - \frac{p_{CH_4} p_{H_2O}^2}{p_{CO_2} p_{H_2}^4 K_{eq}}\right)}{\left(1 + \sqrt{K_{H_2} p_{H_2}} + K_{H_2O} p_{H_2O} + K_{mix} p_{H_2}^{0.5} p_{CO_2}^{0.5}\right)^2}$	a	3
$r = k \frac{p_{H_2}^{2.5} p_{CO_2}}{p_{H_2O}^2} \frac{\left(1 - \frac{p_{CH_4} p_{H_2O}^2}{p_{CO_2} p_{H_2}^4 K_{eq}}\right)}{\left(1 + \sqrt{K_{H_2} p_{H_2}} + K_{H_2O} p_{H_2O} + K_{mix} \frac{p_{H_2}^2 p_{CO_2}}{p_{H_2O}^2}\right)^2}$	a	4
$r = k p_{H_2}^{0.5} p_{CO_2}^{0.33} \frac{\left(1 - \frac{p_{CH_4} p_{H_2O}^2}{p_{CO_2} p_{H_2}^4 K_{eq}}\right)}{\left(1 + \sqrt{K_{H_2} p_{H_2}} + K_{H_2O} p_{H_2O} + K_{mix} p_{CO_2}^{0.33}\right)^2}$	a	4

$r = k p_{\mathrm{H_2}}^{5/6} p_{\mathrm{CO_2}}^{1/3} \frac{\left(1-\frac{p_{\mathrm{CH_4}} p_{\mathrm{H_2O}}^2}{p_{\mathrm{CO_2}} p_{\mathrm{H_2}}^4 K_{\mathrm{eq}}}\right)}{\left(1+\sqrt{K_{\mathrm{H_2}} p_{\mathrm{H_2}}}+K_{\mathrm{H_2O}} p_{\mathrm{H_2O}}+K_{\mathrm{mix}} p_{\mathrm{CO_2}}^{1/3} p_{\mathrm{H_2}}^{1/3}\right)^2}$	a	4
$r = k \frac{p_{\mathrm{H_2}}^{1.5} p_{\mathrm{CO_2}}^{0.5}}{p_{\mathrm{CH_4}}^{0.5}} \frac{\left(1-\frac{p_{\mathrm{CH_4}} p_{\mathrm{H_2O}}^2}{p_{\mathrm{CO_2}} p_{\mathrm{H_2}}^4 K_{\mathrm{eq}}}\right)}{\left(1+\sqrt{K_{\mathrm{H_2}} p_{\mathrm{H_2}}}+K_{\mathrm{H_2O}} p_{\mathrm{H_2O}}+K_{\mathrm{mix}} \frac{p_{\mathrm{H_2}} p_{\mathrm{CO_2}}^{0.5}}{p_{\mathrm{CH_4}}^{0.5}}\right)^2}$	a	5
$r = k \frac{p_{\mathrm{H_2}}^{2} p_{\mathrm{CO_2}}^{0.5}}{p_{\mathrm{CH_4}}^{0.5}} \frac{\left(1-\frac{p_{\mathrm{CH_4}} p_{\mathrm{H_2O}}^2}{p_{\mathrm{CO_2}} p_{\mathrm{H_2}}^4 K_{\mathrm{eq}}}\right)}{\left(1+\sqrt{K_{\mathrm{H_2}} p_{\mathrm{H_2}}}+K_{\mathrm{H_2O}} p_{\mathrm{H_2O}}+K_{\mathrm{mix}} \frac{p_{\mathrm{H_2}}^{1.5} p_{\mathrm{CO_2}}^{0.5}}{p_{\mathrm{CH_4}}^{0.5}}\right)^2}$	a	6
$r = k p_{\mathrm{H_2}}^{0.5} p_{\mathrm{CO_2}}^{0.5} \frac{\left(1-\frac{p_{\mathrm{CH_4}} p_{\mathrm{H_2O}}^2}{p_{\mathrm{CO_2}} p_{\mathrm{H_2}}^4 K_{\mathrm{eq}}}\right)}{\left(1+\sqrt{K_{\mathrm{H_2}} p_{\mathrm{H_2}}}+K_{\mathrm{H_2O}} p_{\mathrm{H_2O}}+K_{\mathrm{mix}} p_{\mathrm{CO_2}}^{0.5}\right)^2}$	b	3
$r = k p_{\mathrm{H_2}}^{0.75} p_{\mathrm{CO_2}}^{0.5} \frac{\left(1-\frac{p_{\mathrm{CH_4}} p_{\mathrm{H_2O}}^2}{p_{\mathrm{CO_2}} p_{\mathrm{H_2}}^4 K_{\mathrm{eq}}}\right)}{\left(1+\sqrt{K_{\mathrm{H_2}} p_{\mathrm{H_2}}}+K_{\mathrm{H_2O}} p_{\mathrm{H_2O}}+K_{\mathrm{mix}} p_{\mathrm{CO_2}}^{0.5} p_{\mathrm{H_2}}^{0.25}\right)^2}$	b	3
$r = k p_{\mathrm{H_2}}^{0.5} p_{\mathrm{CO_2}}^{0.5} \frac{\left(1-\frac{p_{\mathrm{CH_4}} p_{\mathrm{H_2O}}^2}{p_{\mathrm{CO_2}} p_{\mathrm{H_2}}^4 K_{\mathrm{eq}}}\right)}{\left(1+\sqrt{K_{\mathrm{H_2}} p_{\mathrm{H_2}}}+K_{\mathrm{H_2O}} p_{\mathrm{H_2O}}+K_{\mathrm{mix}} p_{\mathrm{CO_2}}^{0.5} p_{\mathrm{H_2}}^{0.5}\right)^2}$	b	4
$r = k p_{\mathrm{H_2}}^{0.75} p_{\mathrm{CO_2}}^{0.5} \frac{\left(1-\frac{p_{\mathrm{CH_4}} p_{\mathrm{H_2O}}^2}{p_{\mathrm{CO_2}} p_{\mathrm{H_2}}^4 K_{\mathrm{eq}}}\right)}{\left(1+\sqrt{K_{\mathrm{H_2}} p_{\mathrm{H_2}}}+K_{\mathrm{H_2O}} p_{\mathrm{H_2O}}+K_{\mathrm{mix}} p_{\mathrm{CO_2}}^{0.5} p_{\mathrm{H_2}}^{0.75}\right)^2}$	b	4

6.7.3 Calculation of specific surface area, dispersion and average crystallite size following the extrapolation theory

During chemisorption measurements the adsorbed gas volume depending on the pressure is determined. Molecules are not only adsorbed by chemisorption, but also by physisorption, which linearly depends on pressure. In the experiment, as shown exemplarily in figure 6.14 for the NiAl11, the combination of chemisorption and physisorption is measured. To extract the chemisorbed gas volume, the linear part of the combined curve above pressures of 200 mmHg is extrapolated to zero pressure and the y-axis intercept is determined.

The specific surface area A_{sp} is calculated following the equation:

$$A_{sp} = n_{ads} \nu A_m \tag{6.24}$$

wherein n_{ads} is the amount of adsorbed molecules, ν the stoichiometry factor (2 for H_2-chemisorption), and A_m the cross section of the active species ($A_{Ni} = 6.49\,\text{Å}^2$). To determine the dispersion D of the active species, the equation

$$D = \frac{n_{ads}\nu M}{100 \cdot w} \tag{6.25}$$

is applied. M represents the molecular weight of Ni and w its weight fraction. The average crystallite size d is calculated according to

$$d = \frac{w \cdot f}{A_{sp} \cdot \rho} \tag{6.26}$$

with f as the shape correction factor (here 6 for spherical particles), ρ as density of Ni ($8.9\,\text{g}\,\text{cm}^{-3}$) (DIN 66136-1).

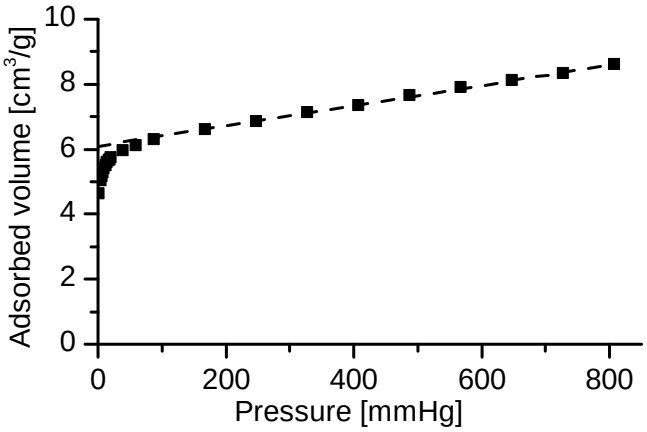

Figure 6.14: Chemisorption measurement for NiAl11

6.7.4 Calculation of local sensitivities

Local sensitivities are approximated by finite differences in form of a relative sensitivity coefficient:

$$S_i = \frac{par_i}{r_{\text{CH}_4}} \frac{\partial r_{\text{CH}_4}}{\partial par_i} = \lim_{\Delta par_i \to 0} \frac{r_{\text{CH}_4,var} - r_{\text{CH}_4,ref}}{r_{\text{CH}_4,ref} \cdot var} \tag{6.27}$$

par_i corresponds to the parameter of interest and var to the respective variation, which was chosen as 1%.

7 Kinetics of deactivation on $Cu/ZnO/Al_2O_3$ methanol synthesis catalysts

7.1 Abstract

Deactivation behavior is an important topic in catalyst development. In case of methanol synthesis, the conventional $Cu/ZnO/Al_2O_3$ system is commonly known to be prone to sintering, however, information about the structural development during deactivation or the sintering mechanism are scarce. We present a systematic deactivation study on three different $Cu/ZnO/Al_2O_3$ catalysts which are aged under constant conditions and periodically analyzed using kinetic measurements and N_2O chemisorption. A power law model for the catalyst activity with time on stream is derived. Furthermore it is found, that the presence of water provokes a steep loss in active surface area and specific activity. Also, the TEM particle size distributions generated during the aging treatment are evaluated and discussed.

Keywords: heterogeneous catalysis, methanol, deactivation, copper, $Cu/ZnO/Al_2O_3$

7.2 Introduction

Methanol is one of the most important basic chemicals and represents an important C1 building block for industrial chemicals. It offers access to a whole variety of important industrial products, like formaldehyde, dimethyl ether (DME) or methyl-tert-butylether (MTBE). The methanol to olefins (MTO) and methanol to gasoline (MTG) processes are a pathway to utilize synthesis gas from various feedstocks to produce valuable hydrocarbons. In the typical low-pressure process over $Cu/ZnO/Al_2O_3$ catalysts pressures ranging from 50 to 100 bar and temperatures of about 483 to 563 K are employed [166]. Apart from usage in the chemical industry, the liquid can also be mixed with gasoline, directly used as fuel for cars or stored and transported as an easy to handle energy carrier. By combining the generation of hydrogen from renewable sources and CO_2

capture methods, methanol can provide sustainable energy storage and feedstock for various chemicals. This concept of a methanol based economy has been extensively studied by Olah et al. [167, 168].

The deactivation behavior of heterogeneous catalysts is an important characteristic in plant operation and has been studied for many industrial catalytic applications. In these processes, the deactivation mechanisms are classified into different types like chemical poisoning or thermal effects [169, 170]. In case of methanol synthesis catalysts, poisoning with sulfur and halogenides from coal derived synthesis gas was early identified as a problem and prohibited initially the application of the more efficient copper based low pressure process in favor of the more poisoning resistant chromium based high pressure process [171]. However, with the development of more sophisticated desulfurization and halogenide removal methods, poisoning should not be a prominent problem in methanol synthesis anymore [172, 173]. In contrast, the intrinsic deactivation by thermal induced processes like sintering or phase segregation still limits the catalyst lifetime [174]. Especially sintering of copper in ternary $Cu/ZnO/Al_2O_3$ catalysts has been identified as a major deactivation mechanism in this process. However, detailed or mechanistic studies on sintering of $Cu/ZnO/Al_2O_3$ are scarce. Hansen and Nielsen mention in their basic introduction to methanol synthesis that under typical operation conditions in a temperature range between 480 and 580 K sintering is a priori not expected according to Tammann's rule ($T_{Tammann} \approx 680\,K$) [175]. However, they argue it might be possible that sintering occurs by the release of atomic or molecular species according to the Hüttig temperature ($T_{Hüttig} \approx 450\,K$). Generally, sintering mechanisms are still under current research and new developments, especially in the field of the transmission electron microscopy, allow a better understanding of the occurring processes [176]. One of the most detailed studies of copper particle growth has recently been presented by Prieto et al. for Cu/ZnO constrained in mesopores of SBA-15 [177]. By sophisticated preparation and calcination techniques they succeeded in depositing Cu nanoparticles either homogeneously or concentrated to few mesopores. Electron tomography was used to quantify particle sizes, location in specific pores and interparticle distances of fresh and aged samples. The authors found that classical mean field Ostwald Ripening models failed in describing the particle size distributions and time dependence of sintering. Considerable improvement was gained by introduction of local correlations between particles. Best results were obtained when virtually only the nearest and next-nearest neighbors contributed to the ripening of a particle. For the system with the inhomogeneously distributed particles, however, the model prediction was significantly worse than for the homogeneous system. It was concluded that for short interparticle distances also a coalescence mechanism might have to be considered.

Recently, we presented a study containing detailed characterization data of different conventionally prepared $Cu/ZnO/Al_2O_3$ catalysts which were systematically aged under controlled conditions [178]. In contrast to metal support systems - analyzed e.g. by Prieto et al. [177] or Hansen et al. [179] - with the metal nano-particles distributed over an extended support, these catalysts represent bulk catalysts with a particularly different microstructure (see below).

The gathered data led to the conclusion that different concurrent mechanisms have to be considered, when discussing the deactivation of methanol synthesis catalysts: The formation of $ZnAl_2O_4$ decreases the Al^{3+} dopant level in ZnO and together with coarsening of ZnO leads to a disruption of the Cu/ZnO synergy. Furthermore, the mobility of the structural spacer ZnO plays a major role in the sintering process and has a large influence on the deactivation behavior. In this study we present a time resolved analysis of the catalyst activity during the aging period and a numerical analysis of the particle size distributions gathered throughout the deactivation process.

7.3 Experimental and computational methods

7.3.1 Catalyst preparation

The preparation, XRD, TEM, TPD and BET characterization of the samples CZA1-3 are accurately described in refs. [178] and [180]. After the activation procedure, CZA1 and CZA2 are mainly characterized by an open microstructure in which copper particles are partially covered with ZnO_x and kept apart by ZnO spacers. This catalyst microstructure is well known and commonly ascribed to ex-zincian-malachite precursor phases [181, 182]. In case of CZA2 also some alumina rich regions of γ-Al_2O_3 and ex-hydrotalcite-like precursors are observed. In case of CZA3 the copper particles are strongly embedded in a ZnO matrix which is attributed to the ZnO rich ex-aurichalcite type structure. Typical characterization results are summarized in table 7.1. It should be noted that in the following context all values based on the mass of calcined catalyst are denoted by m_{calc}, whereas values based on the mass of activated catalyst are denoted by m_{cat}.

7.3.2 Deactivation and kinetic experiments

7.3.2.1 Experimental setup

The catalysts are aged in a single pass setup equipped with four parallel fixed bed reactors which can be operated up to 70 bar and temperatures up to 773 K. The catalyst bed is placed in glass lined steel tubing (diameter 1/2 inch, maximum length 3 inch) and secured with silica wool plugs. Product analysis is performed with an Agilent 7820A gas

Table 7.1: Metal ratio, BET surface area and N_2O-RFC surface area of the analyzed catalyst samples

Catalyst	Cu:Zn:Al[a] [%]	SA_{BET}[b] $\left[m^2\,g_{cat}^{-1}\right]$	SA_{RFC}[b,c] $\left[m^2\,g_{cat}^{-1}\right]$	FHI sample number
CZA1	70:28:2	93.1	50.9	15802
CZA2	58:26:16	86.2	29.5	14382
CZA3	43:49:8	77.7	22.5	14383

[a] molar, determined by EDX and XRF [b] activated catalyst [c] error $\pm 1\,m^2\,g_{cat}^{-1}$[d] for future references and comparison with ref. [178]

chromatograph equipped with two thermal conductivity detectors, a packed Porapack-N column (Sigma Aldrich) for the quantification of CH_4, CO_2, H_2O, CH_2O, CH_3OH and a packed Molsieve 5 Å column (Sigma Aldrich) for the quantification of Ar, N_2, CH_4 and CO. If not reported otherwise, all gas purities are of very high grade (6.0 for Ar, H_2, N_2, 5.5 for CO_2, 5.0 for N_2O, 4.7 for CO) and have been checked for sulfur impurities below 100 ppb. A trap containing 10 g activated methanol synthesis catalyst at room temperature serves as additional guard reactor for traces of sulfur and metal carbonyls. The spent catalysts are dissolved in boiling aqua regia, inspissated and analyzed via ICP-OES (Spectroflame, Spectro Analytical). Within the detection limit of 10 ppm (wt) no traces of iron or nickel were found in the deactivated catalysts, which confirms the absence of metal carbonyl deposition on the catalyst. The synthesis gas used for aging the catalysts and performing the activity tests is a premixed combination of 13.5% CO, 3.5% CO_2, 73.5% H_2 and 9.5% N_2.

7.3.2.2 Measurements

In a typical measurement 1000 mg calcined catalyst (sieve fraction 500-710 µm) mixed with 6000 mg purified silicon carbide (sieve fraction 355-500 µm) is heated up at ambient pressure for 15 h in 2.0% H_2 in Argon raising the temperature from 300 to 448 K at $1\,K\,min^{-1}$, then in H_2 raising the temperature from 448 K to 513 K at $1\,K\,min^{-1}$ and holding for 30 minutes. After the activation procedure the catalysts are cooled down to 308 K in Argon and the first reactive N_2O frontal chromatography (see below) is performed to determine the initial copper surface area. Subsequently the catalysts are heated to 493 K in 2.0% H_2 in Argon, flushed with synthesis gas and pressurized to 60 bar. Initial activity tests are performed for every reactor at 483 K under differential conditions. Afterwards the catalysts are heated up to the aging temperature and aged under a weight hourly space velocity (WHSV, $\frac{\dot{m}_{feed}}{m_{calc}}$) of $0.51\,h^{-1}$. Under these conditions the equilibrium constitution is reached within the first 15% of the catalyst bed length

which was confirmed by varying the catalyst loading. Due to dispersion effects at the low flow aging conditions an equilibrated gas atmosphere is obtained over the whole catalyst bed length. This operation provides a way to age the different catalyst samples under constant conditions, even when the respective catalytic activities are different. Although the temperature and pressure region is relevant for industrial methanol production, it should be noted that these conditions were specifically chosen to ensure a fast and reproducible deactivation by stressing the catalysts under high conversions. Hence, they do not represent the gas phase composition which is typically present in the majority of the catalyst bed in an industrial reactor. Depending on the aging time on stream (TOS) of 1000 h or 1600 h, the catalyst is cooled down to 483 K every 20 or 30 h respectively. After flushing for 30 min with synthesis gas and performing activity measurements under differential conditions, the sample is reheated and further aged. Taking into account the time needed for heating or cooling the reactor, the catalyst is aged under constant conditions for more than 90% of the whole TOS.

To study the influence of the aging temperature, all samples are aged at 523 K as well as at 553 K. In case of CZA1 and CZA3 also aging at 493 K is performed. Here, a second CZA1 sample was further co-fed three times for 12 hours with 4.4 sccm water vapor in order to elucidate its influence on the catalyst stability. In this case the aging WHSV is $0.72\,h^{-1}$ with the following feed gas composition: 11% CO, 2.9% CO_2, 60.3% H_2, 18% H_2O, 7.8% N_2. This leads to an equilibrium water content of roughly 10%, which can be described as hydrothermal aging of the catalyst. A summary of the aging conditions and the resulting equilibrium gas phase composition is given in table 7.2.

Table 7.2: Aging conditions presented in this study

T_{aging} [K]	p_{aging} [bar]	CO	CO_2	H_2	MeOH [%]	H_2O	N_2
493[a]	60	1.39	3.60	62.68	18.20	1.18	12.96
523	60	3.97	3.73	65.28	14.09	0.75	12.18
553	60	7.73	3.50	68.26	8.74	0.61	11.16
493 + H2O[b]	60	1.49	11.28	67.36	1.65	10.17	8.06

[a] CZA1 and CZA3 only [b] CZA1 only

7.3.2.3 Analysis of results

All activity measurements are performed three times in a series which is represented by the error bars in the respective plots. The maximum relative error in methanol yield or CO_x conversion is smaller than 3%. Furthermore, a reduction of the aging period length

between activity measurements down to 12 h yielded essentially the same deactivation pattern which confirms that the activity measurements do not influence the catalyst deactivation behavior. Also, careful analysis prior to the deactivation measurements showed that no pore diffusion limitation or hotspot formation are present within the experimental window.

For further analysis, the relative catalyst activity a_{rel} is approximated using the time-dependent CO_x (= CO + CO_2) conversion X_{CO_x} and a power law model (PLM) given in equation 7.1. Since this description of the deactivation mechanism is a pure empiric one and should not be over-interpreted, only integral reaction orders m are considered.

$$\frac{da_{rel}}{dt} = -k_a \, a_{rel}(t)^m \tag{7.1}$$

$$a_{rel}(TOS) = \frac{X_{CO_x}(TOS)}{X_{CO_x}(TOS = 0)} \tag{7.2}$$

It should be noted that this assumption is only valid for differential conversions. With an initial maximum absolute CO_x conversion of 15% and a maximum CO_x conversion of 18% with respect to the equilibrium conversion this assumption is feasible. A reproduction experiment with 250 mg catalyst yielded essentially the same deactivation pattern, however with proceeding catalyst deactivation the kinetic measurements proved to be too inaccurate for a precise analysis.

7.3.3 Reactive N_2O Frontal Chromatography (N_2O-RFC)

During the aging process, the N_2O adsorption capacity is determined by the method described in ref. [183]. In order to remove surface adsorbates, prior to every measurement the catalyst is flushed for 45 minutes at 523 K with Argon, treated for another 45 minutes with 2% H_2 in Argon at 493 K and cooled down to 308 K in Argon. The surface oxidation is performed with 1% N_2O in an Ar flow and the gas phase composition in the effluent is monitored with a mass spectrometer. It has been shown recently that this method in fact does not measure the metallic copper surface area, but rather a combination of the exposed metallic surface area and oxygen defect sites generated due to the Cu/ZnO interaction [184, 185]. However, it is generally a good indicator for the catalytic activity of copper based methanol synthesis catalysts. In order to establish comparability with previous literature, the chemisorption capacity in this work is reported as copper surface area equivalents (active phase surface area, ASA) assuming a stoichiometric reaction of N_2O with a pure copper surface and a mean surface copper atom density of $1.47 \cdot 10^{19}$ atoms per m^2. In order to ensure comparability with the characterization results presented in ref. [178] all presented N_2O-RFC results are based

on the mass of activated catalyst. Due to subsurface oxidation of copper during the N_2O-RFC experiment, an error margin of $1\,m^2\,g_{cat}^{-1}$ is assumed, which is higher than the actual measured error when reproducing the experiments.

7.3.4 Modeling approach

The copper particle size distribution of the aged catalysts was determined by TEM measurements in ref. [178] after aging at 523 K and an aging period of 0, 240, 480, 720 and 960 h, respectively. Since the catalysts, the aging setup and the aging process are the same as the ones presented in this work these characterization results can be used to describe the measured aging processes, e.g. in terms of numerical sintering models.

In this work, the modified bond-additivity (MBA) approach and a classical coalescence model with a $D \propto r^{-4}$ dependence are examined as kinetic models for Ostwald ripening and coalescence, respectively. A detailed description of the models is presented in chapter 7.7. In addition, particle size distributions are compared to a random collision model, which is based on the assumption that the probability of coalescence of two particles is independent of their radii and hence equal for all particles. The latter model does, however, not contain a kinetic component and does not provide information on temporal progress of sintering.

In case of the random collision model, a dataset comprising 10.000 particles is generated based on the log-normal fits of the TEM particle size data for the fresh catalysts. It has been checked that the number of particles in the generated dataset is sufficient and higher numbers give virtually the same results despite a smaller statistical spread. For a coalescence event, two particles are chosen randomly, removed from the dataset and replaced by a particle of volume equivalent to the sum of the removed particles. This procedure is repeated until the chosen collision number is reached. The results are averaged over several datasets to minimize the statistical spread. To obtain the collision number that best fits the experimental TEM distributions, the sum of squares of the residuals of the discretized size distributions is calculated. Accordingly, the ratio of the collision number in relation to the number of particles initially present in the system characterizes the evolution of the PSD and gives information on how many coalescence events have taken place and how many particles have been involved in relation to the number of particles initially present in the system.

7.4 Results

7.4.1 Deactivation behavior

An important prerequisite for the applicability of the power law deactivation model in 7.1 is that the apparent activation energy of the methanol formation does not change during the deactivation process. An exemplary Arrhenius plot for the deactivated catalysts is given in figure 7.1. A summary of the measured activation energies for the aging process at 523 K is presented in Table 7.3.

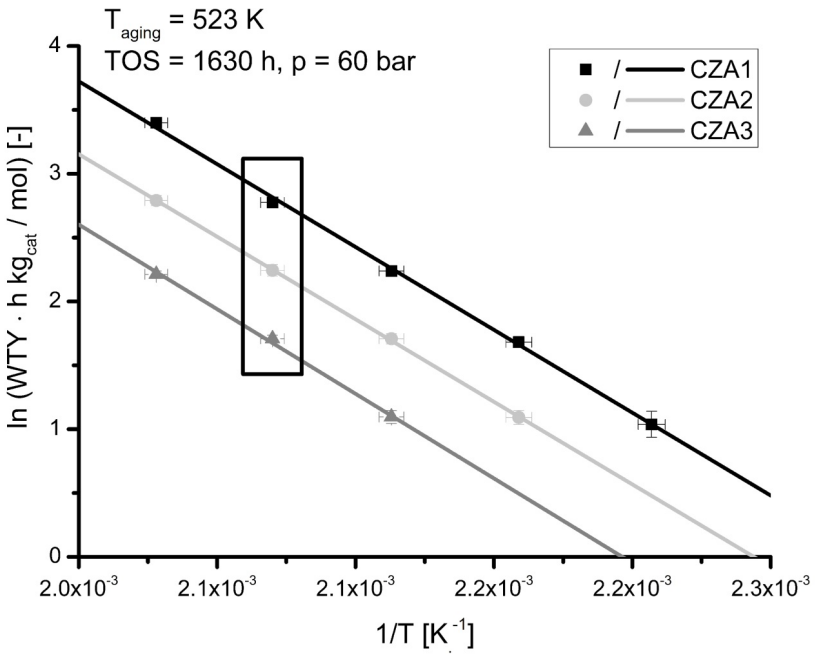

Figure 7.1: Arrhenius plot for the deactivated catalyst samples. The black box represents the conditions for the catalyst activity measurements.

Table 7.3: Activation energy E_A before and after the aging process

Catalyst	CZA1	CZA2	CZA3
$E_{A,0\,h}$ [kJ mol^{-1}]	116.6±7.2	110.5±4.5	105.7±3.1
$E_{A,1630\,h}$ [kJ mol^{-1}]	112.1±2.2	107.1±1.1	106.5±5.8

As the apparent activation energy of methanol formation during the deactivation process is constant within the error margin, the power law model can be applied to describe the rate constant k_d of the deactivation process. For all catalysts, the deactivation can be described by a simple power law model of 3rd order for aging temperatures of 523 and 553 K and 4th order for an aging temperature of 483 K, respectively. A representative example of the deactivation behavior at 523 K is given in figure 7.2.

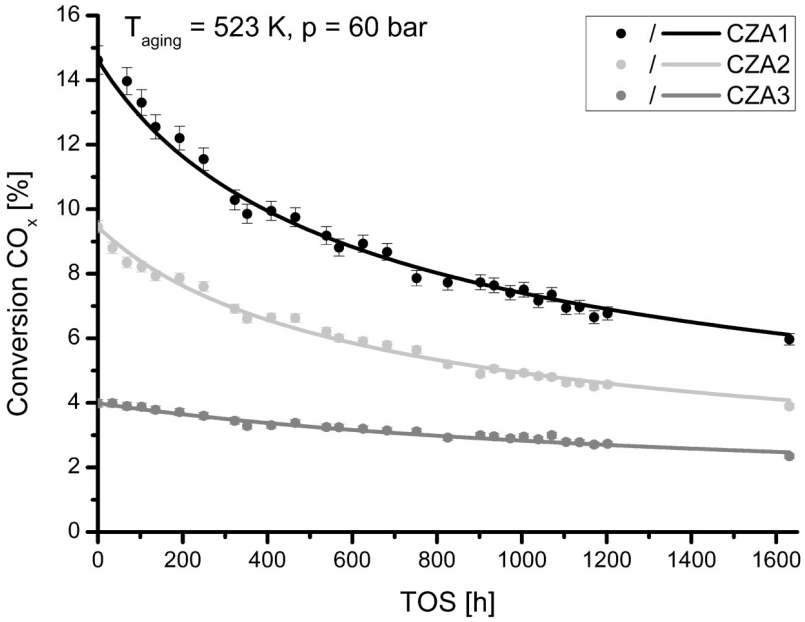

Figure 7.2: Deactivation behavior of the three different catalyst samples at 523 K. The straight lines represent the results according to the PLM fit.

All samples show a good methanol synthesis activity and compare well with other $Cu/ZnO/Al_2O_3$ systems reported in literature [186, 187]. In all cases the selectivity for methanol is beyond 99% and only traces of formaldehyde and methane are found during the equilibrium aging. The material balance is closed within 3% relative accuracy. Although CZA1 contains only 17% more copper than CZA2, the catalyst activity is increased by more than 50%. This is attributed to an optimal incorporation of Al^{3+} into the ZnO lattice, generating oxygen defect sites and acting as an electronic promotor [188]. The lower activity of CZA3 is a result of the catalyst microstructure, resulting from the ex-aurichalcite precursor phase. Here, the copper particles are strongly embedded in a ZnO matrix effectively blocking the Cu surface from contact with the gas phase. In contrast, the structure of CZA1 and CZA2 is represented by an intimate mixture of

spherical ZnO and Cu nanoparticles. This leads to a very porous structure, which is easily accessible for the gas atmosphere. An exemplary image of the microstructure is presented in figure 7.3 and a detailed analysis of the catalyst microstructures is performed in ref. [178].

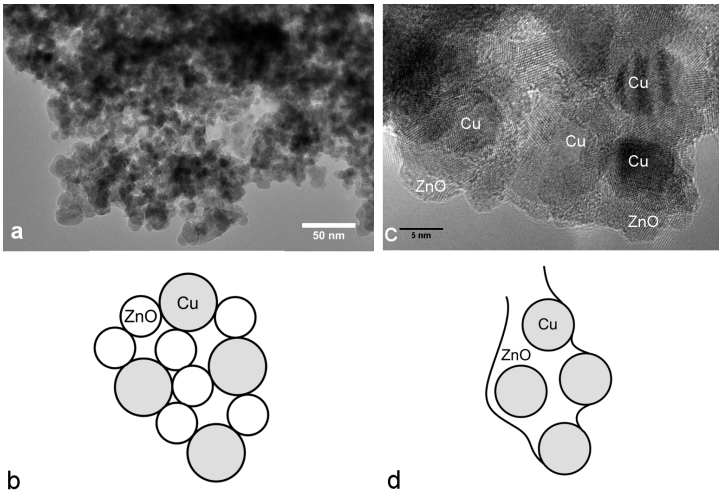

Figure 7.3: TEM images and exemplary representation of the microstructure of CZA1 and CZA2 (a, b) and CZA3 (c, d)

The influence of the aging temperature and the addition of water on the deactivation behavior is presented in figure 7.4. A summary of all determined rate constants of the catalyst deactivation is given in table 7.4.

Table 7.4: Rate constant and reaction order of catalyst deactivation according to the PLM fit

Catalyst	$T_{aging} = 493\,K$		$T_{aging} = 523\,K$		$T_{aging} = 553\,K$	
	k_d $[h^{-1}]$	m	k_d $[h^{-1}]$	m	k_d $[h^{-1}]$	m
CZA1	4.29e-3	4	1.45e-3	3	2.62e-3	3
CZA2	n.d.	n.d.	1.34e-3	3	2.18e-3	3
CZA3	6.08e-4	4	4.95e-4	3	9.34e-4	3

During the aging period of 1630 h at 523 K CZA1 and CZA2 lose 60% of the initial activity, whereas CZA3 only loses about 40%. This is in good agreement with the deactivation rate constants which are quite similar for CZA1 and CZA2 and significantly higher than for CZA3. The strong deactivation in general is attributed to the severe conditions chosen for the aging periods. CZA1 and CZA2 show the same trend at 553 K deactivation temperature; in comparison to $T_{age} = 523\,K$ the deactivation rate constant

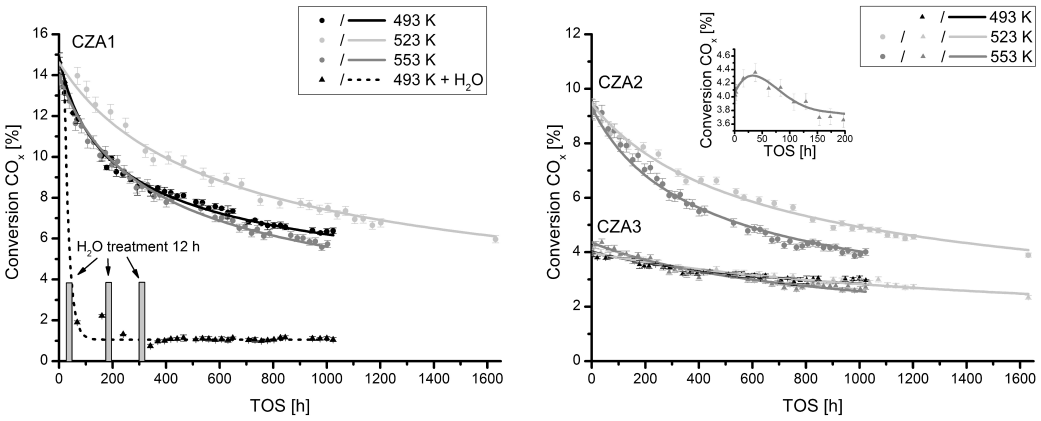

Figure 7.4: Influence of the aging temperature on the deactivation behavior. Straight lines represent the results according to the PLM fit. The inset in the right figure illustrates the transient activation behavior of CZA3 at 553 K.

is roughly doubled. Here, sample CZA3 shows an interesting formation behavior at 553 K, illustrated in the inset in figure 7.4. Whereas all catalysts exhibit a monotonic decrease in activity, CZA3 increases in the first 50 hours. Although the simple power law is not able to describe this behavior, it has no significant impact on the determined deactivation rate, as the activation only covers roughly 5% of the whole TOS. The reason for the initial rise in activity is not yet known; a possible mechanism may be the crystallization of the former amorphous Al_2O_3/ZnO matrix embedding the particles in the ex-aurichalcite phase. This could lead to a more porous matrix with copper particles that are better reachable for the gas phase atoms.

The short-term hydrothermal treatment of CZA1 leads to significant catalyst deactivation which underlines the strong influence of water on the deactivation behavior. To a small fraction, this process is reversible within a timescale of hours as can be seen after the last water addition period. However, this effect is minimal compared to the activity loss of more than 90% of the initial activity. Assuming pure sintering of metallic copper, the lowest deactivation rate is expected at 493 K. Nevertheless, the results show that at this temperature catalyst deactivation is almost as strong as at 583 K. This behavior may be explained by the higher water content during the aging process (see table 7.2).

The results of the reactive N_2O frontal chromatography measurements during the aging period are given in figure 7.5. The trend in active phase surface area is very similar to the development in catalyst activity. After roughly 10 days the loss in ASA levels off. It should be noted that the ASA also very much resembles the ex-situ results presented in ref. [178] which strengthens the assumption that the characterization data acquired therein can be applied to the presented catalysts. An analysis of the activity per active

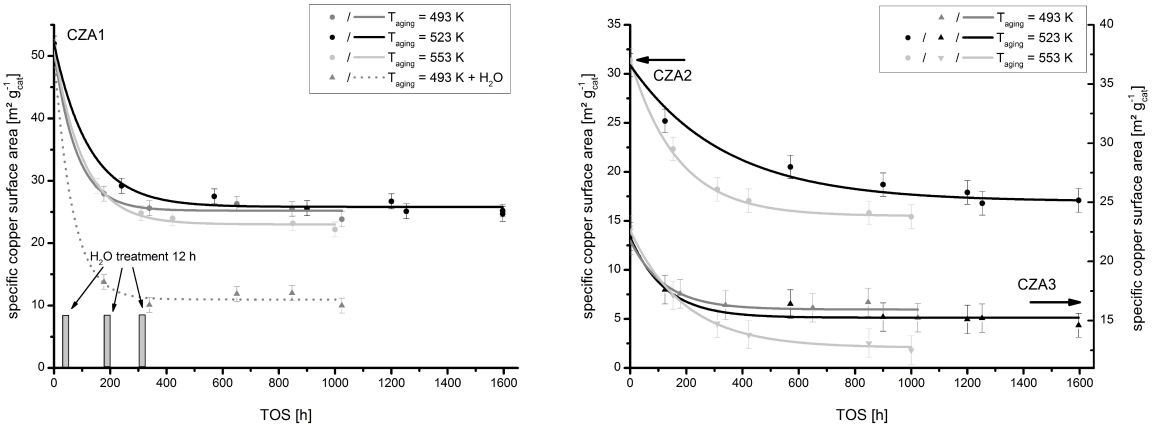

Figure 7.5: Results of the reactive N_2O frontal chromatography. The straight lines represent the trend in the specific copper surface area.

surface area ratio is presented figure 7.6 and shows that the aging temperature has no major impact on the specific activity. After an initial formation period accompanied by an increase in this value, the specific activity drops for roughly the first 600 h and then reaches a slowly deactivating state. The initial increase can be explained by a change in the Al^{3+} doping of ZnO and the wetting behavior of the Cu/ZnO system [178, 180, 188]. Due to the structural similarity of the precursor material it is not surprising that the specific activities of the deactivated CZA1 and CZA2 samples show a close resemblance.

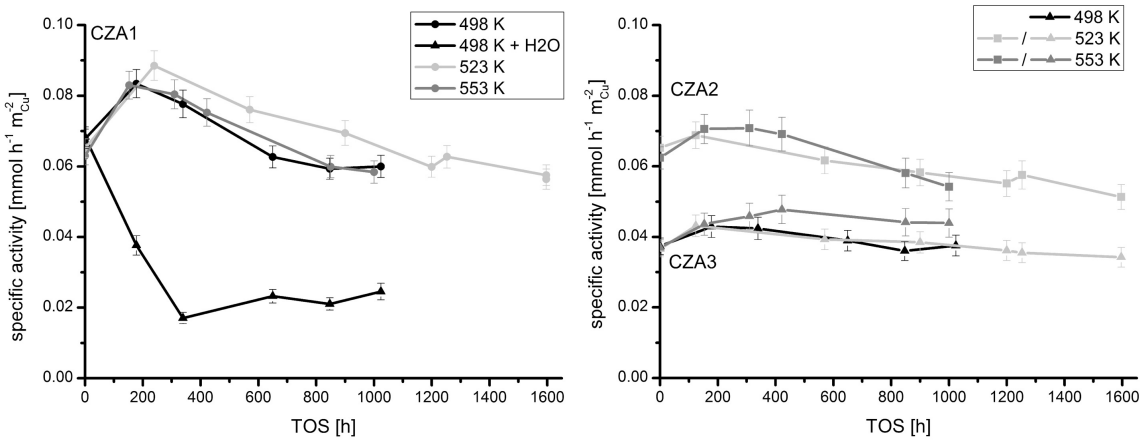

Figure 7.6: Specific catalyst activity in relation to the N_2O-RFC copper surface area

7.4.2 Modeling results

Selected results describing the copper particle size distribution of CZA1 and CZA2 in terms of a MBA Ostwald Ripening model, the classical coalescence model and a random collision model are given in figures 7.10, 7.11 and 7.7, respectively. Assuming the initial particle size distribution of the CZA1 sample, an adsorption energy of approximately $185\,\mathrm{kJ\,mol^{-1}}$ between the mobile species and ZnO is required in the MBA Ostwald Ripening model if the exposed copper surface area is to be decreased to 75% of the initial value after 960 h. However, in this case the predicted particle size distribution is very narrow compared to the experimental data and overemphasizes the vanishing of small particles. The same trend can be observed in the classical $D \propto r^{-4}$ collision model.

In contrast, by assuming that particles coagulate independent of the respective particle diameters, the evolution of the particle size distribution of CZA1 and CZA2 is captured very well (figure 7.7).

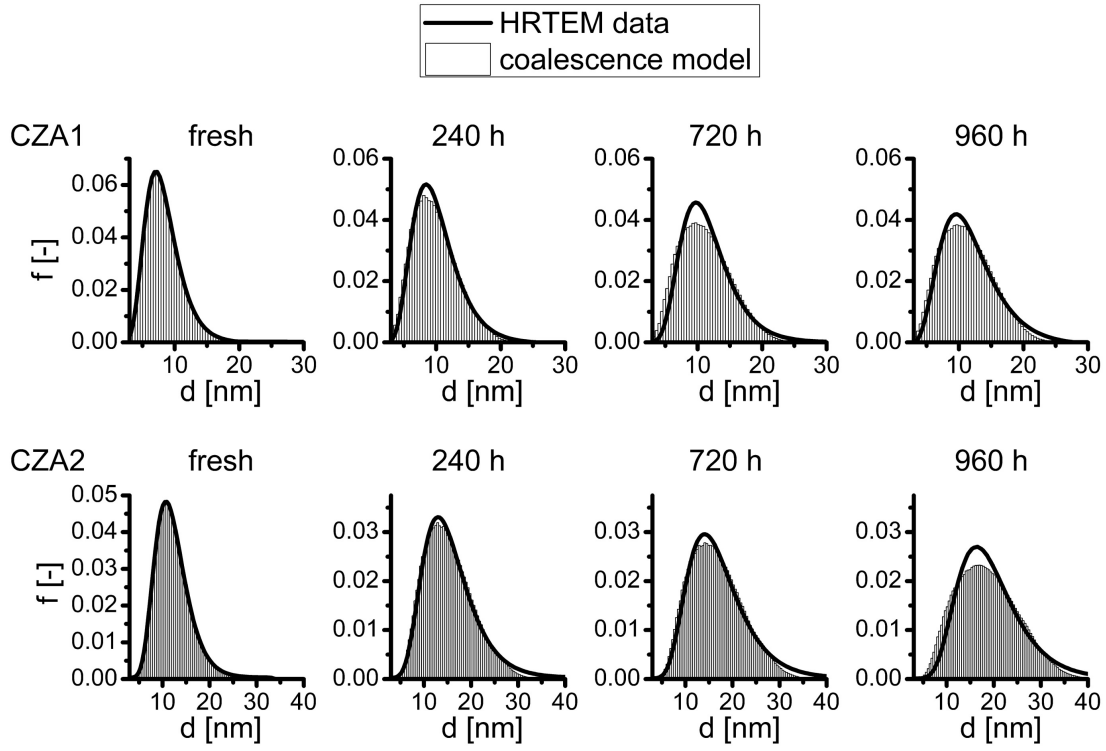

Figure 7.7: Particle Size Distributions according to the random collision model for CZA1 (top row) and CZA2 (bottom row)

7.5 Discussion

To illustrate the deactivation behavior the parameterized power law is extrapolated to a TOS of 400 days and compared with literature values of catalysts aged under similar conditions. As presented in figure 7.8, the gathered data compares well with an industrial $Cu/ZnO/Al_2O_3$ catalyst presented by Skrzypek et al. [189] and very stable Cu/ZnO systems supported on SBA15 presented by Prieto et al. [177]. A similar exponential loss in activity has also been observed in the methanol steam reforming reaction over copper based catalysts [190]. However, it should be noted that the presented catalyst samples were aged under specifically severe conditions, so that the described deactivation patterns do not represent the overall catalyst lifetime in industrial reactors. Although, the extrapolation of data should be generally considered with great caution, it underlined the big variety in the methanol synthesis catalyst stability: whereas the mentioned systems roughly retain 25% of their initial activity after 400 days TOS, other systems deactivate even more rapidly.

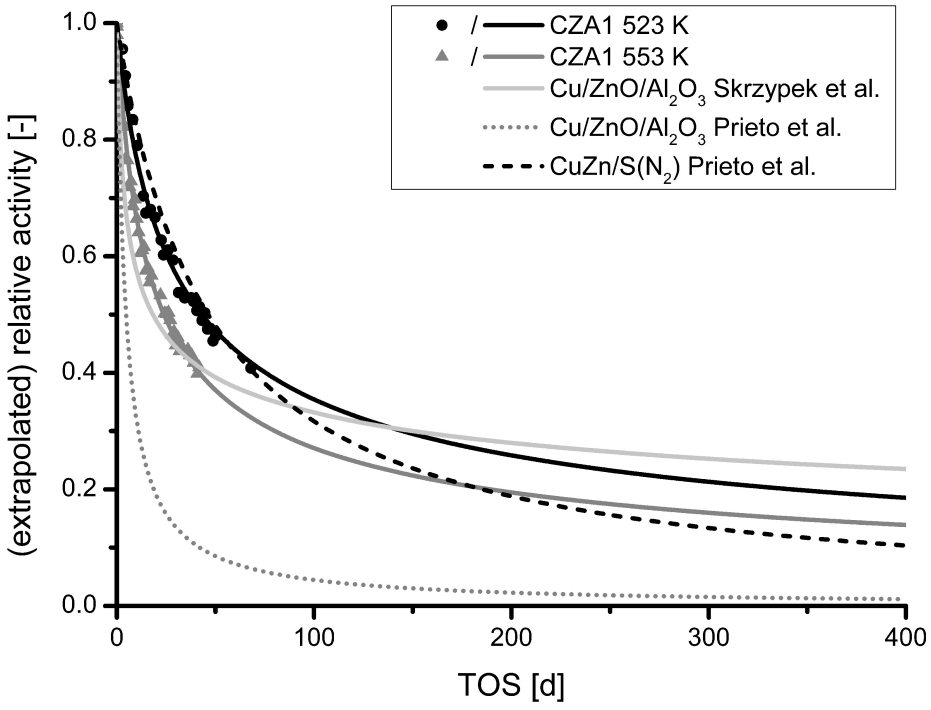

Figure 7.8: Comparison of selected deactivation models with our experimental data for CZA1 (dots and triangles) and the determined PLM fit (straight lines)

Taking into account that in all cases the apparent activation energy for the methanol production is very similar to the one after the aging process, it is reasonable to assume

that under the typical aging conditions presented here the nature of the active site(s) does not change. As poisoning of the catalysts was excluded from the experiments and the maximum temperature of 553 K is too low for bulk formation of brass, the deactivation achieved in this work results most likely from a reduction of the active site concentration [191]. Considering further the significant drop in active phase surface area, the sintering of copper particles appears to be the main source of catalyst deactivation at a first glance. Although this feature would be applicable for many supported metal catalysts, in this case severe restrictions have to be made: The active phase surface area (classically determined by N_2O-RFC), does not represent the actual metallic copper surface area but a combination of the metallic surface area and oxophilic sites at the Cu/ZnO interface. As recently shown, these oxophilic sites can make up to almost 50% the ASA [184]. Furthermore, a significant fraction of the copper particle surface area is present as interface to the stabilizing oxide matrix and hence not accessible for the gas phase (see figure 7.3). This interaction is strongly dependent on the Cu/ZnO wetting behavior and the copper surface decoration which is subject to strong changes (described in [178]). Therefore, also correlations between XRD and TEM-derived copper crystal sizes and surface areas have to be considered very carefully when analyzing catalyst deactivation in this special field. Due to these reasons, no direct correlation between the development of copper particle size and catalyst activity will be evaluated in this work, however general trends in the structure-stability relationship can be explored.

When treating CZA1 with water, a significant drop in specific activity is noticed. This indicates that under hydrothermal conditions the catalyst undergoes structural changes and hence loses significantly copper surface area. However, in contrast to aging the catalysts under different temperatures, also the specific activity is dramatically reduced. In other words, the exposed (copper) surface is not that active for methanol synthesis anymore. This strongly hints to a disruption of the Cu/ZnO synergy which is vital for the catalytic activity. Previous studies by Kandmir et al. [191] suggested the formation of mobile ZnO_x species in such high performance catalysts, but also in model type catalysts mobile ZnO species were reported previously [192]. A reduction of the strong Cu/ZnO interaction could easily occur by retraction of mobile ZnO, which is supported by the observed crystallization of ZnO and $ZnAl_2O_4$ in the presented catalysts during the deactivation period [178]. The hydrothermal treatment of CZA1 leads to a pronounced crystallization of ZnO and hence a loss of the intimate Cu/ZnO contact due to phase segregation. Cu-Zn phase segregation and removal of the promoting effect of the Al^{3+} dopant (see ref. [178]) by $ZnAl_2O_4$ crystallization may also be the main reason for the deactivation behavior of CZA3, which displayed almost no copper particle growth in the TEM analysis. In the very ZnO-rich CZA3 sample this is mainly attributed to a strong embedding of the Cu particles in ZnO. To understand the mechanisms leading to

particle growth in ZMA type systems (CZA1 and CZA2) it is vital to keep in mind that the copper particles are separated by ZnO particles of more or less the same size. Hence, the particles are very densely packed and typical copper interparticle distance is roughly one particle diameter (see figure 7.3). Thus, already slight changes in the ZnO spacer structure or Cu/ZnO wetting behavior may lead to copper-copper particle contact. Such changes include crystallization and coarsening of ZnO as well as the formation of new phases like $ZnAl_2O_4$, which has been observed for those catalysts under deactivation conditions [178].

Although no direct correlation between copper particle size, exposed copper surface area and catalyst activity can be established, the development of the copper particle size distribution with time on stream yields important information. Evaluating the apparent copper particle growth behavior in the catalysts, microstructural similarities and stability issues can be addressed. The question about ripening or coalescence as prevalent sintering mechanism is an open discussion in literature. In order to infer mechanisms of sintering of heterogeneous catalysts, in-situ TEM may be indispensable as proposed by DeLaRiva and coworkers [193]. In this regard, by now the reduction of a CuO/ZnO model system has been studied by Creemer et al. [194] in a hydrogen atmosphere up to temperatures of 500°C using environmental TEM. It has been observed that some crystals migrated immediately after reduction to metallic Cu, but the crystals remained immobile at later stages, which was attributed to Cu strongly pinning at sites that are nonuniformly distributed over ZnO surfaces. However, the time scale of 70 s is probably too short to draw conclusions towards sintering mechanisms. Rasmussen et al. [195] provided an atomistic perspective on sintering in Cu/ZnO systems by DFT calculations. Concerning particle migration and coalescence, diffusion of Cu species on surfaces of Cu crystallites shifts the position of the center of mass of the crystallites, thus leading to crystallite migration. This mechanism is identically assumed in the derivation of radii dependent diffusion coefficients in classical coalescence models. CuCO and Cu_2HCOO were identified to be predominant species for metal transport on Cu particles by DFT. Concerning Ostwald ripening, CuCO was found as species prone for transport of single copper atoms over ZnO. Unfortunately, owing to the very complex sample matrix and limitations in environmental transmission electron microscopy, studies about the Cu/ZnO mobility under or near to typical methanol synthesis conditions have not been performed, yet. With respect to the strong interaction of the gas atmosphere with the Cu/ZnO wetting behavior [178, 179, 196–198], the ex-situ analysis is one of the few methods applicable today. The measured particle size distributions of all samples resemble closely to log-normal distributions. This is a common feature in sintering of heterogeneous catalysts and in principle in agreement to a coalescence mechanism. However, it is well known that inference of the sintering mechanism based on particle

size distributions is very ambiguous. In an experimental study, Datye et al. pointed out that log-normal particle size distributions as most often found experimentally can arise from both Ostwald ripening and a coalescence mechanism [199]. They contradict the common argument that right skewed particle size distributions are in contradiction to Ostwald ripening. Similar conclusions were drawn by Fuentes et al. by mathematical analysis [200]. Ostwald ripening can lead to groups of solutions, some of them similar to log-normal distributions and a direct interpretation of the PSD shape without further information about the sintering behavior seems futile. However, examining the catalysts' microstructure provides an interesting aspect worthy of discussion:

Ex-aurichalcite type catalysts as CZA3 are characterized by Cu particles which are strongly embedded in a partially amorphous ZnO matrix. Over a period of 40 days, the copper particles in this system hardly sinter at all. As CZA3 exhibits a distinct smaller active phase surface area it could be argued that this strong embedding not only prevents the particles from coagulation, but also hinders the detachment of single adatoms from the Cu bulk by covering the copper surface with ZnO. However, comparing the metallic copper surface area values (determined by H_2-TPD in ref. [178]) with CZA1 and CZA2 about 2/3 of the ZMT type catalysts' metal area is accessible for the gas atmosphere so that this argument seems inappropriate. The driving force for Ostwald Ripening might also be influenced by a different ratio of the ZnO/Cu contact area than typically found in similar catalysts like CZA1 or CZA2. However, it seems unlikely that this phenomenon extinguishes the driving force completely. It rather indicates that there is a lack in mobility of individual Cu atoms or Cu species under these conditions.

The described densely packed microstructure of ZMT catalysts distinguishes the catalysts CZA1 and CZA2 from typical metal-support model systems since there is no plane support on which copper particles can diffuse freely and randomly coalesce according to their mobility. Slight changes in the ZnO support structure can lead to the collision and coalescence of copper particles independent of the particular copper particle mobility. Consequently, the classical coalescence model fails in describing the observed sintering behavior of methanol synthesis catalysts in terms of both time dependence and particle size distribution (see figure 7.11). The particle size distributions are too narrow in the model as a result from the r^{-4} dependence of the particle diffusion coefficient. Since the sintering of small particles is highly favored over large particles, first selectively small particles should disappear. The probability for the formation of large particles resulting from coalescence of two large particles is low. In comparison to the experiment, however, the fraction of both small and large particles is systematically underestimated. This indicates that the mobility is either less affected by the radius than assumed or is not the critical factor, but the probability of two particles to sinter is predetermined by the microstructure of the catalyst.

Assuming the probability for coalescence of two particles independent of the radius and consequently equal for all particles, the particle distributions in figure 7.7 can be derived. In particular, the description of formation period in the first 10 days is excellent. There is no tendency observable of small particles disappearing first. However, since the observed sintering behavior depends in contrast less on physical, size-dependent properties or the distance between particles, the time-dependence of sintering cannot be predicted in the random collision model. But the similarity of the time-dependent collision number for systems with alike microstructure is striking (figure 7.9). For instance, both CZA1 and CZA1 feature around 240 h TOS a value of 0.5, which implies that a number of collisions equal to half the amount of initial particles has taken place. Keeping in mind that each collisions involves two particles, the overall number of particles in the system has, thus, already been halved. The similarity between CZA1 and CZA2 is especially interesting as the initial mean copper particle diameter of CZA2 is more than 50% larger than in CZA1 which would generate a significant difference in the size-dependent surface diffusion behavior or driving force for Ostwald ripening. However, both systems show a very similar microstructure and deactivate with almost the same rate constant. Hence, the presented random collision model may state a versatile tool to describe structural changes and the influence of the catalyst microstructure in coprecipitated copper based methanol synthesis catalysts.

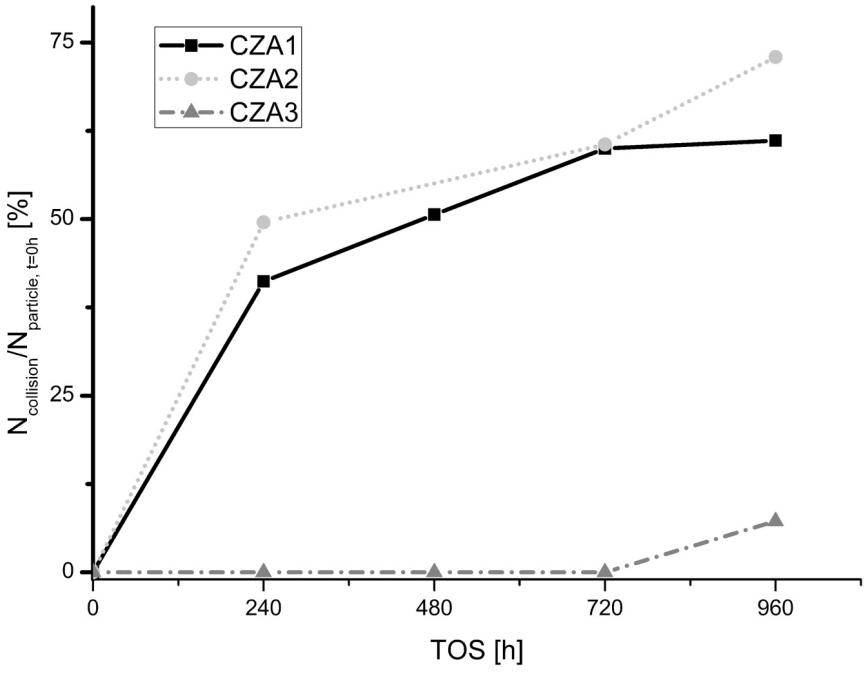

Figure 7.9: Time-dependent collision number according to the random collision model

It should be noted that the described trend in the PSD evolution in CZA1 and CZA2 could also be described by Ostwald ripening. By assuming mobile atomic or molecular species similar distributions might be derived, if ripening is constraint between a small numbers of adjacent particles of even pairs of particles in contrast to mean field models. In line with conclusions by Prieto et al. [177] this shows that the structure of the coprecipitated Cu/ZnO affects the evolving particle size distributions in terms of the pronounced influence of neighboring Cu particles separated by ZnO spacers. However, then the remarkable stability of copper particles in systems with very similar elemental composition like CZA3 (and also a consecutively precipitated system called CZA4 in ref. [178]) is worth of discussion. Our results imply that coprecipitated $Cu/ZnO/Al_2O_3$ shows a sintering behavior which is significantly different from typical model catalysts. In combination with the high scientific and commercial relevance of the methanol synthesis in general, this work also should be seen as an encouragement to further analyze these systems with methods like ETEM studies to discriminate sintering mechanisms and deactivation phenomena.

7.6 Conclusion

The key aspects of this work can be presented as follows:

1. The deactivation behavior of three different methanol synthesis catalysts was systematically examined and characterized using an empiric power law equation.

2. The nature of the active site does not change under the typical conditions employed and the main deactivation mechanism is hence a reduction of active sites. This can be attributed to loss of active phase surface area by sintering and Cu/ZnO phase segregation and leaching of the Al^{3+} dopant with the formation of $ZnAl_2O_4$. Thus, the main mechanism for the reduction of active sites is subject to the specific microstructure and cannot be trivialized as pure sintering.

3. The addition of water, even for a short period, does not only increase the sintering tendency but also permanently reduces the specific catalyst activity, possibly by segregating Cu/ZnO and hence reducing the SMSI effect needed for a high catalyst activity.

4. Evolving particle size distributions can be described adequately by assuming a random collision of particles. Though this does not provide mechanistic information on the sintering process, it is valuable for development of mechanistic models for sintering in coprecipitated systems.

Owing to the time consuming measurements and many-sided possible error source of systematic long time experiments, the results discussed in this work only present a certains aspects of the deactivation mechanism of methanol synthesis catalysts. Also, it should be noted that the usefulness of the presented results for other systems depends on the similarity of the microstructure and should not be transferred to classical supported metal nano-particles. However, it underlines the necessity for detailed studies in order to unravel the processes happening during and influencing the deactivation behavior. Especially with respect to plant operation where the catalyst bed is aged differently along the reactor length, much more insight into the influence of water in the deactivation mechanism is needed. Our results support the findings that the key component of deactivation in methanol synthesis catalysts with the described microstructure is not the low thermal stability of the copper particles but the mobility of ZnO. Hence, more stable catalysts may also be obtained, when stabilizing the ZnO that functions as spacer in between the copper particles. The presented random-collision-coagulation model proved to be a versatile tool and the results encourage to use the model to analyze the sintering behavior of better catalysts for methanol synthesis.

7.7 Supporting information

7.7.1 Ostwald ripening

In general, two sintering mechanisms are distinguished: Ostwald ripening and coalescence. Driving force for the Ostwald ripening is the minimization of the chemical potential of the metal atoms. Since according to the Gibbs-Thomson relation the chemical potential of a metal atom in small particles is largely influenced by the surface energy, large particles are prone to increase in size while smaller particles shrink. Classically, bare metal atoms or molecular species are assumed as mobile species that according to the driving force tend to migrate from smaller to larger particles. As a common in basic models, this net flux results from a concentration difference of a size-specific equilibrium concentration of mobile species present around the particle and the mean-field concentration of mobile species assumed as constant on the oxidic support beyond a screening distance around the metal particles. This equilibrium concentration is smaller for larger particles and vice versa according to the chemical potential of a metal atom in a particle. The mean-field concentration of mobile species on the support is derived from mass conservation. A pioneering Ostwald ripening model was formulated by Wynblatt and Gjostein for the cases of so-called diffusion and interface control, see e.g. reference [201] for details. During the last years, Campbell and coworkers [201–203] have promoted the development of more sophisticated sintering models for nanoparticles motivated by the lack of the former models in terms of description of the chemical potential of metal atoms as a function of the particle size. Since the surface tension used in the Gibbs-Thomson equation in classical ripening models for calculating the chemical potential is a macroscopic property and assumed as independent on the radius, the modified bond-additivity (MBA) approach has been developed to simply derive an approximation of the chemical potential for a metal atom of a nanoparticle by counting the mean number of bonds per metal atom in a nanoparticle of a specific size.

The MBA Ostwald Ripening model is formulated analogously to ref. [201] and has been validated with the data published for Pb on MgO therein. The log-normal fits of the TEM data for the fresh catalysts are discretized into 7.000 equidistant diameters. The system of coupled ordinary differential equations is solved with the Matlab solver ode23s. The contact angle between metal particle and support and vibrational frequency of an adsorbed atom on a particle are assumed constant as 90° and $10^{14}\,s^{-1}$, respectively. Results are presented as bar graphs of 100 bars between 0 and 40 nm particle diameter.

The differential equation for a particle size r can be formulated as

$$\frac{dr}{dt} = \frac{K}{r}\, exp\left(-\frac{E_{tot}}{RT}\right)\left[exp\left(\frac{E(r^*)}{RT}\right) - exp\left(\frac{E(r)}{RT}\right)\right] \tag{7.3}$$

where r^* is the critical particle radius that is by definition in equilibrium with the mean-field concentration of mobile species, $E(r)$ is the size-specific difference of chemical potential related to a metal atom in a particle of infinite size according to the MBA-model, E_{tot} is the sum of all activation energies and K groups parameters that can be assumed as constant. The total activation energy is expressed as contribution from the metal's bulk sublimation energy ΔH_{sub}, the diffusion activation energy of the mobile species on the oxide H_m^s and the adsorption energy of a monomer on the support as

$$E_{tot} = \Delta H_{sub} - E_{ad}^s + H_m^s \tag{7.4}$$

Assuming that the diffusion activation energy of the mobile species can be approximated as $0.25\, E_{ad}^s$ [201], the total activation energy can be formulated as

$$E_{tot} = \Delta H_{sub} - 0.75\, E_{ad}^s \tag{7.5}$$

With these equations the adsorption energy needed for pronounced sintering rates energy can now be approximated. Assuming the initial particle size distribution of the CZA1 sample, an adsorption energy of approximately $185\,\mathrm{kJ\,mol^{-1}}$ is required if the dispersion is to be decreased to 75% after 960 h at an aging temperature of 523 K. This value now can be compared to published adsorption energies for Cu on ZnO. According to a DFT study by Meyer and Marx [204], adsorption energies for single Cu atoms on polar ZnO surfaces range between 166 and $276\,\mathrm{kJ\,mol^{-1}}$ for ideal O- and Zn-terminated polar ZnO surfaces. However, the adsorption energies are found highly dependent on coadsorbates and defect sites which drastically diminish Cu adsorption energies to 79 to $108\,\mathrm{kJ\,mol^{-1}}$. With an adsorption energy of about $100\,\mathrm{kJ\,mol^{-1}}$, Ostwald ripening is many orders of magnitudes too slow to account for the observed sintering and the model predicts virtually no sintering at all. Keeping the dependence of the sintering on the gas composition in mind, one might speculate about mobile species on ZnO that nevertheless might enable Ostwald ripening in reasonable rates.

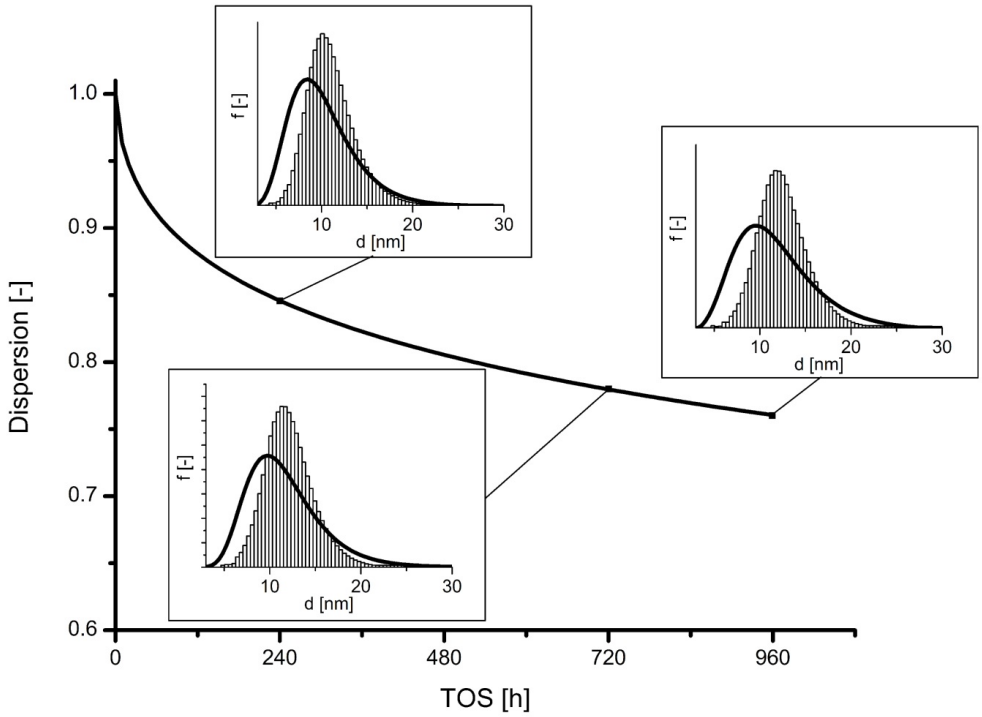

Figure 7.10: Relative dispersion and particle size distribution according to the MBA Ostwald Ripening model ($E_{ads} = 185\,kJ\,mol^{-1}$). The black line in the inset picture represents the measured distribution, whereas the gray bars represent the modeling result.

7.7.2 Coalescence

In classical coalescence models for supported metal catalysts it is assumed that the metal particles diffuse on a plane oxidic support. The probability of a collision of two distinct particles is a function of their diffusion coefficients. More mobile particles tend to hit with higher probability and agglomerate. This behavior can be described using the Smoluchowski equation, where the first term stems from the collision of two crystallites whose sum of volumes is equivalent to the size of s while the second term describes the disappearance of a particle of size s due to collision to any other particle [205]:

$$\frac{df(s,t)}{dt} = \int_0^s D(s')\, f(s',t)\, f(s-s',t)ds' - \int_0^\infty \left[D(s) + D(s')\right]\, f(s',t)\, f(s,t)ds' \quad (7.6)$$

Key parameter here is the particle diffusion coefficient that determines both the rate of sintering and the evolution of the particle size distribution since the diffusion coefficient is classically assumed as function of the particle radius and hence determines the relative probability of a particle of size s to sinter in comparison to a particle of other volume. However, the dependence of the diffusion coefficient on the particle radius depends on the assumed mechanism and is an open discussion. The dependence of the diffusion coefficient on the radius is assumed as r^{-4} in ref. [205–207] and r^{-2} in ref. [208] for the diffusion of 3D particles on a 2D support or as r^{-2} in ref. [209] for diffusion of 2D clusters on a 2D support, for instance. Figure 7.11 illustrates the modeled particle size distributions for $D \propto r^{-4}$. Similarly to the Ostwald ripening model, the distributions are too narrow compared to the experimental ones.

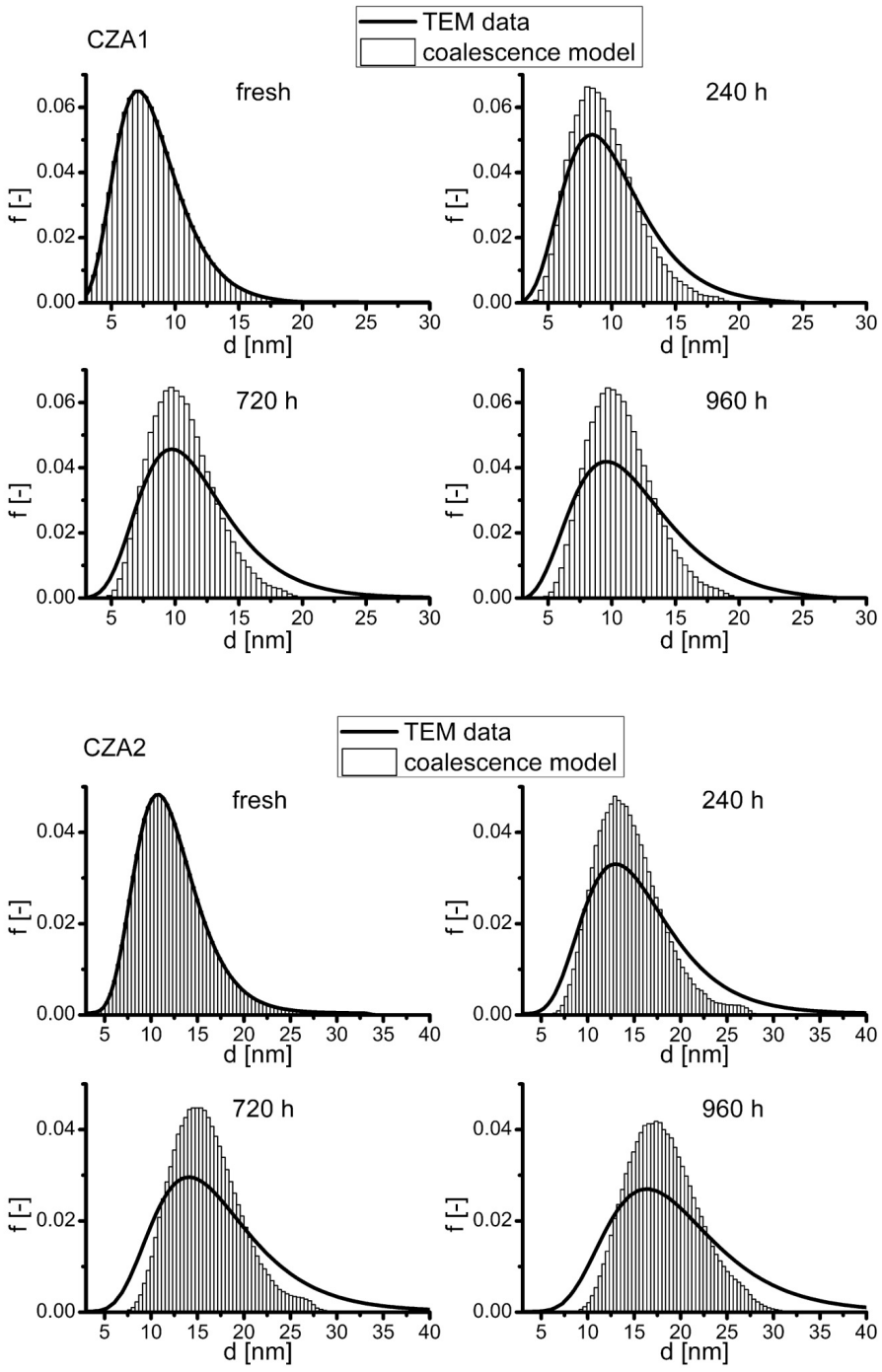

Figure 7.11: Particle Size Distributions according to TEM and classical coalescence model ($D \propto r^{-4}$) for CZA1 (top) and CZA2 (bottom)

8 Closing

8.1 Summary

The methanation of carbon dioxide has gained renewed interest in view of power-to-gas concepts based on methane. It forms the key process by converting hydrogen produced by electrolysis and carbon dioxide to SNG, which can easily be stored, transported and reconverted to electric energy relying on the existing infrastructure of gas grids, storage and power plants. This thesis addressed several questions of kinetics and reaction engineering aspects of this reaction, which is in principle well known, but has not been realized in a commercial process, yet.

The methanation of carbon dioxide is a highly exothermic reaction with volume contraction. Aside from the constraint this sets on reactor outlet temperatures, that is they need to be kept below 300°C at elevated pressure to thermodynamically allow the production of a synthetic natural gas, which can be fed to the gas grid without further purification except condensing of water, temperature control will be challenging in reactor design. This issue is even aggravated, since in technical scale the reaction is operated undiluted with pure hydrogen and carbon dioxide feed streams to avoid extensive gas separation.

In the first part of the thesis, externally cooled, single pass fixed-bed reactors were studied by detailed reactor modeling. Four continuum models were adopted for the methanation reaction and compared to each other on basis of a kinetic model from literature. A pseudo-homogeneous 1D plug flow reactor model neglecting possible transport limitations was taken as reference. The preeminent feature predicted by all models is parametric sensitivity. By varying of process or design variables like cooling temperature or tube diameter, the reactor is operated almost isothermally up to certain values, before the reactor response becomes sensitive to the influencing variable, behaves almost adiabatic and runs to equilibrium such that temperatures easily exceed 900°C. However, even there it is challenging to attain the equilibrium at the reactor outlet, since reaction rates are slow at high contents of product gases and low temperatures. The most complex pseudo-homogeneous model considers a radial distribution of porosity and radial dependence of heat dispersion coefficient. By solving the momentum balance, this results in a flow profile with maximum velocity in vicinity to the tube wall in consequence

of high void fraction in this region, which for this reason also features lower volume averaged reaction rates. Due to the assumption of a radially dependent heat dispersion coefficient it is avoided to artificially introduce a wall heat transfer coefficient and hence this model reflects temperature profiles in the cross section more accurately, in principle. Results concerning pseudo-homogeneous reactor models, however, showed that the 1D PFR model is sufficient for evaluation of maximum temperatures and conversion, because marked temperature profiles in radial direction cannot be established without runaway of the reactor. Since in this region the reaction runs to equilibrium in the hot spot, (mal)distributions of catalyst and consequently also of fluid flow do only little affect the prediction of the reactor performance in comparison to the PFR model. The 1D model was extended to a heterogeneous model by coupling to a particle model, which accounts for external and intraparticle transport of heat and mass. The dusty-gas model was chosen for description of intraparticle mass transfer. This way, no further parameters are introduced aside from tortuosity and permeability of the porous catalyst meanwhile allowing for a detailed description by molecular as well as Knudsen diffusion and viscous flux in a multicomponent gas mixture. In the hot spot region, pronounced temperature differences between gas phase and catalyst surface can be established, in excess of 100°C under certain conditions. Predicted temperature differences in the pellet are considerably smaller, which is also in accordance with the Prater number. Interestingly, maximum temperatures are significantly reduced compared to the pseudo-homogeneous model because intraparticle mass transfer limits reaction rates in particular in the hot spot and thus slows down the heat release so that heat transfer is fast enough to decrease maximum temperatures. Due to lower Knudsen diffusion coefficients in comparison to hydrogen, carbon dioxide is the limiting species.

Two further measures intended to reduce maximum temperatures were studied apart from exploiting mass transfer limitations. By separately feeding CO_2 and H_2 to the reactor so that one component is dispensed over the reactor length, heat release can be distributed over a larger volume. Simulations of fixed-bed membrane reactors, where one component is fed via a central tube, show that maximum temperatures can be kept below 500°C. The second concept addresses an improvement of heat transfer properties by structuring of the reactor, for instance by coating the catalyst on metallic honeycombs. Heat transfer in fixed-beds is dominated by a convective mechanism, since point contacts between individual particles worsen heat transfer by conduction. The basic idea behind metallic honeycombs lies in the switch from the mechanism of non-directed convection as in fixed-bed reactors to conduction in continuous solid material of high conductivity, on which the catalyst is coated. For modeling, first a 2D heterogeneous conductive reactor model has been adopted from literature and validated by comparison to a detailed 3D CFD model. In the latter, heat, mass and momentum balances

are solved with the structure of the honeycomb directly implemented in the model. The comparison for an irreversible, exothermic first-order reaction revealed that the continuum model excellently predicts maximum temperatures and conversions under a wide range of conditions. Systematic deviations observed under drastic conditions prone for establishing sharp radial temperature profiles are caused first by the assumption of 1D channels as supposed for derivation of global heat and mass transfer coefficients. This has also been observed in literature for the case of adiabatic operation by comparing 1D, 2D axial symmetric and 3D models concerning square channels. As second reason for deviation, the disregard of radial dispersion of mass has been identified. However, this assumption can be seen as immanent in derivation of any honeycomb continuum model since the channel scale is intrinsically assumed as infinitely small in comparison to the tube scale. After validation, the continuum model has been adopted to the methanation. According to the assessment of effective overall heat transfer coefficients, honeycombs are expected superior for compact reactors at relevant space velocities. This is also confirmed by modeling results. Honeycomb reactors are operated isothermally up to higher cooling temperatures, before in a narrow range of cooling temperatures hot spots with axial temperature differences smaller than 100°C can be maintained and finally with further increasing cooling temperatures hot spot temperatures jump in a parametric sensitive region to values in excess of 500°C. For maximum temperatures in the hot spot region, mass transfer to the washcoat surface slows down reaction and heat release in comparison to the fully kinetic regime so that maximum temperatures are significantly reduced. Despite preferable heat transfer characteristics, honeycombs are less appropriate in a single reactor system, since the reduced catalyst inventory prevents a fast approach to equilibrium.

Furthermore, kinetic models have been derived and evaluated for the methanation of carbon dioxide. As catalysts, high loaded Ni/Al_2O_3 systems are prepared by coprecipitation out of the metal nitrate solutions with a solution of NaOH and Na_2CO_3 as precipitation agent. XRD analysis of the precipitates shows reflexes of the hydrotalcite phase Takovite. With its characteristic layer structure, high specific surface areas in excess of 200 m^2/g are obtained after calcination at 450°C to the corresponding oxides. According to TPR results, reduction temperatures of 500°C are sufficient to fully reduce Ni. Over a wide range of conditions, kinetics can excellently be described with a simple power law solely comprising the reaction orders of hydrogen and carbon dioxide, as long as conversions are kept differential such that product gases hardly affect the kinetics. However, extrapolation to higher conversions shows that the power law systematically overestimates the reaction rates in approach to equilibrium and thus is inadequate to reflect the kinetics from differential conversion to equilibrium composition. Hence, the power law model has been extended by regard of the reaction order of water and by

introduction of adsorption terms of water or hydroxyl, respectively. Moreover, over 20 LHHW-type rate equations have been derived based on two mechanisms. Compared to the simplest power law, extended power laws reduce the mean residual markedly and systematic deviations are no longer observable. Even better reflection of the kinetic data is obtained with a LHHW-type rate equation, which according to Bartlett's χ^2 test can statistically significantly be discriminated among all formulated rate equations. The chosen kinetic model is capable to reflect the kinetics from differential to complete conversion in a temperature range at least between 180 and 340°C, pressures smaller than 15 bar and H_2/CO_2 ratios between 0.25 and 8.

During the kinetic measurements, it has been observed that methanation catalysts are prone to deactivation at higher temperatures. However, there are hardly any reports available on characterization of aged catalysts or on the prevalent mechanism of deactivation. In contrast, another coprecipitated, high loaded catalyst system, $Cu/ZnO/Al_2O_3$ for methanol synthesis, has been studied in more detail in literature. On basis of supplied characterization results, in particular Cu particle size distributions as derived by HRTEM, the sintering behavior has numerically been investigated. Sintering models of Ostwald ripening and coalescence developed for classical supported metal-oxide systems fail in describing particle size distributions of aged catalysts. It is found that particles agglomerate more randomly as predetermined by structure than predicted by classical sintering models. A random collision model is proposed, which is capable of reflecting evolving copper particle size distributions.

8.2 Outlook

During this study, many interesting questions arose which might encourage further research in this direction. For understanding the deactivation behavior observed, aged catalysts could be characterized by elementary analysis, XRD, TEM and temperature programmed oxidation to gain insight in the underlying deactivation mechanisms, potentially sintering of metallic Nickel or coking of surfaces. It could then be checked, if the presented random collision model could be transferred to this Ni/Al_2O_3 system.

Furthermore, there is still a lack in mechanistic understanding of the methanation reaction itself. In derivation of kinetic models, it is assumed that identical sites on metallic nickel surface act as active centers. One might arise the question about structure sensitivity of the methanation reaction. Do different surface plains exhibit different catalytic activities? One might speculate that this very likely in view of different heats of adsorption derived for carbon dioxide for the (110) surface compared to the denser ones by density functional theory. The observed structure sensitivity of C-O bond cleavage in carbon monoxide methanation concerning steps and kinks

also points in this direction. Furthermore, the influence of the oxide, in particular of basic sites on the support, their interaction to carbon dioxide and influence on the kinetics are still to be answered in view of both rationally synthesizing more active catalysts and understanding of kinetics. First hints could be gained by comparing a pure Ni system to well characterizable supported systems of varying oxide. Desorption experiments or IR studies of adsorbed CO_2 might be promising to probe the basicity of the systems. Concerning the methanation on Ni surfaces, many mechanisms comprising various surface species have been proposed as shortly reviewed in chapter 4, but a clear picture of the mechanism prevalent has not yet been evolved. As discussed, solely based on stationary measurements, interference about different proposed mechanism seems hardly feasible. Spectroscopic in-situ characterization as well as sound theoretical foundation by quantum mechanical calculation of elementary step kinetics as basis for derivation of elementary step kinetics could provoke a deeper understanding.

Bibliography

[1] B. Dunn, H. Kamath, J.-M. Tarascon, *Science* **2011**, *334*, 928–935.

[2] Z. Yang, J. Zhang, M. C. Kintner-Meyer, X. Lu, D. Choi, J. P. Lemmon, J. Liu, *Chemical Reviews* **2011**, *111*, 3577–3613.

[3] A Roadmap for moving to a competitive low carbon economy in 2050, European Commision, Brussels, **2011**.

[4] The Cancun Agreements, Framework Convention on Climate Change, Cancun, **2011**.

[5] Statistisches Bundesamt, Wiesbaden, **2014**.

[6] Gesetz für den Ausbau erneuerbarer Energien (Erneuerbare-Energien-Gesetz - EEG 2014), Berlin, **2014**.

[7] Energiekonzept für eine umweltschonende, zuverlässige und bezahlbare Energieversorgung, Berlin, **2010**.

[8] www.50hertz.com.

[9] F. Adamek, T. Aundrup, W. Glaunsinger, M. Kleimaier, H. Landinger, M. Leuthold, B. Lunz, A. Moser, C. Pape, H. Pluntke, N. Rotering, M. Sauer, M. Sterner, W. Wellßow, *Energiespeicher für die Energiewende. Speicherbedarf und Auswirkungen auf das Übertragungsnetz für Szenarien bis 2050*, Verband der Elektrotechnik Elektronik Informationstechnik e.V., Frankfurt, **2012**.

[10] G. L. Soloveichik, *Annual review of chemical and biomolecular engineering* **2011**, *2*, 503–527.

[11] A. Ter-Gazarian, *Energy storage for power systems*, The Institution of Engineering and Technology, **2011**.

[12] K. Bonhoff, *Chemie Ingenieur Technik* **2009**, *81*, 547–549.

[13] DVGW-Arbeitsblatt G 262, Nutzung von Gasen aus regenerativen Quellen in der öffentlichen Gasversorgung, Bonn, **2004**.

[14] S. Schiebahn, T. Grube, M. Robinius, L. Zhao, A. Otto, B. Kumar, M. Weber, D. Stolten in *Transition to Renewable Energy Systems*, Wiley-VCH, Weinheim, **2013**, pp. 813–848.

[15] M. Sterner, *Bioenergy and renewable power methane in integrated 100% renewable energy systems*, PhD Thesis, Kassel University, **2009**.

[16] M. Specht, J. Brellochs, V. Frick, B. Stürmer, U. Zuberbühler, M. Sterner, G. Waldstein, *Erdöl Erdgas Kohle* **2010**, *126*, 342–346.

[17] J. Mergel, M. Carmo, D. Fritz in *Transition to Renewable Energy Systems*, Wiley-VCH, Weinheim, **2013**, pp. 423–450.

[18] M. Streibel, N. Nakaten, T. Kempka, M. Kühn, *Energy Procedia* **2013**, *40*, 202–211.

[19] P Sabatier, J. Senderens, *Comptes Rendus Chimie* **1902**, *134*, 689.

[20] D. Schlereth, O. Hinrichsen, *Chemical Engineering Research and Design* **2014**, *92*, 702–712.

[21] D. Schlereth, O. Hinrichsen, *Industrial & Engineering Chemistry Research* **2014**, *53*, 11550–11556.

[22] D. Schlereth, P. J. Donaubauer, O. Hinrichsen, *Chemical Engineering & Technology* **2014**, *(submitted)*.

[23] F. Koschany, D. Schlereth, O. Hinrichsen, *Applied Catalysis B: Enviromental* **2015**, *(submitted)*.

[24] M. Fichtl, D. Schlereth, N. Jacobsen, I. Kasatkin, J. Schumann, M. Behrens, R. Schlögl, O. Hinrichsen, *Applied Catalysis A: General* **2015**, *(submitted)*.

[25] W. Wang, S. Wang, X. Ma, J. Gong, *Chemical Society Reviews* **2011**, *40*, 3703–3727.

[26] A. Goguet, F. C. Meunier, D. Tibiletti, J. P. Breen, R. Burch, *The Journal of Physical Chemistry B* **2004**, *108*, 20240–20246.

[27] T. Riedel, M. Claeys, H. Schulz, G. Schaub, S.-S. Nam, K.-W. Jun, M.-J. Choi, G. Kishan, K.-W. Lee, *Applied Catalysis A: General* **1999**, *186*, 201–213.

[28] C. K. Vance, C. H. Bartholomew, *Applied Catalysis* **1983**, *7*, 169–177.

[29] F.-W. Chang, M.-T. Tsay, S.-P. Liang, *Applied Catalysis A: General* **2001**, *209*, 217–227.

[30] F.-W. Chang, M.-S. Kuo, M.-T. Tsay, M.-C. Hsieh, *Applied Catalysis A: General* **2003**, *247*, 309–320.

[31] S. Abelló, C. Berrueco, D. Montané, *Fuel* **2013**, *113*, 598–609.

[32] G. Lee, M. Moon, J. Park, S. Park, S. Hong, *Korean Journal of Chemical Engineering* **2005**, *22*, 541–546.

[33] E. Vesselli, J. Schweicher, A. Bundhoo, A. Frennet, N. Kruse, *Journal of Physical Chemistry C* **2011**, *115*, 1255–1260.

[34] K. Yaccato, R. Carhart, A. Hagemeyer, A. Lesik, P. Strasser, A. F. Volpe Jr, H. Turner, H. Weinberg, R. K. Grasselli, C. Brooks, *Applied Catalysis A: General* **2005**, *296*, 30–48.

[35] M. Schoder, U. Armbruster, A. Martin, *Chemie Ingenieur Technik* **2013**, *85*, 344–352.

[36] D. E. Peebles, D. W. Goodman, J. M. White, *The Journal of Physical Chemistry* **1983**, *87*, 4378–4387.

[37] J. L. Falconer, A. E. Zagli, *Journal of Catalysis* **1980**, *62*, 280–285.

[38] S. Fujita, H. Terunuma, H. Kobayashi, N. Takezawa, *Reaction Kinetetics and Catalysis Letters* **1987**, *33*, 179–184.

[39] C. Schild, A. Wokaun, R. A. Koeppel, A. Baiker, *The Journal of Physical Chemistry* **1991**, *95*, 6341–6346.

[40] E. Vesselli, L. De Rogatis, X. Ding, A. Baraldi, L. Savio, L. Vattuone, M. Rocca, P. Fornasiero, M. Peressi, A. Baldereschi, R. Rosei, G. Comelli, *Journal of the American Chemical Society* **2008**, *130*, 11417–11422.

[41] E. Vesselli, M. Rizzi, L. De Rogatis, X. Ding, A. Baraldi, G. Comelli, L. Savio, L. Vattuone, M. Rocca, P. Fornasiero, A. Baldereschi, M. Peressi, *Journal of Physical Chemistry Letters* **2010**, *1*, 402–406.

[42] P. Bothra, G. Periyasamy, S. K. Pati, *Physical Chemistry Chemical Physics* **2013**, *15*, 5701–5706.

[43] M. Araki, V. Ponec, *Journal of Catalysis* **1976**, *44*, 439–448.

[44] S. V. Ho, P. Harriott, *Journal of Catalysis* **1980**, *64*, 272–283.

[45] I. Alstrup, *Journal of Catalysis* **1995**, *151*, 216–225.

[46] G. D. Weatherbee, C. H. Bartholomew, *Journal of Catalysis* **1982**, *77*, 460–472.

[47] S. J. Choe, H. J. Kang, D. H. Park, D. S. Huh, J. Park, *Applied Surface Science* **2001**, *181*, 265–276.

[48] M. A. Vannice, *Journal of Catalysis* **1975**, *37*, 462–473.

[49] C. P. Huang, J. T. Richardson, *Journal of Catalysis* **1978**, *51*, 1–8.

[50] V. Sanchez-Escribano, M. A. Larrubia Vargas, E. Finocchio, G. Busca, *Applied Catalysis A: General* **2007**, *316*, 68–74.

[51] M. Andersson, F. Abild-Pedersen, I. Remediakis, T Bligaard, G. Jones, J. Engbæk, O. Lytken, S. Horch, J. H. Nielsen, J. Sehested, *Journal of Catalysis* **2008**, *255*, 6–19.

[52] J. W. E. Coenen, P. F. M. T. van Nisselrooy, M. H. J. M. de Croon, P. F. H. A. van Dooren, R. Z. C. van Meerten, *Applied Catalysis* **1986**, *25*, 1–8.

[53] D. W. Blaylock, T. Ogura, W. H. Green, G. J. Beran, *The Journal of Physical Chemistry C* **2009**, *113*, 4898–4908.

[54] H. S. Bengaard, J. K. Nørskov, J. Sehested, B. S. Clausen, L. P. Nielsen, A. M. Molenbroek, J. R. Rostrup-Nielsen, *Journal of Catalysis* **2002**, *209*, 365–384.

[55] J. Engbæk, O. Lytken, J. H. Nielsen, I. Chorkendorff, *Surface Science* **2008**, *602*, 733–743.

[56] A. L. Lapidus, N. A. Gaidai, N. V. Nekrasov, L. A. Tishkova, Y. A. Agafonov, T. N. Myshenkova, *Petroleum Chemistry* **2007**, *47*, 75–82.

[57] G. G. Binder, R. R. White, *Chemical Engineering Progress* **1950**, *46*, 563–574.

[58] J. Dew, R. White, C. Sliepcevich, *Industrial & Engineering Chemistry* **1955**, *47*, 140–146.

[59] M. Solc, *Collection of Czechoslovak Chemical Communications* **1962**, *27*, 2621–2627.

[60] T. Van Herwijnen, H. Van Doesburg, W. A. De Jong, *Journal of Catalysis* **1973**, *28*, 391–402.

[61] J. H. Chiang, J. R. Hopper, *Industrial & Engineering Chemistry Product Research and Development* **1983**, *22*, 225–228.

[62] H. Inoue, M. Funakoshi, *Journal of Chemical Engineering of Japan* **1984**, *17*, 602–610.

[63] T. Kai, T. Takahashi, S. Furusaki, *The Canadian Journal of Chemical Engineering* **1988**, *66*, 343–347.

[64] J. G. Xu, G. F. Froment, *AIChE Journal* **1989**, *35*, 88–96.

[65] Audi Press Release. World premiere: Audi opens power-to-gas facility, **2013**.

[66] Solar Fuel GmbH, *The high efficiency process for the catalytic methanation of gas mixtures containing carbon dioxide and hydrogen* **2011**, *DE 10 2009 059 310 A1.*

[67] R. Bank, J. Dachs, F. Egner, V. Frick, M. Lehr, M. Specht, B. Stürmer, *Shell-and-tube reactor for carrying out catalytic gas phase reactions* **2012**, *WO 2012 035 173 A1.*

[68] S. Rönsch, A. Ortwein, *Chemie Ingenieur Technik* **2011**, *83*, 1200–1208.

[69] J. Kopyscinski, T. J. Schildhauer, S. Biollaz, *Fuel* **2010**, *89*, 1763–1783.

[70] S. Alpert, M. Sherwin, N. Cochran, Slurry phase methanation process, **1976**.

[71] T. Henrich, S. Bajohr, F. Graf, R. Reimert, *DGMK-Fachbereichstagung Energetische Nutzung von Biomassen* **2008**, 2008–2.

[72] S. Bajohr, T. Henrich, *GWF-Gas/Erdgas* **2009**, *150*, 2.

[73] K. H. Eisenlohr, F. W. Moeller, M. Dry, *American Chemical Society Division of Fuel Chemistry* **1974**, *19*, 1–9.

[74] J. Panek, J. Grasser, *Practical experience gained during the first twenty years of operation of the great plains gasification plant and implications for future projects* **2006**, *Technical report prepared for US Department of Energy*.

[75] Haldor Topsøe, *From solid fuels to substitute natural gas (SNG) using TREMP* **2008**, *Technical report*.

[76] R Lohmueller, *Linde - Berichte aus Technik und Wissenschaft* **1977**, 3–11.

[77] H. Harms, B. Höhlein, A. Skov, *Chemie Ingenieur Technik* **1980**, *52*, 504–515.

[78] J. P. Strakey, A. J. Forney, W. P. Haynes, *Energy Research and Development Administration Pittsburgh* **1975**.

[79] R. L. Ensell, H. J. F. Stroud in Proceedings of the international gas research conference, British Gas Corporation UK, **1983**, pp. 472–81.

[80] G. Friedrichs, G. Wismann, *Untersuchung über die Einsatzmöglichkeiten gekühlter Gas-Feststoff-Druckwirbelschichten, insbesondere der COMFLUX-Technik für chemische Prozesse*, Thyssengas-GmbH, **1987**.

[81] N. O. Lemcoff, S. I. Pereira Duarte, O. M. Martinez, *Reviews in Chemical Engineering* **1990**, *6*, 229–292.

[82] G. F. Froment, K. B. Bischoff, J. De Wilde, *Chemical reactor analysis and design*, John Wiley & Sons, New York, **2011**.

[83] G. W. Koning, A. E. Kronberg, W. P. M. van Swaaij, *Chemical Engineering Science* **2006**, *61*, 3167–3175.

[84] P. S. Hagan, M Herskowitz, C Pirkle, *SIAM Journal on Applied Mathematics* **1988**, *48*, 1083–1101.

[85] V. Hlavacek, H. Hofmann, *Chemical Engineering Science* **1970**, *25*, 187–199.

[86] J. Puszynski, D. Snita, V. Hlavacek, H. Hofmann, *Chemical Engineering Science* **1981**, *36*, 1605–1609.

[87] E. Tsotsas in *VDI-Wärmeatlas*, VDI Buch, Springer Berlin Heidelberg, **2006**, Chapter 25, pp. 422–430.

[88] E. Tsotsas in *VDI-Wärmeatlas*, VDI Buch, Springer Berlin Heidelberg, **2006**, Chapter 98, pp. 1213–1227.

[89] A. Iordanidis, *Mathematical modeling of catalytic fixed bed reactors*, PhD Thesis, Twente University Press, **2002**.

[90] K. R. Westerterp, V. V. Dil'man, A. E. Kronberg, *AIChE Journal* **1995**, *41*, 2013–2028.

[91] A. G. Dixon, M. Nijemeisland, E. H. Stitt, *Advances in Chemical Engineering* **2006**, *31*, 307–389.

[92] E. N. Fuller, P. D. Schettler, J. C. Giddings, *Industrial & Engineering Chemistry* **1966**, *58*, 18–27.

[93] R. Villet, R. Wilhelm, *Industrial & Engineering Chemistry* **1961**, *53*, 837–840.

[94] C. Rieckmann, *Lösung des Problems der Diffusion und Reaktion in dreidimensionalen Porennetzwerken für allgemeine Kinetiken*, PhD Thesis, TU Hamburg-Harburg, **1997**.

[95] R. Taylor, R. Krishna, *Multicomponent Mass Transfer*, John Wiley & Sons, New York, **1993**.

[96] R. Krishna, *Chemical Engineering Science* **1993**, *48*, 845–861.

[97] R. Krishna, J. A. Wesselingh, *Chemical Engineering Science* **1997**, *52*, 861–911.

[98] J.-N. Park, E. W. McFarland, *Journal of Catalysis* **2009**, *266*, 92–97.

[99] H. Y. Kim, H. M. Lee, J.-N. Park, *Journal of Physical Chemistry C* **2010**, *114*, 7128–7131.

[100] K. P. Brooks, J. Hu, H. Zhu, R. J. Kee, *Chemical Engineering Science* **2007**, *62*, 1161–1170.

[101] H. Kusama, K. K. Bando, K. Okabe, H. Arakawa, *Applied Catalysis A: General* **2000**, *197*, 255–268.

[102] M. Sudiro, A. Bertucco, G. Groppi, E. Tronconi in *Computer Aided Chemical Engineering*, *Vol. Volume 28*, (Eds.: S. Pierucci, G. B. Ferraris), Elsevier, **2010**, pp. 691–696.

[103] J. Kopyscinski, *Production of synthetic natural gas in a fluidized bed reactor*, PhD Thesis, ETH Zurich, **2010**.

[104] M. C. Seemann, T. J. Schildhauer, S. M. A. Biollaz, S. Stucki, A. Wokaun, *Applied Catalysis A: General* **2006**, *313*, 14–21.

[105] L. M. Aparicio, *Journal of Catalysis* **1997**, *165*, 262–274.

[106] A. P. de Wasch, G. F. Froment, *Chemical Engineering Science* **1972**, *27*, 567–576.

[107] M. Kleiber, R. Joh in *VDI-Wärmeatlas*, VDI Buch, Springer Berlin Heidelberg, **2006**, Chapter 10, pp. 103–132.

[108] M. Winterberg, E. Tsotsas, A. Krischke, D. Vortmeyer, *Chemical Engineering Science* **2000**, *55*, 967–979.

[109] M. Giese, *Strömung in porösen Medien unter Berücksichtigung effektiver Viskositäten*, PhD Thesis, TU München, **1997**.

[110] J. Skrzypek, M. Grzesik, R. Szopa, *Chemical Engineering Science* **1984**, *39*, 515–521.

[111] N. Wakao, S. Kaguei, T. Funazkri, *Chemical Engineering Science* **1979**, *34*, 325–336.

[112] B. Finlayson, *Catalysis Reviews - Science and Engineering* **1974**, *10*, 69–138.

[113] R. E. Hayes, *Introduction to Catalytic Combustion*, Gordon and Breach, Amsterdam, **1997**.

[114] J. Kaspar, P. Fornasiero, N. Hickey, *Catalysis Today* **2003**, *77*, 419–449.

[115] R. M. Heck, *Catalysis Today* **1999**, *53*, 519–523.

[116] G. Groppi, E. Tronconi, *Chemical Engineering Science* **2000**, *55*, 2161–2171.

[117] J. H. Abbott, T. R. Boger, L. He, S. Khanna, K. R. Miller, C. M. Sorensen, *Metal honeycomb substrates for chemical and thermal applications* **2004**, *US 2004 024533*.

[118] W. A. Cutler, L. He, A. R. Olszewski, C. M. Sorensen, *Thermally conductive honeycombs for chemical reactors* **2001**, *US2003 0100448*.

[119] G. Groppi, E. Tronconi, C. Cortelli, R. Leanza, *Industrial & Engineering Chemistry Research* **2011**, *51*, 7590–7596.

[120] C. G. Visconti, E. Tronconi, G. Groppi, L. Lietti, M. Iovane, S. Rossini, R. Zennaro, *Chemical Engineering Journal* **2011**, *171*, 1294–1307.

[121] G. Groppi, E. Tronconi, *AIChE Journal* **1996**, *42*, 2382–2387.

[122] R. E. Hayes, A. Rojas, J. Mmbaga, *Catalysis Today* **2009**, *147*, S113–S119.

[123] J. Galindo, J. R. Serrano, P. Piqueras, O. Garcia-Afonso, *Energy* **2012**, *43*, 201–213.

[124] C. G. Visconti, G. Groppi, E. Tronconi, *Chemical Engineering Science* **2013**, *223*, 224–230.

[125] J. Chen, H. Yang, N. Wang, Z. Ring, T. Dabros, *Applied Catalysis A: General* **2008**, *345*, 1–11.

[126] R. Aris, *Proceedings of the Royal Society of London. Series A. Mathematical and Physical Sciences* **1956**, *235*, 67–77.

[127] G. Groppi, A. Belloli, E. Tronconi, P. Forzatti, *Chemical Engineering Science* **1995**, *50*, 2705–2715.

[128] R. H. Heck, J. Wei, J. R. Katzer, *AIChE Journal* **1976**, *22*, 477–484.

[129] P. Canu, S. Vecchi, *AIChE Journal* **2002**, *48*, 2921–2935.

[130] A. Montebelli, C. G. Visconti, G. Groppi, E. Tronconi, C. Ferreira, S. Kohler, *Catalysis Today* **2013**, *215*, 176–185.

[131] A. Montebelli, C. G. Visconti, G. Groppi, E. Tronconi, S. Kohler, *Chemical Engineering Journal* **2014**, *255*, 257–265.

[132] G. Groppi, E. Tronconi, *Catalysis Today* **2001**, *69*, 63–73.

[133] C. G. Visconti, E. Tronconi, L. Lietti, G. Groppi, P. Forzatti, C. Cristiani, R. Zennaro, S. Rossini, *Applied Catalysis A: General* **2009**, *370*, 93–101.

[134] D. F. Fairbanks, C. R. Wilke, *Industrial & Engineering Chemistry* **1950**, *42*, 471–475.

[135] E. Tronconi, G. Groppi, T. Boger, A. Heibel, *Chemical Engineering Science* **2004**, *59*, 4941–4949.

[136] T. Boger, A. K. Heibel, *Chemical Engineering Science* **2005**, *60*, 1823–1835.

[137] G. Groppi, E. Tronconi, *Catalysis Today* **2005**, *105*, 297–304.

[138] G. F. Carey, B. A. Finlayson, *Chemical Engineering Science* **1975**, *30*, 587–596.

[139] J. R. Rostrup-Nielsen, K. Pedersen, J. Sehested, *Applied Catalysis A: General* **2007**, *330*, 134–138.

[140] J. Amsden, H. Boulc, A. Heibel, N. Partridge, *Multi-Tubular Reactors With Monolithic Catalysts* **2009**, *US 2009 0176895*.

[141] J. Gao, Y. Wang, Y. Ping, D. Hu, G. Xu, F. Gu, F. Su, *RSC Advances* **2012**, *2*, 2358–2368.

[142] E. Novak, K. Fodor, T. Szailer, A. Oszko, A. Erdöhelyi, *Topics in Catalysis* **2002**, *20*, 107–117.

[143] A. Beuls, C. Swalus, M. Jacquemin, G. Heyen, A. Karelovic, P. Ruiz, *Applied Catalysis B: Environmental* **2012**, *113*, 2–10.

[144] E. Zagli, J. L. Falconer, *Journal of Catalysis* **1981**, *69*, 1–8.

[145] T. Abe, M. Tanizawa, K. Watanabe, A. Taguchi, *Energy & Environmental Science* **2009**, *2*, 315–321.

[146] D. Li, N. Ichikuni, S. Shimazu, T. Uematsu, *Applied Catalysis A: General* **1999**, *180*, 227–235.

[147] J. Kopyscinski, T. J. Schildhauer, F. Vogel, S. M. A. Biollaz, A. Wokaun, *Journal of Catalysis* **2010**, *271*, 262–279.

[148] V. M. Shinde, G. Madras, *AIChE Journal* **2014**, *60*, 1027–1035.

[149] G. Peng, S. Sibener, G. C. Schatz, S. T. Ceyer, M. Mavrikakis, *The Journal of Physical Chemistry C* **2012**, *116*, 3001–3006.

[150] F. J. Dumez, L. H. Hosten, G. F. Froment, *Industrial & Engineering Chemistry Fundamentals* **1977**, *16*, 298–301.

[151] G. H. Jonker, J.-W. Veldsink, A. A. Beenackers, *Industrial & Engineering Chemistry Research* **1997**, *36*, 1567–1579.

[152] A. Holleman, E. Wiberg, N. Wiberg, *Lehrbuch der Anorganischen Chemie*, Walter de Gruyter-Verlag, Berlin, 102nd ed., **2007**.

[153] K. Mocala, A. Navrotsky, *Journal of the American Ceramic Society* **1989**, *72*, 826–832.

[154] P. H. De Korte, E. Doesburg, C. P. De Winter, L. L. Van Reijen, *Solid State Ionics* **1985**, *16*, 73–80.

[155] Y.-X. Pan, C.-J. Liu, Q. Ge, *Journal of Catalysis* **2010**, *272*, 227–234.

[156] A. E. Aksoylu, A. N. Akin, Z. I. Önsan, D. L. Trimm, *Applied Catalysis A: General* **1996**, *145*, 185–193.

[157] P. Panagiotopoulou, D. I. Kondarides, X. E. Verykios, *Applied Catalysis B: Environmental* **2009**, *88*, 470–478.

[158] T. Inui, M. Funabiki, *Chemistry Letters* **1978**, *7*, 251–252.

[159] R. Maatman, S. Hiemstra, *Journal of Catalysis* **1980**, *62*, 349–356.

[160] M. Peter, M. B. Fichtl, H. Ruland, S. Kaluza, M. Muhler, O. Hinrichsen, *Chemical Engineering Journal* **2012**, *203*, 480–491.

[161] D. Chen, R. Lodeng, H. Svendsen, A. Holmen, *Industrial & engineering chemistry research* **2010**, *50*, 2600–2612.

[162] L. Maier, B. Schädel, K. Herrera Delgado, S. Tischer, O. Deutschmann, *Topics in catalysis* **2011**, *54*, 845–858.

[163] P. B. Weisz, C. D. Prater, *Advances in Catalysis* **1954**, *6*, 142–196.

[164] J. B. Anderson, *Chemical Engineering Science* **1963**, *18*, 147–148.

[165] D. E. Mears, *Industrial & Engineering Chemistry Process Design and Development* **1971**, *10*, 541–547.

[166] R. Malhotra, *Fossil energy*, Springer, New York, **2012**.

[167] G. A. Olah, A. Goeppert, G. K. S. Prakash, *Beyond Oil and Gas: The Methanol Economy*, Wiley-VCH, Weinheim, **2009**.

[168] G. A. Olah, *Angewandte Chemie* **2013**, *52*, 104–107.

[169] P. Forzatti, L. Lietti, *Catalysis Today* **1999**, *52*, 165–181.

[170] C. H. Bartholomew, *Applied Catalysis A: General* **2001**, *212*, 17–60.

[171] M. V. Twigg, M. S. Spencer, *Topics in Catalysis* **2003**, *22*, 191–203.

[172] G. Hochgesand, *Industrial & Engineering Chemistry* **1970**, *62*, 37–43.

[173] H. H. Kung, *Catalysis Today* **1992**, *11*, 443–453.

[174] M. R. Rahimpour, B. Moghtaderi, A. Jahanmiri, N. Rezaie, *Chemical Engineering & Technology* **2005**, *28*, 226–234.

[175] *Handbook of Heterogeneous Catalysis: Online*, (Eds.: G. Ertl, H. Knözinger, F. Schüth, J. Weitkamp), Wiley-VCH, Weinheim, **2008**.

[176] T. W. Hansen, A. T. DeLaRiva, S. R. Challa, A. K. Datye, *Accounts of Chemical Research* **2013**, *46*, 1720–1730.

[177] G. Prieto, J. Zečević, H. Friedrich, K. P. de Jong, P. E. de Jongh, *Nature Materials* **2013**, *12*, 34–39.

[178] M. B. Fichtl, J. Schumann, N. Jacobsen, W. Busser, M. Muhler, M. Behrens, R. Schlögl, O. Hinrichsen, *Journal of Catalysis* **2015**, *(submitted)*.

[179] P. L. Hansen, J. B. Wagner, S. Helveg, J. R. Rostrup-Nielsen, B. S. Clausen, H. Topsøe, *Science* **2002**, *295*, 2053–2055.

[180] J. Schumann, T. Lunkenbein, A. Tarasov, N. Thomas, R. Schlögl, M. Behrens, *ChemCatChem* **2014**, *6*, 2889–2897.

[181] M. Behrens, R. Schlögl, *Zeitschrift für Anorganische und Allgemeine Chemie* **2013**, *639*, 2683–2695.

[182] M. Behrens, I. Kasatkin, S. Kühl, G. Weinberg, *Chemistry of Materials* **2010**, *22*, 386–397.

[183] O. Hinrichsen, T. Genger, M. Muhler, *Chemical Engineering & Technology* **2000**, *23*, 956–959.

[184] M. B. Fichtl, J. Schumann, I. Kasatkin, N. Jacobsen, M. Behrens, R. Schlögl, M. Muhler, O. Hinrichsen, *Angewandte Chemie* **2014**, *53*, 7043–7047.

[185] S. Kuld, C. Conradsen, P. G. Moses, I. Chorkendorff, J. Sehested, *Angewandte Chemie* **2014**, *53*, 5941–5945.

[186] S. Zander, E. L. Kunkes, M. E. Schuster, J. Schumann, G. Weinberg, D. Teschner, N. Jacobsen, R. Schlögl, M. Behrens, *Angewandte Chemie* **2013**, *52*, 6536–6540.

[187] O. Martin, J. Perez-Ramirez, *Catalysis Science & Technology* **2013**, *3*, 3343–3352.

[188] M. Behrens, S. Zander, P. Kurr, N. Jacobsen, J. Senker, G. Koch, T. Ressler, R. W. Fischer, R. Schlögl, *Journal of the American Chemical Society* **2013**, *135*, 6061–6068.

[189] J. Skrzypek, J. Sloczynski, S. Ledakowicz, *Methanol synthesis: science and engineering*, Polish Scientific Publishers, **1994**.

[190] D. G. Löffler, S. D. McDermott, C. N. Renn, *Journal of Power Sources* **2003**, *114*, 15–20.

[191] T. Kandemir, F. Girgsdies, T. C. Hansen, K.-D. Liss, I. Kasatkin, E. L. Kunkes, G. Wowsnick, N. Jacobsen, R. Schlögl, M. Behrens, *Angewandte Chemie* **2013**, *52*, 5166–5170.

[192] Y. Choi, K. Futagami, T. Fujitani, J. Nakamura, *Applied Catalysis A: General* **2001**, *208*, 163–167.

[193] A. T. DeLaRiva, T. W. Hansen, S. R. Challa, A. K. Datye, *Journal of Catalysis* **2013**, *308*, 291–305.

[194] J. F. Creemer, S. Helveg, G. H. Hoveling, S. Ullmann, A. M. Molenbroek, P. M. Sarro, H. W. Zandbergen, *Ultramicroscopy* **2008**, *108*, 993–998.

[195] D. B. Rasmussen, T. V. W. Janssens, B. Temel, T. Bligaard, B. Hinnemann, S. Helveg, J. Sehested, *Journal of Catalysis* **2012**, *293*, 205–214.

[196] P. C. K. Vesborg, I. Chorkendorff, I. Knudsen, O. Balmes, J. Nerlov, A. M. Molenbroek, B. S. Clausen, S. Helveg, *Journal of Catalysis* **2009**, *262*, 65–72.

[197] J. D. Grunwaldt, A. M. Molenbroek, N. Y. Topsøe, H. Topsøe, B. S. Clausen, *Journal of Catalysis* **2000**, *194*, 452–460.

[198] H. Wilmer, O. Hinrichsen, *Catalysis letters* **2002**, *82*, 117–122.

[199] A. K. Datye, Q. Xu, K. C. Kharas, J. M. McCarty, *Catalysis Today* **2006**, *111*, 59–67.

[200] G. A. Fuentes, E. Salinas-Rodriguez in *Studies in Surface Science and Catalysis*, *Vol. Volume 139*, (Eds.: G. W. R. J.J. Spivey, B. H. Davis), Elsevier, **2001**, pp. 503–510.

[201] S. C. Parker, C. T. Campbell, *Physical Review B* **2007**, *75*, 035430.

[202] C. T. Campbell, *Science* **2002**, *298*, 811–814.

[203] S. C. Parker, C. T. Campbell, *Topics in Catalysis* **2007**, *44*, 3–13.

[204] B. Meyer, D. Marx, *Physical Review B* **2004**, *69*, 235420.

[205] M. J. J. Jak, C. Konstapel, A. van Kreuningen, J. Verhoeven, J. W. M. Frenken, *Surface Science* **2000**, *457*, 295–310.

[206] F. Behafarid, B. Roldan Cuenya, *Surface Science* **2012**, *606*, 908–918.

[207] P. J. F. Harris, *International Materials Reviews* **1995**, *40*, 97–115.

[208] N. L. Wu, J. Phillips, *Journal of Catalysis* **1988**, *113*, 129–143.

[209] D. Kandel, *Physical Review Letters* **1997**, *79*, 4238–4241.

List of Figures

List of Tables

List of Symbols

Latin symbols

A	depending on model	pre-exponential factor
B	[m^2]	permeability
D	[m^2 s^{-1}]	diffusion or dispersion coefficient
Da	[-]	Damköhler number
E_A	[J mol^{-1}]	activation energy
F	[N]	force
G	[J mol^{-1}]	Gibbs free energy
$GHSV$	[h^{-1}]	Gas hourly space velocity
H	[J mol^{-1}]	enthalpy
J	[mol m^{-2} s^{-1}]	molar flux
K	depending on model	adsorption or equilibrium constant
K_h	[W m^{-2} K^{-1}]	heat transfer coefficient
K_m	[kg m^{-2} s^{-1}]	mass transfer coefficient
L	[m]	length
M	[kg mol^{-1}]	molar mass
N	[-]	number
Nu	[-]	Nusselt number
P	[kg m s^{-1}]	momentum
Pe	[-]	Peclet number
Pr	[-]	Prandtl number
R	[J mol^{-1} K^{-1}]	ideal gas constant
Re	[-]	Reynolds number
S	[J mol^{-1} K^{-1}]	entropy
Sc	[-]	Schmidt number
Sh	[-]	Sherwood number
T	[K]	temperature
U_A	[W m^{-2} K^{-1}]	heat transfer coefficient
W	[kg m^{-2} s^{-1}]	mass flux

X	[-]	conversion
Y	[-]	yield
c	[mol m^{-3}]	concentration
c_p	[J mol^{-1} K^{-1}] or [J kg^{-1} K^{-1}]	heat capacity
d	[m]	diameter
f	[-]	friction factor
j_H	[W m^{-2}]	heat flux
j_M	[mol m^{-2} s^{-1}]	molar flux
k	depending on model	rate constant
k_B	[J K^{-1}]	Boltzmann constant
k_H	[W m^{-2} K^{-1}]	heat transfer coefficient
k_M	[m s^{-1}]	mass transfer coefficient
m	[kg]	mass
m	[m]	pitch size
p	[Pa]	(partial) pressure
r	[m]	radial coordinate or radius
r	depending on model	reaction rate
t	[s]	time
u	[m s^{-1}]	velocity
v	[-]	specific diffusion volumen
w	[-]	mass fraction
x	[-]	mole fraction
y	[m]	radial coordinate
z	[m]	axial coordinate

Greek symbols

Λ	[m^2 s^{-1}]	radial dispersion coefficient
Ω	[mol m^{-1} s^{-1}]	auxiliary variable for DGM
α	[W m^{-2} K^{-1}]	heat transfer coefficient
β	[-]	Prater number
δ	[m]	thickness of washcoat
ϵ	[-]	porosity/void fraction
η_i	[-]	effectiveness factor for reaction i

λ	[W m^{-1} K^{-1}]	thermal conductivity
λ	[m]	mean free path
μ	[Pa s]	dynamic viscosity
$\nu_{i,j}$	[-]	stoichiometric coefficient of component i in reaction j
ξ	[-]	volume fraction of washcoat
ρ	[kg m^{-3}]	density
τ	[-]	tortuosity
τ	[s]	hydrodynamic residence time
ψ	[-]	bed porosity

Subscripts

BP	bypass
FB	fixed-bed
HC	honeycomb
P	pore
ax	axial
e	effective
g	gas phase
max	maximum
r	radial
ref	reference
s	solid phase
tot	total
w	wall

Publication list

Journal Publications

First and joint first authorships

- D. Schlereth, O. Hinrichsen, *A fixed-bed reactor modeling study on the methanation of CO_2*, Chemical Engineering Research and Design **2014**, 92, 702-712.
- D. Schlereth, O. Hinrichsen, *Comparison of a Pseudocontinuous, Heterogeneous 2D Conductive Monolith Reactor Model to a 3D Computational Fluid Dynamics Model*, Industrial & Engineering Chemistry Research **2014**, 53, 11550-11556.
- F. Koschany, D. Schlereth, O. Hinrichsen, *On the kinetics of the methanation of carbon dioxide on coprecipitated Ni/Al_2O_3*, Applied Catalysis B: Environmental, submitted.
- M. B. Fichtl, D. Schlereth, N. Jacobsen, I. Kasatkin, J. Schumann, M. Behrens, R. Schlögl, O. Hinrichsen, *Kinetics of deactivation on $Cu/ZnO/Al_2O_3$ methanol synthesis catalysts*, submitted.
- D. Schlereth, P. J. Donaubauer, O. Hinrichsen, *Metallic honeycombs as catalyst supports for the methanation of carbon dioxide*, Chemical Engineering & Technology, submitted.

Selected conference papers

Oral presentations

- D. Schlereth, O. Hinrichsen, *Chemical Reactor Modeling for the Methanation of Carbon Dioxide*, European Congress of Chemical Engineering - ECCE 9 (The Hague, The Netherlands, **2013**).

- D. Schlereth, O. Hinrichsen, *Chemical Reactor Modeling for the Methanation of Carbon Dioxide*, Jahrestreffen Reaktionstechnik (Würzburg, Germany, **2013**).
- D. Schlereth, P.J. Donaubauer, O. Hinrichsen, *Comparison of a Pseudocontinuous, Heterogeneous 2D Conductive Monolith Reactor Model to a 3D CFD Model*, International Symposium on Chemical Reaction Engineering - ISCRE 23 (Bangkok, Thailand, **2014**).

Poster presentations

- D. Schlereth, M. Aumann, O. Hinrichsen *A Modeling Study on Reactor Concepts for the Methanation of Carbon Dioxide*, EuropaCat XI (Lyon, France, **2013**).
- D. Schlereth, O. Hinrichsen, *Reaction engineering for the methanation of carbon dioxide - a modeling study on reactor concepts*, 47. Jahrestreffen Deutscher Katalytiker (Weimar, Germany, **2014**).
- D. Schlereth, K. Mietaschk, F. Koschany, O. Hinrichsen, *Kinetic modeling for the methanation of carbon dioxide*, Jahrestreffen Reaktionstechnik (Würzburg, Germany, **2014**).
- D. Schlereth, F. Koschany, K. Mietaschk, O. Hinrichsen, *Kinetic and Reactor Modeling for the Methanation of CO_2*, International Conference on Chemical Reactors - Chemreactor 21 (Delft, The Netherlands, **2014**).

Licensing Information

License for chapter 4

Chapter 4 is reprinted with permission from *'D. Schlereth, O. Hinrichsen, Chemical Engineering Research and Design 2014, 92, 702-712'.* Copyright 2014 Elsevier.

ELSEVIER LICENSE
TERMS AND CONDITIONS

Nov 05, 2014

This is a License Agreement between David Schlereth ("You") and Elsevier ("Elsevier") provided by Copyright Clearance Center ("CCC"). The license consists of your order details, the terms and conditions provided by Elsevier, and the payment terms and conditions.

All payments must be made in full to CCC. For payment instructions, please see information listed at the bottom of this form.

Supplier	Elsevier Limited The Boulevard,Langford Lane Kidlington,Oxford,OX5 1GB,UK
Registered Company Number	1982084
Customer name	David Schlereth
Customer address	TUM, Department Chemie Garching, 85747
License number	3502480154786
License date	Nov 05, 2014
Licensed content publisher	Elsevier
Licensed content publication	Chemical Engineering Research and Design
Licensed content title	A fixed-bed reactor modeling study on the methanation of CO2
Licensed content author	David Schlereth,Olaf Hinrichsen
Licensed content date	April 2014
Licensed content volume number	92
Licensed content issue number	4
Number of pages	11
Start Page	702
End Page	712
Type of Use	reuse in a thesis/dissertation
Portion	full article
Format	both print and electronic
Are you the author of this Elsevier article?	Yes
Will you be translating?	No
Order reference number	1
Title of your thesis/dissertation	Kinetic and Reactor Modeling for the Methanation of Carbon Dioxide
Expected completion date	Dec 2014
Estimated size (number of pages)	200
Elsevier VAT number	GB 494 6272 12

License for section 5.1

Section 5.1 is reprinted with permission from *'D. Schlereth, O. Hinrichsen, Industrial & Engineering Chemistry Research 2014, 53, 11550-11556'*. Copyright 2014 American Chemical Society.